UNIVERSITY OF SOUTHAMPTON

FACULTY OF ENGINEERING, SCIENCE AND MATHEMATICS

School of Chemistry

Structural studies of layered transition metal oxides

by

Peter James Hickey

Thesis for the degree of Doctor of Philosophy

October 2009

UNIVERSITY OF SOUTHAMPTON

ABSTRACT

FACULTY OF ENGINEERING, SCIENCE AND MATHEMATICS

SCHOOL OF CHEMISTRY

Doctor of Philosophy

Structural studies of layered transition metal oxides

By Peter Hickey

A number of transition metal oxide materials, both new and previously reported, have been synthesised, their structures based on the $n = 2$ Ruddlesden-Popper layered perovskites. Their structures were determined through Rietveld refinement against X-ray and neutron powder diffraction, supported by vibrating sample magnetometry and thermal analysis.

The structure of the double layered phase $Gd_2SrCo_2O_7$ was determined in the temperature range 300 – 973 K by refinement of powder neutron diffraction data. The room temperature structure is tetragonal, and displays small tilts of the oxygen sublattice that are described by a $\sqrt{2}a_0 \times \sqrt{2}a_0 \times c$ supercell model in the space group $P4_2/mnm$ rather than the idealised $Sr_3Ti_2O_7$ $I4/mmm$ structure as previously reported. A structural transition at ~ 580 K is characterised by reduction in the unit cell symmetry and distortion of CoO_6 octahedra; the behaviour is concurrent with a spin crossover in the Co (III) ions from intermediate to high spin.

The structure of the new phase $Nd_2BaCo_2O_7$ was determined in the temperature range 298 – 873 K by refinement of powder neutron diffraction data. At all temperatures, the structure is metrically tetragonal, however the octahedral rotations are best described in the orthorhombic space group *Bbcb*, with $a = b = \sqrt{2}a_0$.

The structures of the phases $Ln_2SrFe_2O_7$ (*Ln* = La, Nd, Gd) have been determined by refinement of variable temperature powder neutron diffraction data. At room temperature all the materials crystallise in the tetragonal space group $P4_2/mnm$, isostructural with the phase $Tb_2BaFe_2O_7$. On heating, the gadolinium and neodymium phases undergo transitions to lower symmetry; the octahedral tilts of the high temperature phases are best described in the space group *Bbmm*.

The new phases $Nd_{2-x}Sr_{1+x}Fe_{2-x}O_7$ have been prepared and their structures determined by Rietveld refinement of room temperature powder neutron diffraction. All the materials crystallise in the tetragonal space group $P4_2/mnm$. The degree of octahedral tilting decreases as x increases, indicating a reduction of compression of the perovskite lattice as the average *A*-site cationic radius increases.

The phase Sr_3CoNbO_7 has been prepared and its structure determined by refinement of powder neutron diffraction data. At room temperature and 3.4 K there is no evidence of magnetic ordering, *B*-site cationic ordering or octahedral tilting. The material is isostructural with the undistorted $Sr_3Ti_2O_7$, which implies that the spin state of Co (III) in the material is low spin.

The material $Sr_3Ti_2O_7$ was prepared and its structure determined in the temperature range 298 – 1073 K. At all temperatures, the structure is tetragonal, with no rotations of octahedra. Unit cell parameters and bond lengths expand smoothly over the temperature range.

Table of contents

DECLARATION OF AUTHORSHIP

I, Peter Hickey, declare that the thesis entitled

Structural studies of layered transition metal oxides

and the work presented in it is my own. I confirm that:

- This work was done wholly or mainly while in candidature for a research degree at this university;
- Where any part of this thesis has previously been submitted for a degree or any other qualification at this University or any other institution, this has been clearly stated;
- Where I have consulted the published work of others, this is always clearly attributed;
- Where I have quoted from the work of others, the source is always given. With the exception of such quotations, this thesis is entirely my own work;
- I have acknowledged all main sources of help;
- Where the thesis is based on work done by myself jointly with others, I have made clear exactly what was done by others and what I have contributed myself;
- Parts of this work have been published as:

P. J. Hickey, C. S. Knee, P. F. Henry and M. T. Weller, *Physical Review*, 2007, **B75**, 024113

Signed:

Date:

Chapter 1 – Introduction

Transition metal oxide materials

Transition metal oxides are materials containing at least one transition metal, often with at least one other metal ion to charge balance and stabilise the structure. Their structures are usually derived from MO_n polyhedra sharing corners, edges or faces, formed into a full crystal structure by stacking. Sharing vertices, edges or faces of octahedra can lead to short *M*-O-*M* distances, leading to unusual properties caused by orbital overlap between the metal sites.

Constraining metal ions in a rigid MO_n lattice can cause stabilisation of unusual oxidation states or coordination geometries, which can be exploited by solid state chemists to tune material properties.

The structure formed by a material is determined by the metal ions it contains, the oxygen content (and non-stochiometry) and by the reaction conditions: all these parameters may be tuned to produce materials with specific properties.

One of the most studied structure types in materials chemistry is based on the mineral perovskite.

Perovskites

Perovskites are formed from corner sharing MO_6 octahedra, with the general formula ABO_3. *A* is a large, charge balancing cation (for example, Sr^{2+}, La^{3+}, K^{+}) and *B*, a smaller cation, typically a transition metal (Cu^{2+}, Fe^{3+}, Co^{2+}). A great deal of structural chemistry can arise simply from the modification of this simple lattice type. Both the *A* and *B* sites can be partially substituted, to form materials of the type $A_{1-x}A'_xBO_3$ or $AB_{1-x}B'_xO_3$, and the oxygen stochiometry can be varied to produce materials such as $ABO_{3-\delta}$. The stochiometric materials $A(BB')_{0.5}O_3$ are collectively known as double perovskites, and the interaction between *d* electrons on the linked *B* sites leads to a number of interesting structures and properties, that will be discussed further below.

Even without substitution, the structures of perovskite materials can be complex. The structure of the cubic perovskite $SrTiO_3$ is shown in Figure 1.1. Because the bonding requirements of the Sr^{2+} and Ti^{4+} ions are satisfied in this structure with no tilting of octahedra, it is stable. In other ABO_3 materials, this may not be the case. The simplest example of this is the original Perovskite material, $CaTiO_3$. The atomic arrangement of atoms was first proposed by the mineralogist Perovski and was similar to the $SrTiO_3$ structure previously discussed, however more recent work has shown that the material adopts an orthorhombic structure at room temperature, derived from the rotation of TiO_6 octahedra. [1]

A wide range of distortions based on correlated tilts and rotation of octahedra are possible. Glazer proposed a notation to characterise the tilt system and examined possible tilting

systems in perovskite materials in 1972. [2] All possible structures are derived purely from octahedral tilts (that is, no significant cation displacements can be described in these terms).

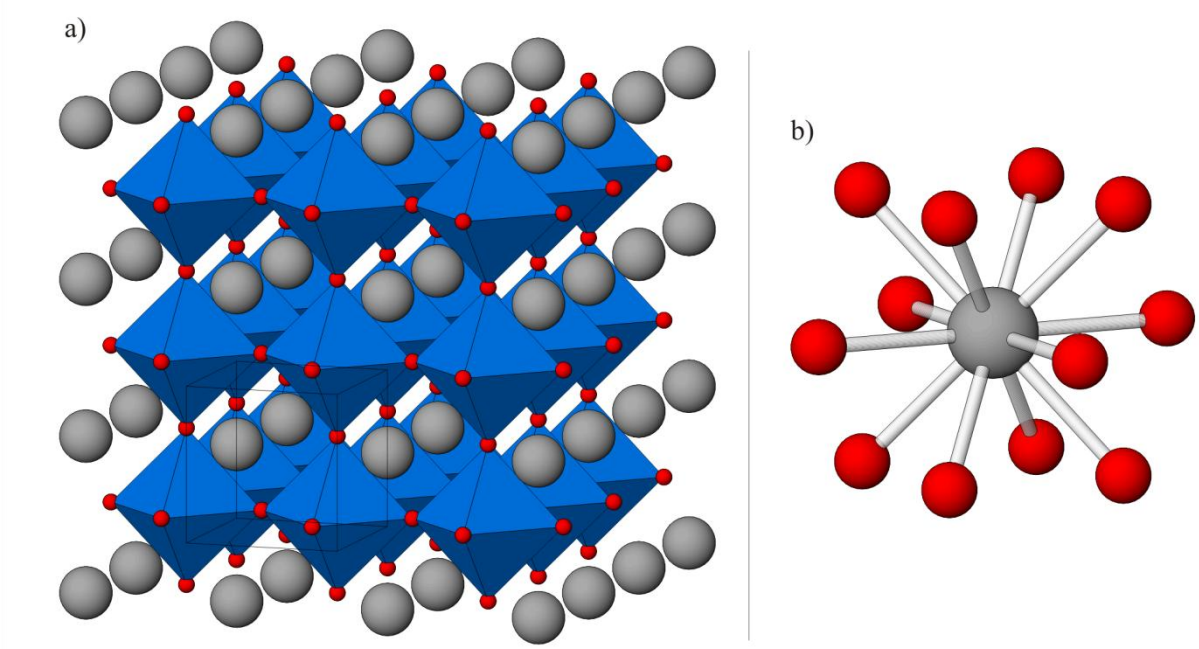

Figure 1.1 – The structure of $SrTiO_3$, a cubic perovskite showing a) the octahedral TiO_6 and strontium positions, unit cell marked in black; b) the SrO_{12} bonding environment of strontium. Grey spheres represent strontium atoms, blue octahedra TiO_6 and red spheres oxygen atoms.

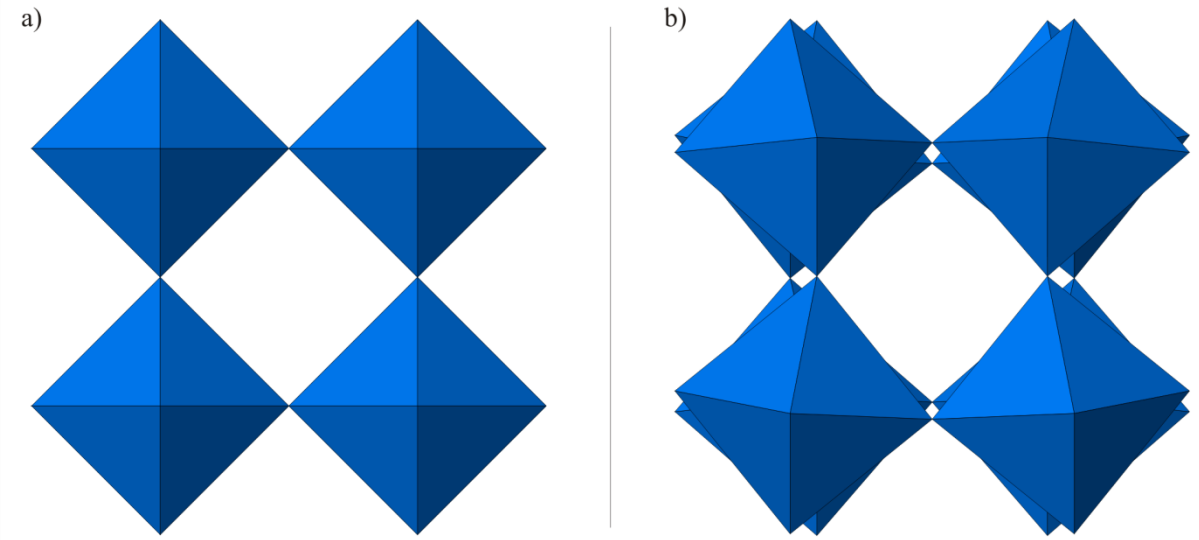

Figure 1.2 – The octahedral tilting of TiO_6 octahedra in $CaTiO_3$ (b) compared to $SrTiO_3$ (a).

By varying the composition of perovskites further, a large number of phases can be formed based on the intergrowth of various structure types with blocks of perovskite. The simplest of these phases are those based on the intergrowth of rock salt (*A*O) and perovskite (ABO_3) blocks, represented by the formula $(AO)_x(ABO_3)_y$. The structures arising from the series of y where $x = 1$ are the Ruddlesden-Popper phases, which are the object of study for this work and will be discussed in detail below.

In recent years the discovery of new properties (or more precisely, improved manifestation of known properties) such as superconductivity and magnetoresistance in perovskite derivatives

has generated a wealth of research interest in the derivatisation of perovskites, and these areas are discussed below.

Properties of materials based on the perovskite structure

Superconductivity

In general, the resistance of metals and metallic oxides drops as temperature is decreased, owing to a reduction in phonon inhibition of electron transport through a material. At absolute zero, the resistance will tend to zero as the thermal motion of atoms is eliminated. In some materials, this inverse proportionality is only true to a certain temperature, below which the resistance drops to zero.

In 1911, Onnes discovered that on cooling to below 4.2 K, the metal mercury immediately loses all resistance to the passage of direct current electricity and remains in this condition at lower temperatures. [3] Meissner later discovered a second unexpected phenomenon in superconducting phases: below this critical temperature (T_c), superconducting materials exclude magnetic field from their interior. [4] This became known as the Meissner effect and is often demonstrated by levitating a small magnet above a block of superconducting material cooled below its T_c.

The discovery in 1950 that the critical temperature of mercury is dependent on its isotopic mass suggested that the mechanism of superconductivity was dependent on the coupling of electron motion and phonon modes. [5] A change in isotope number in a material does not change its electronic properties, however it does change the lattice vibrations and phonon modes. Much work was published throughout the 1950s on theories to explain the observations of superconductivity, leading to the 1957 publication of work by Bardeen, Cooper and Schrieffer containing the first complete microscopic theory of superconductivity. [6, 7] The theory (which became known as BCS theory) explained all the known properties of superconductivity at the time, based on the formation of Cooper pairs in superconducting phases. A simple representation of the interaction of Cooper pairs with phonon modes is shown in Figure 1.3. Although over 50 years have passed since its publication, the underlying results of BCS theory are still used to explain observations in conventional superconductors, and to contrast with observations in "high temperature" superconductors.

Cuprate superconductors

The first oxide material superconductor was reported by Meissner *et al.* in 1933. [8] Although niobium oxide superconducts at the relatively modest temperature of 1.5 K, it heralded a new stage of superconductor research. The first perovskite materials to superconduct were those in the series $BaPb_{1-x}Bi_xO_3$. At the time of their discovery, the T_c of the system, 13 K, was higher than any known oxide. [9] The materials are described as double peroxides, even at low levels of lead doping, as the bismuth site is actually an ordered Bi^{3+}, Bi^{5+} lattice. [10]

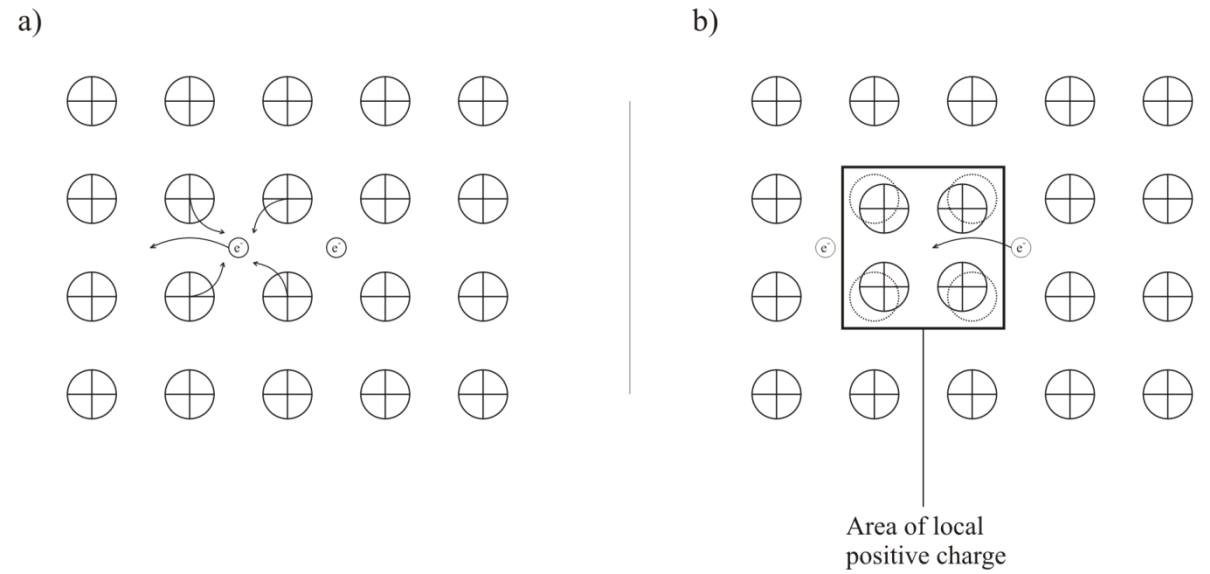

Figure 1.3 – Representation of phonon coupling to electron motion in superconductors. a) an electron moves through the lattice, causing a lattice perturbation. b) an electron is drawn into the area of local positive charge. Dashed circles show atom equilibrium positions.

In 1986 Bednorz and Müller reported superconductivity in the phase $La_{2-x}Ba_xCuO_4$. [11] The material with $x \sim 0.16$ displays superconductivity with a T_c of 35 K. This was remarkable in a new system; the previous maximum T_c achieved for a superconducting material was ~ 20 K in the system Nb_3Ge, which required significant optimisation in synthesis method to produce a near-stochiometric material with peak T_c by chemical vapour deposition. [12-13] The structure of the phase $La_{2-x}Ba_xCuO_4$ (x = 0.16) is shown below – the CuO_6 octahedra are significantly apically distorted by the Jahn-Teller distortion of the $Cu^{2.16+}$, forming planes of CuO_2 separated by La/BaO rock salt layers.

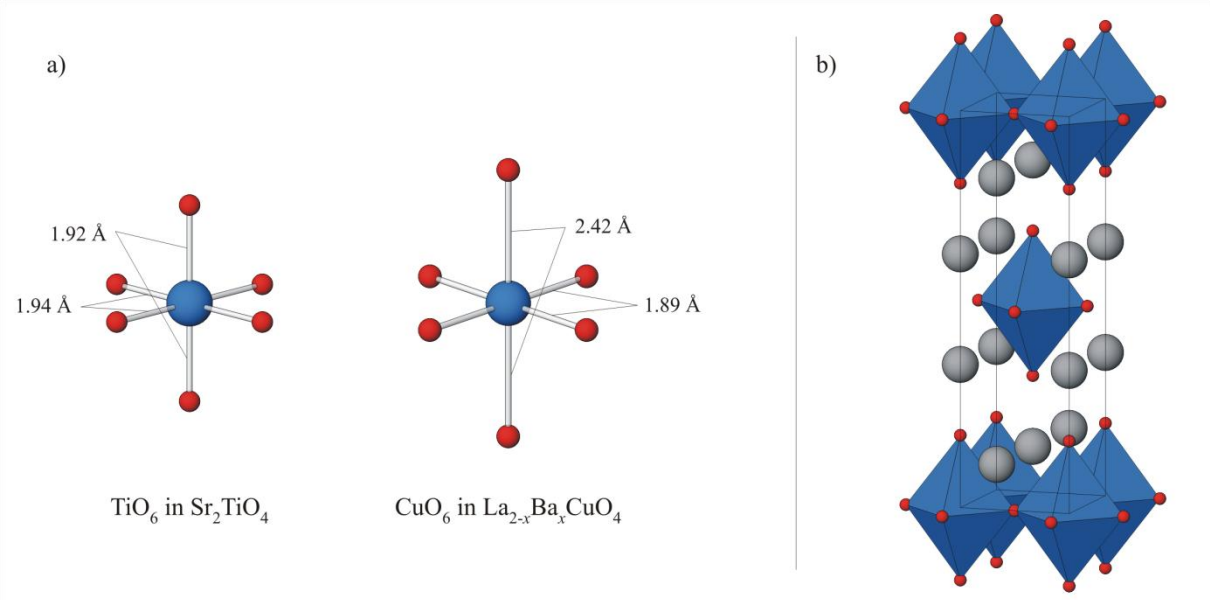

Figure 1.4 – a) The elongation of the axial Cu-O bonds in the material $La_{2-x}Ba_xCuO_4$ compared to the undistorted bonding environment of titanium in Sr_2TiO_4, b) the structure of the superconducting material $La_{2-x}Ba_xCuO_4$ at 10 K. Blue spheres show Cu/Ti atoms, blue octahedra show CuO_6, grey spheres show lanthanum/barium positions and red spheres show oxygen atoms.

The possibility of substitution and derivatisation of these materials led to the development of many new materials. Other hole and electron doped $LnCuO_4$ based superconducting

materials were prepared by substitution on the *Ln* site, [14-15] on the oxygen site [16], and under- and overdoping with oxygen. [17-18] In all cases, the oxidation state of Cu is approximately +2.15.

Work on cuprates led in 1987 to the reporting of $YBa_2Cu_3O_{7-\delta}$ ($\delta \approx 0.07$) by Wu *et al*. [19] This phase is important both as it can be easily formed by standard solid state methods – annealing under oxygen in the final step to raise the oxygen content from O_6 to $O_{7-\delta}$, and because the T_c is above the temperature of liquid nitrogen: a much cheaper alternative to the liquid helium previously required for cooling superconductors. Materials with T_c above that of liquid nitrogen became known as "high T_c / high temperature superconductors", though the definition is often extended to materials with a T_c above ~ 40 K, the theoretical maximum from BCS theory.

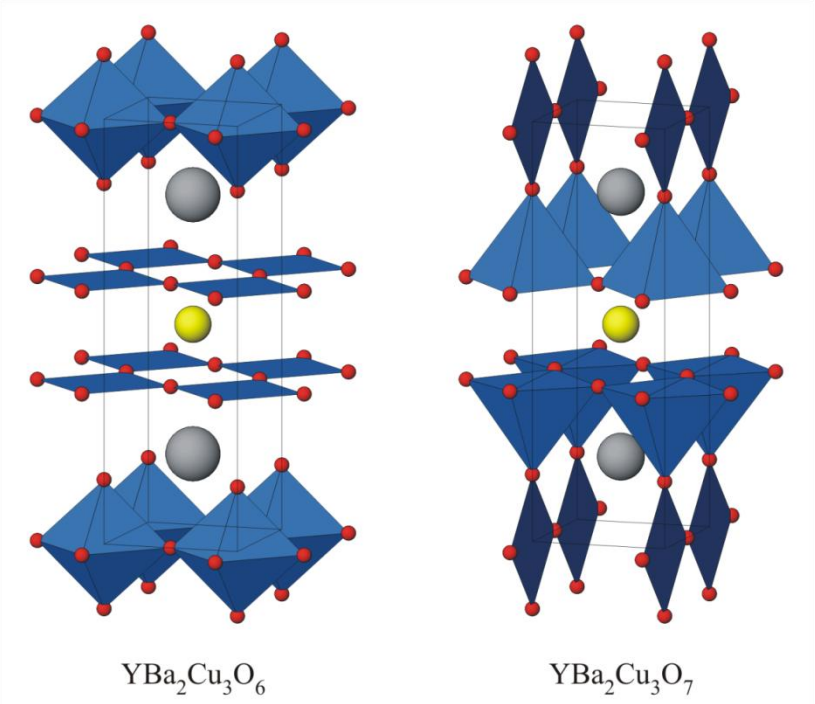

Figure 1.5 – The structures of the phases $YBa_2Cu_3O_6$ and $YBa_2Cu_3O_{7-\delta}$. Blue polyhedral show CuO_4, CuO_5 and CuO_6, yellow spheres yttrium atoms and grey spheres barium atoms.

The structure of the materials $YBa_2Cu_3O_6$ [20] and $YBa_2Cu_3O_{7-\delta}$ are shown in Figure 1.5. As in the previous cuprate superconducting phases, the CuO_2 planes are the location of the superconductivity; in the $O_{7-\delta}$ material this corresponds to the base of the square pyramids. The stochiometric O_6 material does not display superconductivity: the oxidation state of the copper must again be doped to +2.14. Cava *et al.* demonstrated that the onset of orthorhombicity of the phases with changing δ corresponds to the onset of superconductivity. [21] The orthorhombic structure in $YBa_2Cu_3O_{7-\delta}$ is necessary for the formation of both the CuO_4 ribbons and CuO_2 planes that give rise to superconductivity in the material.

The most significant superconducting cuprate phases reported since the early work on the $La_{2-x}Ba_xCuO_4$ and $YBa_2Cu_3O_{7-\delta}$ families are the phases based on $Tl_2BaCa_{n-1}Cu_nO_{2n+4}$ (n = 1, 2, 3...) and $Bi_2Sr_2CaCu_2O_{8+\delta}$. The bismuth based phases are used extensively in

superconductive wiring, and the thallium phases comprise some of the highest T_c materials currently known.

The structures of the n = 1 – 4 thallium phases are shown in Figure 1.6. [22] All of the phases superconduct above the boiling point of liquid nitrogen, with the peak T_c for the n = 3 phase at 125 K under ambient pressure. By substitution with mercury on the thallium site, superconductivity has been reported at 138 K in $Hg_{0.8}Tl_{0.2}Ba_2Ca_2Cu_3O_{8+\delta}$, isostructural with n = 2 thallium phase. [23] At the time of writing, this material displays the highest T_c for any known superconducting material.

The structures of several Bi-Sr-Cu-Ca-O phases are shown in Figure 1.7. The phase $BiSrCaCu_2O_8$ was the first reported member of the family, and also the first high temperature cuprate superconductor without a rare earth element in its composition. [24] The key structural points are the CuO_5 square pyramids, with their bases forming the CuO_2 planes supporting superconductivity, and BiO layers. The greater compressibility of the BiO layers compared to the *Ln*O / YO rock salt layers in previously reported high T_c materials allows improvement in the properties of the superconductors by pressing; critically this allowed wires of $Bi_2Sr_2CaCu_2O_8$ to be produced which can sustain superconductivity at temperatures above that of liquid nitrogen. [25]

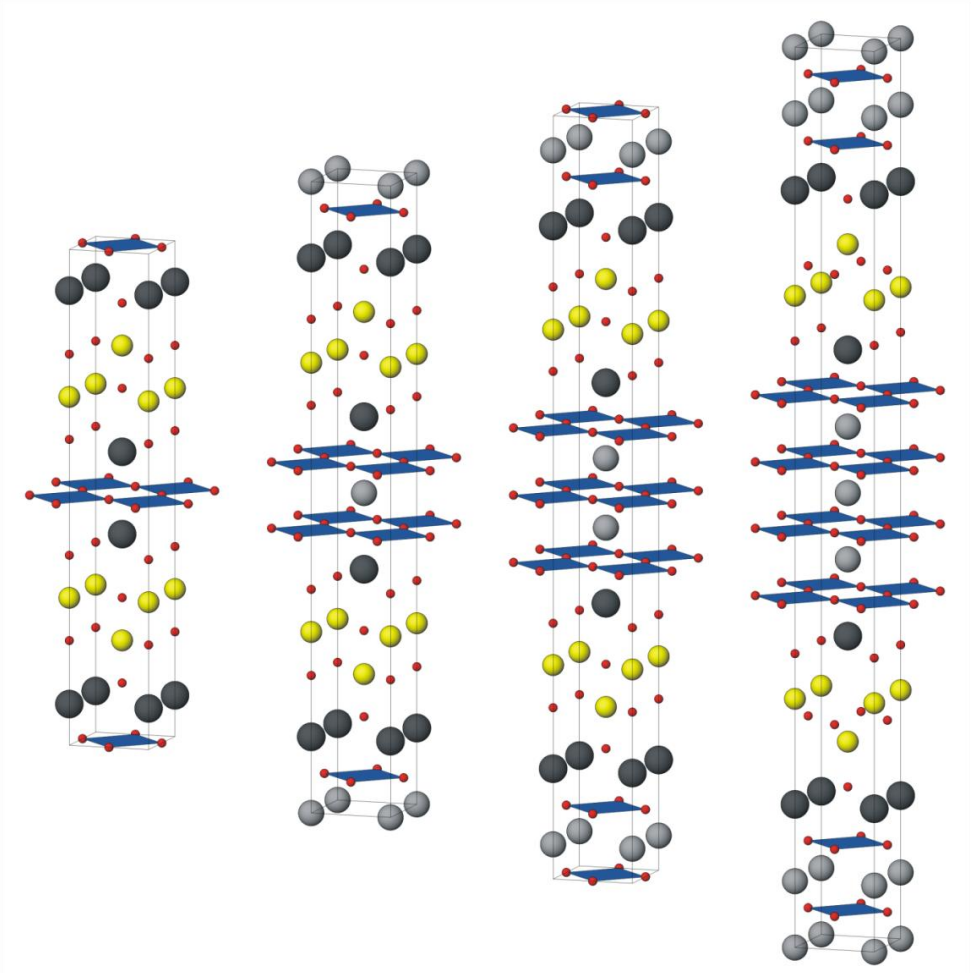

Figure 1.6 – The n = 1, 2, 3 and 4 members of the series $Tl_2BaCa_{n-1}Cu_nO_{2n+4}$. Blue square planes represent CuO_4, dark grey spheres barium atoms, light grey spheres calcium atoms, yellow spheres thallium and red spheres oxygen atoms.

In all high T_c cuprate superconducting phases, key structural features are common to all known phases. CuO_2 planes, doped to a carrier concentration on the copper site of approximately 0.15 carriers per unit copper are required to carry supercurrent. The layered structure is also critical; it is believed that the layers containing the heavy rare earth, yttrium or semimetal oxides provide a "charge reservoir" for the superconducting layers.

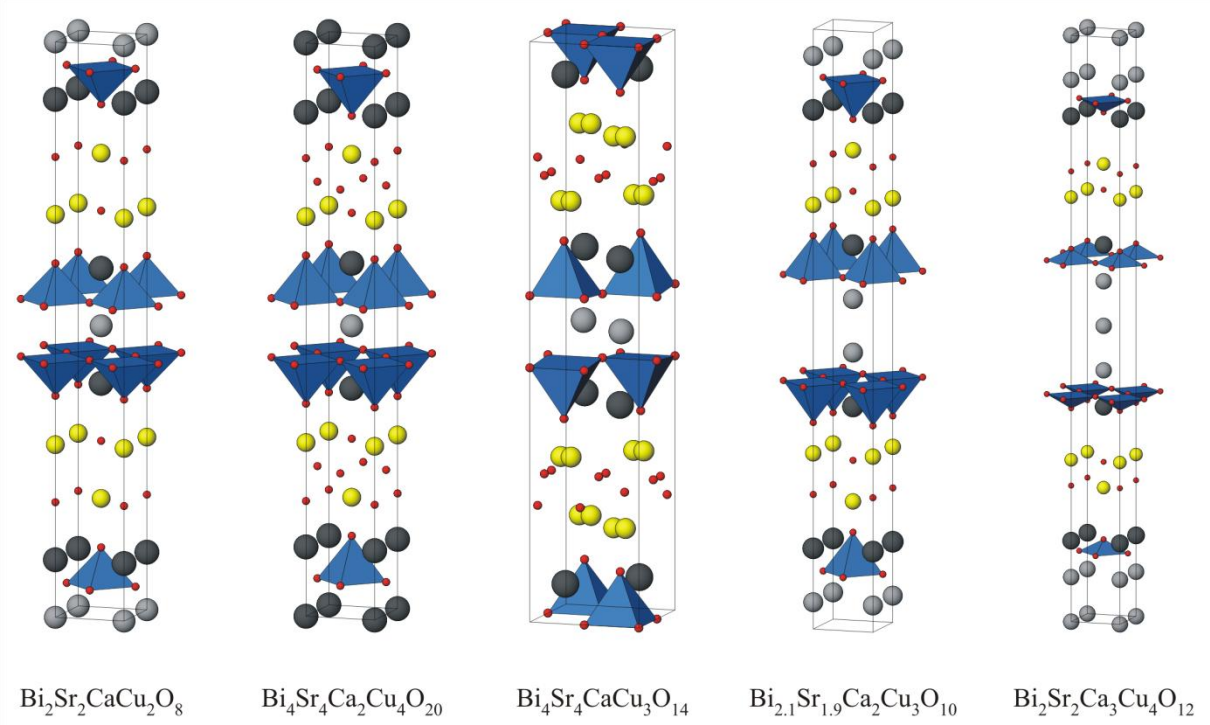

Figure 1.7 – Structures of Bi-Sr-Cu-Ca-O superconducting phases. Blue square pyramids represent CuO_5, yellow spheres show bismuth positions, dark and light grey spheres represent strontium and calcium positions and red spheres oxygen positions.

Superconductivity in iron arsenides

In 2008, the hole-doped materials $LaFeO_{1-x}F_xAs$ ($0.05 \leq x \leq 0.12$) were found to exhibit superconductivity, with the peak T_c at 26 K. [26] Their structures are shown in Figure 1.8. This was both a new family of materials exhibiting relatively high T_c superconductivity, and the first encountered ferrate superconductors. Soon after the original publication of their results, the same group demonstrated that the pressure dependence of T_c of the material $x = 0.12$ is significantly greater than previously encountered in the cuprates – under a pressure of 4 GPa the T_c could be elevated to 43 K. [27] The group attributed this observation to the greater compressibility of the Fe-As layer compared to the CuO_2 planes in cuprates.

The chemistry of the system is open to significant modification, by substitution on the lanthanum, oxygen, and iron sites. Substitution of La for other trivalent rare earth metals produced materials with elevated T_c; at ambient pressure the substitution of Ce, [28] Pr, [29] Nd [30] and Sm [31] forms materials with T_c = 41, 52, 51 and 43 K respectively – all higher than the predicted maximum for conventional superconductors by BCS theory, confirming another series of high temperature superconducting materials. Other mechanisms to alter the charge carrier concentration other than fluorine doping have been attempted, such

as Th^{4+} doping in the phase $Gd_{0.8}Th_{0.2}FeAsO$ (T_c = 56 K), [32] and Sr^{2+} doping in the phase $La_{1-x}Sr_xFeOAs$ (T_c = 25 K). [33] Other phases based on complex arsenides, rather than oxyarsenides, have also been formed, including the high T_c $Sm_{0.5}Sr_{0.5}FeAsF$ (T_c = 56 K). [34]

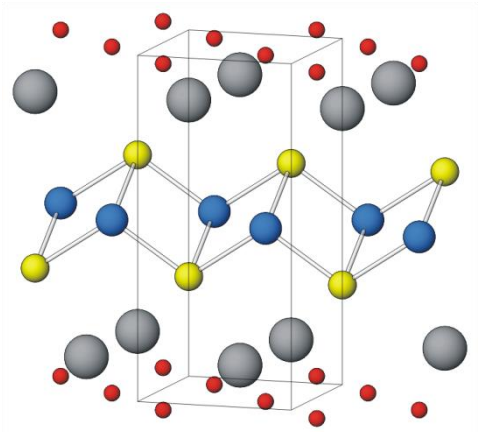

Figure 1.8 – The structure of the ferrate superconductor $LaFeO_{1-x}F_xAs$. Grey spheres represent lanthanum atoms, blue spheres iron, red spheres oxygen and yellow arsenic. Fe-As bonds are shown to emphasise the tetragonal coordination of iron.

Magnetism and magnetoresistance in perovskite derivatives

The magnetic properties of a material define how it behaves in magnetic field. All materials are inherently diamagnetic, tending to exclude an applied magnetic field; however the electronic configuration of many materials produces additional effects that can overwhelm this effect. A material with unpaired, non-interacting electron spins will tend to increase its flux density in an externally applied magnetic field; the field will align the spins along the direction of the magnetic field. Increasing temperature will tend to reduce this alignment as thermal motion randomises the spins. The relationship between magnetic susceptibility (the propensity of a material to increase internal magnetisation in a magnetic field) and temperature is given by $\chi = C/T$ where $\chi = M/H$: M is the magnetisation of the material, H is the applied external flux and χ is the susceptibility. [35] C is a constant relating to the magnetic moment of the material; in a paramagnetic material proportional to the square of the number of unpaired electrons.

In many materials, the paramagnetism of the unpaired spins is modified by interaction of the spins. Spins may correlate in parallel, causing ferromagnetism, or antiparallel, known as antiferromagnetism. A special case of antiferromagnetism is ferrimagnetism, where neighbouring spins are aligned antiparallel but different in magnitude. Figure 1.9 shows the arrangement of magnetic moments in magnetic structures.

In materials built up from corner sharing polyhedra, alignment of magnetic moments in materials containing unpaired electrons commonly occurs by orbital overlap with the anion. In transition metal oxide materials, unpaired *d* electrons interact through next nearest neighbour interactions via the oxide anion *p* orbitals. An example of this mechanism is shown in Figure 1.10. This is known as superexchange. In metallic materials, ferromagnetic superexchange can be induced by electron transport. The mechanism, proposed by Zener, is

known as double exchange. [36] Rather than polarisation of neighbouring e_g orbitals, hopping of electrons from metal centre to metal centre via oxygen orbitals forces ferromagnetic interaction to prevent the switching of electron polarity from metal ion to metal ion.

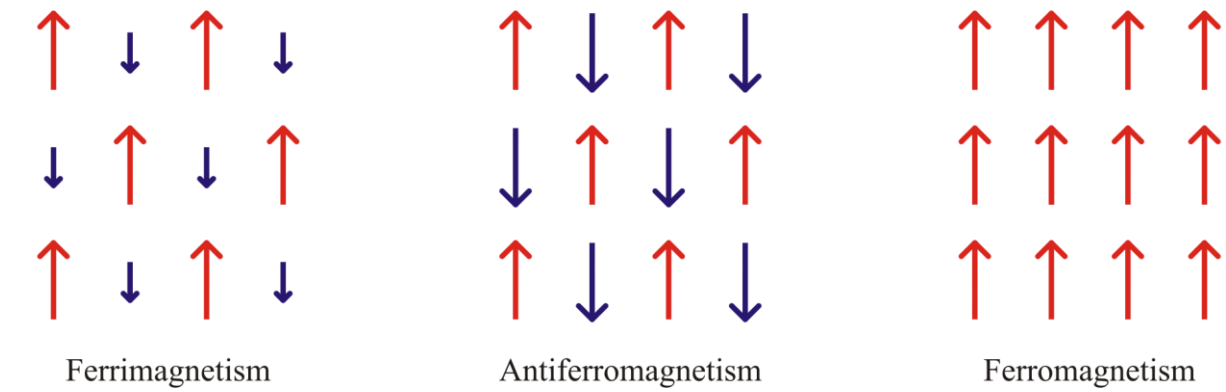

Figure 1.9 – Magnetic ordering of moments in materials.

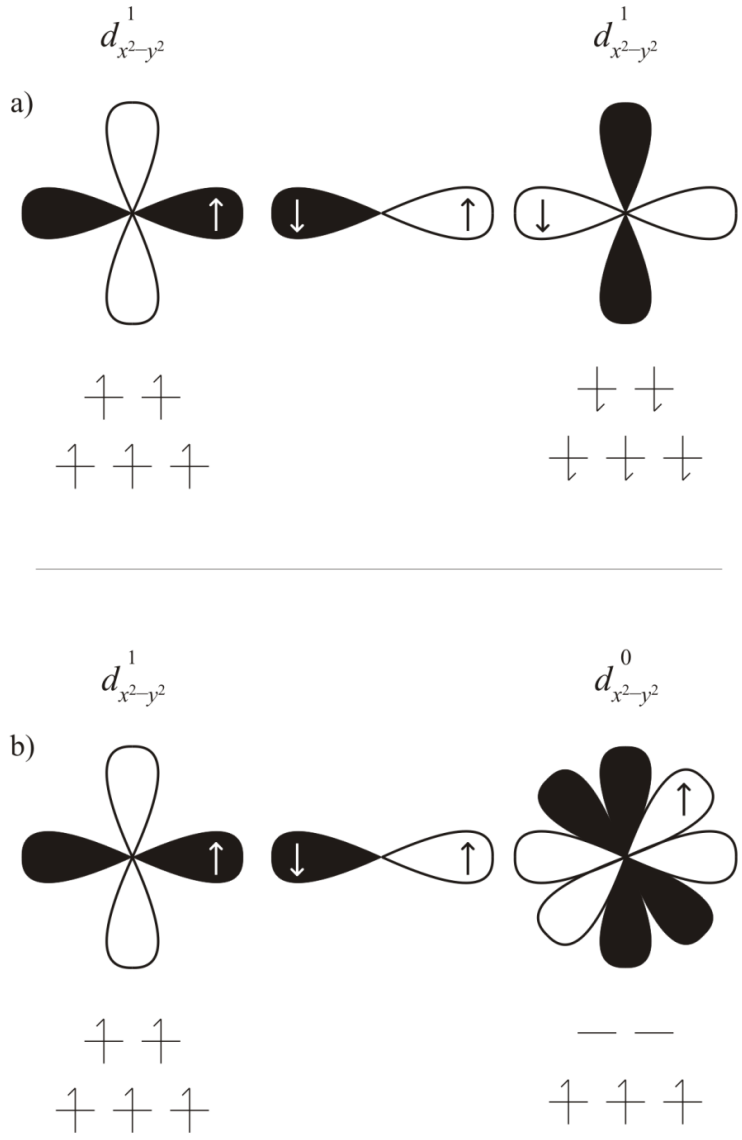

Figure 1.10 – Orbital interactions leading to magnetism in perovskites. a) Covalent interactions between the metal *d* and oxygen *p* orbitals force antiferromagnetic pairing of spins; b) orbital overlap between the oxygen *p* and unfilled metal *d* orbital polarises the moments on the empty *d* orbital, polarising the t_{2g} orbitals through Hund's rules.

In all magnetically ordered materials, the magnetic structure is only stable below a critical temperature, above which thermal randomisation of spins produces a paramagnetic state. For ferromagnets, the critical temperature is known as T_c, the Curie temperature; in antiferromagnets the transition temperature is called T_N, the Néel temperature.

Perovskites are built up from corner sharing octahedra, and as such commonly display long range magnetism through orbital overlap the with bridging anions. Ordered double perovskites (with two different *B*-site cations) may order so that the arrangement of the *B*-sites is rock salt-like, as in tetragonal Sr_2FeMoO_6, illustrated in Figure 1.11. The alternating valence of the metal sites causes this material to be metallic and ferromagnetic, through double exchange. [37] The double perovskite ferromagnetic phases have recently received a great deal of interest as their conducting, ferromagnetic states give rise to magnetoresistance, as in the Sr_2FeMoO_6 system. [38] Magnetoresistance is a material property displayed by thin films of metal atoms in which the resistance of a material changes when a magnetic field is applied to it. Originally, magnetoresistive materials were formed macroscopically. Thin films of ferromagnetic material are separated by a film, nanometers thick, of insulating material. When the orientation of the spins of the ferromagnets are aligned, the tunnelling of electrons through the junction is more energetically favourable than when the spins are aligned antiparallel; the alignment of the spins can be adjusted by application of external magnetism, producing materials with two possible resistivities. Modest differences in resistance, for example 11.8 % at room temperature in a $CoFe/Al_2O_3/Co$ junction are sufficient to produce useful engineering materials. [39] The two configurations can be used as binary memory storage, as shown in Figure 1.12.

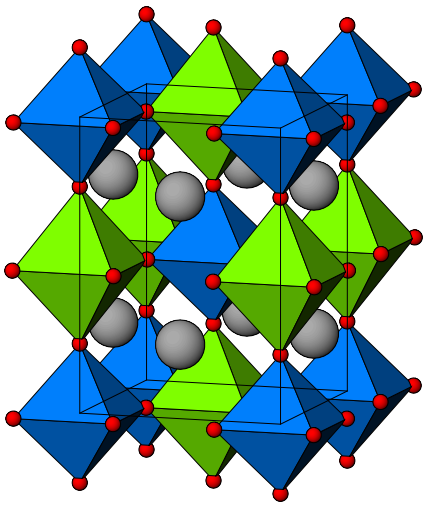

Figure 1.11 – The structure of Sr_2FeMoO_6. Grey spheres show strontium positions, blue and green octahedra FeO_6 and MoO_6.

Figure 1.12 – Binary memory storage in tunnelling magnetoresistive junctions. Here, $R_1 > R_0$.

In 1995, the magnetoresistance of the materials $La_{1-x}Sr_xMnO_3$ were investigated. [40] When the material $LaMnO_3$ was doped by substitution of Sr^{2+} onto the *A* site, phases were formed that exhibited magnetoresistance of a significantly higher degree (that is, a much higher percentagewise increase in resistance on application of magnetic field), when the range of *x* is

$0.2 \leq x \leq 0.4$ and the temperature is below a critical temperature. This behaviour became known as colossal magnetoresistance (CMR) due to its relationship to previously reported magnetoresistive behaviour but greater scale. The scale of the magnetoresistance relates to the ferromagnetic / paramagnetic phase transition at the onset of CMR. [41]

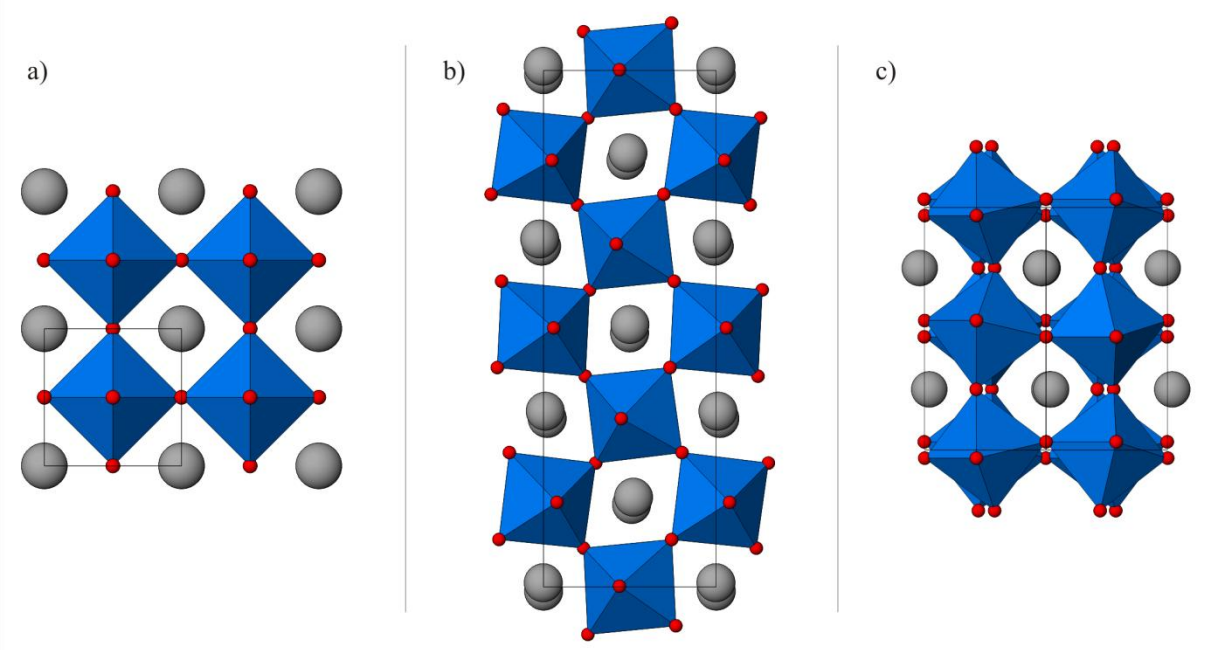

Figure 1.13 – The manganites a) $LaMnO_3$, b) $La_{0.33}Ca_{0.66}MnO_3$, c) $CaMnO_3$. Blue octahedra show MnO_6, grey spheres the La/Ca sites.

By changing the doping alkali earth while maintaining a constant doping concentration, Hwang *et al*. demonstrated that the critical temperature of CMR is directly related to the ionic radius of the *A* site; as the radius of *A* in the series $La_{1-x}A_xMnO_3$ decreases, the critical temperature of the onset of CMR decreases and that the magnitude increases. [42]

A simplistic mechanism for CMR is that application of a magnetic field to a material exhibiting CMR causes electron hopping through induced Zener double exchange; though this does not explain all the observations in CMR materials such as the electron phonon coupling attributed to the Jahn-Teller distortion in Mn (III) ions. [41]

In 1996, Moritomo *et al.* found that layered analogues of $La_{1-x}Sr_xMnO_3$ exhibit CMR. [43] In the phase $La_{2-x}Sr_{1+x}Mn_2O_7$ and the analogous $Nd_{2-x}Sr_{1+x}Mn_2O_7$, [44] two types of magnetoresistance are observable. At low temperatures, standard CMR (up to 240 %) and a metallic, ferromagnetic ground structure are exhibited by the lanthanum material, and ferromagnetic domains and colossal magnetoresistance in the neodymium. At temperatures slightly above the three dimensional ordering temperature (90 K for $La_{2-x}Sr_{1+x}Mn_2O_7$), very large magnetoresistance (10^4 % increase in resistance at 14 T) is observed. [45] This second magnetoresistive phase has been paraphrased tunnelling magnetoresistance, TMR, for the microscopic parallel with the macroscopic thin film junction materials described above. A full review of the unusual transport, magnetic and orbital ordering properties of the manganites was carried out by Dagotto *et al*. in 2001. [46]

Ruddlesden-Popper phases

In 1958, Ruddlesden and Popper prepared and characterised the family of materials $SrO(SrTiO_3)_n$, where the phases n = 1, 2 and 3 were formed phase pure. [46-47] All crystallise in the same space group *I*4/*mmm*, with alternating layers of rock salt SrO and perovskite $SrTiO_3$ blocks. The structure of the first three materials as prepared by Ruddlesden and Popper are shown in Figure 1.15. A representation of the layered structure of the materials is shown in Figure 1.14; the Ruddlesden-Popper phases are defined by the single rock salt layer to multiple perovskite blocks. In their original work, Ruddlesden and Popper reported stacking faults in the products of attempted syntheses of materials with $n > 3$: this is frequently seen in Ruddlesden-Popper materials resulting in diffraction pattern peak broadening.

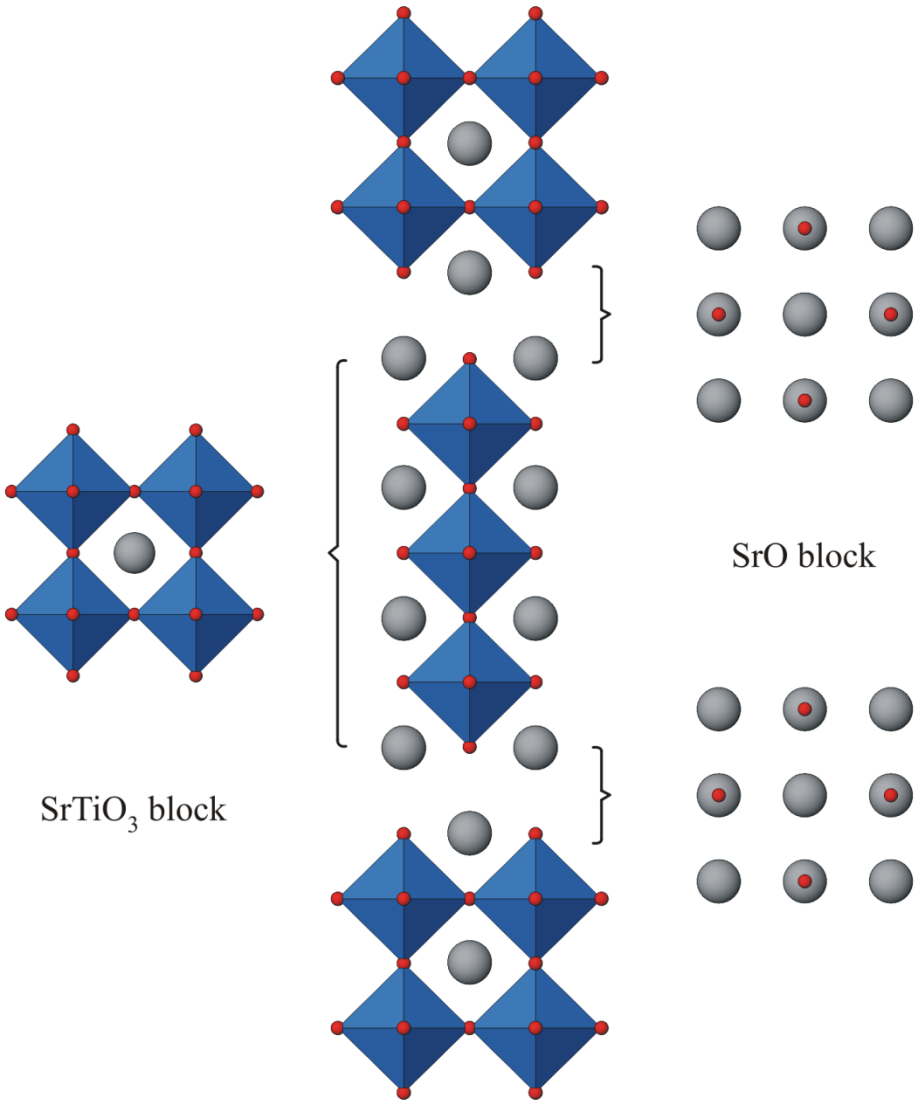

Figure 1.14 – $Sr_4Ti_3O_{10}$ showing the intergrowth of perovskite and rock salt layers. Grey spheres show Sr atoms, blue octahedra TiO_6. Red spheres show oxygen atom positions.

$A_3M_2X_7$

The stochiometric materials $A_3M_2X_7$ can broadly be subdivided by the cation *A*. Several A^{n+} cations are known in the materials, although chemistry reported in literature is not as broad as for the perovskites. Phases are known for *A* = Ca, Sr, Ba; La and K, Rb, which will be discussed below.

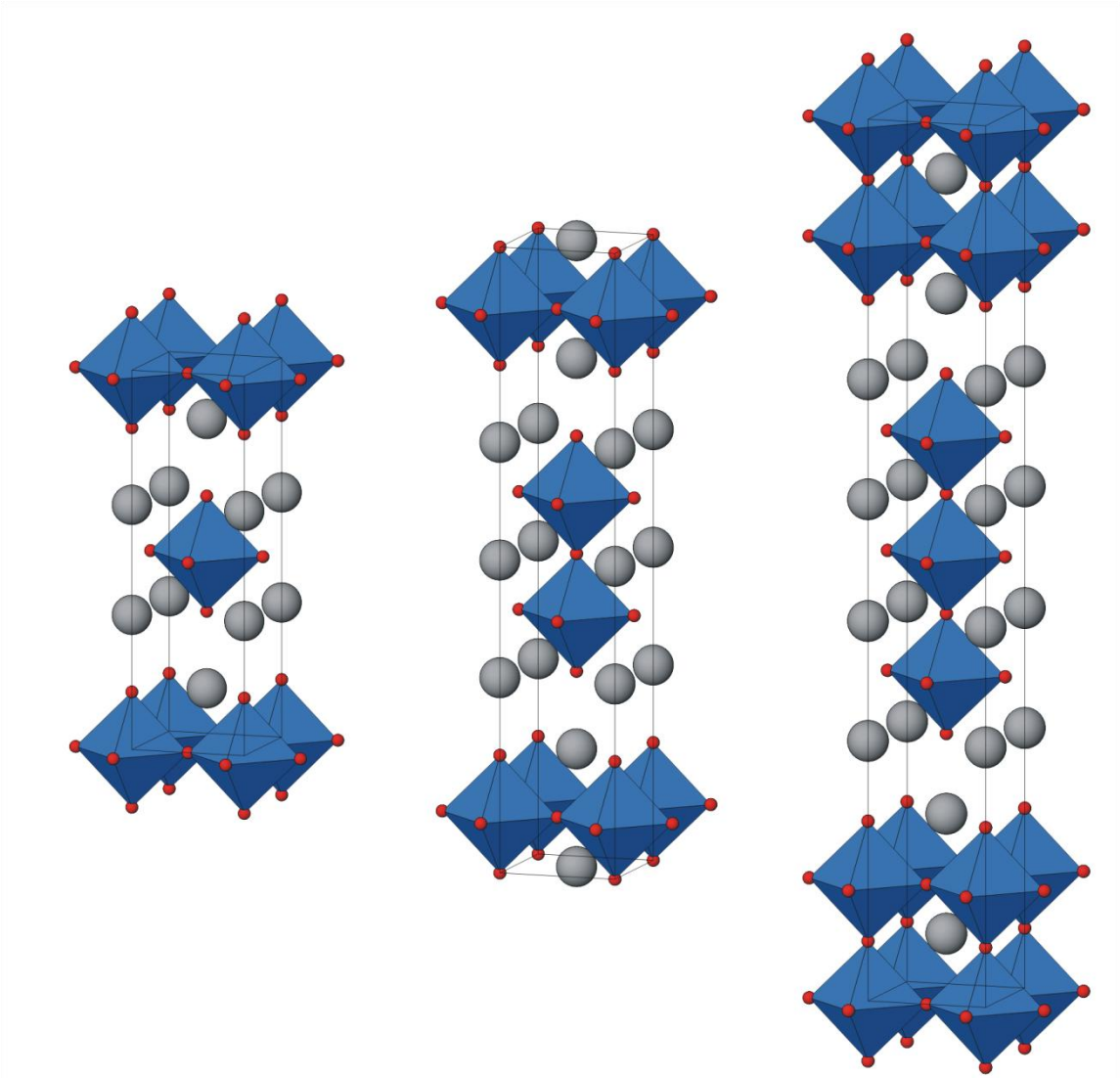

Figure 1.15 – *n* = 1, 2 and 3 Ruddlesden-Popper phases Sr_2TiO_4, $Sr_3Ti_2O_7$ and $Sr_4Ti_3O_{10}$. Grey spheres show Sr atoms, blue octahedra TiO_6. Red spheres show oxygen atom positions.

A = *K, Rb*

$A_3M_2X_7$ materials are only known for *X* = F, Cl and Br. Known potassium materials are the bilayered analogues of the materials K_2MF_4. The phases $K_3M_2F_7$ (*M* = Mn, [48-49] Co, [48, 50] Ni, [51, 52] Cu, [53, 54] and Zn [55, 56]) and $K_3Mn_2Cl_7$ [57] have been previously reported. The phases are reported as isostructural with $Sr_3Ti_2O_7$, crystallising in the space group *I*4/*mmm*. The manganese chloride shows significantly increased lattice parameters (*a* = 5.027 Å, *c* = 25.325 Å) compared to the fluoride material (*a* = 4.187 Å, *c* = 21.586 Å) as expected from the larger anion, however all other materials have similar lattice parameters to $Sr_3Ti_2O_7$. The copper fluoride material shows an expanded *a* lattice parameter and

contraction in *c* – the Cu^{2+} ions are equatorially elongated by Jahn-Teller distortion. The materials $K_3M_2F_7$ (*M* = Mn, Co, Ni and Cu) exhibit antiferromagnetic ordering within the two dimensional perovskite blocks, similarly to the *n* = 1 Ruddlesden-Popper phase K_2MnF_4. [49]

Rubidium materials with *X* = F are not known; the very large MX_6 octahedra form perovskite block layers that are size matched to the RbCl / RbBr rock salt layers. The only Rb_3 materials currently known in the literature are $Rb_3Mn_2Br_7$, [58] $Rb_3Cu_2Cl_7$, [59] and $Rb_3Mn_2Cl_7$. [60, 61] The structures of $Rb_3Cu_2Cl_7$ and $Rb_3Mn_2Br_7$ are shown in Figure 1.16. The MX_6 bonding environment is also shown to illustrate the long *M*-*X* bonds and the Jahn-Teller distortion in the d^7 Cu^{2+} ions. The magnetic behaviour of the phase $Rb_3Mn_2Cl_7$ has been studied by several groups. [61, 62] As for the potassium phases, in the temperature range $64.5 \leq T \leq 100$ K the material displays two dimensional antiferromagnetism in the layers and no three dimensional ordering; below 64.5 K the magnetic structure orders in three dimensions.

A = *La*

The phases $La_3Ni_2O_{7-\delta}$ (δ = 0, 0.08, 0.16 and 0.65) were originally characterised in 1994 by Zhang *et al*. [63] The δ = 0.08 phase is formed by calcination of the oxides in air, and the other phases formed by reduction in argon and hydrogen (δ = 0.65) and nitrogen and hydrogen (δ = 0.16); and oxidation (δ = 0.00) under high pressure oxygen. The δ = 0.65 phase crystallises in the space group *I*4/*mmm*, isostructural with $Sr_3Ti_2O_7$ with disordered oxygen vacancies on the interlayer site, producing two nickel sites (one octahedral, one square pyramidal) leading to a split nickel site. [64] It is a semiconductor, [63] and Zhang *et al*. suggest that it may be ferromagnetic, though the majority of the magnetism observed in the trace was attributed to a nickel impurity. The δ = 0.08 phase is also semiconducting, however the stochiometric $La_3Ni_2O_{7.00}$ phase is a metallic conductor. The authors attribute the conductivity of the phase to the partial occupation of the Ni-O σ* antibonding bands, compared to the trapping of electrons in the oxygen vacancy bands. Further work on the transport properties of the stochiometric material has revealed a transition to a more conductive phase at 550 K. [65] This is attributed to an increase in temperature causing an improved overlap in the $\sigma^*_{x^2-y^2}$ band originating in a Mott transition. The phase La_3LiMnO_7 is tetragonal, refined in the space group $P4_2/mnm$, and although the diffraction patterns show no evidence of cation order, ^{6}Li magic angle spinning NMR shows local 1:1 ordering of the lithium and manganese sites. [66] The sites are ordered in a rock salt configuration within each layer, however there is no long range ordering between layers.

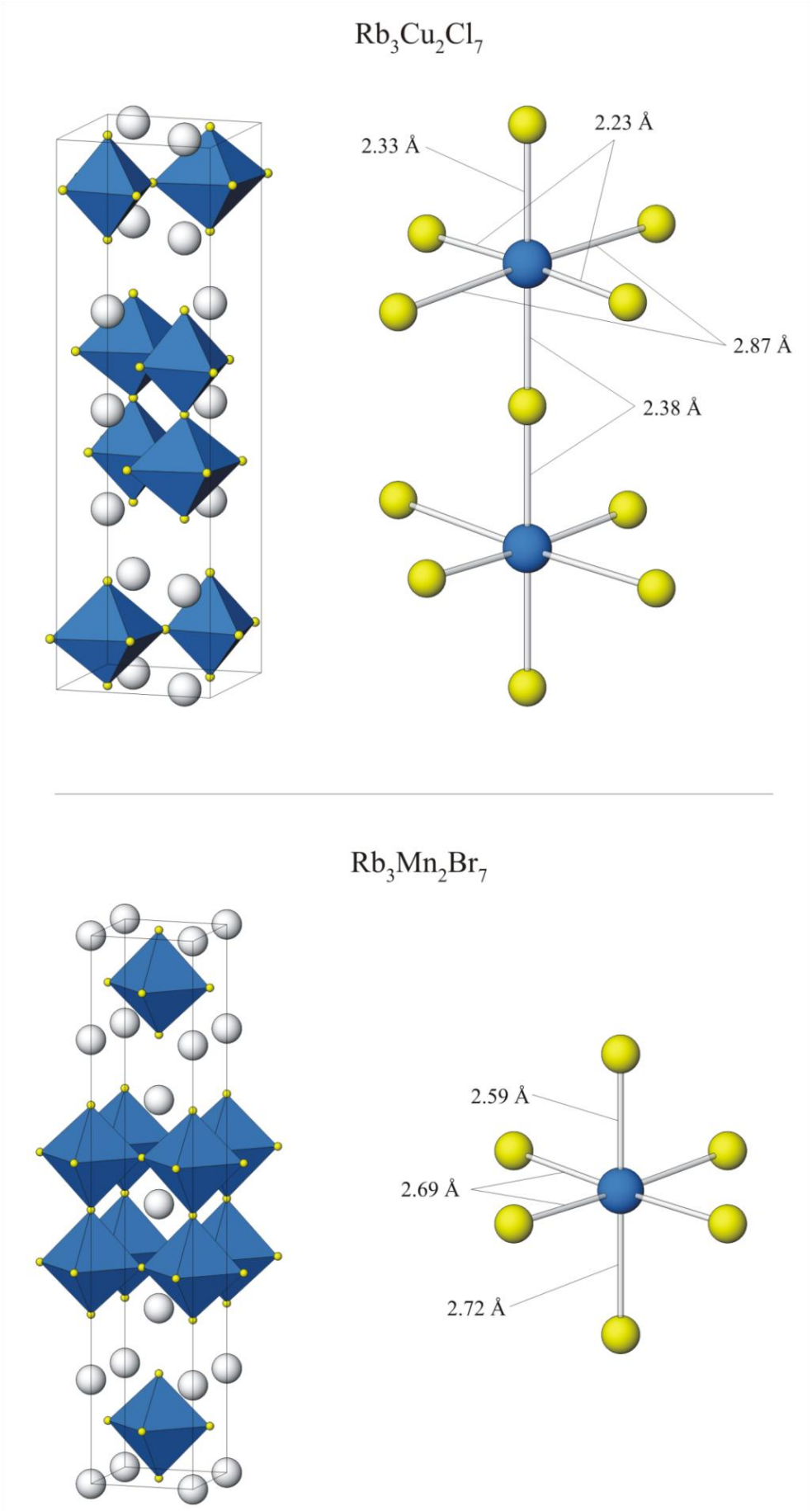

Figure 1.16 – The structures of $Rb_3M_2X_7$ at room temperature. White spheres show rubidium positions, yellow spheres halide positions and blue spheres M^{2+}. Blue octahedra show MX_6.

A = *Ca, Sr, Ba*

The materials $Ca_3M_2O_7$ are known for *M* = Ti, Mn and Ru. The structure of the material $Ca_3Ti_2O_7$, the *n* = 2 Ruddlesden-Popper analogue of $CaTiO_3$, Perovskite, was first reported in 1991. [67] Similarly to the ABO_3 phase, octahedral rotation caused by compression of the octahedral sublattice leads to a distorted superstructure. The unit cell is double the volume of the $Sr_3Ti_2O_7$, *I*4/*mmm* base, with an approximate $\sqrt{2}a_0 \times \sqrt{2}a_0 \times c_0$ relationship to the unit cell parameters. The structure of $Ca_3Ti_2O_7$ is compared to $Sr_3Ti_2O_7$ in Figure 1.17.

Other work on $Ca_3Ti_2O_7$ has examined the improvement in the material purity when formed by sol-gel synthetic routes [68] and its thermodynamic stability. [69]

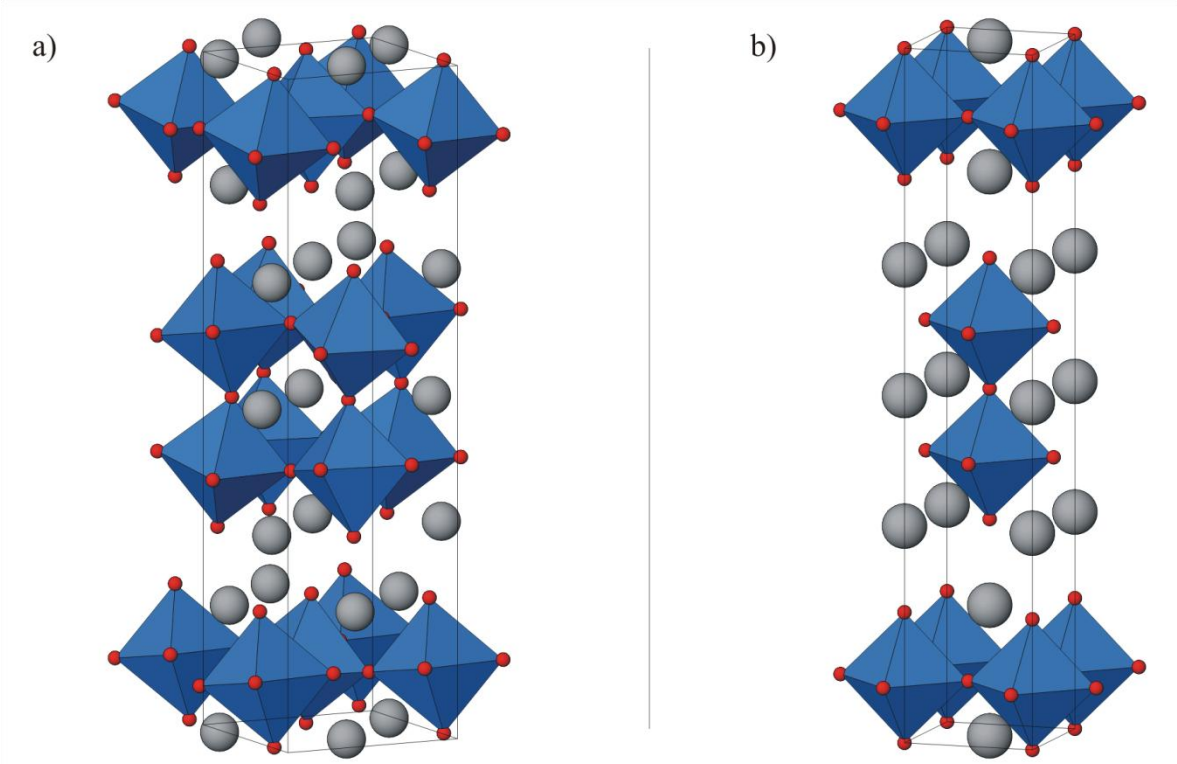

Figure 1.17 – The structure of $Ca_3Ti_2O_7$ (a) and $Sr_3Ti_2O_7$ (b). Grey spheres show Ca/Sr positions and blue octahedra show TiO_6.

The structure of the material $Ca_3Mn_2O_7$ has been reported by several groups. In 1998, [70] Fawcett *et al*. proposed that the material was isostructural to $Sr_3Ti_2O_7$. Zhu *et al*. also reported an undistorted *I*4/*mmm* unit cell in 2002. [71] With the benefit of transmission electron microscopy, [72] single crystal X-ray diffraction [73] and neutron and synchnotron X-ray powder diffraction, [74] the true structure of the majority phase at room temperature has been identified as a $Cmc2_1$ superstructure originating in MnO_6 octahedral rotations. Lobanov *et al*. [73] also confirmed that at room temperature a small tetragonal impurity consistent with $Ca_3Mn_2O_7$ in the space group *I*4/*mmm* exists in a "phase pure" polycrystalline sample, attributed by the authors to an incomplete phase transition. Although this work does not include structural data from the heating of a sample of $Ca_3Mn_2O_7$, the low temperature diffraction data contains no *I*4/*mmm* minor phase. This, and the orthorhombic to tetragonal transition observed in the phase $Ca_{3-x}La_xMn_2O_7$, [72] support the partial phase transition assumption.

The magnetic properties of the material $Ca_3Mn_2O_7$ have been studied through powder neutron diffraction, [73] magnetometry [75] and theoretically through density functional theory. [76] The magnetometry study demonstrates similar magnetic behaviour to the $K_3M_2F_7$ phases, with the material undergoing two magnetic transitions on cooling; first to antiferromagnetic in layer, then to antiferromagnetic in layer with weak ferromagnetic coupling between layers. The magnetic structure of the material as determined through Rietveld refinement of neutron powder diffraction at 10 K by Lobanov and co-workers are consistent with this result.

The structure of the material $Ca_3Ru_2O_7$ has been studied between room temperature and 8 K by neutron powder diffraction by Yoshida *et al*. [77] At all temperatures, the material structure was refined in the space group $Bb2_1m$ (isostructural with calcium manganite, with a different unique axis choice). Below 48 K, the *c* lattice parameter markedly contracts, corresponding to the point of the metal-nonmetal transition reported previously by the same group. [78] The temperature dependence of the lattice parameters as reported by the authors is reproduced in Figure 1.18, showing the point of the transition.

$Ca_3Ru_2O_7$ exhibits a range of unusual physical properties. Cao and co-workers discuss several of the electronic and magnetic properties arising from the two dimensional structure of the material. [79] The transition temperature of the metallic-nonmetallic crossover, nominally at 48 K, can be elevated by pressure (5.5 GPa) [80] on the material, stabilising the denser nonmetallic phase. Unlike the other $Ca_3M_2O_7$ phases, the ruthenium spins appear ferromagnetically coupled within the bilayer, but coupled antiferromagnetically between perovskite blocks. Similarly to other ruthenates and bilayered Ruddlesden-Popper phases, $Ca_3Ru_2O_7$ exhibits colossal magnetoresistance with a drop in resistivity of three orders of magnitude. [79]

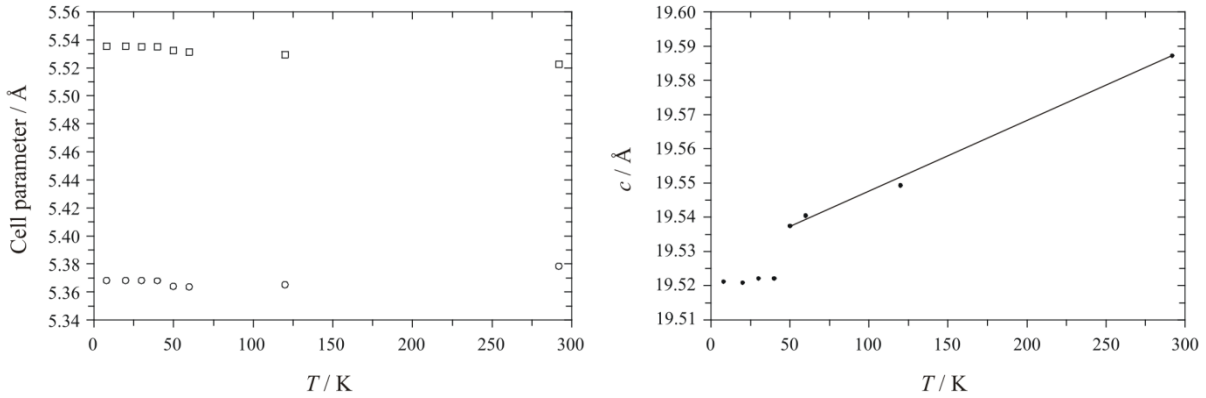

Figure 1.18 – *Left*: *a* (□) and *b* (○) cell parameters, *right*: *c* cell parameter of $Cu_3Ru_2O_7$ between 8 and 292 K, reproduced from the data of Yoshida *et al.* [30] Trend line above 50 K added purely as a guide to the eye.

As for the rubidium phases already discussed, the large barium ion allows the formation of phases with larger MX_6 octahedra. The best reported stochiometric $Ba_3M_2X_7$ phase is the material $Ba_3Zr_2S_7$. $Ba_3Zr_2S_7$ was originally prepared in 1991 by the solid state reaction of CS_2 with $BaCO_3$ and $BaZrO_3$. [81] Three structures have been proposed for the material. The polycrystalline $Ba_3Zr_2S_7$ as originally reported crystallises in the orthorhombic space group *Cccm*. Two separate polymorphs have been proposed by single crystal X-ray crystallography

on crystals formed by reaction of Zr, BaS and S in a $BaCl_2$ molten flux: the high temperature (1323 K) phase crystallises in the space group *I*4/*mmm* and is isostructural with $Sr_3Ti_2O_7$, [82] while the low temperature (1203 K reaction temperature) polymorph crystallises in the space group $P4_2/mnm$, originating in rotation of the ZrS_6 octahedra. [83] The relationship between the three phases is shown in Figure 1.19: it is possible that the structure determined by powder diffraction was a mixture of the two polymorphic phases.

Several materials with mixed *A* or *M* sites have been currently reported for *X* = O; notably the layered analogue of the superconducting $Ba(Pb_{0.75}Bi_{0.25})O_3$, $Ba_3(Pb_{1-x}Bi_x)_2O_7$, [84] the oxygen deficient $Ba_3InBiO_{7-\delta}$ [85] and $(Ba_{1-x}K_x)_3Bi_2O_7$ (x = 0.435). [86, 87] Unlike the perovskite phases, none of the n = 2 Ruddlesden-Popper bismuth materials are superconducting, attributed to the buckling of the perovskite layers by Khasanova *et al*. The lead and potassium substituted materials are stable only for a small range of x. The indium material is unstable in air, readily taking up water by intercalation. Other known barium oxides of the type $(Ln_{1-x}Ba_x)_3M_2O_7$ are discussed further below.

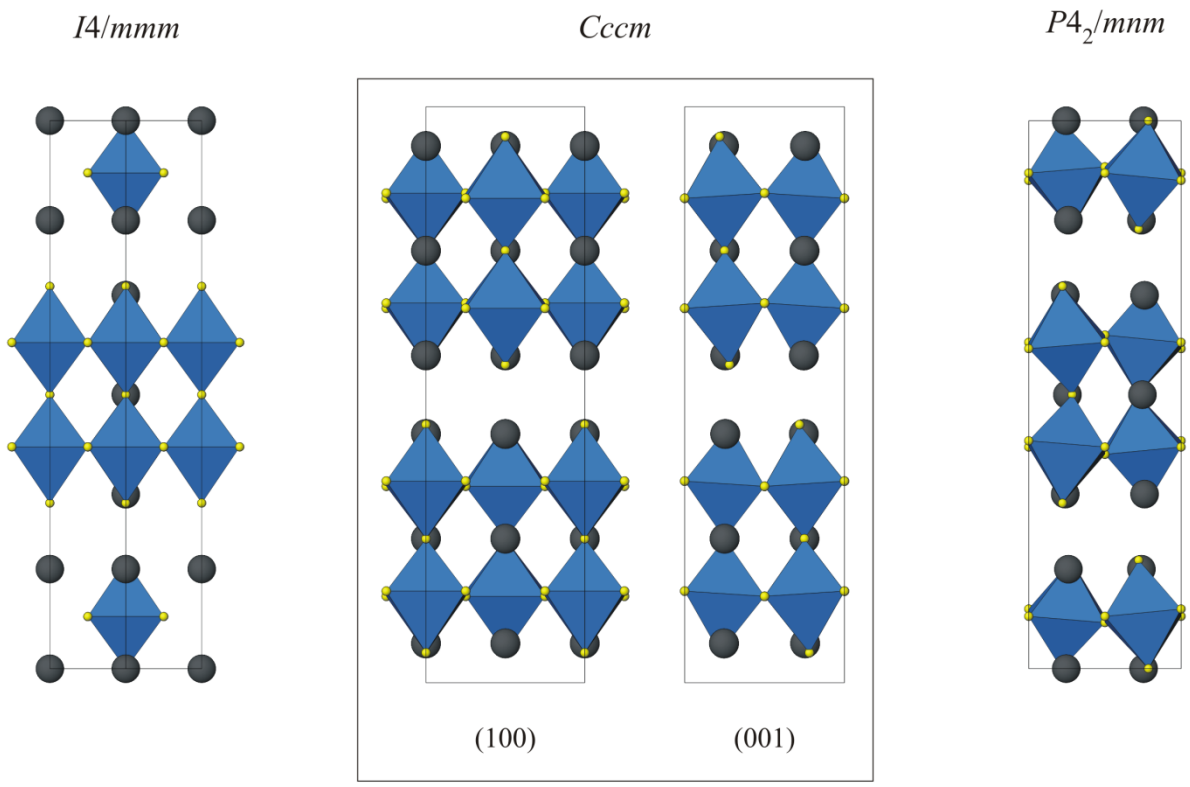

Figure 1.19 – Relationship between the two polymorphs of $Ba_3Zr_2S_7$ as determined by single crystal diffraction, and their relationship to the structure derived by powder diffraction.

Several of the materials $Sr_3M_2X_7$ are discussed throughout this work. In the introduction to chapter 6, the structure and chemistry of the mixed *B*-site $Sr_3MM'O_7$ previously known to the literature are discussed. Also in the chapter the results of efforts made to synthesise and characterise new $Sr_3MM'O_7$ phases, and a study of the room temperature and 3.4 K structure of the phase Sr_3CoNbO_7 are presented.

The system of ferrates with the general formula $Sr_3Fe_2X_{7-\delta}$ has been widely studied. For all of these ferrates reported in open literature, the structures are tetragonal, however anion non-stochiometry and substitution has produced a wide range of structural chemistry.

The first reported strontium ferrate Ruddlesden-Popper phases were in the low doping range, $\delta \approx 0.8$. Lucchini *et al*. reported a structure for the material "α-$Sr_3Fe_2O_7$" in 1973, with $\delta = 0.84$. [88] The unit cell is tetragonal, with a doubled *c* cell parameter. Through structural refinement of powder X-ray diffraction data, the space group *P*4*mmm* was selected for the material. On heating this material on a platinum matrix, the same group found that new phases, dubbed β- and γ-$Sr_3Fe_2O_7$ were formed, with further elongation of the *c* call parameter. [89] Later work by Dann *et al*. [90] demonstrated the link between structure and oxygen stochiometry in the series $0 \leq \delta \leq 1$, reporting a new structure for $Sr_3Fe_2O_6$ based on corner sharing square pyramids formed by removing the layer bridging oxygen from the standard $Sr_3Ti_2O_7$ structure. All other materials in the series contained octahedral FeO_6 iron sites with all oxygen absences on the same crystallographic site as the vacant site in the $\delta = 1$ material. Further work by Dann and co-workers on the stochiometric $Sr_3Fe_2O_7$ demonstrated that rather than the tetravalent iron suggested by the stochiometry of the system, at room temperature the material contains a mixture of Fe (III) and Fe (V). [91] Despite the mixed valence, only one crystallographic site is available for the iron, as determined by powder neutron diffraction. Neutron diffraction also placed the magnetic ordering temperature, T_N, at 90 K through the emergence of weak magnetic reflections in diffraction patterns below this temperature. The magnetic structure is antiferromagnetic in two dimensions. Later work by Kuzushita placed the Néel temperature at 120 K through variable temperature Mössbauer spectroscopy, and determined the temperature of charge disproportionation for the reaction $2Fe^{4+} \xrightarrow{T_c} Fe^{5+} + Fe^{3+}$ at 343 K, above which only a single peak corresponding to Fe^{4+} is observed in the spectrum. [92] Further studies on the chemistry of the strontium ferrate system have demonstrated a propensity to water intercalation into the system together with protons, reducing the iron valence. [93] Simultaneous doping of barium and zirconium onto the strontium and iron sites produce materials with high catalytic activity for the decomposition of NO. [94]

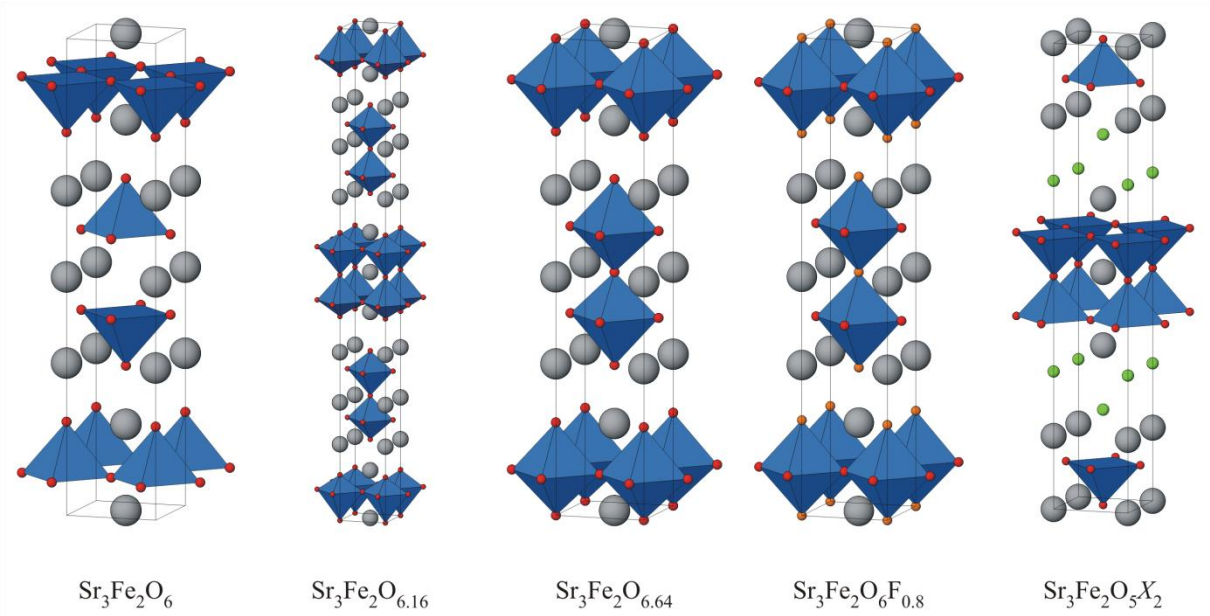

Figure 1.20 – The structures of a range of n = 2 Ruddlesden-Popper strontium ferrate materials. Grey spheres show strontium atom positions, blue polyhedra FeO_5 and FeO_6 octahedra, red spheres oxygen positions, orange spheres show mixed fluorine/oxygen sites and green spheres show the positions of X atoms (X = Cl, Br).

Substitution of the halides X = Br and Cl onto the apical oxygen site of $Sr_3Fe_2O_7$ forms the Fe (III) materials $Sr_3Fe_2O_5X_2$. The material $Sr_3Fe_2O_5Cl_2$ was first reported in 1984 by Lieb and Mullerbuschbaum, [95] and the bromide material and mixed B-site $Sr_3FeCoO_5Cl_2$ synthesised and characterised by Knee *et al*. in 2004. [96] The materials are described as layers of corner sharing FeO_5 square pyramids separated by SrX rock salt layers. The magnetic and crystal structures of the materials $Sr_3Fe_2O_5Br_2$ and $Sr_3FeCoO_5Cl_2$ were studied at room temperature and 2 K, and $Sr_3Fe_2O_5Cl_2$ in the temperature range 17 to 625 K. The Néel temperature of the chloride was determined at 590 K, with all three materials adopting two dimensional antiferromagnetic structures. Case and co-workers have reported the synthesis of $Sr_3Fe_2O_6F_{0.87}$, [97] produced by the reaction of fluorine with $Sr_3Fe_2O_6$. Unlike the larger bromine and chlorine ions in the stochiometric $Sr_3Fe_2O_5X_2$, the smaller fluorine ions substitute onto oxygen positions in the structure, occupying approximately one third of the apical and interlayer oxygen sites. As in the undoped oxides, the iron was shown to be a mixture of Fe^{5+} and Fe^{3+} through Mössbauer spectroscopy.

The materials $Sr_3Mn_2O_{7-\delta}$ (δ = 0, 0.45) were the first reported single ion A-site analogues of the layered CMR manganites. [98] The structures of both materials were refined in the space group $I4/mmm$, with the stoichiometric δ = 0 material demonstrating only small distortions of the MnO_6 octahedra. Powder neutron diffraction work by the same group demonstrated that the disordered oxygen vacancies in the non-stochiometric material produce a non-magnetic structure, while the δ = 0 material is an antiferromagnetic insulator. [99] The structures and transport properties of the Mn^{4+} manganites, both studied experimentally and through density functional theory calculations, [100] offer insight into the behaviour of the mixed A-site CMR materials.

The high cobalt valence phases $Sr_3Co_2O_{7-\delta}$, also known as $O_{5+\delta}$ for lower oxygen stochiometry, were first reported in 1995 by Dann and Weller. [101] As formerly seen for the ferrate analogues, the cobaltate with $\delta < 1$ crystallises in the tetragonal space group *I*4/*mmm*, with a $Sr_3Ti_2O_7$-like structure, oxygen vacancies statically disordered on exclusively the site linking the two perovskite planes. The cobalt bonding environment is highly distorted, with the cobalt site located close to the oxygen deficient anion site. The two materials with $\delta > 1$ crystallise in the orthorhombic space group *Immm*, with ordered oxygen vacancies producing a superstructure with tripled *b* cell parameter compared to the $Sr_3Ti_2O_7$ model. The reported structures for the materials are shown in Figure 1.21. Later work by Hill *et al*. expanded the range of known phases $Sr_3Co_2O_x$ to include $5.64 \leq x \leq 6.60$. [102] All phases are reported as adopting the space group *Immm*, with oxygen non-stochiometry on the interlayer and in-plane oxygen sites. The ordered vacancy superstructure previously reported by Dann and Weller was not observed, however the structure reported by Hill and co-workers shows a disordered 50 % occupation of this site. All materials order antiferromagnetically at low temperature, as determined by neutron powder diffraction. Viciu *et al*. reported several further cobaltates in the oxygen stochiometry range $5.38 \leq x < 6$. [103] In these materials the oxygen superstructure is implied by an unrefined half occupancy of the in-layer oxygen site, however again the space group selected for the phases is *Immm*. The magnetic properties of the materials were investigated, with ferromagnetic interactions present in the materials $x = 5.91$ and 5.64. The oxygen nonstochiometry in the strontium cobaltate system has been further reduced in recent work by Demont *et al*., [104] by doping the strontium site with cerium. The oxygen content in the system $Sr_{2.75}Ce_{0.25}Co_2O_{7-\delta}$ can be increased by sintering an as-prepared sample in oxygen to form a material with $\delta = 0.3$. The stochiometric phase $Sr_3Co_2O_5Cl_2$, formed by molten flux reaction, has been reported, crystallising in the space group *I*4/*mmm*. [105] The material is isostructural with the iron oxychlorides discussed above, with the chlorine occupying the apical octahedral (or rock salt) site. Novel hydroxide materials have been reported by Pelloquin and co-workers, [106] formed by hydration of $Sr_3Co_2O_{7-\delta}$. The long axis of the hydrated material is significantly lengthened by the inclusion of water into the rock salt layer, the phase crystallising in the monoclinic space group *I*2/*m*, with $b = 28.59$ Å. The phase is unstable on mild heating or vacuum, and dehydrates according to the sequence: $Sr_3Co_2O_5(OH)_2 \cdot (H_2O)_x \xrightarrow{\Delta} Sr_3Co_2O_5(OH)_2 \xrightarrow{\Delta} Sr_3Co_2O_{7-\delta}$.

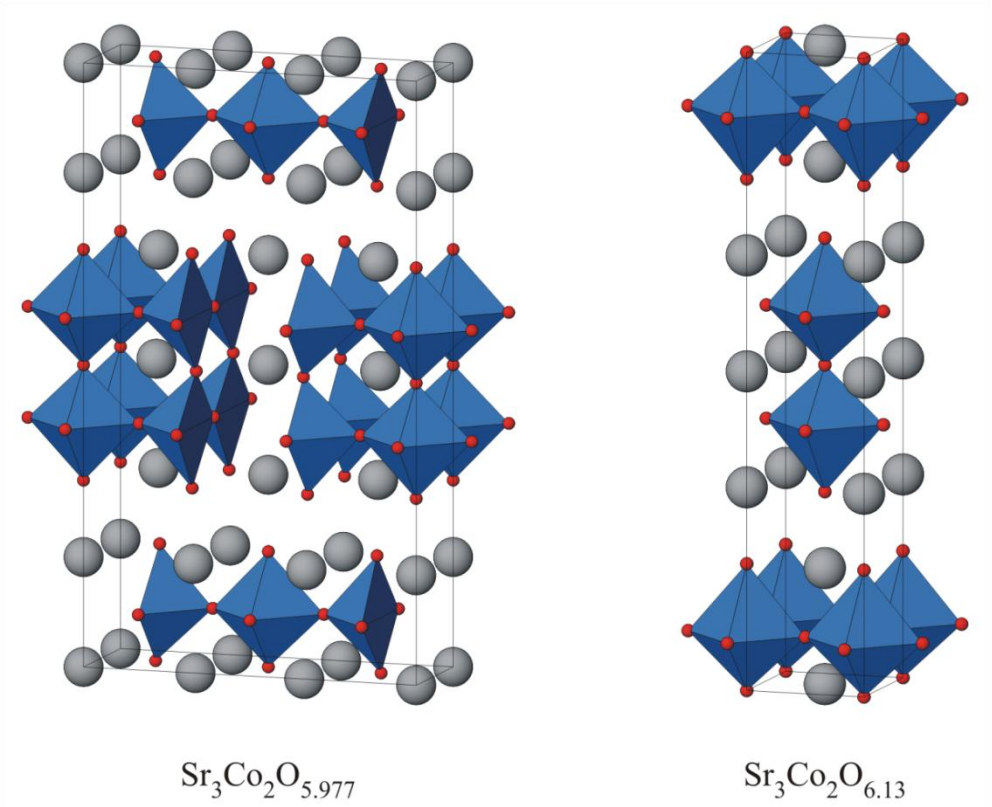

Figure 1.21 – The structure of $Sr_3Co_2O_{7-\delta}$ phases: the orthorhombic *Immm* $\delta = 1.23$ and tetragonal *I*4/*mmm* $\delta = 0.87$. Grey spheres show strontium positions, blue polyhedra CoO_5 and CoO_6, and red spheres oxygen atoms.

The structure of $Sr_3V_2O_7$ has been reported by a number of groups, based on Rietveld refinements of powder X-ray diffraction, and single crystal crystallography. [107-110] The material crystallises in *I*4/*mmm*, with the $Sr_3Ti_2O_7$ structure. Suzuki *et al*. determined that the variation of inverse magnetic susceptibility of the material with temperature is composed of a Curie-Weiss-like term and a static magnetisation term from the V^{4+}. [108] The residual magnetisation, 0.37 μ_B, is smaller than expected for the ion. Work by Niu *et al*. interpreted the magnetism of the material as a spin glass. [111] The phase is metallic, conducting through electron hopping. [108, 110, 111] Doping of chromium onto the vanadium site by Fukushima *et al*. changes the phase from a metallic conductor to insulator, while retaining the magnetic behaviour of the V_2 material. [112] The material $Sr_3Cr_2O_{7-\delta}$ (δ = 0.05) also crystallises in the space group *I*4/*mmm*, and is an insulator with two dimensional magnetic structure. [113]

A phase transition with accompanying change of structure was reported for the material $Sr_3Zr_2O_7$ using variable temperature X-ray diffraction [114] and conductivity methods. [115] At room temperature, the material is orthorhombic, crystallising in the space group *Pmmm*, isostructural with $Sr_3Ti_2O_7$ with $a > b$. Above ~ 950 K the symmetry of the system increases to tetragonal, $a = b$.

The material $Sr_3Sn_2O_7$ also crystallises in an orthorhombic space group. Green and co-workers have illustrated that the orthorhombic superstructure arises from tilting of SnO_6 octahedra, identified by the observation and fitting of supercell reflections in the powder

neutron diffractogram collected at room temperature. [116] The room temperature structure is in the space group *Cmcm*, $a \approx b \approx \sqrt{2}a_{I4/mmm}$.

$Sr_3Ir_2O_7$ was originally reported with the tetragonal *I*4/*mmm* structure, isostructural with $Sr_3Ti_2O_7$. [117] The authors reported significant (12 °) rotations of IrO_6 octahedra around the *c* axis in the room temperature structure, as determined by single crystal X-ray diffraction, however no long range order was determined, hence the overall tetragonal symmetry. Later structural work based on transmission electron microscopy and electron diffraction determined that these rotations were correlated, and proposed a room temperature structure in the space group *Bbcb* (lattice parameters not reported, however the text implies that $a = b$) by observation of weak supercell reflections in the diffraction patterns. [118] The same group examined the physical properties of the material in a later work. [119] The group conclude that the weak ferromagnetism observed below $T_c \approx 280$ K results from canted antiferromagnetic coupling between the Ir^{4+} sites. The material is semiconducting, with a discontinuity in the temperature dependence of conductivity around the magnetic transition temperature, however no structural changes are observed over the magnetic transition temperature.

Strontium rhodate also crystallises in the space group *Bbcb*, determined by neutron powder diffraction. [120] Similarly to polycrystalline samples of $Sr_3Ir_2O_7$, the material is formed by high temperature and pressure reaction of strontium carbonate and rhodium oxide. The material is metallic, with paramagnetic structure over the studied temperature range $2 \leq T \leq 390$ K.

The synthesis of $Sr_3Ru_2O_7$ for structure determination was reported twice in the early 1990s. In 1990, single crystals were prepared by Mullerbuschbaum and Wilkens, [121] and the sturucture of the material reported as a tetragonal *I*4/*mmm* $Sr_3Ti_2O_7$ isotype. Williams and co-workers reported the first synthesis of polycrystalline $Sr_3Ru_2O_7$ in 1991, [122] reporting a similar structure as determined by powder X-ray diffraction and electron microscopy. After the 1995 preparation of a highly phase pure sample of $Sr_3Ru_2O_7$ via an $Sr_2RuO_4{\cdot}(CO_2)_{0.25}$ precursor for examination of its physical properties, [123] particularly so soon after after the discovery of superconductivity in Sr_2RuO_4, [124] the $n = 1$ Ruddlesden-Popper analogue, many other publications on the structure and properties of the material were produced – more publications currently exist with $Sr_3Ru_2O_7$ listed in keywords or title than works on all the remaining $Sr_3M_2O_7$ (203 compared to 394, through a topic search on the ISI Web of Knowledge). [125] The structure of the material was determined by Shaked *et al*., with full fitting of neutron powder diffraction in the space group *Bbcb*, $a = b$. In their 1995 work, Cava and co-workers reported the material to be a metallic conductor, and paramagnetic with antiferromagnetic ordering below $T_N = 15$ K, [123] though a later single crystal study reported that the material is weakly ferromagnetic below 104 K. [126] Several later studies reported that this ferromagnetism must in fact be attributed to another phase (for example further work by the Cava group [127] or the work of Ikeda *et al*. on single crystals). [128] The metallic,

paramagnetic ground state of the material is the basis of much of the literature on this system, as these properties are also observed in the superconducting Sr_2RuO_4. [124] No superconductivity has however been reported in the $n = 2$ material.

*(*AA*')*$_3$$M_2X_7$

The majority of $n = 2$ Ruddlesden-Popper phases reported in current literature contain only one *A*-site cation, or are doped to low levels with a second *A*-site cation to induce changes in physical properties. These materials have been addressed in the previous section. For materials containing a mixed *A*-site, a relatively narrow range of systems have been studied. The Co (III) phases $Ln_2ACo_2O_7$ are discussed in chapter 3, including the synthesis and characterisation of a new phase and structural determinations of a room temperature superstructure and structural phase transition in the known material $Gd_2SrCo_2O_7$. The structures of the ferrate materials $Ln_2SrFe_2O_7$ are investigated in chapter 4, and the materials $Ln_2SrAl_2O_7$ reinvestigated in chapter 5. The phase $La_2SrSc_2O_7$, with orthorhombic room temperature structure in the space group *Fmmm*, has been previously reported. [129] On heating, the material undergoes two phase transitions, through a second orthorhombic phase to a tetragonal high temperature phase. In chapter 6, the structures of new mixed *A*-, mixed *B*-site materials $Nd_{2-x}Sr_{1+x}Ti_xFe_{2-x}O_7$ are discussed. The materials $Sr_2LaCuRuO_{7-\delta}$ and $Sr_{2.15}La_{0.85}CuRuO_{7-\delta}$, prepared by Attfield *et al.*, are two further examples of mixed *A* and *B* site materials. [130] The materials are semiconducting, and do not order magnetically at low temperature.

The most studied mixed *A*-site materials are the CMR materials, $(Ln,A)_3Mn_2O_7$ (*A* = Ca, Sr, Ba). The first report of a manganite material with the Ruddlesden-Popper structure was the 1981 publication of the structures of $BaLn_2Mn_2O_7$. [131] The materials were reported as tetragonal isostructures with the materials $BaLn_2Fe_2O_7$, with elongation of the MnO_6 octahedra originating in the Jahn-Teller distortion of the Mn (III) ions. The materials $Sr_{3-x}Ln_xMn_2O_7$ (*Ln* = La, Nd, Sm, Gd, $0 \leq x \leq 1.5$), which include the manganite CMR phases, were first prepared by Lamire and Daoudi. [132] The structures were all reported as tetragonal $Sr_3Ti_2O_7$-type, with the *c* cell parameter related to the size of Ln^{3+} and the doping of the material – the higher proportion of Jahn-Teller active Mn^{3+} with increased *x* gives a longer *c* for materials with the same *Ln*. After the discovery of CMR in the material family, the volume of work published on the materials rapidly increased in an attempt to elucidate the link between structure and properties of the materials. Battle *et al*. reported that the colossalmagnetoresistive materials $La_2SrMn_2O_7$ and $Nd_2SrMn_2O_7$ crystallise in the space group *I*4/*mmm*, [133, 134] as determined by refinements of powder neutron diffraction, and also report that in apparently phase pure materials, secondary $n = 2$ Ruddlesden-Popper impurities can be detected. The two phases observed in the lanthanum material demonstrate contrasting magnetic behaviour; with manganese spins the majority phase ordering antiferromagnetically below $T_N \approx 210$ K and the minor phase adopting a ferromagnetic structure below $T_c \approx 125$ K. The same group later reported the structures of the materials

$Sr_2HoMn_2O_7$ and $Sr_2YMn_2O_7$. [135] The smaller lanthanide ions preferentially occupy the 9-coordinate rock salt site in the structure, and ordered octahedral tilting leads to a $\sqrt{2}a_0 \times \sqrt{2}a_0 \times c$ superstructure in the space group $P4_2/mnm$. Unlike the materials containing larger *A*-site cations, the cation order in the Ho and Y materials stabilises the lattice, leading to only one Ruddlesden-Popper phase per composition. The materials are insulating, do not exhibit CMR and do not order magnetically, undergoing a transition from paramagnetic to spin glass at ~ 20 K. The group attribute the differences in electronic and magnetic properties as the *A*-site cation changes to the variation in relative strengths of super- and double exchange mechanisms across the series. [136] The unusual transport and magnetic properties of the materials are discussed in the CMR section above.

Scope of this work

The Ruddlesden-Popper, $n = 2$ materials display a range of unique magnetic, electronic and structural properties. The interplay of the structural and electronic properties in the phases leads to bulk physical properties such as magnetism, conductivity and CMR. In closely related systems, a similar interplay has caused ferroelectricity and superconductivity. Through the study of structural properties of materials, their properties can be understood.

This work focused on identifying structural trends in the Ruddlesden-Popper series. Initially, the materials $Ln_2ACo_2O_7$ were studied. Materials formed by high temperature synthesis crystallise in supercell structures, and the *Ln* = Gd, A = Sr material undergoes a structural phase transtition at high temperature to lower symmetry. This uncommon type of transition (apparently not previously reported for a Ruddlesden-Popper material) is accompanied by a spin crossover electronic transition in the Co (III) centres, suggests a complex interplay of electronic and structural properties in these materials.

To investigate the possible origins of the transition in $Gd_2SrCo_2O_7$, the evolution of the structure of $Gd_2SrFe_2O_7$ was examined on heating. In this material, too, a structural transition to lower symmetry is apparent on heating. This transition is at a higher temperature than in the cobaltate, suggesting that while the spin crossover of Co may be related to the structural change, it is not necessarily critical to the transition.

The observation of superstructures in all the ferrate and cobaltate materials studied in this work suggested a possible overarching distorted structure for $Ln_2SrM_2O_7$ materials. Samples of the recently reinvestigated $Ln_2SrAl_2O_7$ were prepared, and as predicted, the phases studied by powder neutron diffraction crystallise in the space group $P4_2/mnm$.

Finally, the structure of $Sr_3Ti_2O_7$ was examined with powder neutron diffraction as a function of temperature for the first time. The instrument HRPD, with excellent diffraction peak resolution, was used to search for any small changes in symmetry on heating, as a point of comparison for the unusual behaviour observed in the ferrate and cobaltate materials.

References

1. H. D. Megaw, *Proc. Phys. Soc*., 1946, **58**, 133-134
2. A. M. Glazer, *Acta Cryst*., 1972, **B28**, 3384-3392
3. H. K. Onnes, *Proc. Koninklijke Acad*., 1911, **14**, 113-115
4. W. Meissner and R. Ochsenfeld, *Naturwissenschaften*, 1933, **21**, 787-788
5. E. Maxwell, *Phys. Rev*., 1950, **78**, 477
6. J. Bardeen, L. N. Cooper and J. R. Schrieffer, *Phys. Rev*., 1957, **106**, 162-164
7. J. Bardeen, L. N. Cooper and J. R. Schrieffer, *Phys. Rev*., 1957, **108**, 1175-1204
8. W. Meissner, H. Franz and H. Westerhoff, *Annal. Phys*., 1933, **17**, 593-619
9. A. W. Sleight, J. L. Gillson, P. E. Bierstedt, *Solid State Comm*., 1975, **17**, 27-28
10. G. R. Rao, R. Seshadri, C. N. R. Rao, *Appl. PPhys. Lett*., 1990, **57**, 1823-1824
11. J. G. Bednorz and K. A. Müller, *Zeit. Phys. B, Cond. Matter*, 1986, **64**, 189-193
12. B. T. Matthias, T. H. Geballe, R. H. Willens, E. Corenzwit and G. W. Hull, *Phys. Rev*., 1965, **A139**, 1501-1503
13. L. Newkirk, F. Valencia, A. Giorgi, E. Szklarz and T. Wallace, *IEEE Trans., Mag*., 1975, **11**, 221-224
14. C. K. Loong and L. Soderholm, *Phys. Rev*., 1993, **B48**, 14001-14004
15. K. Takegahara and T. Kaswya, *J. Phys. Soc. Jap*., 1990, **59**, 2098-2109
16. A. C. W. P. James, D. W. Murphy and S. M. Zahurak, *Nature*, 1989, **338**, 240-241
17. J. T. Markert and M. B. Maple, *Solid State Comm*., 1989, **70**, 145-147
18. J. D. Jorgensen, B. Dabrowski, S. Y. Pei, D. G. Hinks, L. Soderholm, B. Morosin, J. E. Schirber, E. L. Venturini and D. S. Ginley, *Phys. Rev*., 1988, **B38**, 11337-11345
19. M. K. Wu, J. R. Ashburn, C. J. Torng, P. H. Hor, R. L. Meng, L. Gao, Z. J. Huang, Y. Q. Wang and C. W. Chu, *Phys. Rev. Lett*., 1987, **58**, 908-910
20. G. Roth, B. Reneher, G. Heger, M. Hervieu, B. Domenges and B. Ravenau, *Zeit. fur Phys*., 1987, **B69**, 53-59
21. R. J. Cava, A. W. Hewat, E.A. Hewat, B. Batlogg, M. Marezio, K. M. Rabe, J. J. Krajewski, W. F. Peck and L. W. Rupp, *Physica*, 1990, **C165**, 419-433
22. K. Yang, L. Yu, S. H. Han, H. Zhang and Y. Zhao, *Physica*, 2001, **C357**-360, 305-308
23. P. Dai, B. C. Chakoumakos, G. F. Sun, K. W. Wong, Y. Xin and D. F. Lu, *Physica*, 1995, **C243**, 201-206
24. H. Maeda, Y. Tanaka, M. Fukutomi and T. Asano, *Jap. J. Appl. Phys*., 1988, **27**, L209-L210
25. K. Togano, H. Kumakura, H. Maeda, E. Yanagisawa and K. Takahashi, *Appl. Phys. Lett*., 1988, **53**, 1329-1331
26. Y. Kamihara, T. Watanabe, M. Hirano and H. Hosono, *J. Am. Chem. Soc*., 2008, **130**, 3296-3297
27. A. Takahashi, K. Igaua, K. Arii, Y. Kamihara, M. Hirano and H. Hosono, *Nature*, 2008, **453**, 376-378
28. G. F. Chen, Z. Li, D. Wu, G. Li, W. Whu, J. Dong, P. Zheng, J. L. Luo and N. L. Wang, *Phys. Rev. Lett.*, 2008, **100**, 226402
29. Z. A. Ren, J. Wang, W. Lu, W. Yi, G. C. Che, X. L. Dong, L. L. Sun and Z. X. Zhao, *Mater. Res. Innovations*, 2008, **12**, 105-106
30. Z. A. Ren, J. Yang, W. Lu, W. Yi, X. L. Shen, Z. C. Li, G. C. Che, X. L. Dong, L. L. Sua, F. Zhou, Z X. Zhao, *Emerging Physics Letters*, 2008, **82**, 57002
31. X. H. Chen, T. Wu, G. Wu, R. H. Liu, H. Chen and D. F. Fang, *Nature*, 2008, **453**, 761-762
32. A. S. Sefat, R. Y. Jin, M. A. McGuire, B. C. Sales, D. J. Singh and D. Mandrus, *Phys. Rev. Lett.*, 2008, **101**, 117004
33. H. H. Wen, G. Mu, L. Fang, H. Yang and X. Y. Zhu, *Emerging Physics Letters*, 2008, **82**, 17009
34. G. Wu, Y. L. Xie, H. Chen, M. Zhong, R. H. Liu, B. C. Shi, Q. J. Li, X. F. Wang, T. Wu, Y. J. Yan, J. J. Ying and X. H. Chen, *J. Phys. Cond. Matter*, 2009, **21**, 142203
35. A. Guinier and R. Jullien, "*The Solid State: From Superconductors to Superalloys*", Oxford Science Publications, 1989
36. C. Zener, *Phys. Rev*., 1951, **82**, 403-405
37. R. P. Borges, R. M. Thomas, C. Cullinan, J. M. D. Coey, R. Suryanarayanan, L. Ben-Dor, L. Pinsard-Gaudart and A. Revcolevschi, *J. Phys. Cond. Matt*., 1999, **11**, L445-L450
38. T. H. Kim, M. Urehara, S. W. Cheong and S. Lee, *Appl. Phys. Lett*., 1999, **74**, 1737-1739
39. J. S. Moodera, L. R. Kinder, T. M. Wong and R. Meservey, *Phys. Rev*., 1995, **74**, 3273-3276
40. A. Urushibara, Y. Moritomo, T. Arima, A. Asamitsu, G. Kido and Y. Tokura, *Phys. Rev*., 1995, **B51**, 14103-14109
41. A. P. Ramirez, *J. Phys. Cond. Matt*., 1997, 9, 8171-8199
42. H. Y. Hwang, S. W. Cheong, P. G. Radaelli, M. Marezio and B. Batlogg, *Phys. Rev. Lett*., 1995, **75**, 914-917

43. Y. Moritomo, A. Asamitsu, H. Kuwahara and Y. Tokura, *Nature*, 1996, **380**, 141-144
44. P. D. Battle, S. J. Blundell, M. A. Green, W. Hayes, M. Honold, A. K. Klehe, N. S. Laskey, J. E. Millburn, L. Murphy, M. J. Rosseinsky, N. A. Samarin, J. Singleton, N. E. Sluchanko, S. P. Sullivan and J. F. Vente, *J. Phys. Cond. Matter*, 1996, **8**, L427-L434
45. T. Kimura, Y. Tomioka, H. Kuwahara, A. Asamitsu, M. Tamura and Y. Tokura, *Science*, 1996, **274**, 1698-1701
46. E. Dagotto, T, Hotta and A. Moreo, *Phys. Reports*, 2001, **344**, 1-153
47. S. N. Ruddlesden and P. Popper, *Acta Cryst.*, 1957, **10**, 538
48. S. N. Ruddlesden and P. Popper, *Acta Cryst.*, 1958, **11**, 54-55
49. D. Babel and E. Herdtweck, *Zeit. Anorg. Allg. Chem*., 1982, **487**, 75-84
50. C. M. J. Vanuijen, E. Frikkee and H. W. Dewijn, *Phys. Rev*., 1979, **B19**, 509-520
51. H. Manaka, Y. Miyashita, Y. Watanabe and T. Masuda, *J. Phys. Soc. Jap*., 2007, **76**, 085003
52. J. Ferguson, E. R. Krausz, G. B. Robertson and H. J. Guggenheim, *Chem. Phys. Lett*., 1972, **17**, 551-553
53. D. Babel and E. Herdtweck, *Zeit. Anorg. Allg. Chem*., 1981, **474**, 113-122
54. H. Manaka, Y. Miyashita, Y. Watanabe and T. Masuda, *J. Phys. Soc. Jap*., 2007, **76**, 044710
55. C. Brisi and P. Rolando, *Ricerca Scientifica*, 1966, **36**, 48-50
56. E. Herdtweck and D. Babel, *Zeit. Krist*., 1980, **153**, 189-199
57. H. J. Seifert and F. W. Koknat, *Zeit. Anorg. Allg. Chem*., 1965, **341**, 269-280
58. J. Goodyear, E. M. Ali and H. H. Sutherland, *Acta Cryst*., 1982, **B38**, 600-602
59. W. J. Crama, *Acta Cryst*., 1981, **B37**, 662-664
60. M. Amit, A. Horowitz and J. Makovsky, *Isreal J. Chem*., 1972, **10**, 715-719
61. E. Gurewitz, J. Makovsky and H. Shaked, *Phys. Rev*., 1976, **B14**, 2071-2077
62. K. Katsumata and J. Tuchendler, *J. Phys*., 1987, **20**, 4873-4879
63. Z. Zhang, M. Greenblatt and J. B. Goodenough, *J. Solid State Chem*., 1994, **108**, 402-409
64. V.V. Poltavets, K. A. Lokshin, T. Egami and M. Greenblatt, *Mat. Res. Bull*., 2006, **41**, 955-960
65. Y. Kobayashi, S. Taniguchi, M. Kasai, M. Sato, T. Nishioka and M. Kontani, *J. Phys. Soc. Jap*., 1996, **65**, 3978-3982
66. P. D. Battle, J. C. Burley, D. J. Gallon, C. P. Grey and J. Sloan, *J. Solid State Chem*., 2004, **177**, 119-125
67. K. D. Hawkins and T. J. White, *Phil. Trans. Royal Soc*., 1991, **336**, 541-569
68. G. Pfaff, *Chem. Mater*., 1994, **6**, 58-62
69. K. T. Jacob and K. P. Abraham, *J. Chem. Therm*., 2009, **41**, 816-820
70. I. D. Fawcett, J. E. Sunstrom, M. Greenblatt, M. Croft and K. V. Ramanujachary, *Chem. Mater*., 1998, **10**, 3643-3651
71. J. L. Zhu, R. C. Yu, F. Y. Lin and C. Q. Jin, *Phys. Stat. Solid*., 2002, **A194**, 159-166
72. L. A. Bendersky, R. Chen, I. D. Fawcett and M. Greenblatt, *J. Solid State Chem*., 2001, **157**, 309-323
73. N. Guiblin, D. Grenbille, H. Leligny and C. Martin, *Acta Cryst*., 2002, **C58**, I3-I5
74. M. Lobanov, M. Greenblatt, E. N. Caspi, J. D. Jorgensen, D. V. Sheptyakov, B. H. Toby, C. E. Botez and P. W. Stephens, *J. Phys. Cond. Matt*., 2004, **16**, 5339-5348
75. W. H. Jung, *J. Mat. Sci. Lett*., 2000, **19**, 2037-2038
76. S. F. Matar, V. Eyert, A. Villesuzanne, M. H. Whangbo, *Phys. Rev*., 2007, **B76**, 054403
77. Y. Yoshida, S. I. Ikeda, H. Matsuhata, N. Shirakawa, C. H. Lee and S. Katano, *Phys. Rev*., 2005, **B72**, 054412
78. E. Ohmichi, Y. Yoshida, S. I. Ikeda, N. Shirakawa and T. Osada, *Phys. Rev*., 2004, **B70**, 104414
79. G. Cao, L. Balicas, Y. Xin, E. Dagotto, J. E. Crow, C. S. Nelson, D. F and Agterberg, *Phys. Rev*., 2003, **B67**, 060406
80. C. S. Snow, S. L. Cooper, G. Cao, J. E. Crow, H. Fukzazwa, S. Nakatsuji and Y. Maeno, *Phys. Rev. Lett*., 2002, **89**, 226401
81. M. Saeki, Y. Yakima and M. Onodo, *J. Solid State Chem*., 1991, **92**, 286-294
82. B. H. Chen, B. W. Eichhorn and N. W. Wong, *Acta Cryst*., 1994, **C50**, 161-164
83. Y. C. Hung, J. C. Fettinger and B. W. Eichhorn, *Acta Cryst*., 1997, **C53**, 827-829
84. R. J. Cava, H. Takagi, H. W. Zandbergen, B. Hessen, J. J. Krajewski and W. F. Peck, *Phys. Rev*., 1992, **B46**, 14101-14104
85. A. Baszczuk, *J. Alloys Comp*., 2006, 414, 287-292
86. R. J. Cava, T. Seigrist, W. F. Peck, J. J. Krajewski, B. Batlogg and J. Rosamilia, *Phys. Rev*., 1991, **B44**, 9746-9748
87. N. R. Khasanova, M. L. Kovba, S. N. Putilin, E. V. Antipov, O. I. Lebedev and G. Van Tendeloo, *Solid State Comm*., 2002, **122**, 189-193
88. E. Lucchini, D. Minichelli and G. Sloccari, *Acta Cryst*., 1973, **B29**, 2356-2357

89. E. Lucchini, D. Minichelli and G. Sloccari, *J. Mat. Sci*., 1974, **9**, 212-216
90. S. E. Dann, M. T. Weller and D. B. Currie, *J. Solid State Chem*., 1992, **97**, 179-185
91. S. E. Dann, M. T. Weller, D. B. Currie, M. F. Thomas and A. D. Alrawwas, *J. Mat. Chem*., 1993, **3**, 1231-1237
92. K. Kuzushita, S. Morimoto, S. Nasu and S. Nakamura, *J. Phys. Soc. Jap*., 2000, **69**, 2767-2770
93. M. Matvejeff, M. Lahtimaki, A. Hirasa, Y. H. Huang, H. Yamauchi and M. Karppinen, *Chem. Mater*., 2005, **17**, 2775-2779
94. T. Ishihara, Y. Shinmyo, K. Goto, N. Nishiyama, H. Iwakuni and H. Matsumoto, *Chem. Lett*., 2008, **37**, 318-319
95. W. Lieb and H. Mullerbuschbaum, *Zeit. Anorg. Allg. Chem*., 1984, **518**, 115-119
96. C. S. Knee, M. A. L. Field and M. T. Weller, *Solid State Sci*., 2004, **6**, 443-450
97. G. S. Case, A. L. Hector, W. Levason, R. L. Needs, M. F. Thomas and M. T. Weller, *J. Chem. Mater*., 1999, **9**, 2821-2827
98. J. F. Mitchell, J. E. Millburn, M. Medarde, S. Short, J. D. Jorgensen and M. T. Fernandez-Diaz, *J. Solid State Chem*., 1998, **141**, 599-603
99. J. F. Mitchell, J. E. Millburn, M. Medarde, D. N. Argyriou and J. D. Jorgensen, *J. Appl. Phys*., 1999, **85**, 4352-4354
100. H. Meskine, Z. S. Popovic and S. Satpathy, *Phys. Rev*., 2002, **B65**, 094402
101. S. E. Dann and M. T. Weller, *J. Solid State Chem*., 1995, **115**, 449-507
102. J. M. Hill, B. Dabrowski, J. F. Mitchell and J. D. Jorgensen, *Phys. Rev*., 2006, **B74**, 174417
103. L. Viciu, H. W. Zandbergen, Q. Xu, Q. Huang, M. Lee and R. J. Cava, *J. Solid State Chem*., 2006, **179**, 500-511
104. A. Dermont, S. Herbert, D. Pelloquin and A. Maignan, *J. Solid State Chem*., 2008, **181**, 1314-1320
105. S. M. Loureiro, C. Felser, Q. Huang and R. J. Cava, *Chem. Mater*., 2000, **12**, 3181-3185
106. D. Pelloquin, N. Barrier, A. Maignan and V. Caignaert, *Solid State Sci*., 2005, **7**, 853-860
107. A. Nozaki, H. Yoshikawa, T. Wada, H. Yamauchi and S. Tanaka, *Phys. Rev*., 1991, **A43**, 181-185
108. N. Suzuki, T. Noritake, N. Yamamoto and T. Hioki, *Mat. Res. Bull*., 1991, **26**, 1-9
109. K. J. Range, F. Rau and U. Klement, *Zeit. Natur*., 1991, **B46**, 1315-1318
110. M. Itoh, M. Shikano, H. Kawaji and T. Nakamura, *Solid State Comm*., 1991, **80**, 545-548
111. H. Niu, N. Fukushima and K. Ando, *Phys. Rev*., 1991, **B44**, 4724-4726
112. N. Fukushima, S. Tanaka, H. Niu and K. Ando, *Jap. J Appl. Phys*., 1990, **29**, L2190-L2192
113. E. Castillo-Martinez and M. A. Alario-Franco, *Solid State Sci*., 2007, **9**, 564-573
114. V. Longo and D. Minichelli, *Annali di Chimica*, 1974. **64**, 471-476
115. S. Roitti, *J. Mat. Sci.Lett*., 1982, **1**, 217-218
116. M. A. Green, K. Praddides, P. Day and D. A. Neumann, *Int. J. Inorg. Mat*., 2000, **2**, 35-41
117. M. A. Subramanian, M. K. Crawford and R. L. Harlow, *Mat. Res. Bull*., 1994, **29**, 645-650
118. H. Matsuhata, I. Nagai, Y. Yoshida, S. Hara, S. Ikeda and N. Skirakawa, *J. Solid State Chem*., 2004, **177**, 3776-3783
119. I. Nagai, Y. Yoshida, S. I. Ikeda, H. Matsuhata, H. Kito and M. Kosaka, *J. Phys. Cond. Matt*., 2007, **19**, 136214
120. K. Yamaura, Q. Huang, D. P. Young, Y. Noguchi and E. Takayama-Muromachi, *Phys. Rev*., 2002, **B66**, 134431
121. H. Mullerbuschbaum and J. Wilkens, *Zeit. Anorg. Allge. Chem*., 1990, **591**, 161-166
122. T. Williams, F. Lichtenberg, A. Reller, G. Bednorz, *Mat. Res. Bull*., 1991, **26**, 763-770
123. R. J. Cava, H. W. Zandbergen, J. J. Krajewski, W. F. Peck, B. Batlogg, S.Carter, R. M. Fleming, O. Zhou and L. W. Rupp, *J. Solid State Chem*., 1995, **116**, 141-145
124. Y. Maeno, H. Hashimoto, K. Yoshida, S. Nishizaki, T. Fujita, J. G. Bednorz, F. Lichtenberg, *Nature*, 1994, **372**, 532-534
125. "ISI Web of Knowledge", *http://www.isiknowledge.com*
126. G. Cao, S. McCall and J. E. Crow, *Phys. Rev*., 1997, **B55**, R672-R675
127. Q. Huang, J. W. Lynn, R. W. Erwin, J. Jarpatrakorn and R. J. Cava, *Phys. Rev*., 1998, **B58**, 8515-8521
128. S. Ikeda, Y. Maeno, S. Nakatuji, M. Kosaka and Y. Uwatoko, *Phys. Rev*., 2000, **B62**, R6089-R6092
129. I. S. Kim, H. Kawaji, M. Itoh and T. Nakamura, *Mat. Res. Bull*., 1992, **27**, 1193-1203
130. M. P. Attfield, P. D. Battle, S. K. Bollen, S. H. Kim, A. V. Powell and M. Workman, *J. Solid State Chem*., 1992, **96**, 344-359
131. M. N. Cheruy and J. C. Joubert, *J. Solid State Chem*., 1981, **40**, 14-19
132. M. Lamire and A. Daoudi, *J. Solid State Chem*., 1984, **55**, 327-330
133. P. D. Battle, D. E. Cox, M. A. Green, J. E. Millburn, L. E. Spring, P. G. Radaelli, M. J. Rosseinsky and J. F. Vente, *Chem. Mater*., 1997, **9**, 1042-1049

134. P. D. Battle, M. A. Green, N. S. Laskey, J. E. Millburn, P. G. Radaelli, M. J. Rosseinsky, S. P. Sullivan and J. F. Vente, *Phys. Rev*., 1996, **B54**, 15967-15977
135. P. D. Battle, J. E. Millburn, M. J. Rosseinsky and P. G. Radealli, *Chem. Mater*., 1997, **9**, 3136-3143
136. P. D. Battle, M. A. Green, N. S. Laskey, N. Kasmir, J. E. Millburn, L. E. Spring, S. P. Sullivan, M. J. Rosseinsky and J. F. Vente, *J. Mater. Chem*., 1997, **7**, 977-988

Chapter 2 – Experimental methods

Introduction

In this work, solid state methods were used to prepare oxide materials. The aim of this work was the structural analysis of layered oxide materials, so characterisation methods that determine material structures make up the bulk of the analysis. All materials were prepared as powders, so powder diffraction techniques (X-ray and neutron powder diffraction) are used in the first instance for structural determination. When the origin of structural observations was not clear from structural information alone, other techniques (magnetometry and thermal analysis techniques) were used to elucidate results.

In this chapter, the theory and practise of experimental methods used in this work are discussed in more detail.

Synthesis methods

All materials in this work were prepared by solid state synthesis methods, forming microcrystalline powders.

Calcination

The majority of the materials used in this work were synthesised using high temperature solid state synthesis. Thermal energy provided to the reactants allows ions to become mobile enough to migrate through crystallites to form new materials. Reactants must be intimately mixed to ensure that the starting materials are able to react, and products are homogeneous. Small reactant crystallites produce a higher surface area for reaction, increasing reaction rate. [1] To ensure good mixing and maximise surface area and surface contact of starting materials, reactants were ground together for several minutes. The length of time for grinding is not constant, and depends on the hardness of reactants. When the starting mixture is homogeneous and the grain size is minimised, then mixing is complete.

One starting material will often be chosen for its propensity to decompose on heating: this initial reaction with the evolution of gas aids in breaking down larger crystallites. For materials containing alkali earth metals, the carbonates ACO$_3$ (A = Sr, Ba) were used for this purpose. As AO materials are hygroscopic, forming A(OH)$_2$.(H$_2$O)$_n$ in air, this has the added advantage of allowing more straightforward control of stochiometry. When target phases contain lanthanides, the oxide starting material is dried prior to use. When stored in air, lanthanide oxides sequentially form hydrates and hydroxides, which can be decomposed to the oxide on heating. After drying, Ln_2O_3 were weighed out immediately, ideally while still hot.

To allow ions to more easily move through the reaction mixture it is usually necessary to compress the reactants into a pellet before annealing; for less reactive starting materials the application of high pressure during the reaction may also aid reaction.

To ensure uniformity of products and to aid the reaction going to completion, several annealing steps were carried out for a typical high temperature synthesis. After each heating stage the mixture of reactants and products were ground and pelletized prior to another heating cycle. For a new synthesis, the reaction mixture was characterised after each anneal to check on the progress of the reaction. A reaction is considered to be complete when either:

1. No starting material is measurable in the reaction mixture and the full width half maxima of product phase peaks do not change after repeated anneals (successfully completed reaction),
2. The levels of impurities and/or starting materials do not change after two or more additional annealing steps (reaction complete but target phase not formed or formed with impurities).

The oxidation states of ions in a material formed by calcination can be controlled by the atmosphere in which the reaction takes place. Oxidative environments used in this work include oxygen and air (strictly, 21 % oxygen), reductive environments (though not featuring in this work) include hydrogen gas in variable dilution in nitrogen and an oxygen free, dry atmosphere can be achieved under flowing nitrogen or argon.

Sol-gel reactions

If it is possible to form a pure product using only a calcination method, then the ease and speed of this method make it desirable for a lab synthesis. If it is not possible to form a phase pure target material using this method, however, then reaction conditions can be altered to attempt to favour production of the desired phase. As well as altering the heating profile of the reaction mixture, the degree of mixing can be increased to aid the reaction of the starting materials.

Gel reactions aim to mix starting materials by chemical rather than physical means. Co-precipitation reactions are used to produce mixtures in which are only separated on the level of recrystallisation of the nitrate starting materials. By mixing at the atomic rather than microscopic level, a greater intimacy is achievable. For reactions carried out in this work, citrate gels were used.

Nitrates of the appropriate metals were dissolved in a minimum volume of hot water (or hot, dilute nitric acid), and a solution of dilute citric acid added to the mixture. Ethylene glycol was added to the mixture to form a gel, and heating the mixture to dryness with stirring distributes ions. On drying, a gel of the metal citrates is formed. Decomposition of these citrates at moderate temperatures (573 K) forms a thoroughly mixed mixture of the metal oxides. As well as improving the quality of products, reactions may take place at lower temperatures or milder conditions.

Characterisation methods – diffraction methods

X-ray diffraction

The first observation of X-rays were reported by Röntgen in 1895. While working on the scattering properties of crystals, Laue discovered that X-rays were of an appropriate wavelength to diffract from the crystal lattice of materials.

When X-rays interact with materials, the radiation is scattered from the electron cloud of the atoms in the material. This scattered radiation will then interfere constructively and destructively with scattering from neighbouring atoms. In a crystalline material with a regularly repeating structure, the large number of scatterers act like a diffraction grating with a large number of lines, producing very sharply defined points of constructive interference and no signal in the regions where the diffraction condition is not satisfied. So when monochromated X-rays interact with a single crystal, the planes of regularly arranged atoms diffract the radiation along directions related to the interplanar distances in the crystal.

The repeating unit of a crystal is known as the unit cell: it contains all the information required to completely reconstruct the structure of the crystal.

William Bragg found that the angles at which diffraction events occur can be related to these interplanar distances by analogy to reflections of the X-rays from the planes. [2] As for all scattering, constructive interference occurs only when a path difference between two scattering incidents is equal to an integer number of wavelengths. At any other path difference, averaging over a theoretical infinite number of destructive events in a crystal will produce overall no intensity.

Figure 2.1 shows the representation used to derive the Bragg equation from the reflection description of diffraction. From the diagram, the path difference between the two beams is the length shown between the two dotted lines. Trigonometrically this length is equal to $2\sin\theta$, so the Bragg equation for a constructive diffraction event is $n\lambda = 2d\sin\theta$.

Any plane of atoms in a crystal will cause constructive interference and diffraction at some value of θ. By defining the minimum uniquely repeating unit in a crystal it becomes straightforward to identify these planes using the Bragg equation and predict where reflections would be expected for given values of d.

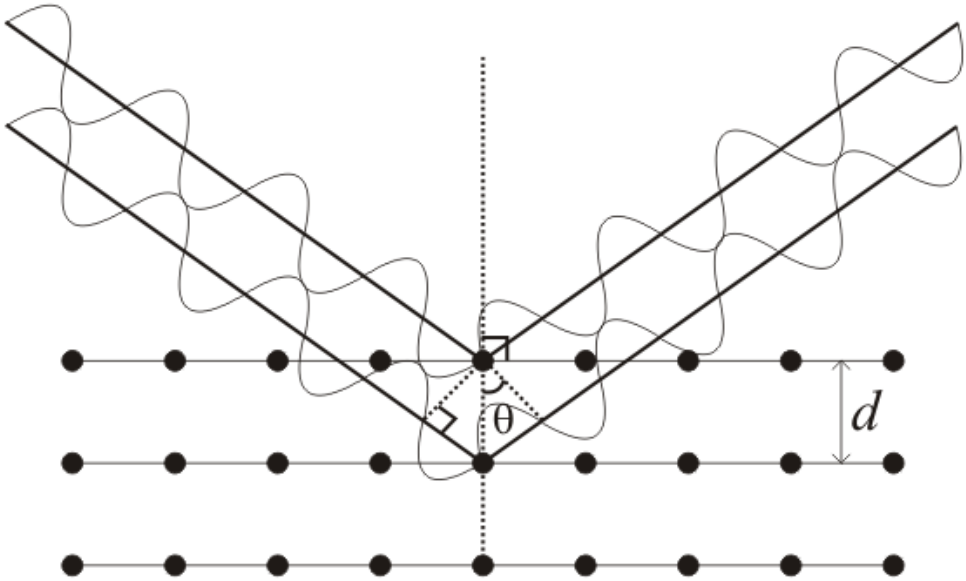

Figure 2.1 – Reflection description of Bragg's Law.

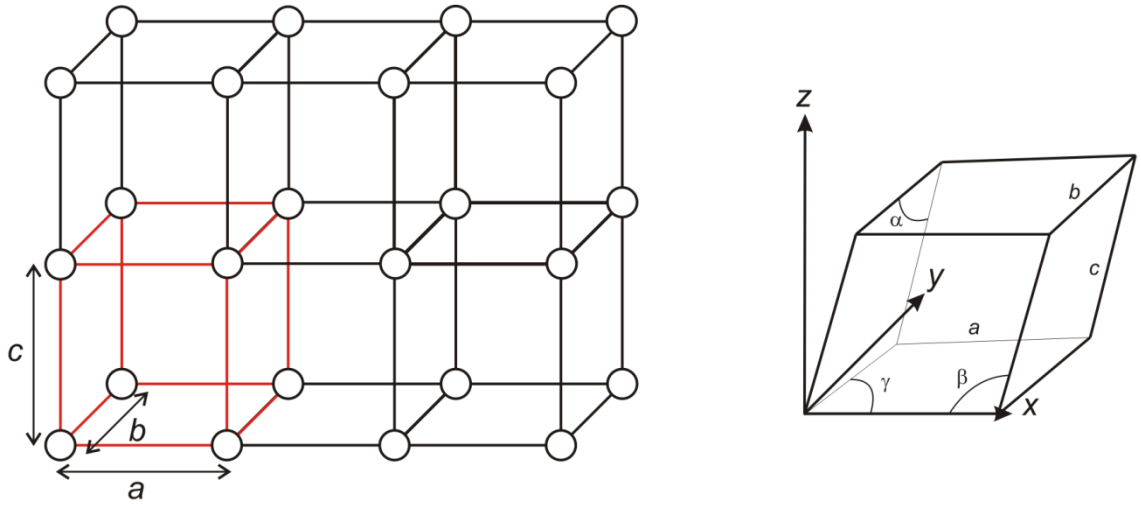

Figure 2.2 - The unit cell – stacking a unit cell within a crystal (left), unit cell parameters (right).

Figure 2.2 illustrates the unit cell in a crystalline material. The unit cell is the smallest unique repeating unit in the structure which exhibits the full symmetry of the material. The lattice parameters a, b and c are the unit cell lengths along the x, y and z axes respectively. The angles α, β and γ are the angles opposing a, b and c in the unit cell. In the lowest symmetry system, $a \neq b \neq c$ and $\alpha \neq \beta \neq \gamma \neq 90$. Possible crystal systems are shown below in Table 2.1.

Table 2.1 – The seven crystal symmetries, from lowest to highest symmetry

Triclinic	$\alpha \neq \beta \neq \gamma \neq 90$ °	$a \neq b \neq c$
Monoclinic	$\alpha \neq 90$, $\beta = \gamma = 90$ °	$a \neq b \neq c$
Orthorhombic	$\alpha = \beta = \gamma = 90$ °	$a \neq b \neq c$
Rhombohedral	$\alpha \neq \beta \neq \gamma \neq 90$ °	$a = b = c$
Tetragonal	$\alpha = \beta = \gamma = 90$ °	$a = b \neq c$
Hexagonal	$\alpha = \beta = 90$ °, $\gamma = 120$ °	$a = b \neq c$
Cubic	$\alpha = \beta = \gamma = 90$ °	$a = b = c$

All the possible planes of atoms that can cause diffraction events in a crystal can be defined in terms of fractions of the unit cell. Miller indices are used to describe these planes: these are the reciprocal lengths of the distance along each unit cell length cut by the plane. Figure 2.3 shows examples of Miller planes in a crystal.

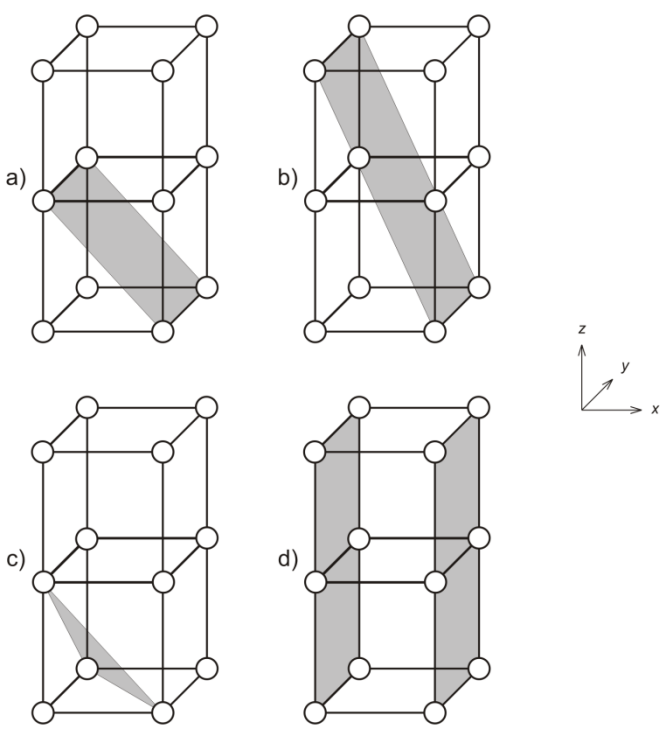

Figure 2.3 – a) (101), b) (10-2), c) (111), d) (100) planes.

Knowing that each peak is attributable to one (or more than one equivalent) set of Miller indices it is possible to work back from peak positions to calculate lattice parameters if the crystal symmetry is known or can be worked out. For example, in the case for cubic systems, $a = b = c$, $\alpha = \beta = \gamma = 90$ °.

Given that: $\frac{1}{d^2} = \frac{h^2}{a^2} + \frac{k^2}{b^2} + \frac{l^2}{c^2}$ (1)

and: $n\lambda = 2d \sin\theta$

$\lambda_{hkl} = 2d \sin\theta$ Using (hkl) to define the *n*th diffraction plane

$\lambda_{hkl}^2 = 4d^2 \sin^2\theta$ (2)

$\frac{\lambda_{hkl}^2}{4a^2}(h^2 + k^2 + l^2) = \sin^2\theta$ Substituting (1) into (2), given that $a = b = c$.

So for a set of reflections it is possible to calculate the cubic lattice parameter from the angle of the diffracted beam.

Similar derivations are possible for crystal symmetries lower than cubic. These are tabulated in Table 2.2.

Table 2.2 – Equations used to index non-cubic diffraction peaks.

Crystal symmetry	d_{hkl}
Tetragonal	$\frac{1}{d^2} = \frac{h^2 + k^2}{a^2} + \frac{l^2}{c^2}$
Orthorhombic	$\frac{1}{d^2} = \frac{h^2}{a^2} + \frac{k^2}{b^2} + \frac{l^2}{c^2}$
Rhombohedral	$\frac{1}{d^2} = \frac{4}{3}\left[\frac{h^2 + hk + k^2}{a^2}\right] + \frac{l^2}{c^2}$
Monoclinic	$\frac{1}{d^2} = \frac{1}{\sin^2\beta}\left[\frac{h^2}{a^2} + \frac{k^2\sin^2\beta}{b^2} + \frac{l^2}{c^2} - \frac{2hl\cos\beta}{ac}\right]$
Triclinic	$\frac{1}{d^2} = \frac{1}{V^2}[h^2b^2c^2\sin^2\alpha + k^2a^2c^2\sin^2\beta + l^2a^2b^2\sin^2\gamma + 2hkabc^2(\cos\alpha\cos\beta - \cos\gamma) + 2klbca^2(\cos\beta\cos\gamma - \cos\alpha) + 2hlacb^2(\cos\alpha\cos\gamma - \cos\beta)]$ $V = abc\sqrt{[1 - \cos^2\alpha - \cos^2\beta - \cos^2\gamma + 2\cos\alpha\cos\beta\cos\gamma]}$

The positions of diffraction peaks in a diffraction pattern are entirely dependent on the unit cell dimensions and symmetry, however the peak intensities are determined by the atoms in the unit cell. [3] This effect can be summed into a structure factor, which determines how the atoms in the unit cell will affect the phase of diffracted X-rays. A change in phase of X-rays caused by an atom placed on a symmetry element is related to its position in the unit cell, so for perfect crystals with no thermal motion of atoms:

$$F_{hkl} = \sum_{j=1}^{N} f_j \exp\left[2\pi i\left(hx_j + ky_j + lz_j\right)\right]$$

For small crystals, diffracted intensity is proportional to the square of the form factor:

$$I_{hkl} \propto L^2|F_{hkl}|^2$$

where L is the Lorentz constant, dependent on the data collection method and instrumentation. For real crystal structures, the effect of thermal motion on the scattering of atoms must be included for real peak intensities, giving an overall scattering intensity:

$$F_{hkl} = \sum_{j=1}^{N} f_j\, n_j \exp\left[-B_j\frac{\sin^2\theta_j}{\lambda^2}\right]\exp[2\pi i\left(hx_j + ky_j + lz_j\right)]$$

This equation can be combined with the equations previously discussed to produce predicted diffraction patterns based on a structural model which can then be refined (that is, the positions of atoms within the unit cell varied systematically and the improvement to the fit to data monitored) to produce a structural model.

Powder X-ray diffraction

Single crystal diffraction gives a complete set of diffraction points in three dimensions and so given high enough quality data it will always be possible to derive lattice parameters for a crystal if a single crystal can be synthesised. For many materials, however, growing a large enough crystal to perform single crystal diffraction on is difficult. For these materials structural information can be derived from diffraction experiments using a polycrystalline powder of the material.

As discussed above, a single crystal will diffract at highly defined angles from the incident beam. Adding another crystallite at a near the orientation of the first will add another set of diffracted points, and so on. Figure 2.4 shows this concept. With a perfect powder sample of randomly aligned crystallites, the diffraction cones will be untextured; with some alignment of crystallites the circles will appear speckled.

Powder diffraction techniques scan across these circles. Full three dimensional information (three coordinate position and diffracted intensity) as obtained with single crystal diffraction is effectively reduced to one dimension (scanning angle against X-ray intensity), making full structural solution more of a challenge.

When a powder sample is well prepared with crystallites well randomised, diffraction circle intensities are representative of actual diffraction from the crystal structure. If the crystallites are not well randomised, the diffraction circles can show texture as diffraction beams are not properly averaged.

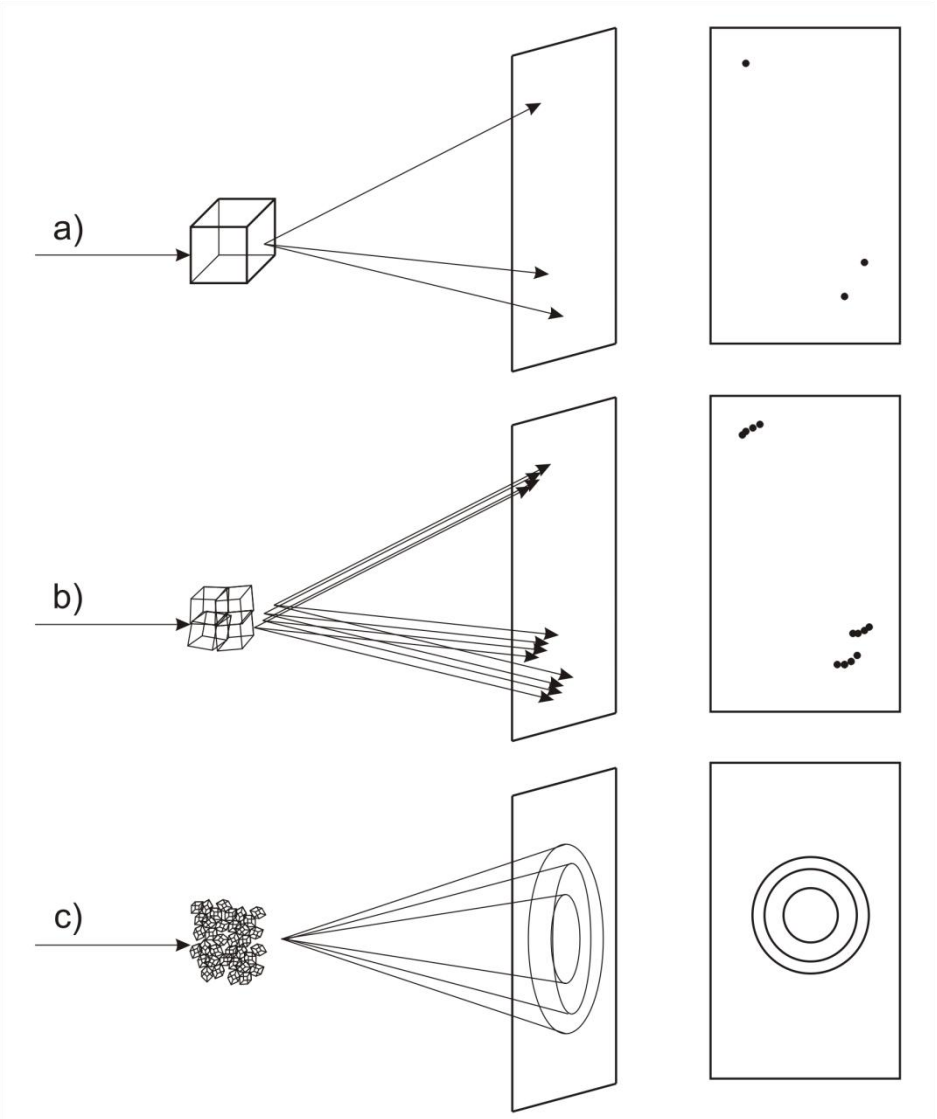

Figure 2.4 – Powder diffraction. a) Diffraction of a single crystal, b) diffraction of several closely aligned crystallites, c) diffraction of a randomly aligned mixture of crystallites.

Instrumentation

For all diffraction patterns collected in this work, X-ray diffractometers operating in Bragg-Brentano geometry were used. In this geometry, the sample and detector are scanned to reduce "glancing" surface interaction as a function of angle. This geometry is a "reflection" setup – transmission geometries are also possible but very thin samples are required to allow X-rays to penetrate. The instrumental setup is shown in Figure 2.5. θ and 2θ are varied while maintaining the position of the X-ray tube. For room temperature measurements, samples are mounted in a disc of plastic or aluminium and packed by pressing over the surface with a glass slide to prevent spillage when the sample is rotated. A sample holder covered by a Mylar window can be used for materials that are air sensitive. During a scan, the sample and the detector head are moved in steps of θ and 2θ respectively, before waiting a specified time for data to collect and scanning to the next point. A typical data collection setup would be a 0.02 ° 2θ step between collections, and a wait time of two seconds – giving 5000 steps for a typical 10-110 ° 2θ scan and a total collection time of around two hours.

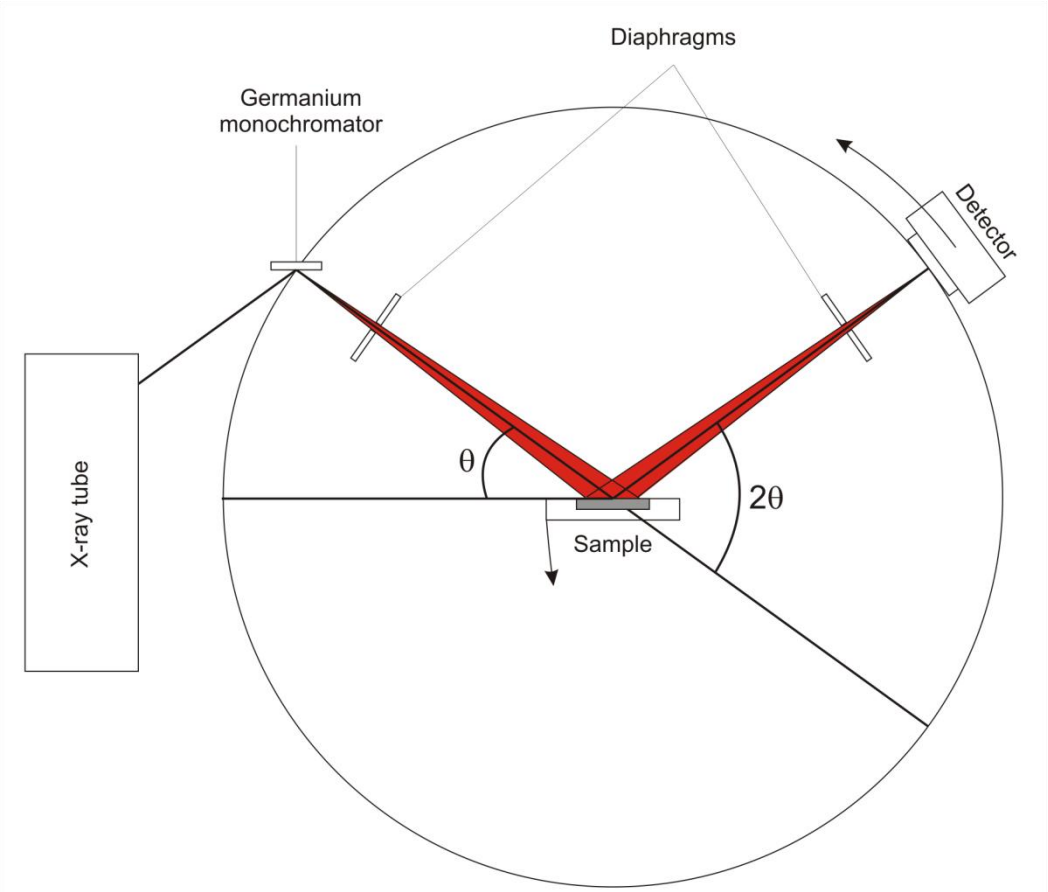

Figure 2.5 – A schematic representation of a powder X-ray diffractometer set up in Bragg-Brentano geometry.

The X-ray tube generates X-rays by bombarding a copper target with high energy electrons produced from a heated tungsten filament. The spectrum of X-rays produced by this method comprises a Bremsstrahlung produced by the deceleration of the majority of electrons overlaid with sharp peaks corresponding to electronic transitions in the copper metal.

For diffraction it is important to use monochromatic X-rays to give sharp, single diffraction peaks. If multiple wavelengths diffracted from the sample reach the detector, each will produce a peak, broadening the apparent peak position. Monochromation is achieved using a germanium single crystal aligned so that when it is illuminated with X-rays from the source the diffracted beam produced from one specific electronic transition in the copper will be focussed on the sample, directing light at other wavelengths away from the sample plate. For all diffraction experiments in this work, monochromated Cu $K_{\alpha 1}$ radiation is used, $\lambda = 1.5406$ Å.

The monochromated X-rays are collimated through an aperture diaphragm before passing onto the sample, then passing through a collection aperture before detection at the detector optics.

D5000 diffractometer

A Siemens D5000 diffractometer was used for the majority of phase identification. The detector head for this diffractometer is a standard scintillation counter. For a phase identification scan, the full 10-110 ° 2θ angular range was not measured, as the majority of phase identification critical peaks appear in the range 20-50 ° 2θ. A typical phase identification scan would be measured between 10 and 70 ° 2θ, with a step size of 0.02 ° and collection time of one second per step.

D8 diffractometer

A Bruker D8 diffractometer was used for structural analysis in this work. The incident X-rays are monochromated to Cu $K_{\alpha 1}$. Three detectors can be equipped to the instrument: a scintillation counter, which offers good resolution; the SOLEX detector which allows selection of specific energies to eliminate the signal from X-ray fluorescence of Fe / Co; and the Braun PSD (position sensitive detector), a detector covering a 6 ° 2θ angular range to increase the speed or intensity of diffraction experiments. The PSD is a wire containing gas that is ionised by X-rays, and the position of the ion produced along the wire is measured.

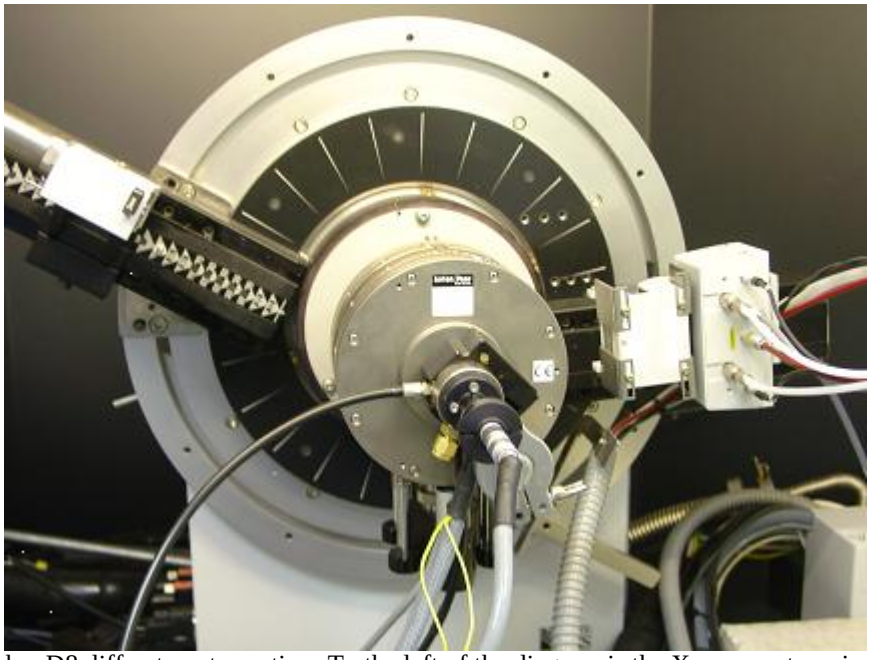

Figure 2.6 – Bruker D8 diffractometer optics. To the left of the diagram is the X-ray aperture, in the centre the Anton-Paar furnace sample stage, and to the right the PSD detector. The beam stop is fitted below the PSD to prevent direct beam damaging the detector.

Good quality diffraction data for structure refinement is typically collected over the full range possible with the detector, so for non fluorescent samples a typical refinement data set would be recorded using the PSD in the range 10-110 ° 2θ with a step size of 0.017 ° and two seconds of collection per step, and for a fluorescent sample 5-120 ° 2θ using the SOLEX detector, with a 0.02 ° step and three seconds per step. The available angular range of the PSD is reduced by the gas tubing and wiring to the detector head, which cannot be put under strain, and by the sensitivity of the detector to degradation from high X-ray intensity preventing small angle measurements.

Variable temperature powder diffraction

As powder diffraction gives information on the average structure of a crystalline material, variable temperature diffraction data gives information on the evolution of the average structure with changing temperature. For solids, this gives information on thermal expansion properties and structural phase changes.

In this work, variable temperature X-ray diffraction measurements were carried out using an Anton-Paar HTK-1200 furnace stage. Samples are mounted in the base of the furnace on an alumina sample holder and heated up to a maximum of 1473 K during data collection. Flowing gas can be passed through the stage during heating either to prevent reaction with the air or to aid *in situ* reactions, and the sample stage can be rotated to reduce surface texture and aid in randomising crystallite orientations. A photograph of the D8 diffractometer with the furnace stage attached is shown in Figure 2.6.

Structural refinement

While solving a complex structure from its powder diffraction pattern is difficult, refining a known structure is much more straightforward. In many cases, knowing the structure of a closely related material allows the structure of a new phase to be determined. Rietveld pioneered the technique, now widely used by solid state chemists, to fit a modelled diffraction pattern to a whole data set. [4]

The aim of structural refinement is to minimise the difference between the calculated diffraction pattern and the observed pattern recorded from the phase of interest:

$\text{Residual} = \frac{\sum|F_O - F_C|}{\sum|F_O|}$ where F_o and F_c are the observed and calculated intensities for any given reflection. The method for producing calculated intensities is discussed above.

Rietveld refinement is typically carried out using a computer, which is able to minimise the residual factors many times per second. The software package GSAS [5] was used exclusively in this work for structural refinement. The user inputs a starting model, and provides the path of the diffraction data set for modelling, and the software calculates the best possible fit to the data. The difference in intensity between the calculated diffraction pattern and the collected diffraction pattern is calculated at each point of the pattern and summed. Using an iterative least squares method, parameters specified by the user are refined to gradually improve the model to match the observed diffraction data.

A typical refinement will follow these steps:

1. Refinement of the scale factor for the calculated diffraction pattern – assuming a good starting point has been chosen for the refinement this value will refine smoothly by linear interpolation.
2. Refinement of the background – usually a straightforward linear interpolation with rapid convergence.

3. Refinement of the zero point error – small changes in the sample height can cause significant errors in the observed position of diffraction peaks. This parameter corrects for this displacement.
4. Refinement of the unit cell parameters – initial parameters must be close to their refined values or the calculated pattern will not contain intensity at the correct angles. If suitable starting values have been chosen then this step should be straightforward. In only slightly distorted structures (e.g. an orthorhombic structure where $a \neq b \approx c$) it may be difficult to firmly fix the unit cell parameters at this stage and approximate values may need to be constrained until a good fit to the data has been achieved.
5. Refinement of peak shape parameters – for X-ray diffraction patterns a convolution of Gaussian and Lorentzian peak shapes will usually give a good fit to the data.
6. Refinement of positional parameters of atoms in the unit cell – as allowed by symmetry. For X-ray diffraction refinements, the scattering from heavier (larger electron cloud) elements will have the greatest effect on the diffraction pattern of the phase, so these parameters will be refined initially. Lighter elements (particularly oxygen) can then be refined, though a degree of damping may be required to allow smooth refinement.
7. Refinement of the isotropic temperature factors may be the last stage in a refinement. These parameters represent the averaging effect of thermal motion on atomic position.
8. If the data is of sufficiently high quality and additional information can be gleaned from the structure, then the isotropy of thermal factors can be unconstrained and anisotropic temperature factors refined. In this work this is often beyond the scope of the materials studied.

For a typical refinement parameters must be alternately constrained and unconstrained throughout the refinement process until very near to completion. Several of the refined parameters discussed above are complimentary, for example, atomic coordinates and temperature factors both affect peak intensity, so must first be refined independently. Refining two complimentary parameters simultaneously before either has been minimised may cause a divergent refinement, that is, one in which two conflicting parameters each move the refinement away from a minimum.

The quality of a refinement can be measured by reliability indices that quantify the difference between a calculated and observed diffraction profile.

The goodness of fit of a profile is quantified by the parameter R_p:

$$R_{profile} = \frac{\sum_i \left| y_i^{obs} - y_i^{calc} \right|}{\sum_i y_i^{obs}}$$

where y^{obs} and y^{calc} are the observed and calculated intensities at every point i. A measure of the optimal fit to diffraction data, R_e, is defined as:

$$R_{expected} = \sqrt{\left[\frac{(N - P + C)}{\sum_i W_i (y_i^{obs})^2} \right]}$$

where N is the number of observables, P is the number of refined parameters, C is the number of constraints imparted onto the system, and W is a weighting factor.

The weighted profile fitting parameter, R_{wp} can also be defined:

$$R_{weighted\ profile} = \sqrt{\left[\frac{\sum_i W_i(y_i^{obs} - y_i^{calc})^2}{\sum_i W_i(y_i^{obs})^2}\right]}$$

and finally the value χ^2 can be reported:

$$\chi^2 = \left[\frac{R_{wp}}{R_e}\right]$$

For all refinements in this work, all three goodness of fit indicies (R_p, R_{wp} and χ^2) will be reported, however the value which will be used as the minimisation target will be χ^2. For a given data set, a decrease in χ^2 indicates a fit closer to the best fit achievable with the data. It is also important to note that a consequence of the equation for R_e is that the value of χ^2 is inversely proportional to the number of observables, indicating that high resolution diffraction data will tend to produce higher χ^2 values. A χ^2 value is therefore not comparable from one diffraction experiment to another, unless controls are in place to ensure that data are equivalent. Refinement quality can therefore be quantitatively measured in several ways using outputs from the refinement software, but to properly assess the refinement quality it is necessary to evaluate the structure that has been developed.

Neutron diffraction

The wave-like properties of neutrons allow diffraction experiments to be carried out using an incident neutron source rather than X-rays. The advantages of this technique for the characterisation of inorganic materials are many.

- Neutrons are diffracted from the nucleus of an atom, rather than its electron cloud. For typical inorganic materials, the diffraction from high atomic mass metal ions contributes more to a diffraction pattern than that of the anions due to the higher number of electrons in the cloud. Neutron diffraction is independent of the cloud size and can typically be used for much more accurate location of light anions
- Neutron diffraction intensities are independent of θ. This means that a wider range of diffraction data is available for analysis in a typical neutron diffraction pattern. The limiting factor to refinement of data tends to be peak shape, which is still a factor of θ.
- Neutrons possess a magnetic spin and can be used to probe the magnetic structure of materials

Neutron diffraction typically requires a larger sample size than X-ray diffraction. Because neutrons interact with nuclei rather than the far more diffuse electron cloud, additional material must be used to compensate for the reduced probability of diffraction events.

Due to the disadvantageous diffraction statistics of neutrons, large neutron fluxes are required for experiments. Central facilities are used for these experiments and can be one of two types, reactor or spallation.

Reactor sources

Reactor sources generate neutrons through nuclear fission. As in X-ray diffraction, neutrons are monochromated by diffraction from precisely oriented single crystals. For all fixed wavelength neutron diffraction data collected on samples in this work, the optimal wavelength for high neutron flux, $\lambda \approx 1.594$ Å was used, monochromated from diffraction from the [3 3 5] plane of the germanium monochromator.

D2B and D20

The D2B and D20 diffractometers collect neutrons diffracted from the sample using a series of linear detectors, allowing a full two-dimensional slice of the cones of diffraction to be collected with only a small movement of the detector array. The averaging of these data gives very accurate diffraction intensity information. Both instruments are placed close to the reactor at the Institut Laue-Langevin, ensuring high neutron flux.

A schematic representation of the diffractometers is shown in Figure 2.7. In the instrument D2B, 64 linear detector elements are separated by a spacing of 2.5 ° 2θ, covering an arc of 160 °. By scanning through 100 steps at 0.025 ° per step, the full 2.5 ° 2θ between elements is covered, collecting a full scan. In D20, 1536 detector elements are separated by only 0.1 ° 2θ, providing extremely fast collection times or very high peak intensities. The high intensities allow constant data collection when performing variable temperature diffraction experiments.

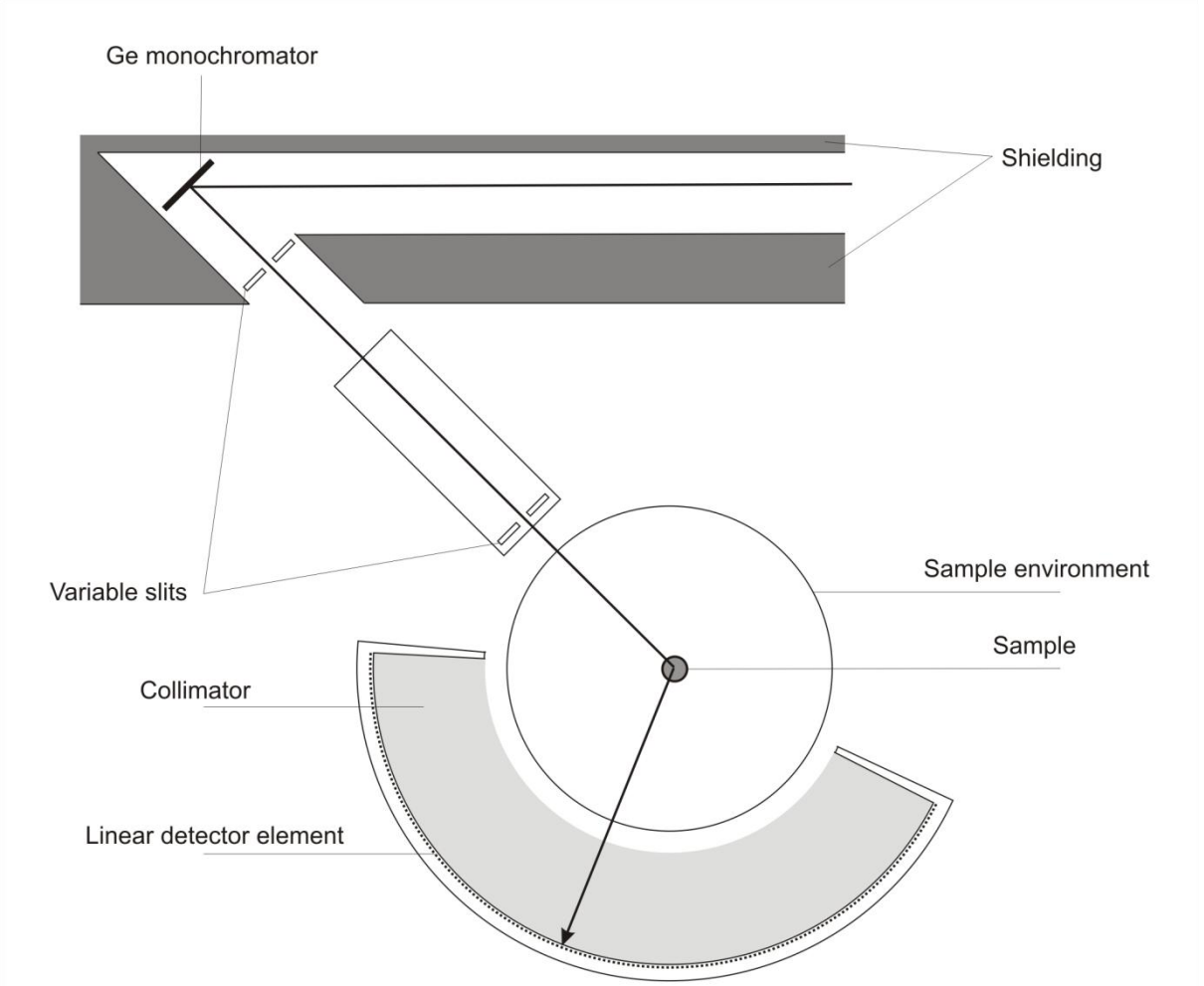

Figure 2.7 – Schematic representation of the instruments D20 and D2B at the ILL.

Spallation sources

Spallation sources generate neutrons by stripping them from the nuclei of a target metal after collision with high velocity protons. The method of generating these protons is shown in Figure 2.8 and described below.

- H^- ions are produced through ion discharge in an ion source pumped with caesium ion vapour and hydrogen gas
- The H^- ions are focussed, accelerated and bunched through a quadrupole field. These ions are then passed to a linear accelerator to further raise the velocity.
- Final acceleration is carried out in the synchrotron. On entry to the accelerator the electrons are stripped from the H^- particles to form the required protons by passing through an aluminium oxide foil. This method of injection allows more protons to be stored in the synchrotron than would normally be possible – the repulsion of the protons is somewhat mitigated by carrying a negative charge into the loop.
- The 160 kW protons hit the tungsten target and produces neutrons. The target is water cooled to remove the dissipated heat.
- The fast neutrons produced by the collision are cooled to produce useful energies and wavelengths for scattering experiments – for a typical diffraction experiment water at room temperature is used, producing thermal neutrons.

The kinetic energy and thermal energy of neutrons are equal, so: $\frac{1}{2}mv^2 = k_B T$ (1)

The momentum of the neutron is related to its wavelength as $\lambda = \frac{h}{p}$ (2)

Substituting for momentum ($p = mv$) into (1): $\frac{(mv)^2}{2m} = k_B T$ (3)

Rearranging (3): $p = \sqrt{2mk_B T}$ (4)

Substituting (4) into (2) gives: $\lambda = \frac{h}{\sqrt{2mk_B T}}$

So for neutrons at 298 K, $\lambda = 1.262 \times 10^{-10}\ m = 1.262$ Å which is close to interatomic spacing as required for diffraction.

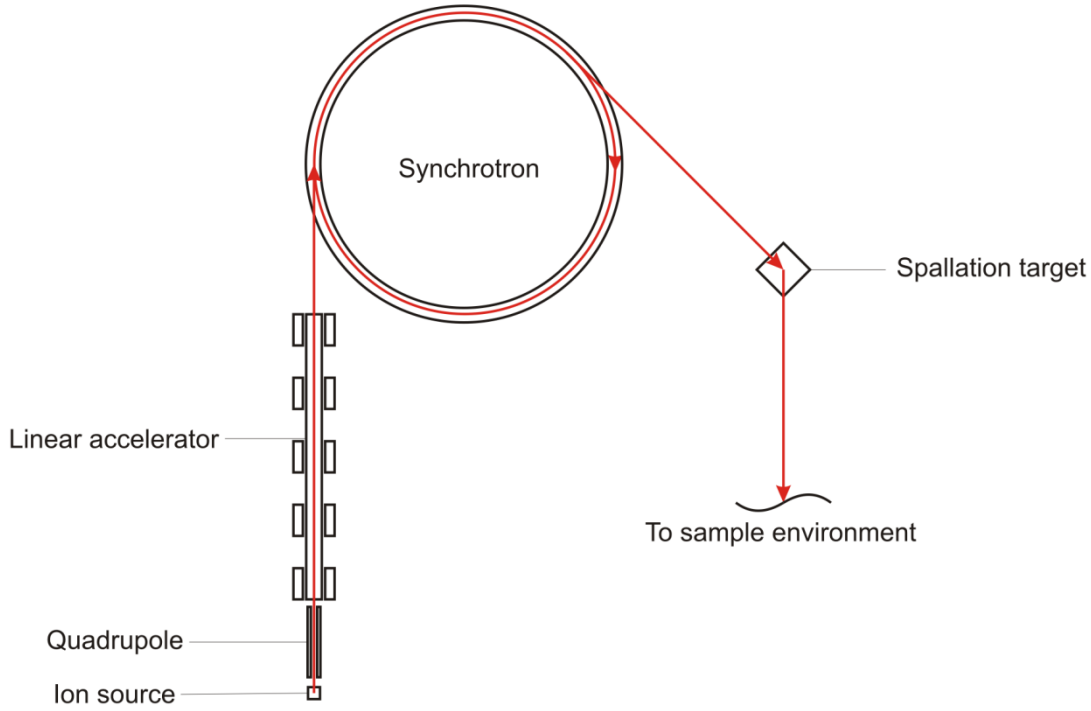

Figure 2.8 – Illustration of the path of hydride ions, protons and neutrons in a spallation source.

The pulsing of spallation sources allows diffraction experiments to be carried out in time-of-flight mode. Because the bunch of neutrons is delivered to the sample in a tightly packed time packet, the time taken for neutrons to reach a detector can be measured in relation to a $t = 0$ condition defined by the neutron packet. Rather than moving the detector, a full diffraction pattern to be collected for every neutron packet at any diffraction angle. This can be demonstrated algebraically:

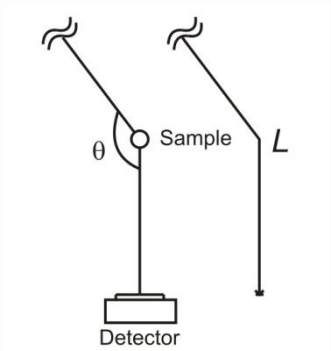

Figure 2.9 - Time-of-flight neutron diffraction geometry. The distance to source is much larger than sample to detector.

In the geometry above, $v = \frac{L}{t}$ and from the de Broglie relationship, $\lambda = \frac{h}{mv}$.

$$v = \frac{h}{\lambda m} = \frac{L}{t}$$

$$t = \frac{\lambda m L}{h}$$

$$t = \frac{2d \sin\theta \, mL}{h}$$

So for a fixed θ as in the geometry shown in Figure 2.9, *t* (the time of flight of a neutron to the detector) is proportional to *d* (the interplanar distance as discussed previously).

A consequence of the equation shown above is that for time of flight diffraction, the maximum resolution possible for an experiment is proportional to the total flight length. The error in measurement of time of flight at the detector is due only to the error in measurement in path length of the neutrons. As neutrons do not originate at a point source, but at a moderator of finite size, this error is minimised by increasing the path length.

So for a time of flight diffractometer, for the best possible resolution a long flight length is preferable. The HRPD (High Resolution Powder Diffractometer) instrument at ISIS at the Rutherford Laboratories uses a path length of 100 m to optimise resolution. However, to prevent overlap between successive pulses over this long flight time, only one in every five source neutrons is used for diffraction. Although this is an extreme example, there must always be a trade off between the higher neutron flux and diffracted intensity nearer the source and the higher resolution further from the source.

Diffraction data collected at central neutron sources can be analysed using Rietveld refinement in the same way that X-ray diffraction data can.

POLARIS

Neutrons are moderated to produce a range of neutron energies (hence wavelengths) suitable to the application prior to reaching the sample for time of flight neutron diffraction. For the POLARIS instrument at ISIS, neutrons are moderated using 316 K water poisoned with gadolinium. The path length, L_1, from moderator to sample is 12 m. The instrument is close to the spallation source, and provides high neutron flux with medium resolution. The path

length, L_2, to the detectors depends on the detector bank. Table 2.3 lists important attributes of the detector banks. The best resolution detectors are the backscattered bank, also providing a useful *d* spacing range for oxide material characterisation.

Table 2.3 – Detector banks on the POLARIS instrument at ISIS.

Bank position	Very low angle	Low angle	90 degree	Backscattering
Type	ZnS scintillator	^{3}He gas tubes	ZnS scintillator	^{3}He gas tubes
2θ range / °	13 - 15	28 - 42	85 - 95	130 - 160
Resolution / $\Delta d/d$	3×10^{-2}	1×10^{-2}	7×10^{-3}	5×10^{-3}
L_2 / m	~ 2.2	1.72 - 2.65	~0.8	0.60 - 1.30
d spacing range / Å	0.5 - 21.0	0.5 - 8.15	0.3 - 4.1	0.2 - 3.2

HRPD

A 100 K methane moderator is used to provide incident neutrons at wavelengths $0.5 \leq \lambda \leq 12$ Å, with peak flux at 2 Å. As mentioned above, the 100 m L_1 path length provides the best resolution of any instrument at ISIS. The key parameters of the instrument detector banks are shown in Table 2.4.

Table 2.4 – Detector banks on the HRPD instrument at ISIS.

Bank position	Low angle	90 degree	Backscattering
Type	^{3}He gas tubes	ZnS scintillator	ZnS scintillator
2θ range / °	28 - 32	87 - 93	160° - 176°
Resolution / $\Delta d/d$	2×10^{-2}	2×10^{-3}	4×10^{-4}

Characterisation methods – non-diffraction methods

Thermogravimetric analysis and differential scanning calorimetry

Thermogravimetric analysis (TGA) is a technique to measure the change in mass observed when a material is heated. A crucible containing a known mass of the material is suspended inside an accurate furnace and heated under flowing gas. The mass of material to be used can be measured prior to analysis, or internally on the instrument. TGA can be used to observe structural changes in a material as changes in mass are attributed to loss or gain of material over the course of the analysis. The technique can provide information for structural analysis if a mass change can be attributed to a specific molecule, for example the loss of oxygen (particularly when heating under flow of hydrogen) provides structural information on the oxygen content of defect materials.

Differential scanning calorimetry (DSC) allows phase changes to be identified by analysing the heating profile of a material against a reference. Within one phase in a material, the specific heat capacity will be constant and so a linear heating response will be observed when energy is supplied to the material. At a phase transition the specific heat capacity may change between phases, in which case a gross change in gradient will be observed, or the latent heat of the change of state will cause a discontinuity in the heating profile. The sample and the

reference material are placed in crucibles and heated, with the difference in heat transferred to the reference and sample measured and recorded against temperature. The area under a discontinuity in the heating profile corresponds to the latent heat of the transition.

TGA and DSC can be combined to provide information on phase transitions in solid materials: the DSC locating the transition and quantifying its energy, and the TGA providing structural information on each phase involved in the transition through identification of the lost mass. A schematic of a TGA instrument is shown in Figure 2.10.

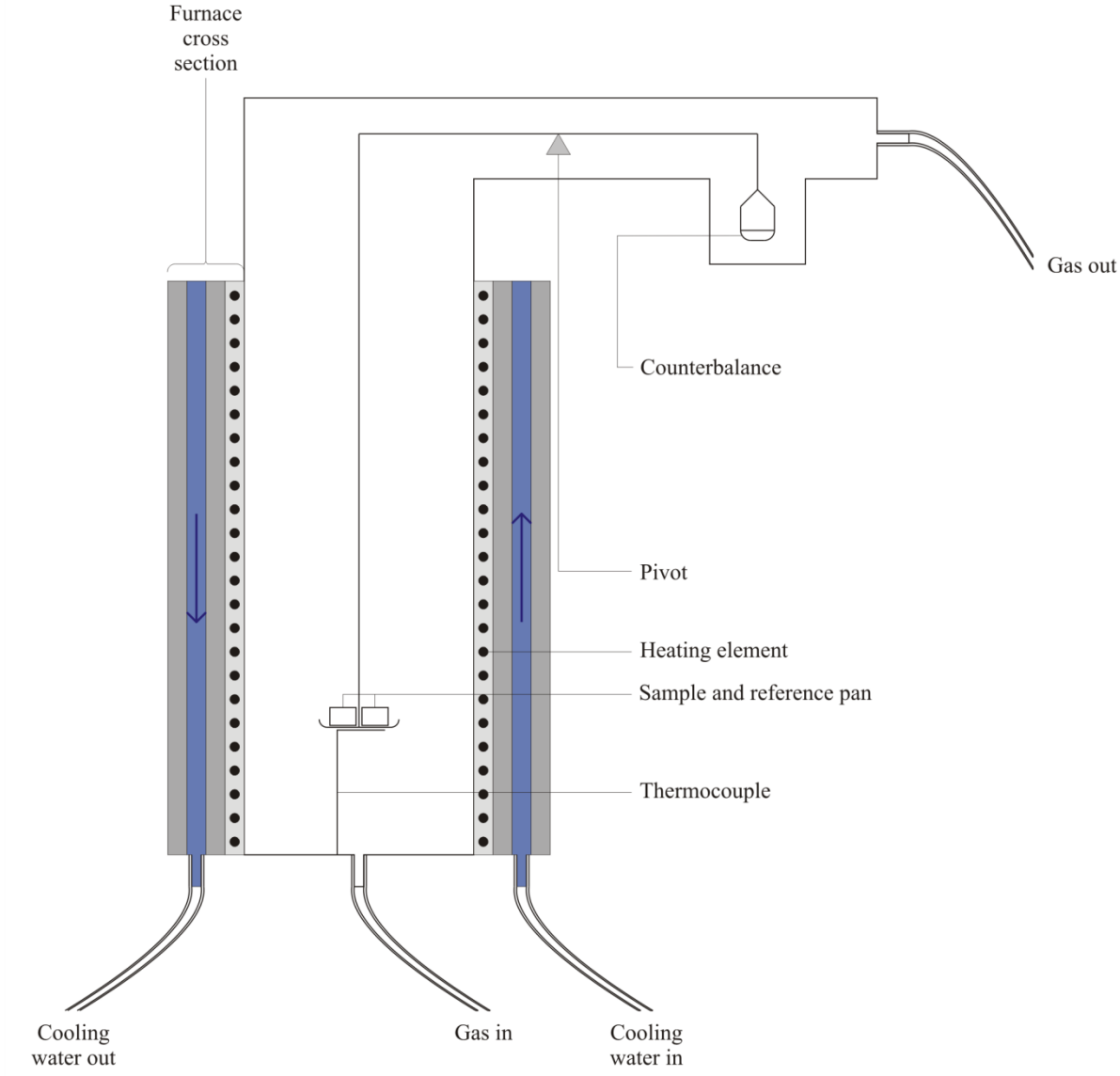

Figure 2.10 – Schematic diagram of a TGA instrument.

Vibrating Sample Magnetometry

Vibrating sample magnetometry (VSM) can be used to measure magnetism in materials. The sample loaded into a non-magnetic container, suspended in a fixed magnetic field between two coils of wire. The sample is mechanically vibrated, and the resultant magnetism induced in the coils is measured. The temperature of the chamber is heated, and the temperature dependence of the inverse magnetic susceptibility recorded.

References

1. A. R. West, "*Solid State Chemistry and its Applications*", Wiley, 1984
2. W. L. Bragg, *Proc. Camb. Phil. Soc*., 1913, **17**, 43
3. M. M. Woolfson, "*An Introduction to X-ray Crystallography*", Cambridge University Press, 1997
4. A. C. Larson and R. B. Von Dreele, *General Structure Analysis System*, 1990, MS-H805, Los Alamos, NM 87545

Chapter 3 – $Gd_2SrCo_2O_7$ and related cobaltates

Introduction

Cobalt (III) materials are of interest to materials chemists due to the large range of electronic and magnetic properties exhibited by their oxides. These properties are heavily influenced by the range of spin states accessible in a crystal field: both the more widely known low and high spin and the uncommon intermediate spin.

Spin states of cobalt (III)

When an ion is octahedrally coordinated by ligands (anions), orbitals that are oriented along the axes, pointing to the positions of the ions, are raised in energy due to the increased electronic repulsion between ion and ligand orbitals. This causes the valence orbitals to split into two energy levels centred around the energy of the spherically coordinated ion. This is illustrated in Figure 3.1. Electrons with aligned spins provide an energy contribution to the spin state, J, however occupation of the $d_{x^2-y^2}$ and d_{z^2} orbitals has an associated energy cost, Δ_o.

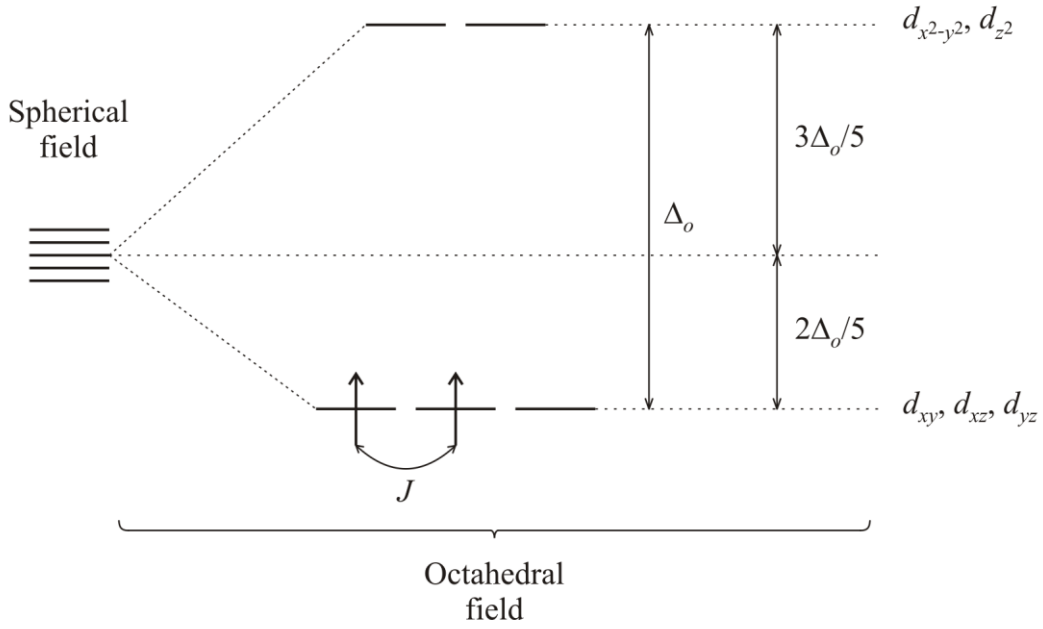

Figure 3.1 – Octahedral field splitting, illustrating the two energy contributions to the spin state, J and Δ_o.

If multiple electronic configurations are possible for the valence shell of a given ion, the competition between J and Δ_o usually allows two spin states: high spin, maximising the contribution of J while paying the energy cost Δ_o, and low spin.

The electronic configurations of the three spin states observed in cobalt (III) materials are shown in Figure 3.2. Through simple crystal field considerations, the intermediate spin state appears to be disfavoured for any value of Δ_o, to either the low or high spin alternative. The intermediate spin state is possible for d^6 configurations as it can be stabilised (the value of Δ_o effectively reduced) by Jahn-Teller distortion. As the e_g orbital is singly occupied, the ion

distorts, elongating the ion-ligand distance along either the *z* axis or in the *xy* plane. This reduces the effective value of Δ_o, as shown in Figure 3.3.

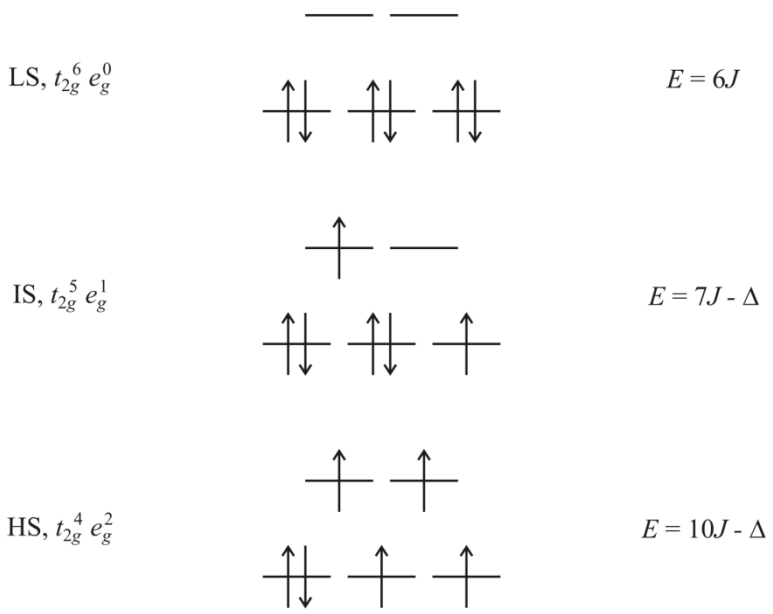

Figure 3.2 – The low, intermediate and high spin states for cobalt (III).

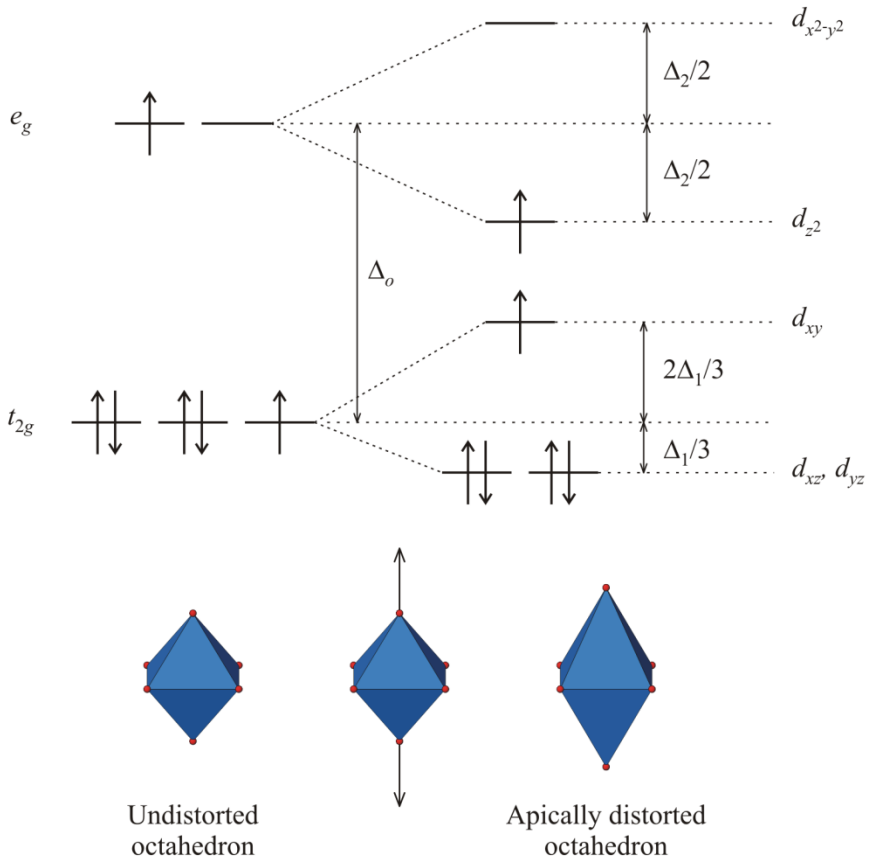

Figure 3.3 – Stabilisation of the intermediate spin state of a d^6 ion through Jahn-Teller distortion.

n = 2 Ruddlesden-Popper cobaltates

Despite the large volume of work carried out on the related perovskites ($LnCoO_3$, particularly Ln = La, and $SrCoO_3$) and K_2NiF_4 structures ($Ln_{1-x}Sr_{1+x}CoO_4$), the n = 2 Ruddlesden-Popper

phases remain relatively unexplored. Likewise, other transition metal Ruddlesden-Popper phases have been more extensively studied than this family. These have been previously examined in Chapter 1.

At the time of writing only four papers, including a paper based on this work, were in print on the family of materials $Ln_2ACo_2O_7$. Initially reported in 1994 for the materials *Ln* = Sm and Gd, the structure and magnetic properties were discussed by Siwen and Yufang, [1-2] and later specific heat capacity measurements and further structural work was carried out by Akiyama *et al*. [3]

In this chapter, the structures of these materials are studied in detail, with reference to the interaction between the accessible spin states in the Co^{3+} ion and the physical properties of the material exhibited.

Synthesis of $Ln_2ACo_2O_7$ phases (*Ln* = trivalent lanthanide ion, *A* = divalent alkali earth)

Synthesis of $Ln_2SrCo_2O_7$ *phases*

Syntheses of the materials as originally reported by Siwen and Yufang were attempted. [1] Ln_2O_3 (*Ln* = Sm and Gd), $SrCO_3$ and Co_3O_4 were ground together in a pestle and mortar and heated to 1273 °C overnight before regrinding, pelletising in a 10 mm die at 14 MN and heating to 1423 K for a further three days under flow of oxygen. Further anneals could be added to further improve the crystallinity of the product, however reaction between the alumina boats used for reaction and the cobalt in the material leads to a less pure product when taken to extremes.

Several attempts were necessary to determine the required flow rate of oxygen required to produce a phase-pure sample of $Gd_2SrCo_2O_7$ (eventually a flow rate of ~ 2 1 cm^3 bubbles per second was found to be sufficient without causing significant cooling of the hot zone of the furnace). The Sm analogue could not be produced with good phase purity; a large proportion of $SmSrCoO_4$ was consistently present in the final product. Referring to the original Siwen paper showed that in this work too the single layer impurity was present in their diffractograms.

Extension of the series was attempted for other *Ln*: Nd, Eu, Tb, and Dy. It was found to be possible to produce the Eu analogue; however similar purity problems were experienced as for the Sm material. No other analogues were successfully produced in proportions that could be described as a major phase. Due to the lack of success in production of the Nd material and apparent lack of stability of lanthanum-based $Ln_2SrM_2O_7$ with respect to a mixed perovskite and K_2NiF_4-type product the synthesis of $La_2SrCo_2O_7$ was not attempted. Likewise, as the formation of a dysprosium material was unsuccessful, *Ln* of smaller ionic radii were not used. Syntheses of the cerium and praseodymium phases were not attempted due to the likelihood of forming an Ln^{4+} material in oxidising conditions. The lack of success forming a terbium material (favouring formation of a $TbSrCoO_4$ phase with excess starting

materials) supports this supposition. It seems that apart from the Gd material, the size mismatch between the rock salt and perovskite layers destabilises the bilayer Ruddlesden-Popper phase relative to a mixture of (*Ln*,Sr)CoO_3 perovskite, Ln_2SrCoO_4 and starting material phases. Trial reactions in a high pressure oxygen atmosphere at ~ 1173 K in an in-house furnace were unsuccessful. Higher temperatures were not accessible with the apparatus, and this, combined with the shorter reaction times required by the pressurised oxygen tanks, seems the likely reason for failure to reproduce even the $Gd_2SrCo_2O_7$ synthesis under these conditions.

A sample of isotopically enriched $^{160}Gd_2SrCo_2O_7$ was prepared for neutron diffraction using the least neutron absorbing isotope available for gadolinium. Unfortunately, due to the prohibitive cost and availability of highly purified $^{160}Gd_2O_3$, the enrichment of ^{160}Gd was limited to 98.2 %. As other gadolinium isotopes have the highest neutron absorption cross sections known, this meant that even the enriched samples were highly absorbing.

Synthesis of $Ln_2BaCo_2O_7$ *phases*

The synthesis of $Sm_2BaCo_2O_7$ was described by Siwen and Yufang, [2] and involved a similar decomposition and pelletised annealing methodology as described above for $Ln_2SrCo_2O_7$. The paper reports a longer annealing time required to form this material – in the region of several weeks of annealing rather than days, for the strontium materials. However, all attempts to reproduce this synthesis produced large proportions of impurity phases, particularly $SmCoO_3$. Although no diffractograms are presented in the Siwen and Yufang work, if their report of a phase pure synthesis is accurate then it is clear that the current method must be responsible for poor target phase yield. One possible explanation for this could be the cobalt source: Siwen and Yufang report the use of Co_2O_3 as a starting reagent which was unavailable for this work (it could not be sourced from United Kingdom distributors). It seems likely that this more reactive cobalt source could produce the required bilayer phase before the formation of the thermodynamically stable $SmCoO_3$. Alternatively, the reactive cobalt source could produce further reaction in otherwise dead-end side products of the reaction.

Whilst a samarium material could not be produced with high enough purity to warrant further investigation, the reaction of rigorously dried Nd_2O_3 with Co_3O_4 and $BaCO_3$ at 1473 K under oxygen for one week produced a bilayer Ruddlesden-Popper phase with purity sufficient for further investigation. The low neutron absorption cross-section of neodymium allowed neutron diffraction to be carried out on this sample without the need for expensive isotopically enriched starting materials.

Structural study of $Gd_2SrCo_2O_7$

X-ray diffraction

Initially, phases were analysed for purity using X-ray powder diffraction. Diffraction data were collected on a Bruker D8 instrument between 15 and 100 ° 2θ with a 0.02 ° step size and 2.5 s per step. A digital SOLEX detector was employed to eliminate X-ray fluorescence emitted by the cobalt in the material. Sets were collected at 50 K steps between 298 and 1273 K.

Refinement of room temperature X-ray diffraction data collected on $Gd_2SrCo_2O_7$ was carried out using the program GSAS. Structural information extracted from this refinement agreed with parameters previously reported, fitting well to a model based on tetragonal *I*4/*mmm* $Sr_3Ti_2O_7$. On heating above 573 K a reduction in cell symmetry could be clearly observed in the splitting of several peaks. Closer examination of peak full width half maximum values below the transition confirmed that this was indeed a phase transition, rather than simply divergence of the *a* and *b* unit cell lengths in a previously lower symmetry system.

At very high temperatures peaks began to coalesce, however a very high temperature tetragonal phase was not isolated due to decomposition of the material at ~ 1473 K in air (the formation temperature in an oxygen environment).

The diffraction data collected above this transition temperature could be indexed to an orthorhombic unit cell of dimensions $a \approx b \approx \sqrt{2}\ a_0$ and $c = c_0$. This supercell corresponds to ordered tilting or concerted rotation of CoO_6 octahedra with a repeating length equal to the unit cell length of the lower temperature phase. A portion of the diffraction data are shown in Figure 3.4. The zoomed region shows an example of the splitting in the *I*4/*mmm* {110} peaks.

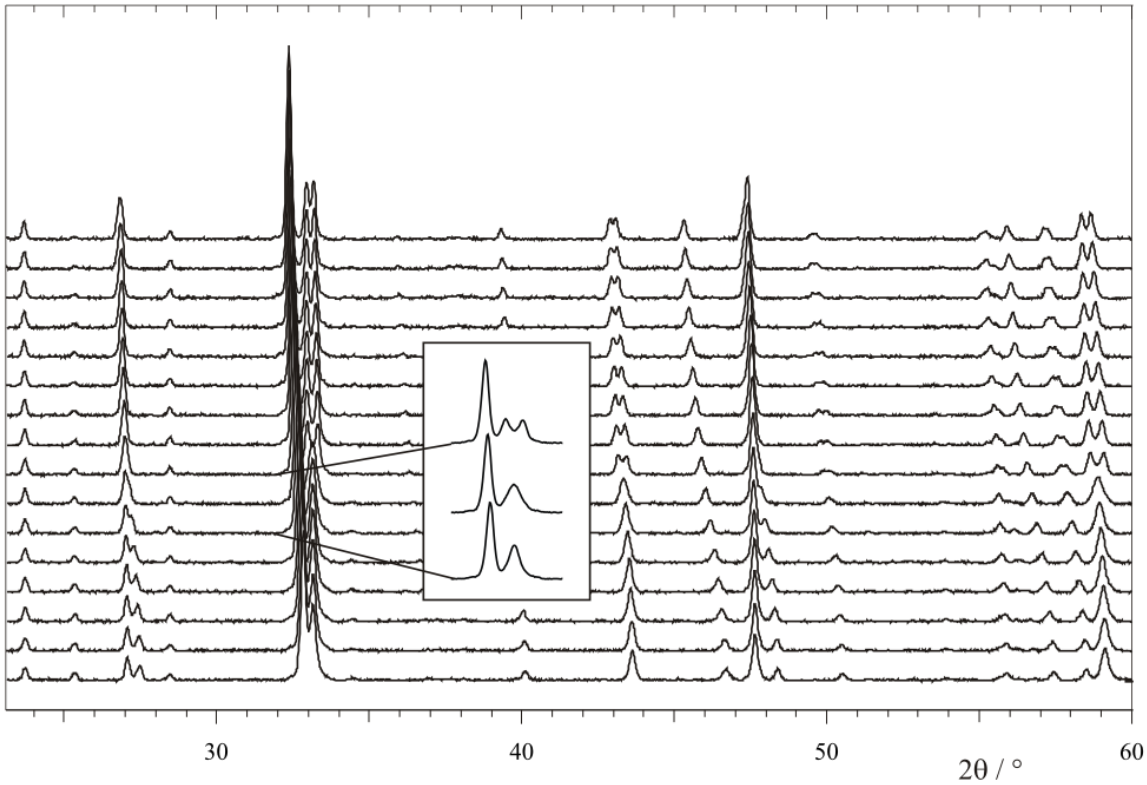

Figure 3.4 – Part of the thermodiffractogram collected on a sample of $Gd_2SrCo_2O_7$ collected on the D8 diffractometer using SOLEX detector. Data sets are stacked with increasing temperature from 323 to 1073 K in 50 K intervals. Zoomed region shows the {105} (left) and {110} (right) peaks at 523, 573 and 623 K.

Neutron diffraction

Previous studies by Shaked and Jorgensen [4] have determined that for such distortions in bilayered Ruddlesden-Popper phases there are nine possible space groups possible corresponding to octahedral rotation or tilting (no translation of the *B*-site cation). Due to the relative insensitivity of X-ray diffraction to oxygen positions in a heavy metal rich environment such as this, it was impossible to determine the space group symmetry of the orthorhombic phase from X-ray diffraction data. Neutron diffraction data were therefore collected on a sample of isotopically enriched $^{160}Gd_2SrCo_2O_7$. Although the pure 160 isotope of gadolinium is relatively non-absorbing, even small percentages of the other Gd isotopes give large neutron absorption, often resulting in poor statistics and long collection times. The material used in these diffraction experiments was enriched to 98.2 %, with the residual absorbing isotopes generating an approximate absorption cross section of 830 barns – still very high for neutron diffraction experiments.

Powder neutron diffraction data were collected on the fixed wavelength instrument D2B at the Institut Laue-Langevin (λ = 1.59432 Å). A fault in the instrumentation reduced neutron flux in the initial experiment, reducing the number of data sets that could be collected. As a result a second experiment was carried out on the D20 (high flux, medium resolution) station on 0.5 g of $^{160}Gd_2SrCo_2O_7$. Diffraction data were collected over the temperature range 298 to 973 K (λ = 1.4965 Å). 30 s data sets were collected while heating between static temperature collections at which thermal equilibration was allowed. On equilibration these data were collected for 300 s every 100 K. Figure 3.5 shows the equilibrated data sets between 373 and

973 K (room temperature data set omitted for clarity of the region of phase transition). Collection of higher temperature data was not possible due to decomposition of the sample – the broad peak at ~ 40 ° 2θ growing in the 973 K range is indicative of a quantity of poorly crystalline Gd_2O_3 forming. As the final diffraction sets were collected at temperatures approaching the formation temperature in a pseudo-vacuum, the decomposition was to be expected.

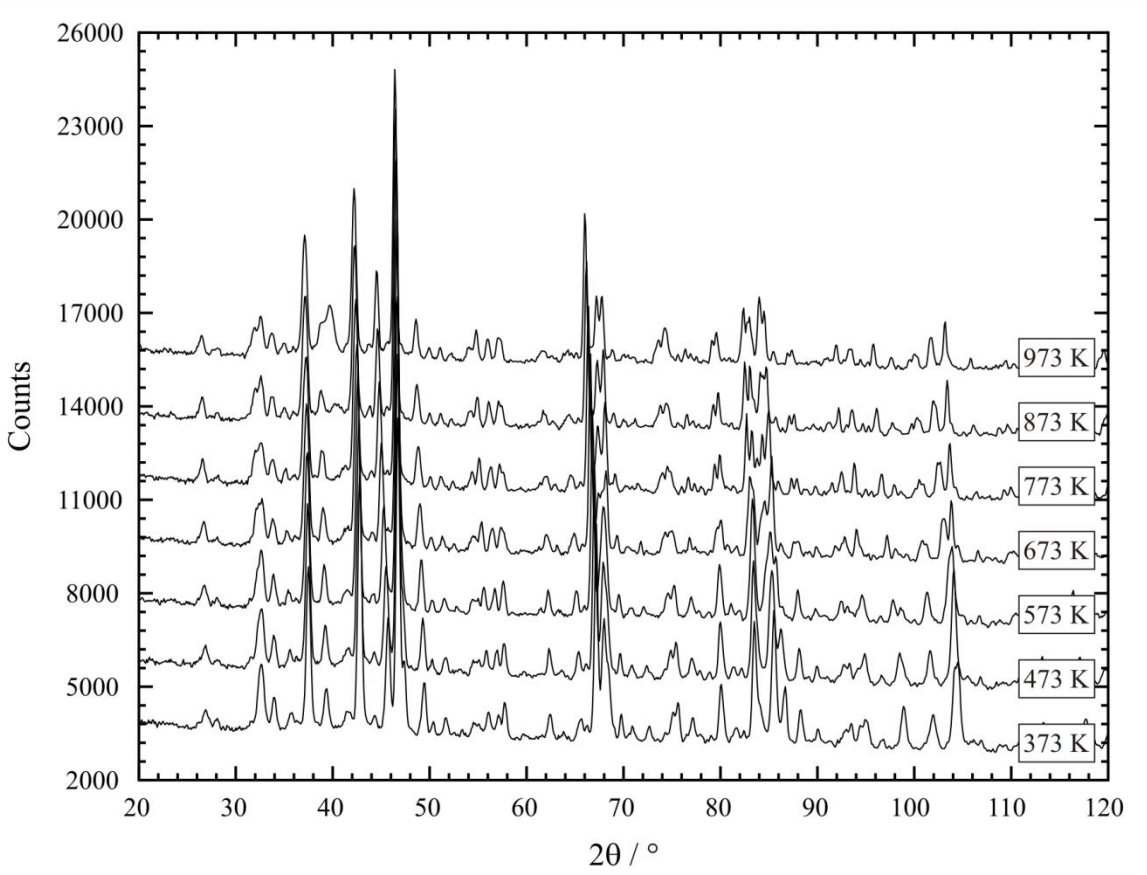

Figure 3.5 – Selected angular range from thermodiffractogram collected on $^{160}Gd_2SrCo_2O_7$ collected on the D20 diffractometer at the ILL, λ = 1.4965 Å.

Room temperature structure of $^{160}Gd_2SrCo_2O_7$ by neutron diffraction

It was apparent that even the room temperature data sets could not be adequately fitted with a standard $Sr_3Ti_2O_7$ model. Several additional reflections appeared in the diffraction pattern, which could be indexed assuming a $\sqrt{2}a_0 \times \sqrt{2}a_0 \times c_0$ tetragonal unit cell.

Referring again to work by Shaked and Jorgensen it was clear that only a limited number of oxygen lattice distortions could be responsible for the observed supercell, assuming that only oxygen octahedral rotation modes were responsible for the superstructure. This was a reasonable assumption to make as the X-ray diffraction patterns did not demonstrate additional reflections indicative of superstructure at room temperature.

In order to determine the correct room temperature structure of $^{160}Gd_2SrCo_2O_7$ from the diffraction data, a series of refinements were carried out on the data. Initially unweighted LeBail extractions were performed on the room temperature data. In each case, if the space

group allowed symmetry lower than tetragonal then constraints were added to the model to enforce tetragonal cell symmetry. Table 3.1 shows the fit parameters for these initial extractions together with *I*4/*mmm* ($Sr_3Ti_2O_7$ model) for comparison. Note that throughout this chapter, non-standard space group settings are used. This allows direct comparison to the *I*4/*mmm* model as the *c* axis remains the long axis on conversion to the listed space group settings.

Table 3.1 – Fit parameters for LeBail extractions of room temperature neutron diffraction data collected on $^{160}Gd_2SrCo_2O_7$ on D20.

SG	R_{wp} / %	R_p / %	χ^2
Bbcm	2.79	1.84	7.595
Bbcb	2.84	1.92	7.872
Bbmm	1.91	1.43	3.536
$P4_2/mnm$	1.80	1.32	3.147
$P4_2/mcm$	2.51	1.66	6.127
$P4_2/m$	1.76	1.29	3.035
*B*112/*m*	2.00	1.47	3.912
$Bb2_1m$	2.10	1.57	4.281
*B*112/*n*	2.23	1.49	4.805
*I*4/*mmm*	6.08	3.57	35.67

Although the results of the LeBail extractions showed that the best fit to the data could be achieved using the space group $P4_2/m$, this model was not chosen for eventual study. Full Rietveld refinements were carried out in both $P4_2/m$ and $P4_2/mnm$ using GSAS to compare the relative merits of each space group selection.

Refinements proceeded smoothly, refining 16 shifted Chebyshev polynomial background terms (neutron absorption due to absorbing Gd isotopes caused a complex background shape), histogram scale factor, four pseudo-Voight peak shape coefficients for the main phase, [5] *a* and *c* unit cell lengths for the main phase, zero point error, atomic coordinates, isotropic temperature factors and fractional occupancy of the *A*-site cation for the main phase, and phase fraction, one peak shape coefficient and *a* unit cell length for the vanadium phase originating from the sample environment. In total 47 parameters were refined for the $P4_2/mnm$ model and 54 for the $P4_2/m$ model. A manual correction was made to the data to correct for the neutron absorption of the sample with the scattering length of Gd changed to that of the ^{160}Gd isotope.

Although the lower space group symmetry model did indeed give an improved fit (χ^2 = 6.165 for $P4_2/m$ vs. 6.251 for $P4_2/mnm$), this was offset by the far larger number of atomic degrees of freedom in this model (17 translational degrees of freedom for $P4_2/m$ to 11 for $P4_2/mnm$). Additionally, the extra refined parameters in the $P4_2/m$ model caused problems in achieving a stable refinement in the lower quality data sets. As a result the model in $P4_2/mnm$ was chosen for further study.

Refinement of the occupancy of the *A*-site cations showed that rather than the disordered distribution of Gd and Sr previously reported by Siwen and Yufang, [2] the Sr^{2+} ion preferentially occupies the larger 12 coordinate site, and the Gd^{3+} the smaller nine coordinate site. This can be explained by the difference in ionic radius of these two ions (1.11 Å for Gd^{3+} in a 9 coordinate site, 1.44 Å for Sr^{2+} in a 12 coordinate site). [6]

The structural parameters extracted from both the $P4_2/m$ and the $P4_2/mnm$ models are shown below in Table 3.2 and Table 3.4, refinements are shown in Figure 3.6 and Figure 3.7, and a full list of bond lengths from each refinement is shown in Table 3.3 and Table 3.5. A comparison of the fit afforded by the $P4_2/mnm$ model compared to the original $I4/mmm$ is shown in Figure 3.8. Several bad detector points were removed from the data by the data processing software at ~ 69 ° 2θ, which may in part be responsible for the poor fitting of peak shape to the intense reflections at around this angle.

Table 3.2 – Extracted structural parameters from refinement of room temperature diffraction data for $^{160}Gd_2SrCo_2O_7$ in $P4_2/m$. R_{wp} = 2.47 %, R_p = 1.78 %, χ^2 = 6.177.

Atom	*x/a*	*y/b*	*z/c*	U_{iso} / 10^{-2}Å^2	Site occupancy
Sr1	0.265 (3)	0.732 (2)	0	1.59 (20)	0.82 (5)
Gd1	0.265 (3)	0.732 (2)	0	1.59 (20)	0.17 (5)
Sr2	0.2419 (17)	0.7323 (13)	0.18088 (15)	1.18 (8)	0.09 (3)
Gd2	0.2419 (17)	0.7323 (13)	0.18088 (15)	1.18 (8)	0.91 (3)
Co	0.251 (6)	0.238 (5)	0.0983 (6)	0.4 (2)	1
O1	0.288 (2)	0.245 (4)	0	2.0 (3)	1
O2	0.204 (2)	0.275 (3)	0.2046 (3)	1.80 (19)	1
O3	0	0.5	0.0928 (8)	1.2 (3)	1
O4	0.5	0.5	0.1034 (13)	3.2 (7)	1
O5	0	0	0.1051 (12)	2.4 (5)	1
O6	0.5	0	0.1127 (8)	0.4 (2)	1

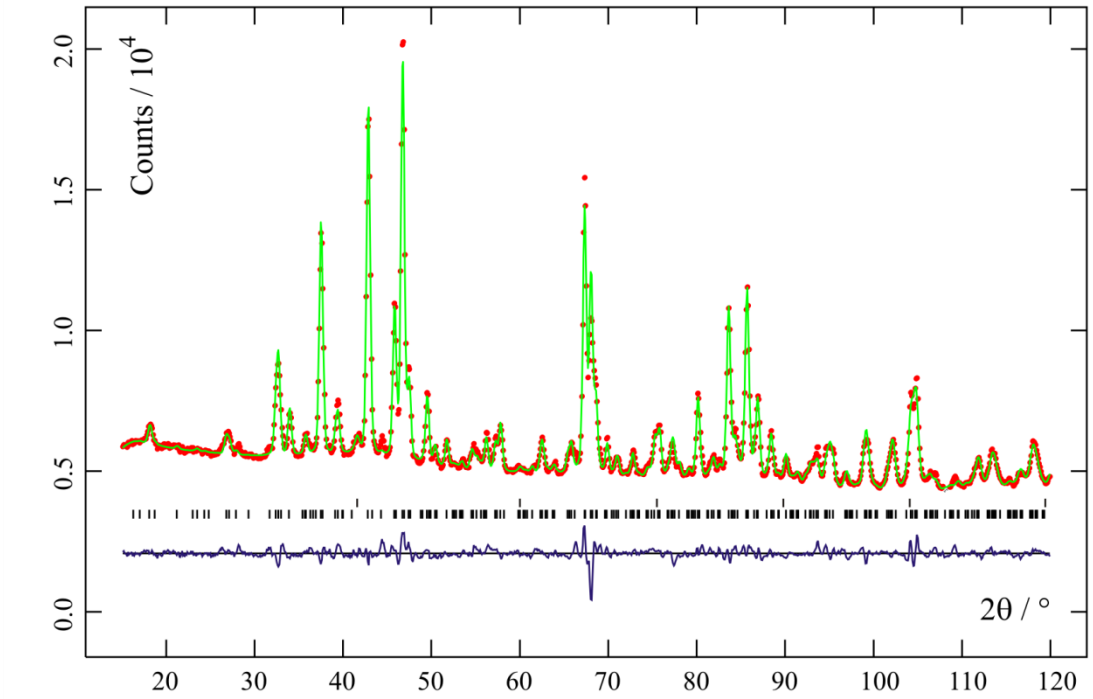

Figure 3.6 – Profile fit of room temperature powder neutron diffraction data collected on $^{160}Gd_2SrCo_2O_7$ in $P4_2/m$. Upper tick marks show vanadium reflection positions and lower tick marks from the sample. Red points show the data, the green line the calculated profile and the blue line the different plot.

Table 3.3 – Bond lengths extracted from refinement of room temperature refinement of neutron diffraction on $^{160}Gd_2SrCo_2O_7$ in $P4_2/m$.

Bond	Bond length / Å	Bond	Bond length / Å
Co-O1	1.915 (11)	$(Sr_{0.82}Gd_{0.17})$-O4 × 2	2.68 (2)
Co-O2	2.086 (14)	$(Sr_{0.82}Gd_{0.17})$-O5 × 2	2.88 (2)
Co-O3	1.95 (2)	$(Sr_{0.82}Gd_{0.17})$-O6 × 2	2.905 (14)
Co-O4	1.95 (3)	$(Gd_{0.91}Sr_{0.09})$-O2	2.505 (17)
Co-O5	1.86 (3)	$(Gd_{0.91}Sr_{0.09})$-O2	2.966 (16)
Co-O6	1.87 (3)	$(Gd_{0.91}Sr_{0.09})$-O2	2.446 (15)
$(Sr_{0.82}Gd_{0.17})$-O1	2.62 (2)	$(Gd_{0.91}Sr_{0.09})$-O2	3.011 (15)
$(Sr_{0.82}Gd_{0.17})$-O1	2.77 (2)	$(Gd_{0.91}Sr_{0.09})$-O2	2.251 (6)
$(Sr_{0.82}Gd_{0.17})$-O1	2.980 (20)	$(Gd_{0.91}Sr_{0.09})$-O3	2.482 (12)
$(Sr_{0.82}Gd_{0.17})$-O1	2.40 (2)	$(Gd_{0.91}Sr_{0.09})$-O4	2.396 (18)
$(Sr_{0.82}Gd_{0.17})$-O3 × 2	2.614 (15)		

Table 3.4 – Extracted structural parameters from refinement of room temperature diffraction data for $^{160}Gd_2SrCo_2O_7$ in $P4_2/mnm$. R_{wp} = 2.49 %, R_p = 1.78 %, χ^2 = 6.251.

Atom	*x/a*	*y/b*	*z/c*	U_{iso} / 10^{-2}Å^2	Site occupancy
Sr1	0.2548 (15)	0.2548 (15)	0	2.02 (15)	0.81 (5)
Gd1	0.2548 (15)	0.2548 (15)	0	2.02 (15)	0.18 (5)
Sr2	0.2633 (6)	0.2633 (6)	0.18092 (15)	1.26 (9)	0.09 (3)
Gd2	0.2633 (6)	0.2633 (6)	0.18092 (15)	1.26 (9)	0.90 (3)
Co	0.252 (3)	0.252 (3)	0.4020 (6)	0.32 (18)	1
O1	0.7742 (20)	0.2258 (20)	0	2.5 (3)	1
O2	0.2146 (11)	0.2146 (11)	0.2955 (3)	1.80 (19)	1
O3	0	0	0.1128 (9)	0.7 (3)	1
O4	0	0	0.4074 (9)	1.6 (3)	1
O5	0	0.5	0.1040 (9)	2.2 (3)	1

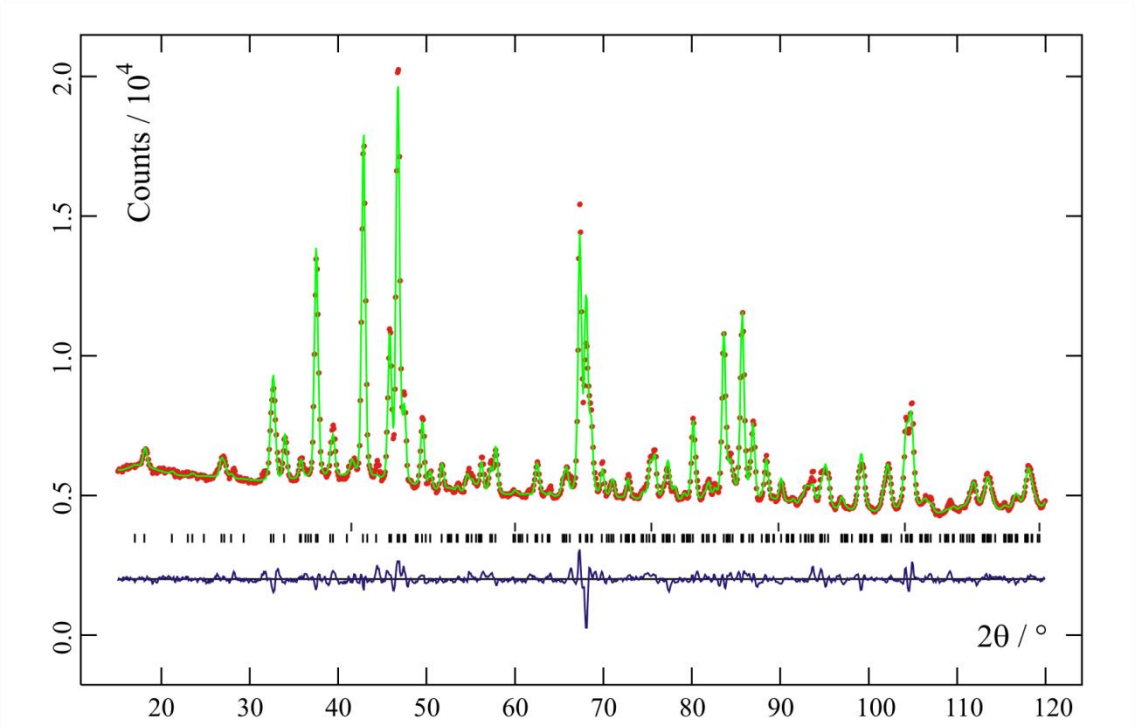

Figure 3.7 – Profile fit of room temperature powder neutron diffraction data collected on $^{160}Gd_2SrCo_2O_7$ in $P4_2/mnm$. Upper tick marks show vanadium reflection positions.

Table 3.5 – Bond lengths extracted from refinement of room temperature refinement of neutron diffraction on $^{160}Gd_2SrCo_2O_7$ in $P4_2/mnm$.

Bond	Bond length / Å	Bond	Bond length / Å
Co-O1	1.906 (11)	$(Sr_{0.81}Gd_{0.18})$-O4 × 2	2.588 (15)
Co-O2	2.082 (14)	$(Sr_{0.81}Gd_{0.18})$-O5 × 2	2.769 (12)
Co-O3	1.906 (22)	$(Sr_{0.81}Gd_{0.18})$-O5 × 2	2.769 (12)
Co-O4	1.922 (22)	$(Gd_{0.90}Sr_{0.09})$-O2	2.252 (7)
Co-O5 × 2	1.9048 (11)	$(Gd_{0.90}Sr_{0.09})$-O2 × 2	2.988 (6)
$(Sr_{0.81}Gd_{0.18})$-O1	2.590 (12)	$(Gd_{0.90}Sr_{0.09})$-O2 × 2	2.472 (6)
$(Sr_{0.81}Gd_{0.18})$-O1	2.590 (12)	$(Gd_{0.90}Sr_{0.09})$-O3	2.396 (10)
$(Sr_{0.81}Gd_{0.18})$-O1 × 2	2.797 (12)	$(Gd_{0.90}Sr_{0.09})$-O4	2.483 (12)
$(Sr_{0.81}Gd_{0.18})$-O3 × 2	2.924 (14)	$(Gd_{0.90}Sr_{0.09})$-O5 × 2	2.419 (10)

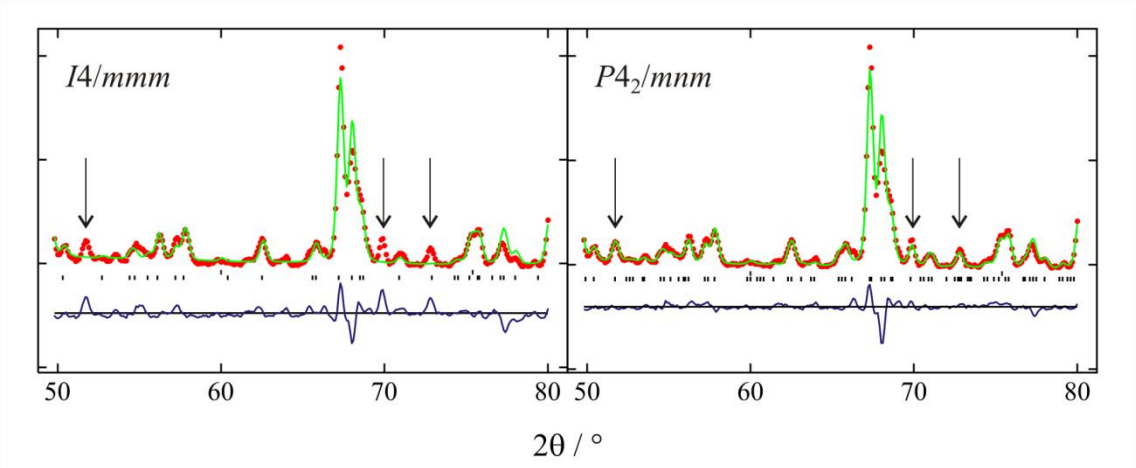

Figure 3.8 – Illustration of improvement of fit afforded by using the $P4_2/mnm$ $\sqrt{2}a_0 \times \sqrt{2}a_0 \times c_0$ unit cell compared to the tetragonal $Sr_3Ti_2O_7$, $I4/mmm$ model for powder neutron diffraction data collected at room temperature on $^{160}Gd_2SrCo_2O_7$. Upper check marks show positions of vanadium reflections.

High temperature structure of $^{160}Gd_2SrCo_2O_7$ by neutron diffraction

Comparison of X-ray diffraction data showed that the 673 K data set exhibited the maximum degree of peak splitting. For this reason the 673 K powder neutron diffraction data set was used for structural characterisation of the high temperature phase.

Once again a series of LeBail extractions were carried out on this set of diffraction data. The fit parameters obtained in these extractions are shown in Table 3.6, again compared to $I4/mmm$. In this case the unit cell lengths were unconstrained so that $a > b \approx \sqrt{2}a_0$ and $c \approx c_0$. The angle γ was also left unconstrained in the case of monoclinic cell symmetry. Note that significantly better fit statistics were achieved in all these extractions compared to the room temperature extractions. This is caused by the shorter collection time at 673 K and overall poorer statistics for these diffraction data sets.

Table 3.6 – Fit parameters for LeBail extractions of neutron diffraction data collected at 673 K on $^{160}Gd_2SrCo_2O_7$ on D20.

SG	R_{wp} / %	R_p / %	χ^2
Bbcm	2.85	1.85	5.051
Bbcb	2.92	1.90	5.307
Bbmm	2.37	1.62	3.482
$P4_2/mnm$	3.80	2.53	9.003
$P4_2/mcm$	3.87	2.57	9.350
$P4_2/m$	3.64	2.37	8.236
*B*112/*m*	2.06	1.48	2.640
$Bb2_1m$	2.47	1.71	3.798
*B*112/*n*	2.14	1.51	2.836
*I*4/*mmm*	4.92	3.36	15.00

The orthorhombic space group *Bbmm* and the two monoclinic space groups *B*112/*m* and *B*112/*n* all gave good fits to the data and full structural models in these space groups were compared to produce a good model for the high temperature phase.

20 shifted Chebyshev polynomial background terms, a histogram scale factor, four pseudo-Voight peak shape coefficients for the main phase, *a*, *b* and *c* unit cell lengths and the angle γ where applicable for the main phase, zero point error, atomic coordinates, isotropic temperature factors and fractional occupancy of the *A*-site cation for the main phase, phase fraction, one peak shape coefficient and *a* unit cell length for the vanadium phase were refined. In total 50 parameters were refined for the *Bbmm* model, 58 for *B*112/*m* and 54 for *B*112/*n*. Once it was determined that the fractional occupancy of the *A*-site did not vary through the transition to within one standard error this value was no longer refined, and is not reported in any further results. All refinements after this point were carried out with occupancies fixed at those determined for the room temperature model.

It was found that although *B*112/*m* did indeed produce the best fit statistics for full structural refinement, this was once again at the expense of a larger number of degrees of freedom. *B*112/*m* produced a refinement with χ^2 of 3.205 for 17 positional parameters, compared to 3.366 for the 10 atomic parameters fitted in *Bbmm*. Refinement of the structure in *B*112/*n* allowed 13 degrees of positional freedom for all atoms, but produced a significantly poorer fit (χ^2 = 7.798). This poorer fit appears to be caused by the symmetry of this space group only allowing one positional degree of freedom per oxygen site, hence not adequately describing the oxygen sublattice. Additionally, the larger number of refined isotropic temperature factors (caused by containing more atomic positions) made refinements in this model very unstable. One additional degree of freedom in the lattice destabilised the refinements of the shorter data sets for both monoclinic space groups.

Due to both providing a good fit to the data with the smallest number of refined parameters and the best stability of refinement in the case of shorter data sets the model in the

orthorhombic space group *Bbmm* was selected for further study. Structural parameters extracted from the refinement are shown in Table 3.7, bond lengths in Table 3.8, and the refined profile fit is shown in Figure 3.9.

Table 3.7 – Extracted structural parameters from refinement of 673 K diffraction data for $^{160}Gd_2SrCo_2O_7$ in *Bbmm*. R_{wp} = 2.29 %, R_p = 1.69 %, χ^2 = 3.366.

Atom	*x/a*	*y/b*	*z/c*	U_{iso} / 10^{-2}Å^2
Sr1	0.2382 (19)	0.25	0	2.03 (15)
Gd1	0.2382 (19)	0.25	0	2.03 (15)
Sr2	0.2667 (9)	0.75	0.31791 (16)	1.74 (8)
Gd2	0.2667 (9)	0.75	0.31791 (16)	1.74 (8)
Co	0.245 (4)	0.25	0.4032 (6)	1.28 (19)
O1	0.286 (3)	0.75	0	3.7 (3)
O2	0.2899 (17)	0.25	0.2945 (3)	3.11 (17)
O3	0.5	0	0.4039 (4)	2.33 (17)
O4	0	0	0.3882 (3)	2.41 (18)

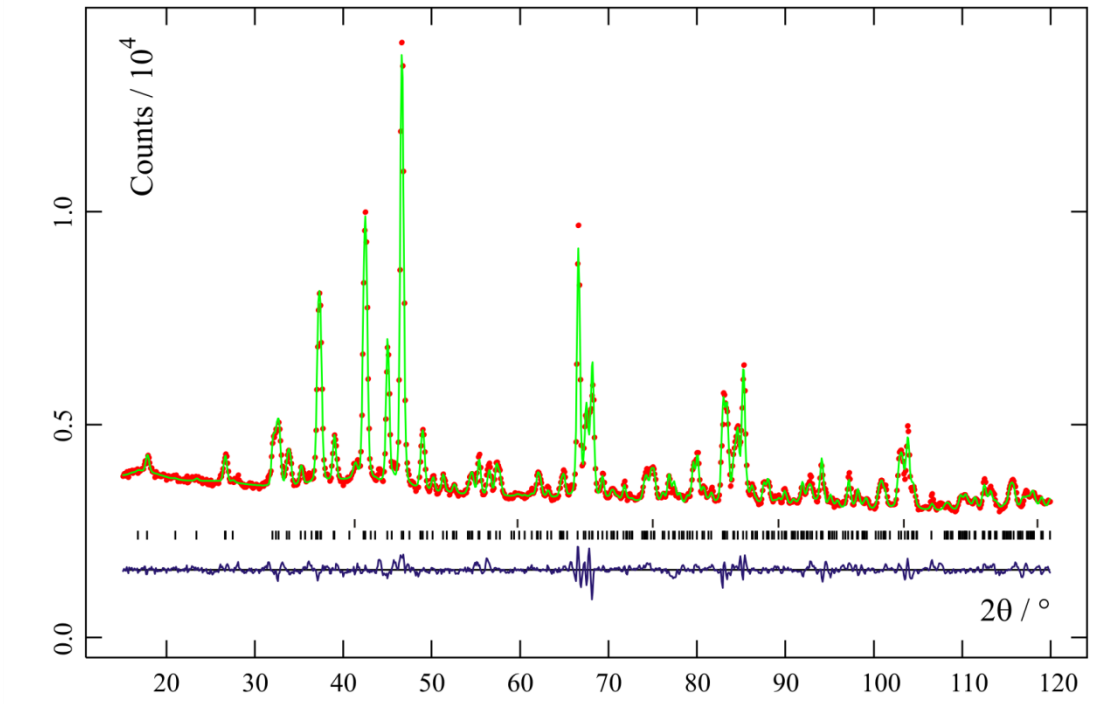

Figure 3.9 – Profile fit of 673 K powder neutron diffraction data collected on $^{160}Gd_2SrCo_2O_7$ in *Bbmm*. Upper tick marks show vanadium reflection positions.

Table 3.8 – Bond lengths extracted from refinement in *Bbmm* of 673 K neutron diffraction data collected on $^{160}Gd_2SrCo_2O_7$.

Bond	Bond length / Å	Bond	Bond length / Å
Co-O1	1.915 (13)	$(Sr_{0.81}Gd_{0.18})$-O4 × 4	2.942 (7)
Co-O2	2.156 (15)	$(Gd_{0.90}Sr_{0.09})$-O2 × 2	2.7259 (11)
Co-O3 × 2	1.924 (17)	$(Gd_{0.90}Sr_{0.09})$-O2	3.049 (10)
Co-O4 × 2	1.911 (16)	$(Gd_{0.90}Sr_{0.09})$-O2	2.445 (10)
$(Sr_{0.81}Gd_{0.18})$-O1 × 2	2.6961 (19)	$(Gd_{0.90}Sr_{0.09})$-O2	2.235 (7)
$(Sr_{0.81}Gd_{0.18})$-O1	2.842 (17)	$(Gd_{0.90}Sr_{0.09})$-O3 × 2	2.505 (7)
$(Sr_{0.81}Gd_{0.18})$-O1	2.573 (17)	$(Gd_{0.90}Sr_{0.09})$-O4 × 2	2.409 (5)
$(Sr_{0.81}Gd_{0.18})$-O3 × 4	2.655 (9)		

Variable temperature neutron diffraction refinement

Once suitable space groups had been selected for each phase, all available data sets were refined using the model appropriate for the temperature range. For longer data collections collected at equilibration temperatures all parameters were refined as described above. Heating data were refined based on the structural model of the previous equilibration range and the background terms, lattice parameters, zero point error and profile shape coefficients were refined. Shorter data ranges were refined using the application SEQGSAS in the GSAS program suite, refining only lattice parameters and peak shape coefficients. Above each equilibration temperature the refinement of the equilibrated data collection was used as the starting point for the sequential refinement. For each data set the unit cell lengths were extracted, and for the longer, 100 K interval sets the Co-O bond lengths were also extracted. Figure 3.10 and Figure 3.11 show the extracted values as a function of temperature.

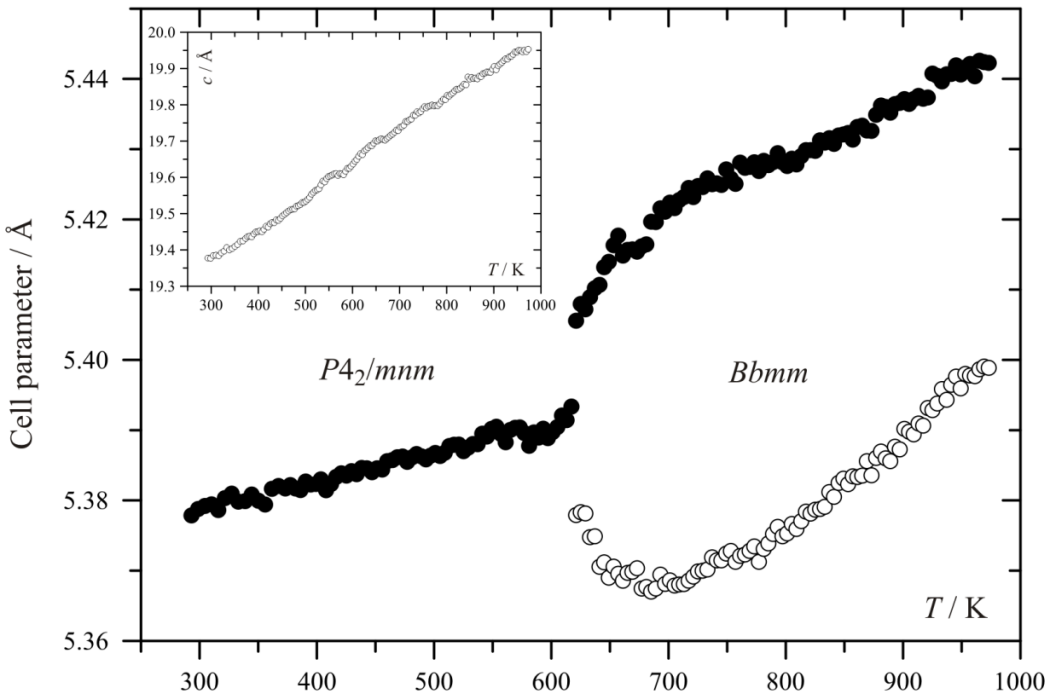

Figure 3.10 – Cell parameters extracted from refinements of diffraction data collected during a temperature ramp on $^{160}Gd_2SrCo_2O_7$ on D20. Filled circles show *a* cell parameter, open circles *b* cell parameter. *c* cell parameter is shown in inset. Errors lie within point size.

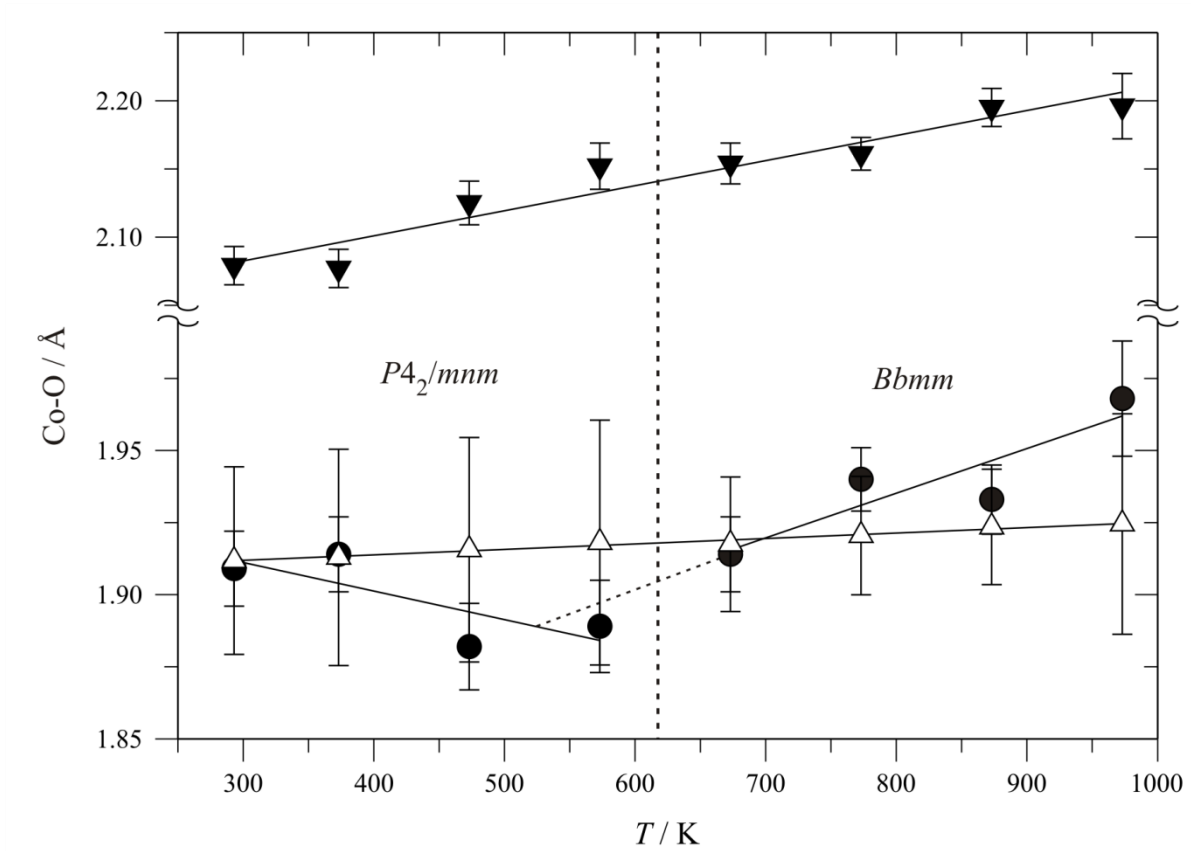

Figure 3.11 – Co-O bond lengths extracted from longer data sets collected on $^{160}Gd_2SrCo_2O_7$ on D20. ● represent the bond length Co-O1, ▼ represent the bond length Co-O2 and Δ represent the averaged length Co-O3 to O5 (*Bbmm*) or O6 ($P4_2/mnm$). A representation of these oxygen atoms is shown in Figure 3.12.

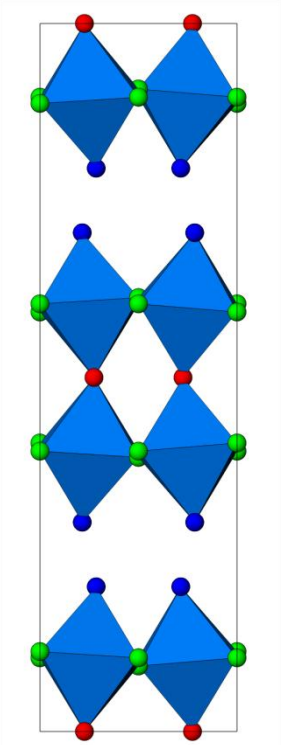

Figure 3.12 – Refined octahedral tilts in room temperature structure of $^{160}Gd_2SrCo_2O_7$. Red oxygen atoms show O1 from results tables (● from Figure 3.11), blue oxygen atoms O2 (▼) and green O3-O6 (Δ).

From the inset of Figure 3.10 we see the effect of data collection whilst heating: directly above an equilibration point the cell parameters appear to plateau, caused by the temperature

of the sample being slightly higher than the programmed temperature prior to the equilibration.

Within the error range shown, Figure 3.11 shows several features of the structure of the material as a function of temperature. For clarity, each data range will be discussed separately.

The equatorial Co-O bonds (green oxygens in Figure 3.12, O3-O6) appear to expand linearly with temperature; however within error ranges the lengths are constant throughout the temperature range. The error bars decrease in magnitude after the phase transition due to the smaller number of oxygen atoms in the *Bbmm* model producing a smaller error.

The Co-O bond to the oxygen bridging the twin perovskite layers (red in Figure 3.12, O1) contracts from its room temperature length before the phase transition, then expands above the transition. The dashed line in Figure 3.11 shows that this trend includes the final data set prior to the transition temperature.

The bond to the capping oxygen (blue oxygens in Figure 3.12, O2) is significantly longer than other Co-O bonds in the model. Once again the bond expands constantly with temperature. This length is the best defined within the material, and the errors in the bond length are small enough that within any reasonable error window this bond is longer than the others in the structure and is clearly expanding through the temperature range.

It is clear from Figure 3.11 that the most significant changes to bond lengths through the phase transition are in the bond to the bridging oxygen atom. This is an intuitive result as the bridging oxygen experiences the full effect of CoO_6 tilting which distinguishes the two different structures.

It should be noted that although these bond lengths provide a useful description of the changes that the material undergoes through the transition, within a three standard error margin the Co bonding environment must strictly be described as a distorted octahedron with 5 ×1.9 Å Co-O bonds and one elongated Co-O bond at 2.07 Å with expansion over the studied temperature range.

Magnetic susceptibility data

Variable temperature magnetic susceptibility measurements were collected on a pelletised 0.5 g sample of $Gd_2SrCo_2O_7$ (pure by X-ray diffraction) over the temperature range 12 to 980 K using a combination of a Quantum Design MPMS-5S superconducting quantum interferometry device (SQUID) in a 100 Oe applied field and an Oxford Instruments vibrating sample magnetometer (VSM, 300 – 980 K). The VSM data were normalised to the data collected on the SQUID. VSM data are shown below in Figure 3.13 and Figure 3.14, and SQUID data in Figure 3.15. All magnetism data were collected by Dr. Martin Lees, University of Warwick.

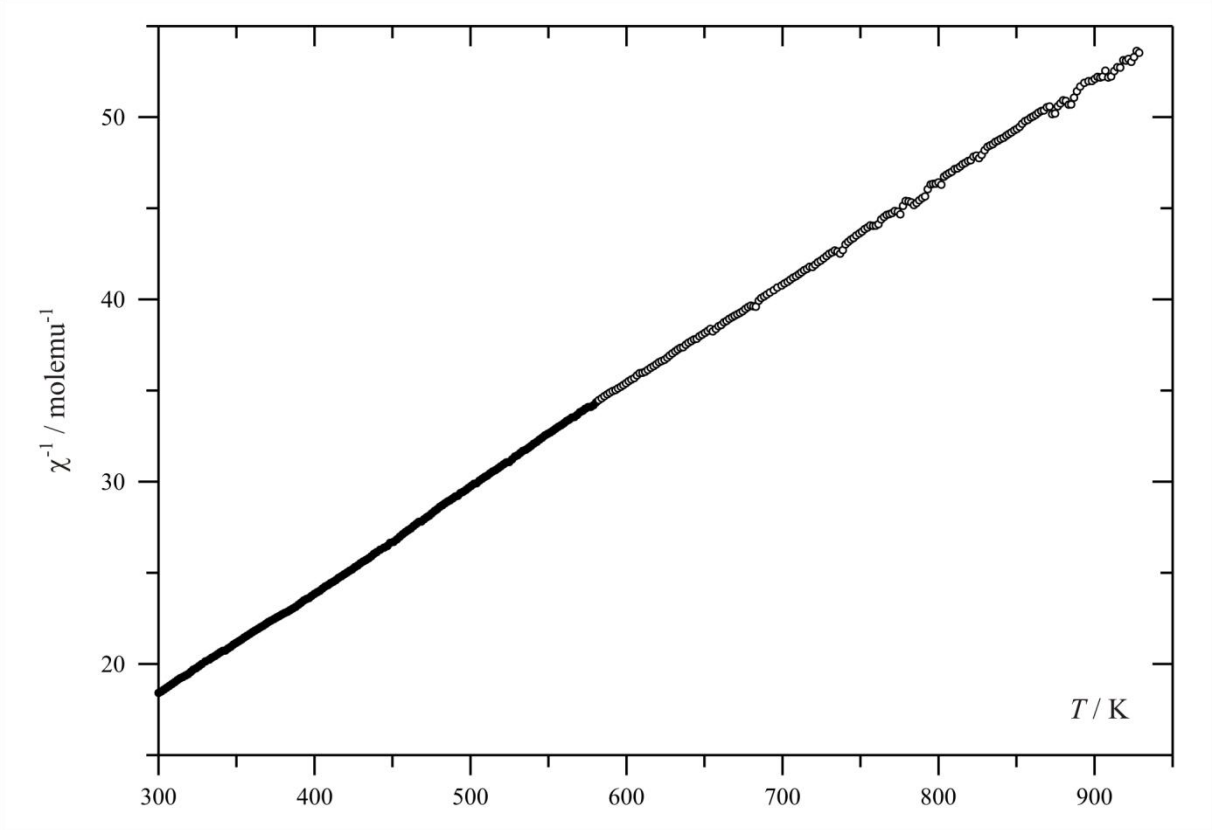

Figure 3.13 – Inverse magnetic susceptibility data as a function of temperature collected on a VSM for $Gd_2SrCo_2O_7$. Filled circles show data collected below the transition temperature, open above the transition.

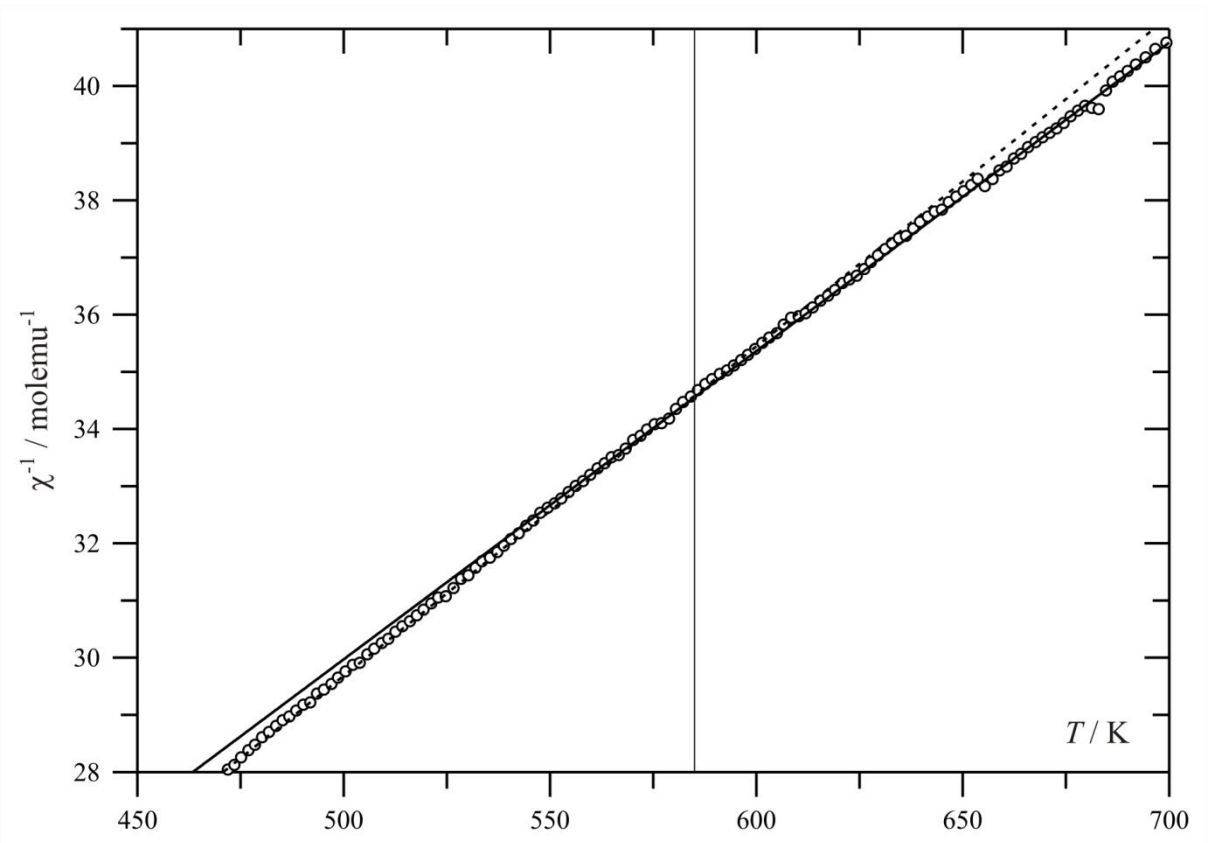

Figure 3.14 – Zoomed region in inverse magnetic susceptibility data as a function of temperature collected on a VSM for $Gd_2SrCo_2O_7$. Dashed line shows fit to data below transition temperature, solid line a fit to data collected above transition temperature. Vertical line shows the intersection of the two fit lines.

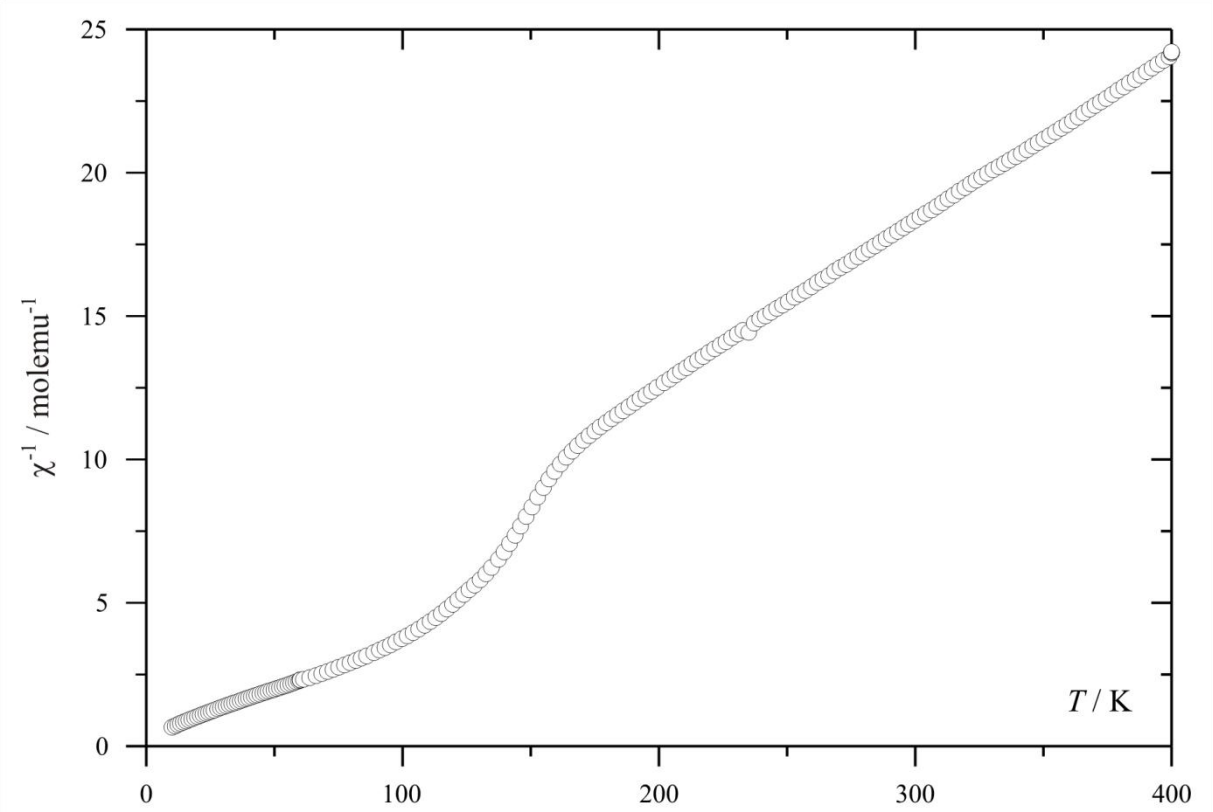

Figure 3.15 – Inverse magnetic susceptibility data as a function of temperature collected on a SQUID for $Gd_2SrCo_2O_7$. Data are sampled every third point for clarity.

The inverse susceptibility trace is overwhelmingly dominated by Gd^{3+} paramagnetism, showing a near-linear trace throughout the entire range collected on the VSM. Around 570 K however, a small change in gradient can be observed, as in Figure 3.14. The change in gradient is consistent with an increase in unpaired electron density and is concurrent with the structural phase transition.

Linear fitting of these data below and above the transition temperature gives two Weiss constants: θ = -19.07 K below the transition temperature and -36.12 K above the transition temperature. The statistical significance of fitting these two ranges separately rather than modelling the whole data range with one straight line can be estimated by comparing the sum of residuals obtained from each fitting method: 603.8 for a single gradient compared to 554.0 with two lines.

From the Curie-Weiss behaviour observed in the SQUID data in the temperature range 200 – 400 K the effective cobalt magnetic moment is estimated at 2.48 (1) μ_B. The deviation from linearity at ~ 170 K appears to be caused by an impurity phase as no deviation from Curie-Weiss behaviour is observed in work by Akiyama *et al*. This impurity phase is apparently very minor as it was undetectable by X-ray powder diffraction, typically suggesting 5% or less impurity. The temperature of the onset of deviation from linearity corresponds to an $Ln_{1-x}Sr_xCoO_3$ type phase.

Thermogravimetric analysis and calorimetry

Simultaneous differential scanning calorimetry (DSC) and thermogravimetric analysis (TGA) were collected on a NETZSCH STA 409 PC Luxx instrument at a heating rate of 10 $Kmin^{-1}$ under flowing nitrogen gas by Dr. C. S. Knee at the University of Gothenburg. The DSC and TGA traces are shown in Figure 3.16 and Figure 3.17.

Figure 3.16 shows a broad trough in the DSC trace centred approximately at the transition temperature previously determined for $Gd_2SrCo_2O_7$. Integration of the trough gives an endothermic energy change associated with the transition of approximately 2.5 $kJmol^{-1}$. Figure 3.17 shows the TGA trace for the same temperature range, and confirms that the sample mass remains constant throughout the temperature range to within 0.3 % mass. It is significant that no changes in mass or gradient of TG trace are observed in the region of the transition temperature, demonstrating that the transition is not associated with a loss or gain of mass.

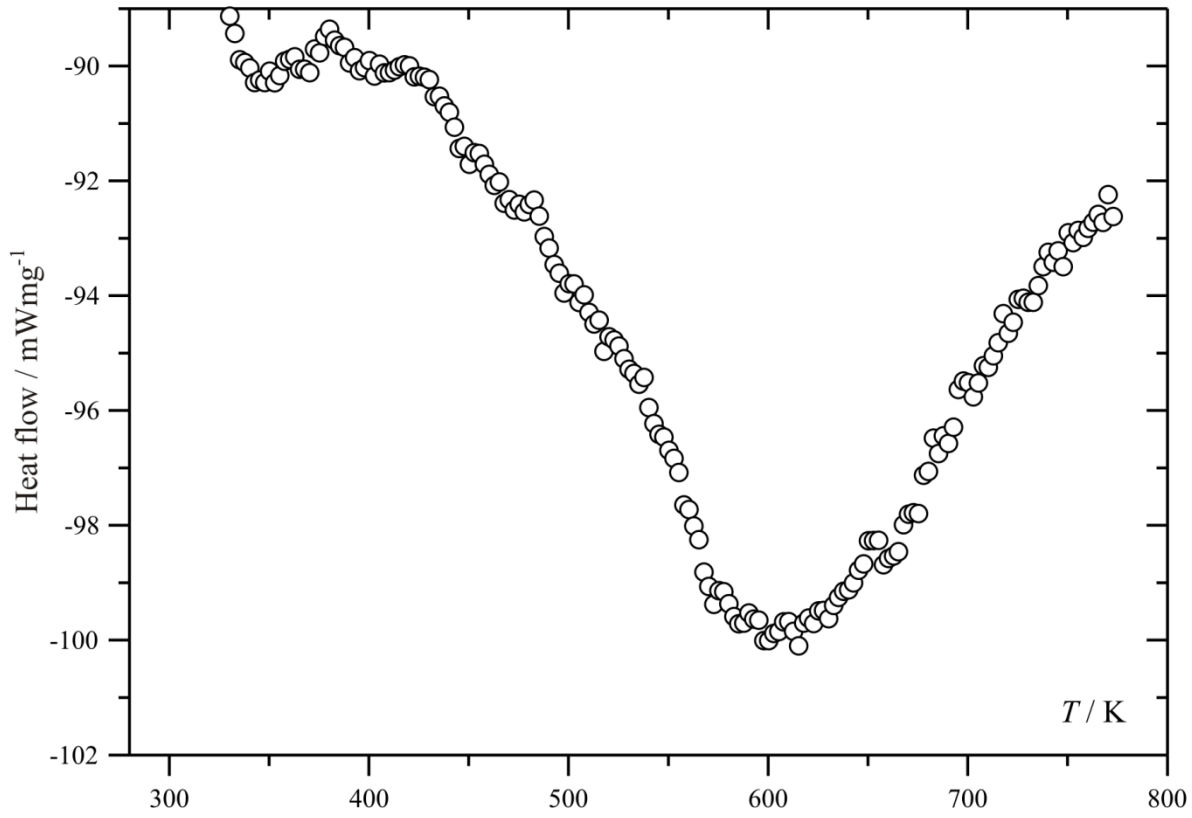

Figure 3.16 – DSC trace collected on a sample of $Gd_2SrCo_2O_7$ between 300 K and 773 K.

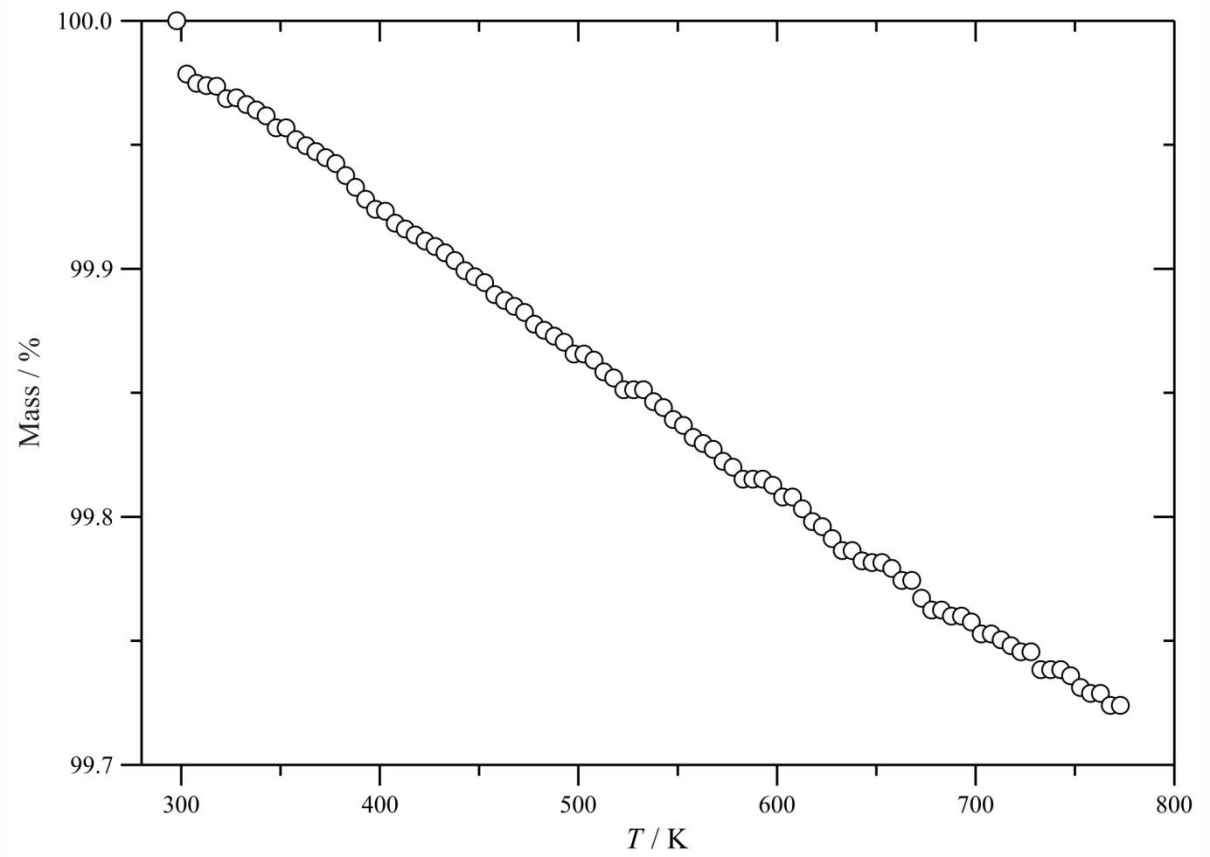

Figure 3.17 – TGA trace collected on a sample of $Gd_2SrCo_2O_7$ between 300 K and 773 K. Data sampled every second point for clarity. Negligible (0.3 %) mass loss attributable to balance drift or buoyancy effects.

Structural study of $Nd_2BaCo_2O_7$

A phase pure sample of $Nd_2BaCo_2O_7$ was prepared and its structure studied by diffraction methods. Initially variable temperature X-ray diffraction data were collected between room temperature and 973 K under flowing nitrogen. To minimise X-ray fluorescence collected, the SOLEX detector was used with an energy collection band appropriate for Cu K_α. Diffraction data are shown in Figure 3.18.

Unlike the previously studied gadolinium strontium material, no reduction in symmetry was apparent on heating. Close inspection of peaks suggested that above ~ 773 K peaks may have broadened. Small quantities of perovskite ($Nd_{1-x}Ba_xCoO_3$) and neodymium oxide impurities were present in the sample at room temperature, hence the "broadening" of peaks in this case could be better interpreted as the beginnings of a moderately low temperature decomposition of the sample and increased quantity of these impurities.

Again the oxide substructure was critical to structural determination, hence powder neutron diffraction data were again collected. Neodymium neutron absorption is sufficiently low that an isotopically enriched sample was not needed for this experiment, and intensities were much improved compared to those observed with $^{160}Gd_2SrCo_2O_7$.

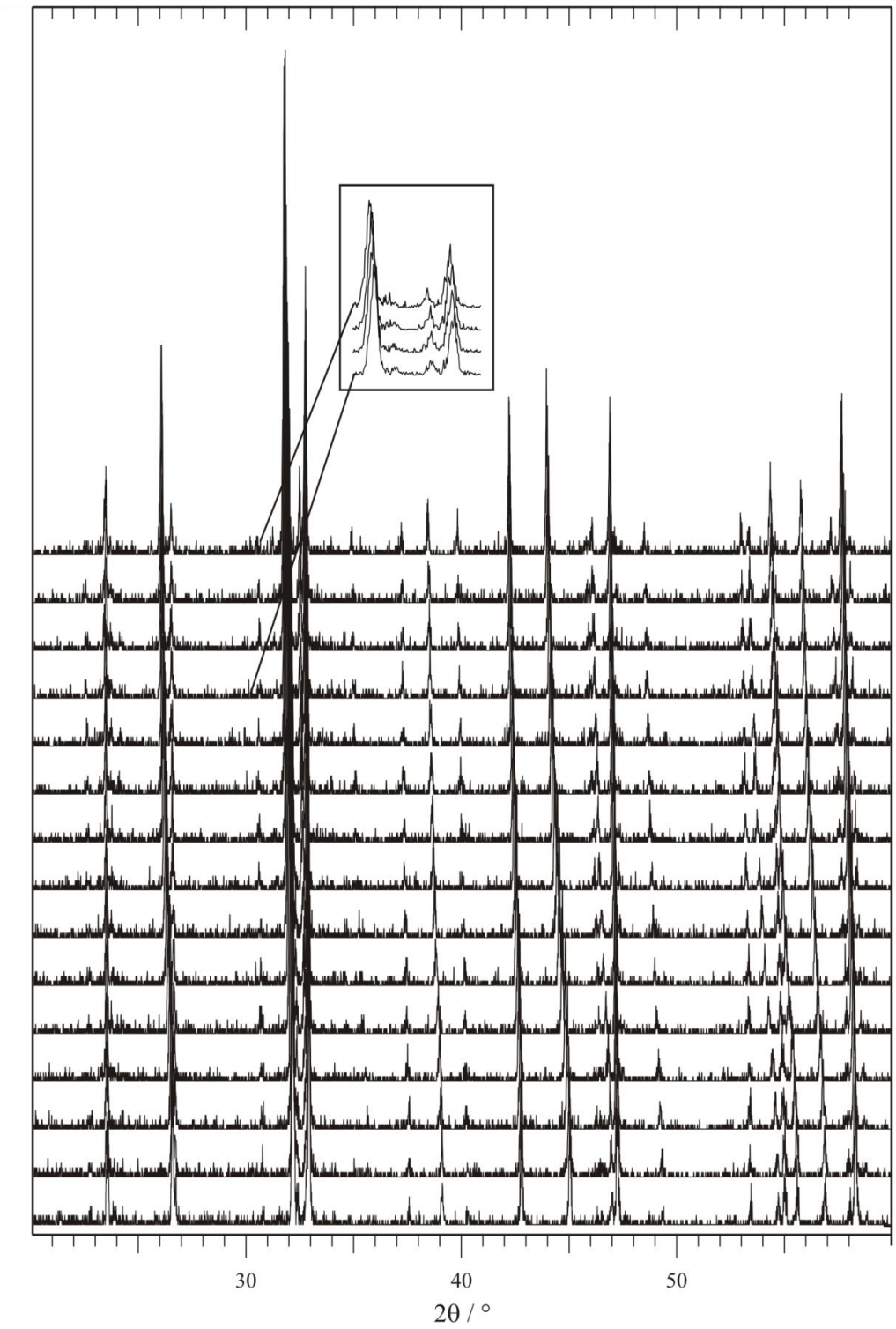

Figure 3.18 – Thermodiffractogram collected on a sample of $Nd_2BaCo_2O_7$ using a SOLEX detector. Plots are stacked along the *y* axis with increasing temperature.

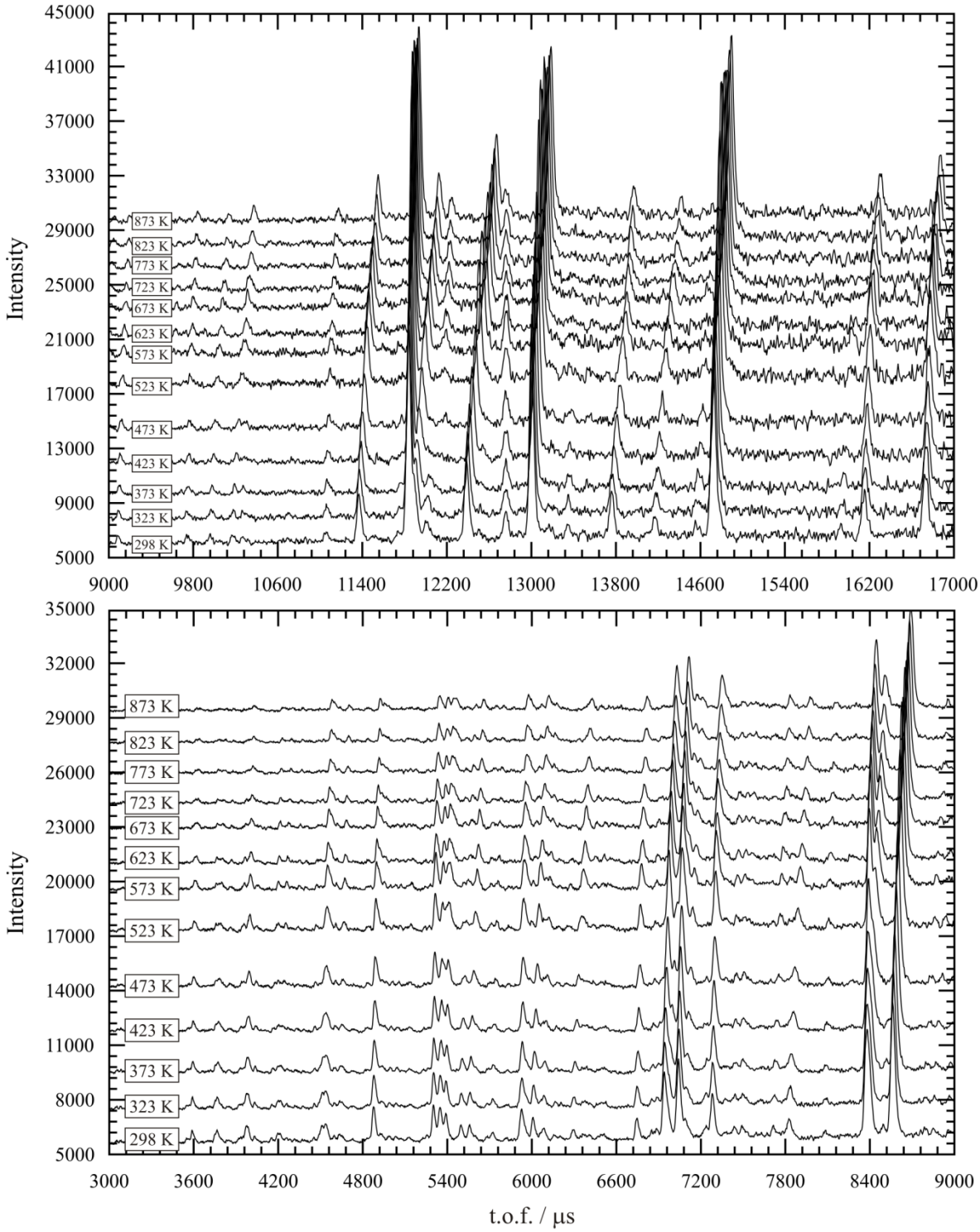

Figure 3.19 – Neutron thermodiffractogram collected on $Nd_2BaCo_2O_7$ on POLARIS. Backscattered diffraction data are shown, between 3000 and 9000 μs (below) and 9000 and 17000 μs (above).

Neutron diffraction data were collected on the time-of-flight instrument POLARIS at the ISIS spallation neutron source. 150 μAhr were collected at each temperature between room temperature and 873 K, collecting every 50 K. Backscattered diffraction data (collected at 145 ° to the incident neutron beam) are shown in Figure 3.19.

Room temperature structure of $Nd_2BaCo_2O_7$ by powder neutron diffraction

Again, it was found that room temperature diffraction data could not be adequately fitted using a $Sr_3Ti_2O_7$ model. A trial refinement using the room temperature structure determined for $Gd_2SrCo_2O_7$ proved similarly ineffective. A series of *ab initio* LeBail extractions based on a $\sqrt{2}a_0 \times \sqrt{2}a_0 \times c$ unit cell were once again carried out to determine the symmetry of the structure. Again, space groups with symmetry lower than tetragonal were constrained to be metrically tetragonal, and impurity phases were not modelled as this was found to destabilise the extractions and give incomparable fit statistics.

Table 3.9 – Fit parameters for LeBail extractions of room temperature neutron diffraction data collected on $Nd_2BaCo_2O_7$ on POLARIS.

S.G.	R_{wp} / %	R_p / %	χ^2
*B*112/*m*	0.86	2.33	0.3043
*B*112/*n*	0.99	2.40	0.4089
Bb2_1*m*	0.92	2.36	0.3534
Bbcb	0.90	2.45	0.3393
Bbmm	1.01	2.45	0.4261
Bmcm	1.05	2.49	0.4602
P2_1/*m*	0.92	2.40	0.3511
P4_2/*mcm*	0.92	2.40	0.4278
P4_2/*mnm*	1.01	2.44	0.4758
*I*4/*mmm*	1.08	2.69	0.4865

Table 3.9 shows the fit parameters extracted from these LeBail extractions. Once again, all space groups provided better fit statistics than *I*4/*mmm*. The three space groups with best fit statistics (based on χ^2) were fully modelled to determine the best representation of the room temperature structure.

The refinement in *P*2_1/*m* again proved to be very unstable due to the high number of atomic positions necessary to describe the structure in this low point symmetry space group. A stable refinement could not be achieved whilst fully refining oxygen positions, hence this space group was disregarded in further study. Similarly, both low point group monoclinic space groups (*B*112/*m* and *B*112/*n*) could not be refined to a satisfactory minimum, and were not pursued for further study.

The refinements in both *Bbcb* and *Bb*2_1*m* gave satisfactory fitting to the diffraction data, and final fits to the data from the backscattered (168 °) detector bank are shown in Figure 3.20 and Figure 3.21. Refined parameters and extracted bond lengths for these refinements are presented in Table 3.10, Table 3.11, Table 3.12 and Table 3.13. Once again the impurity phases were not modelled to allow a direct comparison between the two models.

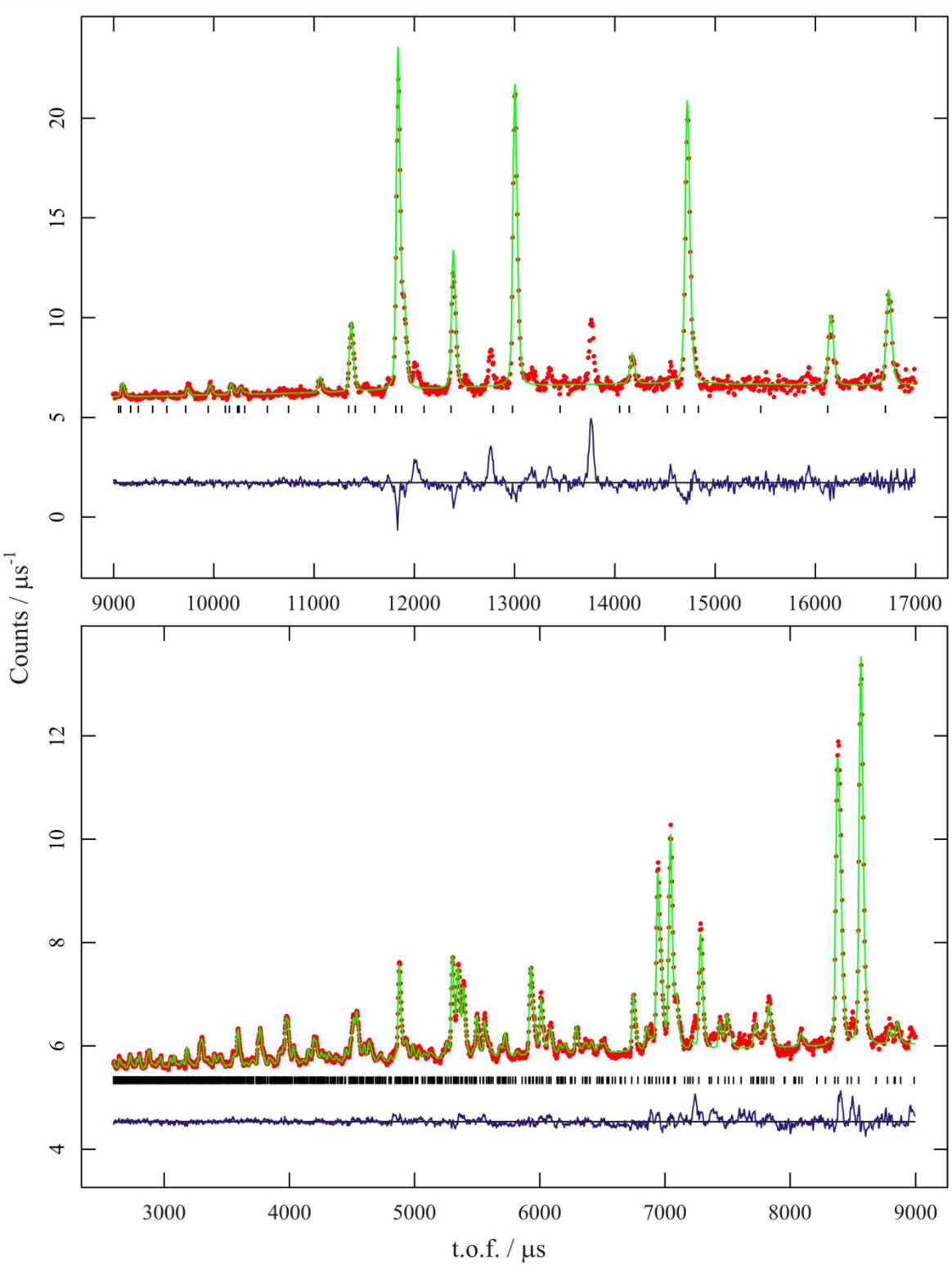

Figure 3.20 – Profile fit of backscattered neutron diffraction data collected on $Nd_2BaCo_2O_7$ in *Bbcb*, impurity phases omitted for direct comparison.

Table 3.10 – Extracted structural parameters from refinement of RT neutron diffraction data omitting impurity phases for $Nd_2BaCo_2O_7$ in *Bbcb*. R_{wp} = 1.07 %, R_p = 2.34 %, χ^2 = 0.4759, $a = b$ = 5.42941 (14), c = 20.0873 (7).

Atom	*x/a*	*y/b*	*z/c*	U_{iso} / 10^{-2}Å^2	Site occupancy
Co	0.25	0.25	0.40165 (25)	0.47 (6)	1
Ba1	0.25	0.25	0	0.38 (6)	0.89 (3)
Nd1	0.25	0.25	0	0.38 (6)	0.11 (3)
Ba2	0.25	0.25	0.18117 (8)	0.37 (2)	0.057 (15)
Nd2	0.25	0.25	0.18117 (8)	0.37 (2)	0.943 (15)
O1	0.25	0.25	0.5	1.89 (8)	1
O2	0.25	0.25	0.29607 (14)	1.08 (5)	1
O3	0.4951 (18)	0.003 (3)	0.10486 (10)	0.85 (3)	1

Table 3.11 – Bond lengths extracted from refinement of RT neutron diffraction data collected on $Nd_2BaCo_2O_7$ in *Bbcb*.

Bond	Bond length / Å
Co-O1	2.121 (6)
Co-O2	1.976 (5)
Co-O3 × 2	1.933 (14)
Co-O3 × 2	1.916 (14)
$(Ba_{0.89}Nd_{0.11})$-O2 × 4	2.71470 (7)
$(Ba_{0.89}Nd_{0.11})$-O3 × 4	2.830 (7)
$(Ba_{0.89}Nd_{0.11})$-O3 × 4	2.870 (7)
$(Nd_{0.94}Ba_{0.06})$-O1	2.3081 (34)
$(Nd_{0.94}Ba_{0.06})$-O1 × 4	2.7530 (5)
$(Nd_{0.94}Ba_{0.06})$-O3 × 2	2.433 (8)
$(Nd_{0.94}Ba_{0.06})$-O3 × 2	2.479 (8)

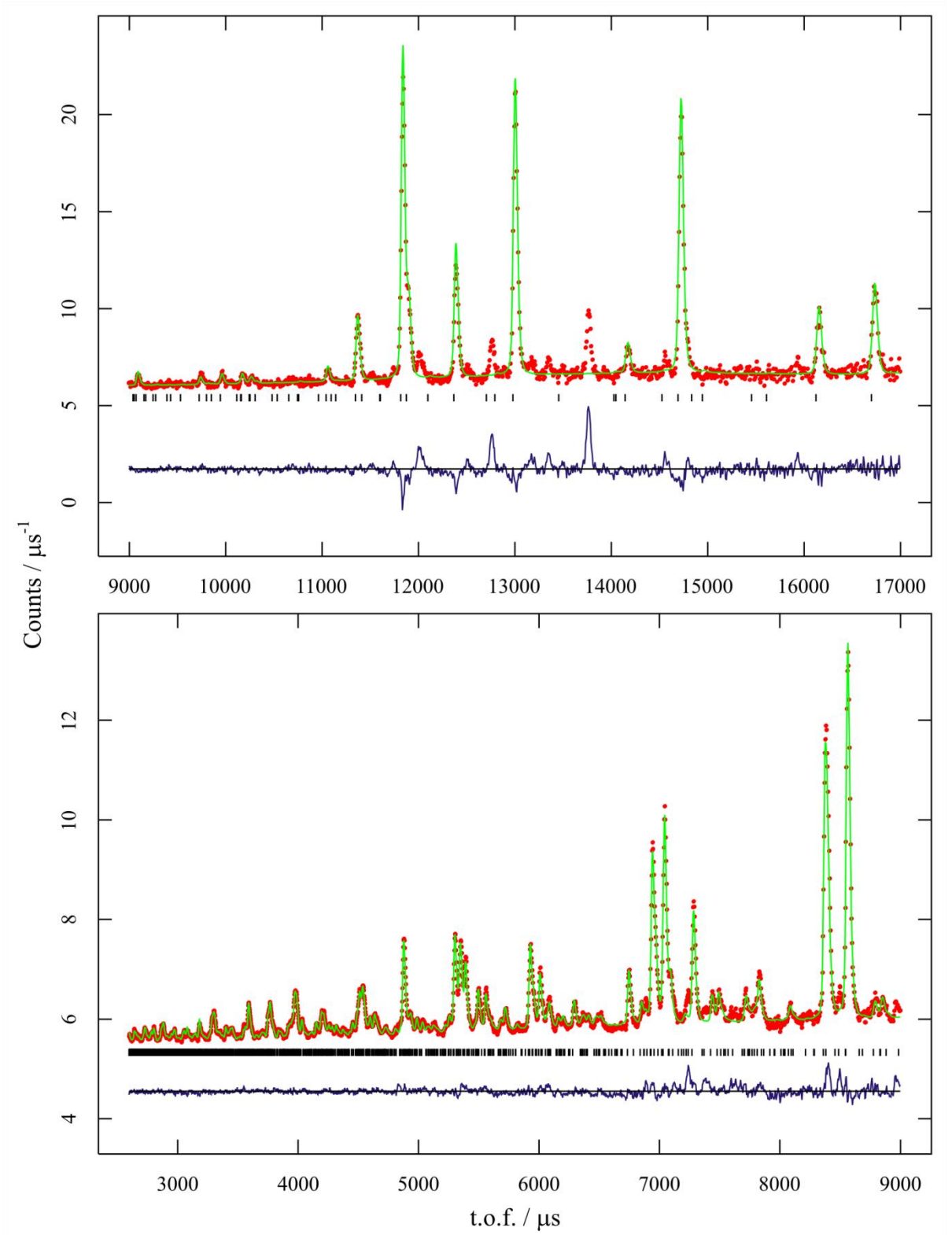

Figure 3.21 – Profile fit of backscattered neutron diffraction data collected on $Nd_2BaCo_2O_7$ in $Bb2_1m$, impurity phases omitted for direct comparison.

Table 3.12 – Extracted structural parameters from refinement of RT neutron diffraction data for $Nd_2BaCo_2O_7$ in $Bb2_1m$. R_{wp} = 1.08 %, R_p = 2.34 %, χ^2 = 0.4901, $a = b$ = 5.42942 (14), c = 20.0871 (7).

Atom	*x/a*	*y/b*	*z/c*	U_{iso} / 10^{-2}Å^2	Site occupancy
Co	0.249 (7)	0.234 (7)	0.4019 (3)	0.46 (8)	1
Ba1	0.247 (6)	0.241 (4)	0	0.38 (12)	0.87 (3)
Nd1	0.247 (6)	0.241 (4)	0	0.38 (12)	0.13 (3)
Ba2	0.248 (3)	0.233 (2)	0.18116 (9)	0.39 (3)	0.066 (16)
Nd2	0.248 (3)	0.233 (2)	0.18116 (9)	0.39 (3)	0.934 (16)
O1	0.242 (5)	0.226 (5)	0.29607 (16)	1.05 (9)	1
O2	0.263 (9)	0.755 (5)	0	1.32 (17)	1
O3	0.500 (9)	0.491 (6)	0.1051 (15)	0.9 (3)	1
O4	0.501 (16)	0.487 (6)	0.3954 (15)	1.1 (3)	1

Table 3.13 – Bond lengths extracted from refinement of RT neutron diffraction data collected on $Nd_2BaCo_2O_7$ in $Bb2_1m$.

Bond	Bond length / Å	Bond	Bond length / Å
Co-O1	2.128(7)	$(Ba_{0.87}Nd_{0.13})$-O2	2.79 (4)
Co-O2	1.974 (6)	$(Ba_{0.87}Nd_{0.13})$-O2	2.77 (6)
Co-O3	1.90 (6)	$(Ba_{0.87}Nd_{0.13})$-O2	2.66 (6)
Co-O3	1.95 (5)	$(Nd_{0.93}Ba_{0.07})$-O1	2.309 (4)
Co-O4	1.94 (8)	$(Nd_{0.93}Ba_{0.07})$-O1 × 2	2.79 (3)
Co-O4	1.91 (7)	$(Nd_{0.93}Ba_{0.07})$-O1 × 2	2.72 (3)
$(Ba_{0.87}Nd_{0.13})$-O3 × 4	2.86 (4)	$(Nd_{0.93}Ba_{0.07})$-O3	2.48 (4)
$(Ba_{0.87}Nd_{0.13})$-O4 × 2	2.82 (5)	$(Nd_{0.93}Ba_{0.07})$-O3	2.44 (3)
$(Ba_{0.87}Nd_{0.13})$-O4 × 2	2.85 (6)	$(Nd_{0.93}Ba_{0.07})$-O4	2.45 (5)
$(Ba_{0.87}Nd_{0.13})$-O2	2.64 (4)	$(Nd_{0.93}Ba_{0.07})$-O4	2.46 (5)

It is clear from the refined atomic coordinates that within one standard error, these models are identical. This is reflected in the bond lengths: whilst the degeneracies vary with the change of space group, within error the coordination sphere of the *A* and *B* site cations is identical. Furthermore, the refined parameter-independent fit parameters (R_{wp} and R_p) are identical for the two models whilst χ^2 is significantly lower for *Bbcb* with its fewer refined atomic positions. The final choice of space group for the structural model is therefore *Bbcb*: it combines the best fitting parameters (χ^2 of 0.4759 compared to 0.4901 for *B*112/*m*) with fewest refined parameters. Examination of the errors in refined positions in the models shows very small deviation from the positions that are expected for a standard *I*4/*mmm* model. Six atomic positions, six thermal parameters and one site occupancy were refined in the main phase. Removing constraints on the *a* and *b* unit cell parameters also produced refined lengths equal to within one standard error, confirming that the cell was indeed metrically tetragonal. Other parameters refined to fit the profile were a total of six cell parameters and two zero point errors, three phase fractions and one histogram scale factor, twelve background

parameters for the backscattered bank and eight for the low angle bank and twelve total profile parameters (six for the main phase and one per histogram for each impurity) resulting in a total of 57 refined parameters for two histograms.

Overall the final refinement was a good fit to the data (R_{wp} = 1.27 %, R_p = 2.34 %, χ^2 = 0.3284), however another unidentified impurity phase was clearly present as shown by unfitted peaks either side of 13000 μs in the backscattered bank and several shoulders on peaks in the low angle bank, shown in Figure 3.22 and Figure 3.23.

Table 3.14 – Refined atomic parameters for neutron diffraction data collected on a sample of $Nd_2BaCo_2O_7$ on POLARIS in *Bbcb*.

Atom	*x/a*	*y/b*	*z/c*	U_{iso} / 10^{-2}Å^2	Site occupancy
Co	0.25	0.25	0.40159 (18)	0.53 (4)	1
Ba1	0.25	0.25	0	0.60 (5)	0.796 (17)
Nd1	0.25	0.25	0	0.60 (5)	0.204 (17)
Ba2	0.25	0.25	0.18126 (5)	0.305 (16)	0.102 (9)
Nd2	0.25	0.25	0.18126 (5)	0.305 (16)	0.898 (9)
O1	0.25	0.25	0.5	1.83 (6)	1
O2	0.25	0.25	0.29647 (10)	1.10 (3)	1
O3	0.4935 (10)	0.0007 (22)	0.10514 (7)	0.809 (21)	1
O4	0.25	0.25	0.40159 (18)	0.53 (4)	1

Once again the occupancies of the *A* coordinate site were refined, and once again the larger alkali earth ion occupied the 12-coordinate site preferentially.

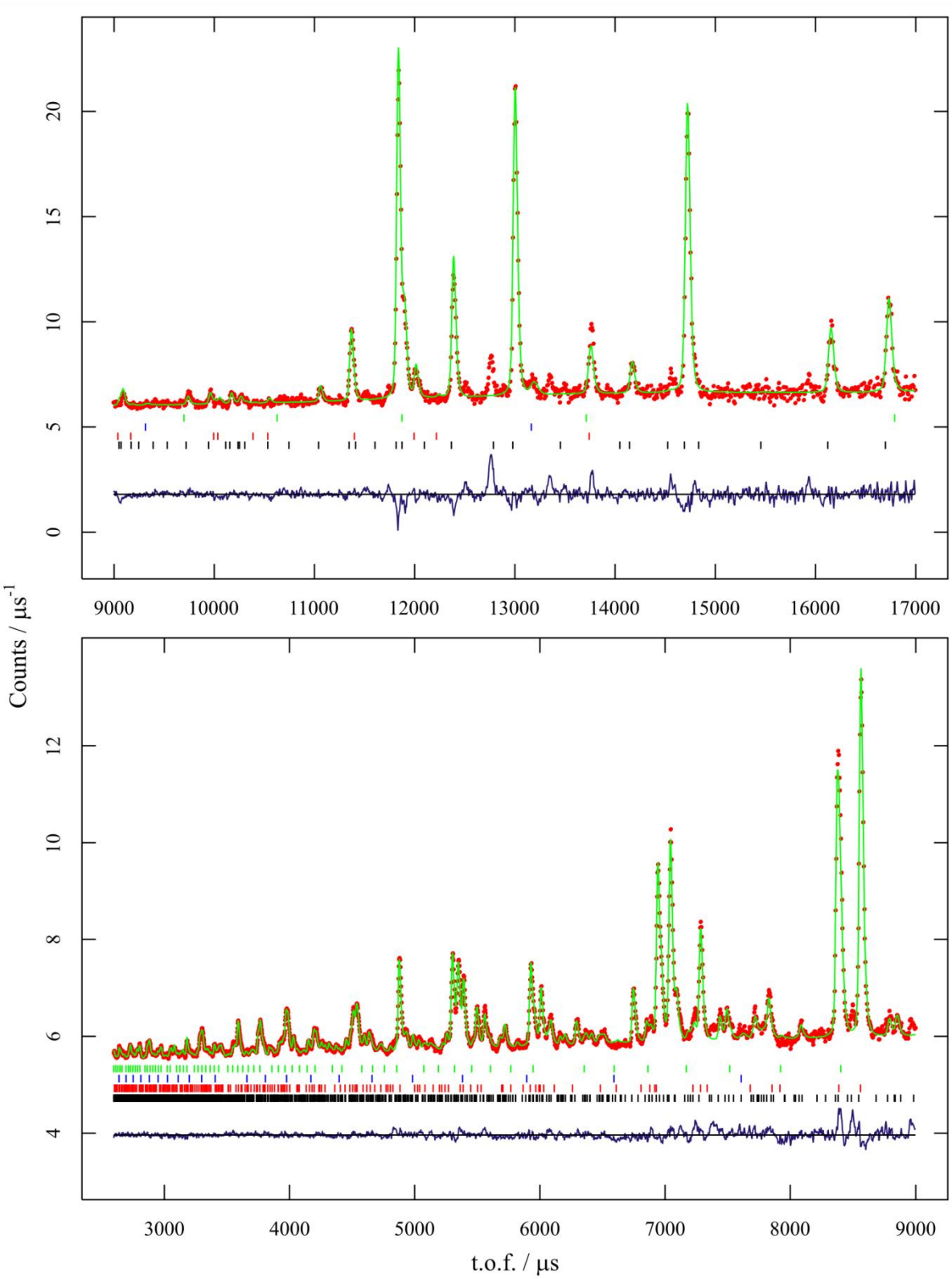

Figure 3.22 – Profile fit of the backscattered bank diffraction data collected on $Nd_2BaCo_2O_7$ at POLARIS in *Bbcb* space group. R_{wp} = 1.03 %, R_p = 2.23 %. Black tick marks show reflection positions for main phase, red for Nd_2O_3, blue the vanadium can and green the perovskite $(NdBa)_{0.5}CoO_3$.

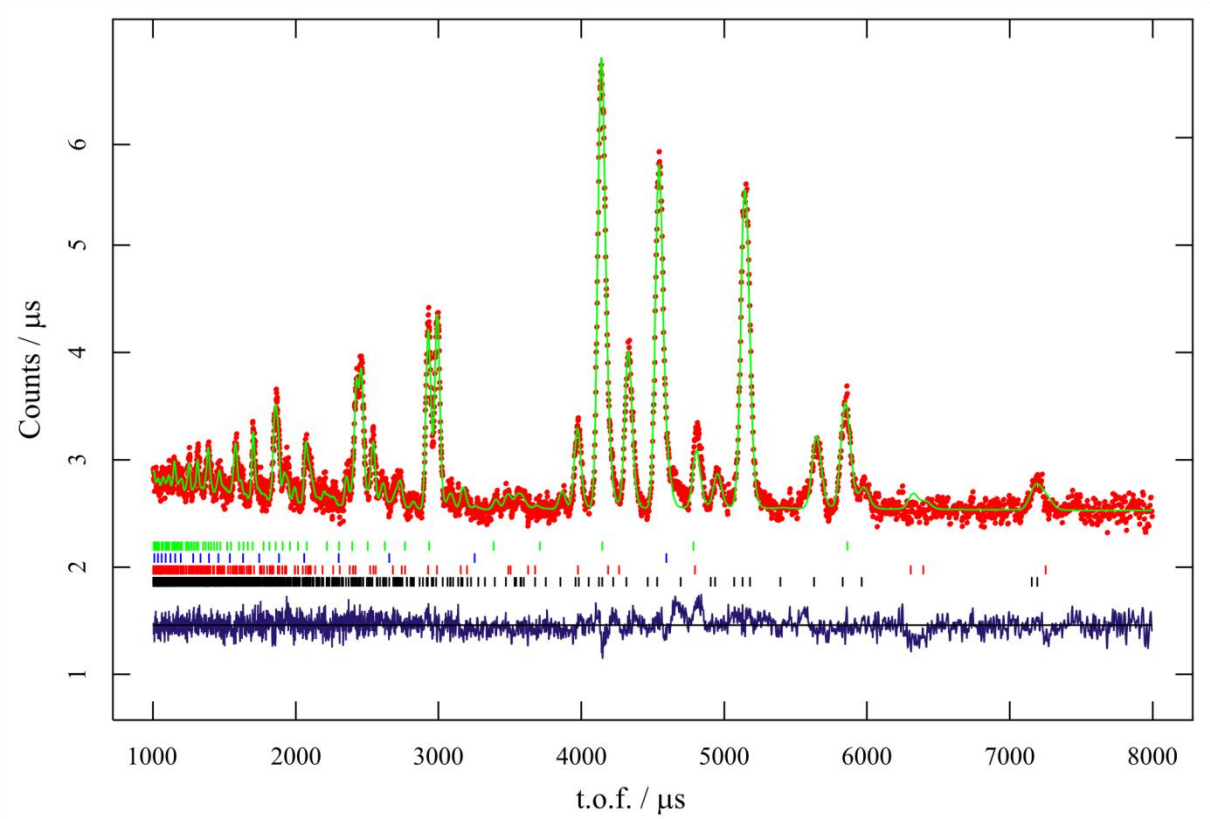

Figure 3.23 – Profile fit of low angle bank neutron diffraction data collected on $Nd_2BaCo_2O_7$ at POLARIS. R_{wp} = 3.10 %, R_p = 2.69 %. Black tick marks show reflection positions for main phase, red for Nd_2O_3, blue the vanadium can and green the perovskite $(NdBa)_{0.5}CoO_3$.

Variable temperature neutron diffraction study of $Nd_2BaCo_2O_7$

No reduction in symmetry was apparent in the diffraction patterns collected on heating $Nd_2BaCo_2O_7$. For this reason, the room temperature model developed for $Nd_2BaCo_2O_7$ in the space group *Bbcb* was used to fit all diffraction data sets. For all diffraction sets above room temperature, 29 parameters were refined: 12 background parameters, one peak shape parameter, one zero point error, one histogram scale factor, two lattice parameters, six atomic displacements and six isotropic temperature factors. The fractional occupancy of the *A*-sites was not refined above room temperature. Neither peak shapes, phase fractions nor isotropic temperature factors were included in final refinements to allow smooth convergence. As the sample was heated, peaks from the four phases refined at room temperature began to overlap to the point that at 623 K a stable refinement was not possible if these were included.

Figure 3.24 shows the thermal expansion of $Nd_2BaCo_2O_7$ as a function of temperature. No discontinuities are seen in the variation of the lattice parameters *a* and *c* on heating; and no orthorhombic splitting is observed throughout the whole range. For the purposes of refinement, the *a* and *b* lattice parameters were constrained together, however when this constraint was removed, the *a* and *b* lattice parameters remained identical within one standard error, for example see the profile fits in Figure 3.26. The refinement is not visibly improved by removing constraints, confirmed by the fitting parameters shown in Table 3.15.

Figure 3.25 shows the Co-O bond lengths as a function of temperature. Over the entire temperature range, the equatorial and bridging bond lengths (Co-O3 and Co-O1, Δ and ○ in the diagram respectively) each expand linearly. The apical bond length (Co-O2, □) remains approximately constant at 2.12 Å between room temperature and 373 K, then expands between 373 K to 623 K to a second plateau of 2.21 Å. Although this could be indicative of changes in spin state as seen in $Gd_2SrCo_2O_7$, it is not accompanied by an orthorhombic splitting of the unit cell. Unlike $Gd_2SrCo_2O_7$, measurements of magnetism on this sample were not carried out: the many impurity phases would prevent unambiguous interpretation of results.

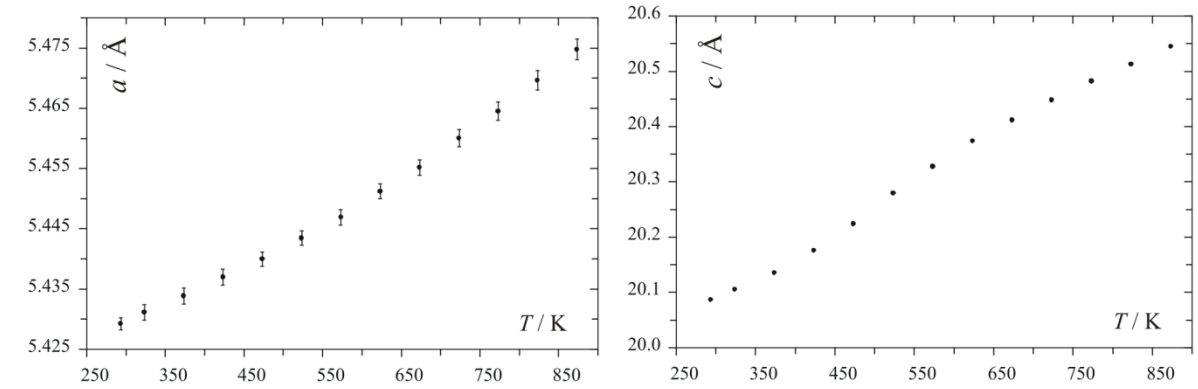

Figure 3.24 – Cell parameters extracted from refinements of the structure of $Nd_2BaCo_2O_7$ to variable temperature neutron diffraction data. Error bars show one standard error, errors in *c* lie within point size.

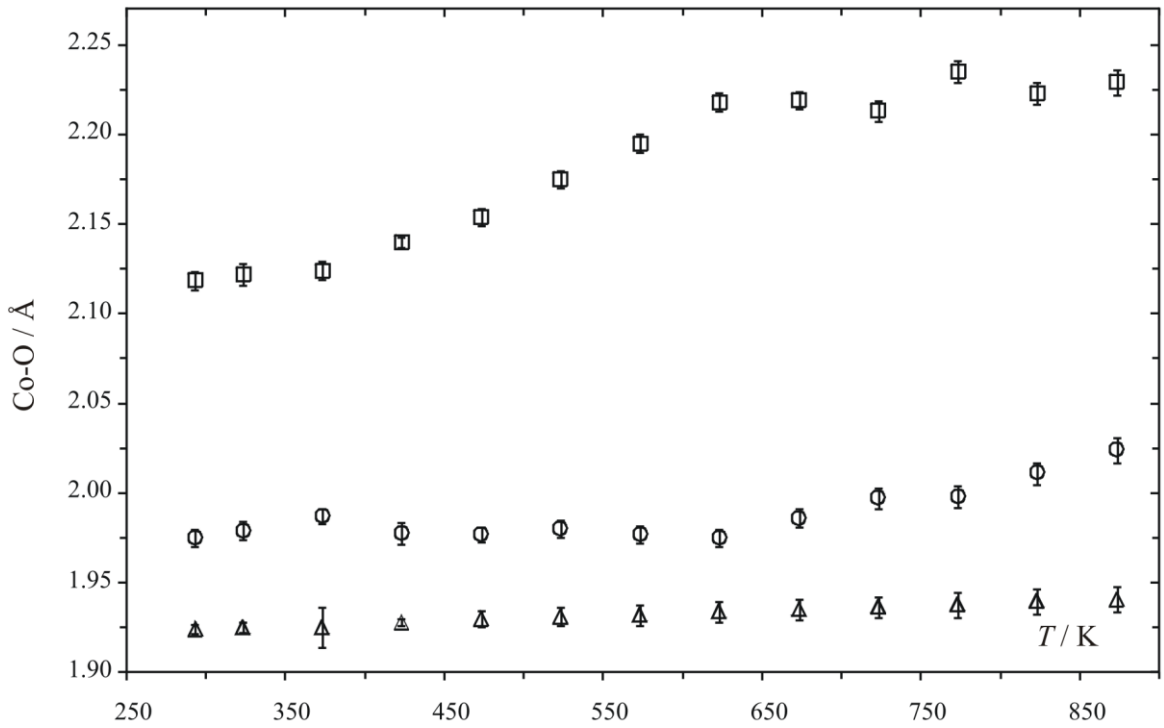

Figure 3.25 – Co-O bond lengths extracted from the refinements of variable temperature powder neutron diffraction data for $Nd_2BaCo_2O_7$. Co-O1 (○), Co-O2 (□) and Co-O3 (average of two sites, Δ) are plotted with error bars representing one standard error.

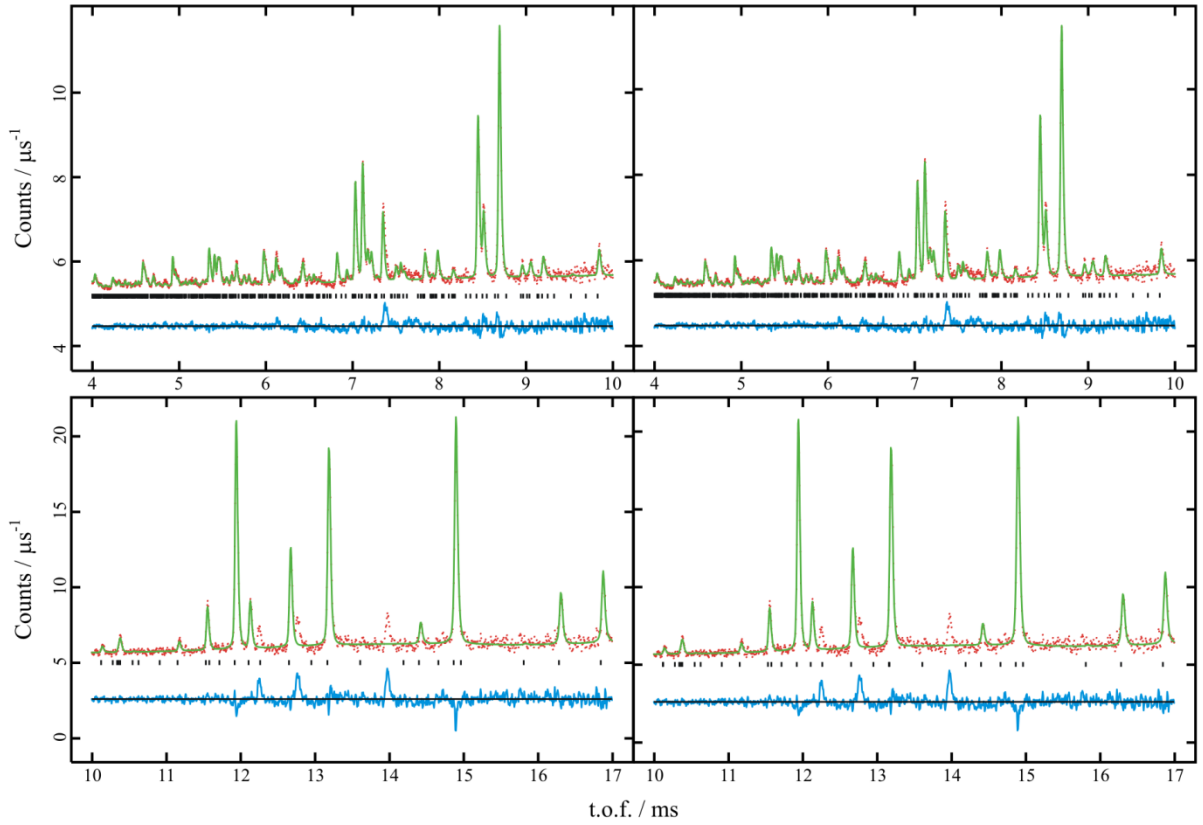

Figure 3.26 – Comparison of structural refinements for $Nd_2BaCo_2O_7$ based on 873 K neutron diffraction data with *a* constrained to *b* (left) and $a \neq b$ (right). Only the main phase is shown for clarity.

Table 3.15 – Comparison of lattice parameters and fitting values from the structural refinements based on 873 K diffraction data collected on $Nd_2BaCo_2O_7$.

	$a = b$	$a \neq b$
a	5.475 (3)	5.476 (3)
b	5.475 (3)	5.475 (3)
c	20.5449 (8)	20.5449 (8)
R_{wp}	0.96%	0.96%
R_p	2.34%	2.32%
χ^2	0.3774	0.3767

Discussion and conclusions

$Gd_2SrCo_2O_7$

An improved model has been developed for the material $Gd_2SrCo_2O_7$ based on a $\sqrt{2}a_0 \times \sqrt{2}a_0 \times c$ supercell of the $Sr_3Ti_2O_7$ structure. The structure is based on tilts of CoO_6 octahedra in the *ab* plane away from the *c* axis. The direction of the octahedral tilts changes phase by 180 ° from one bilayer to the next. This tilting appears to serve a dual purpose in the structure: the tilting allows the layer capping oxygen (blue in Figure 3.12) move away from the *c* axis, hence lengthening the short Gd-O bond length and avoiding unfavourable electronic interaction. The bond is lengthened from 2.22 Å in the *I*4/*mmm* model to 2.25 Å in $P4_2/mnm$. Additionally, this allows a lengthening of the Co-O bond to this oxygen. As the *A* site is ordered, with Sr occupying the larger 12-coordinate site and Gd the smaller nine-

coordinate, it seems that this ordering allows the structure to distort without increasing interaction between electron density associated with oxygen and strontium.

In perovskite oxides it is not unusual to observe a range of symmetries in the solid state on heating. Unlike the transition in this work, transitions tend to be to higher symmetry with increased temperature as strain in the material by accommodating *A* and *B* site cation coordination is relaxed due to thermal motion and expansion.

Other driving forces causing phase transitions to higher symmetry include charge, magnetic or spin state ordering. In this work we are examining a stochiometric Co^{3+} material, which precludes possibility of charge ordering here. Over the entire temperature range no magnetic ordering was observed, as is consistent with magnetic measurements and previous magnetic studies on this material. As discussed at the start of this chapter, as we are studying a cobalt (III) material, the possibility of spin state playing a role in the transition is a very good one. Our magnetic data agree with the findings of the 2007 thermodynamic work of Akiyama *et al*. [3] proposing an IS ground state for the material. This ion would be expected to undergo Jahn-Teller distortion, explaining the extreme apical distortion of the oxygen octahedra observed in diffraction data.

On heating then we expect an increase of some or all the spins from IS to HS. Our magnetic data, as previously discussed, supports this observation, showing an increase of unpaired electrons above the transition temperature. Diffraction data are also consistent with an increase in average Co-O bond length as would be expected with the formation of larger HS centres. Figure 3.27 shows the increase in expansion rate of the unit cell above the transition temperature, indicated by the solid vertical line.

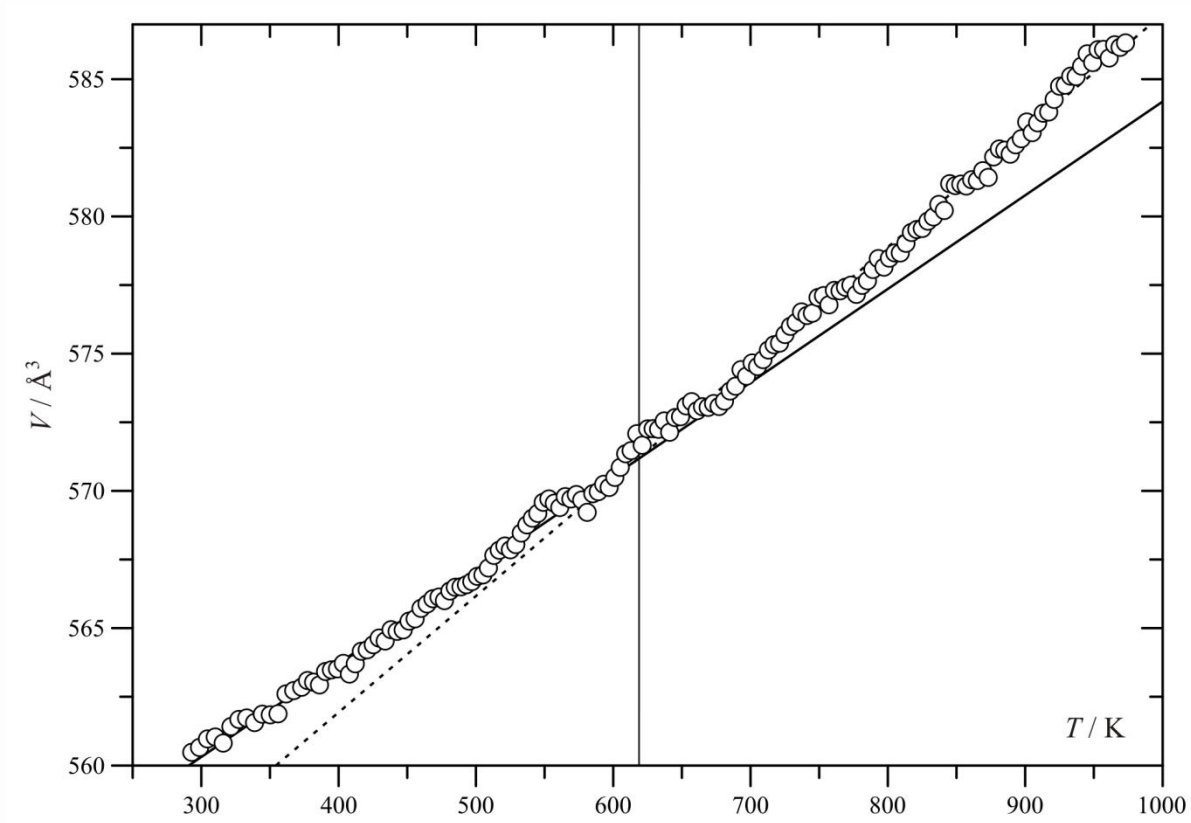

Figure 3.27 – Volume of unit cell of $^{160}Gd_2SrCo_2O_7$ extracted from powder neutron diffraction as a function of temperature. The solid line shows a linear fit to data below the transition temperature, the dashed line to data above the transition. The vertical line shows the intersection of these two lines. Errors lie within point size.

Our transition can be explained in terms of the structure distorting further to accommodate the high spin Co^{3+} centres. Determining whether this accommodation takes the form of orbital ordering leading to two distinct *a* and *b* unit cell lengths or simply an additional strain on the already compressed oxygen sublattice as observed in a number of other $A_3B_2O_7$ materials is unfortunately beyond the scope of this work. Differentiation between these situations could be determined by sufficiently high quality diffraction data, but would certainly require far better quality than available here.

$Nd_2BaCo_2O_7$

The new material $Nd_2BaCo_2O_7$ has been produced and characterised by powder diffraction methods. Neutron diffraction data collected on the material are best refined in a metrically tetragonal *Bbcb* space group: although distortion from a standard *I*4/*mmm* $Sr_3Ti_2O_7$ model is almost indistinguishable within the error bounds of the refined structure, a much improved fit to the diffraction data is achieved. When refinement is attempted in *I*4/*mmm*, the achievable fit to diffraction data is far worse, and thermal parameters extracted from the refinement are unacceptably large, especially on the oxygen site which becomes split by the distortion to *Bbcb*.

Diffraction data sets over the whole data range 293 – 873 K have been fitted by structural refinement based on the room temperature model. In all data sets the unit cell is metrically tetragonal, with no discontinuities in the expansion of the *a* or *c* cell parameter expansion over

the full temperature range. In-layer and bridging Co-O bond lengths expand linearly throughout the temperature range, however the apical bond plateaus between room temperature and 373 K at 2.12 Å, then 2.21 Å between 673 to 873 K. This may be indicative of spin crossover as previously seen for $Gd_2SrCo_2O_7$, however this is not supported by the continuous expansion of the unit cell.

Magnetic measurements were not collected on this material, as the many magnetic impurity phases would make interpreting these results highly subjective.

Comparison of $Gd_2SrCo_2O_7$ and $Nd_2BaCo_2O_7$

Both $Gd_2SrCo_2O_7$ and $Nd_2BaCo_2O_7$ can be synthesised by annealing an intimate mixture of Ln_2O_3, ACO_3 and Co_3O_4 at ~ 1473 K under flowing oxygen, and both form stochiometric bilayered Ruddlesden-Popper phases which are stable over the temperature range 300 – 1473 K. Although electronically the materials are similar, structurally they behave very differently, within the limits defined by their structure type.

At room temperature, both the space group and absolute level of octahedral distortion vary between the materials. $Nd_2BaCo_2O_7$ is isostructural with the $A_3B_2O_7$ material $Sr_3Ru_2O_7$ whose structure is discussed in detail by Shaked and Jorgensen. [4] The distortion of the ruthenium phase arises from a simple compression of the oxygen lattice caused by size mismatch between the *A*-site size and the *A*-site cation. From this we can deduce that regardless of the *A*-site ordering which we observe in $Nd_2BaCo_2O_7$, the material is behaving as an $A_3B_2O_7$ phase with a compression on the oxygen lattice of the perovskite blocks caused by the size mismatch of the octahedra and *A*-site. In $Gd_2SrCo_2O_7$, the distortion is significantly larger, and the material is isostructural with other $A_2A'MO_7$ phases such as $LnCa_2Mn_2O_7$. [7] The size of *A*-site cations are therefore linked to both the level and type of distortion observed in this structure type. This will be further discussed in later chapters.

In $Gd_2SrCo_2O_7$ a transition to orthorhombic symmetry is observed on heating above 623 K while the space group remains constant throughout the temperature range studied in $Nd_2BaCo_2O_7$. This transition corresponds to a spin crossover in the cobalt ions from IS to HS. In both $Gd_2SrCo_2O_7$ and $Nd_2BaCo_2O_7$ the cobalt octahedra are significantly apically distorted at room temperature, which in $Gd_2SrCo_2O_7$ is attributed to Jahn-Teller distortion of the IS Co (III) ions.

Magnetic data collected on a pure sample of $Nd_2BaCo_2O_7$ would provide much information on these systems: both a confirmation of the IS Co^{3+} ground state assumed based on structural evidence and support for a link between sublattice distortion and structural transition in $Gd_2SrCo_2O_7$. Unfortunately magnetic measurements were not possible in this work as all samples of $Nd_2BaCo_2O_7$ contained moderate levels of the magnetically active Nd_2O_3 and $NdCoO_3$.

References

1. L. Siwen and R. Yufang, *Mat. Res. Bull*., 1994, **29**, 993-1000
2. L. Siwen and R. Yufang, *J. Solid State Chem*., 1995, **114**, 286-288
3. K. Akiyama, H. Aoyama, N. Abe, T. Tojo, H. Kawaji and T. Atake, *J. Therm. Anal. Calorimetry*, 2005, **81**, 583-586
4. H. Shaked, J. Jorgensen, O. Chmaissem, S. Ikeda and Y. Maeno, *J. Solid State Chem*., 2000, **154**, 583-586
5. W. I. F. David, *J. Appl. Cryst*., 1986, **19**, 63-64
6. R. D. Shannon, *Acta Cryst*., 1976, **A32**, 751-758
7. P. D. Battle, J. E. Millburn, M. J. Rosseinsky, L. E. Spring and V. F. Vente, *Chem. Mater*., 1997, **9**, 3136-3143

Chapter 4 – $Gd_2SrFe_2O_7$ and related ferrates

Introduction

Materials in the series $Ln_2AFe_2O_7$ were originally reported by Samaras *et al*. [1] The material $La_2BaFe_2O_7$ was reported as a standard $Sr_3Ti_2O_7$ Ruddlesden-Popper phase, but the substituted $Tb_2BaFe_2O_7$ was reported with a then-unknown structure in the space group $P4_2/mnm$. The synthesis and structure of the material $La_2SrFe_2O_7$ was originally reported in 1971 by Brisi and Rolando, [2] and was not revisited until 1995 by Sharma *et al*. [3] The same group later reported the structures, transport properties and magnetic properties of $Ln_2SrFe_2O_7$, *Ln* = La, Nd, Gd and Dy. [4] Nishi *et al*. later reported the structure of $La_2SrFe_2O_7$, together with the $n = 1$ and $n = 3$ Ruddlesden-Popper materials and of a number of phases derived from the intercalation of water into the $n = 3$ phase. [5] In all these studies, structures of $Ln_2SrFe_2O_7$ were determined by refinement to fit X-ray powder diffraction data, and in each case the structures were reported as undistorted $Sr_3Ti_2O_7$ $I4/mmm$ isostructures.

Other works on the $Ln_2SrFe_2O_7$ series have focussed on their formation mechanism and kinetics. Two papers by Zvereva *et al*. report that, similarly to $Sr_3Ti_2O_7$, [6] formation progresses initially to a mixture of $LnFeO_3$ and $LnSrFeO_4$, then on further reaction to completion. [7-8]

In this chapter, the structures of the ferrates $La_2SrFe_2O_7$, $Nd_2SrFe_2O_7$ and $Gd_2SrFe_2O_7$ are re-examined. As in the previous chapter, the structures previously reported for these materials are based on X-ray diffraction, which will be less effective than neutron diffraction for determining the structure of materials containing both oxygens and lanthanides with much higher electron density. Variable temperature neutron diffraction data will provide an accurate structural probe for the entire temperature range.

Syntheses

Air syntheses

Lanthanide oxides were dried by heating to 1273 K overnight. After drying, required masses were measured immediately to prevent excessive formation of $Ln_2O_3.nH_2O$ and $Ln(OH)_3$. The dry Ln_2O_3 was mixed with stochiometric amounts of Fe_2O_3 and $SrCO_3$ and intimately ground. Reaction mixtures were heated overnight to 1273 K to begin the decomposition of carbonate and reaction of materials, then reground and pelletised in a 10 mm die under 14 MN. The pellets were heated to 1473 K in air for up to two weeks. For longer heating times, pellets were air quenched, reground and pelletised several times to ensure homogeneity of products.

The Ruddlesden-Popper products were brown/red powders. Products were characterised by X-ray powder diffraction and Rietveld refinement.

Oxygen-free syntheses

It is possible that in air furnaces, Fe (IV) materials can be formed from Fe (III) starting materials (for example, the Brownmillerite phase $Ca_2Fe_2O_5$). [9] To ensure that the desired stochiometric phases (rather than, for example, $Ln_2SrFe_2O_{7+\delta}$) were formed by reaction in air, several modifications to literature syntheses were carried out and the products compared.

Two additional syntheses were carried out and the lattice parameters obtained by Rietveld refinement compared to the parameters obtained by air synthesis. Products previously formed were re-pelletised and annealed under flowing nitrogen, and new materials were formed by carrying out all annealing stages under nitrogen. The formation of materials with oxygen non-stochiometry would be expected to produce materials with expanded unit cell parameters.

Lattice parameters obtained from refinements of the structures of products of these three methods were found to be the same to within one standard error, suggesting that air synthesis of these materials will not form non-stochiometric materials.

Structural study of $Ln_2SrFe_2O_7$

Variable temperature X-ray powder diffraction of $Gd_2SrFe_2O_7$

A sample of $Gd_2SrFe_2O_7$ was prepared and confirmed to be phase pure to the limits of detection by X-ray diffraction. Variable temperature powder diffraction sets were collected between room temperature and 1273 K using a D8 Advance diffractometer equipped with a SOLEX energy discriminating detector to eliminate Fe fluorescence. Sets were collected in the range 20 to 80 ° 2θ, with a step size of 0.02 ° and collection time of 3 s per step. The data are shown in Figure 4.1. Two areas of the diffractograms are shown zoomed to show the splitting clearly. The lower region shows the (105) and (110) peaks of the tetragonal phase to emphasise the splitting of the (110) group. This splitting is the same as previously observed for $Gd_2SrCo_2O_7$. The upper region shows a zoomed area containing many peaks demonstrating the splitting at 873 K. In each zoomed region, the critical 873 K data range is highlighted.

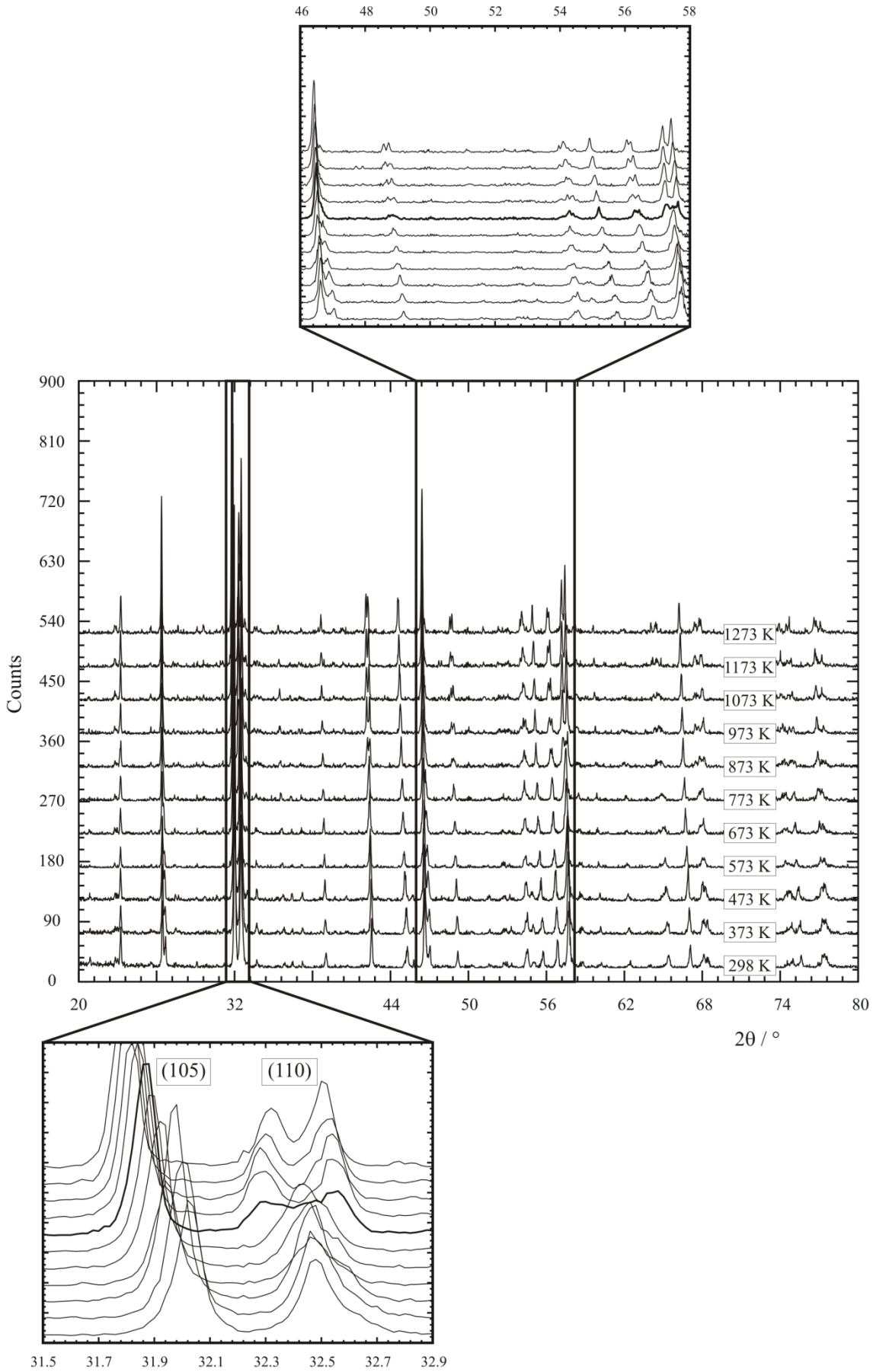

Figure 4.1 – Variable temperature powder X-ray diffraction data collected on a sample of $Gd_2SrFe_2O_7$. Lower zoomed region shows the (105) and (110) reflections of the *I*4/*mmm* parent phase, upper zoomed region shows some of the smaller peaks to emphasise splitting. The 873 K range is highlighted in each zoomed region.

Above ~ 873 K, splitting of the (110) tetragonal phase peaks is once again observed, indicative of a decrease in unit cell symmetry as previously encountered for $Gd_2SrCo_2O_7$. Once again, the structure at room temperature could be refined in the tetragonal space group *I*4/*mmm* which adequately fitted the X-ray powder diffraction. In order to accurately determine the structure, however, powder neutron diffraction data were required. The oxygen substructure is once again critical to the overall structure of the material, and this cannot be accurately determined using only X-rays.

Variable temperature neutron powder diffraction of $^{160}Gd_2SrFe_2O_7$

A sample of $^{160}Gd_2SrFe_2O_7$ was prepared and confirmed to be phase pure to the limit of detection of the Bruker D8 diffractometer with SOLEX detector. As for $^{160}Gd_2SrCo_2O_7$, the isotopic enrichment of the gadolinium oxide was 98.2 %, leaving a residual neutron absorption cross section of 830 barns.

Variable temperature powder diffraction was collected on this sample on the POLARIS medium resolution, high intensity beam line at the ISIS time-of-flight neutron source. Initial trial data sets collected demonstrated that the high absorption of the residual ^{157}Gd caused very poor counting statistics for diffraction experiments and produced very high backgrounds. For this reason, rather than collecting data sets in the same temperature range as the X-ray diffraction data, only data sets around the expected phase transition temperature were collected. Diffraction data sets are shown in Figure 4.2. The unusual shape of the background in these data sets is due to a manual linear correction for absorption applied to the data. After applying the correction, the baseline backgrounds were not horizontal, implying an overcorrection for absorption. It is possible that the percentages of different gadolinium isotopes presented in the assay were slightly inaccurate, which with the high absorptions of different isotopes corresponds to large inaccuracies in absorption calculations.

The splitting of peaks can be seen in the neutron diffraction sets (for example in the parent (200) peak group at ~ 17000 μs, labelled in the diagram), occurring at a higher temperature to that seen in the X-ray diffraction sets. The modest resolution of the POLARIS instrument may account for this observation, as the splitting is present, but less obvious.

Rather than attempt to solve the structure of $^{160}Gd_2SrFe_2O_7$ from these relatively low quality data, the structures of other ferrates showing less neutron absorption were first determined to aid the structural refinement of the analogous, and possibly isostructural, $Gd_2SrFe_2O_7$.

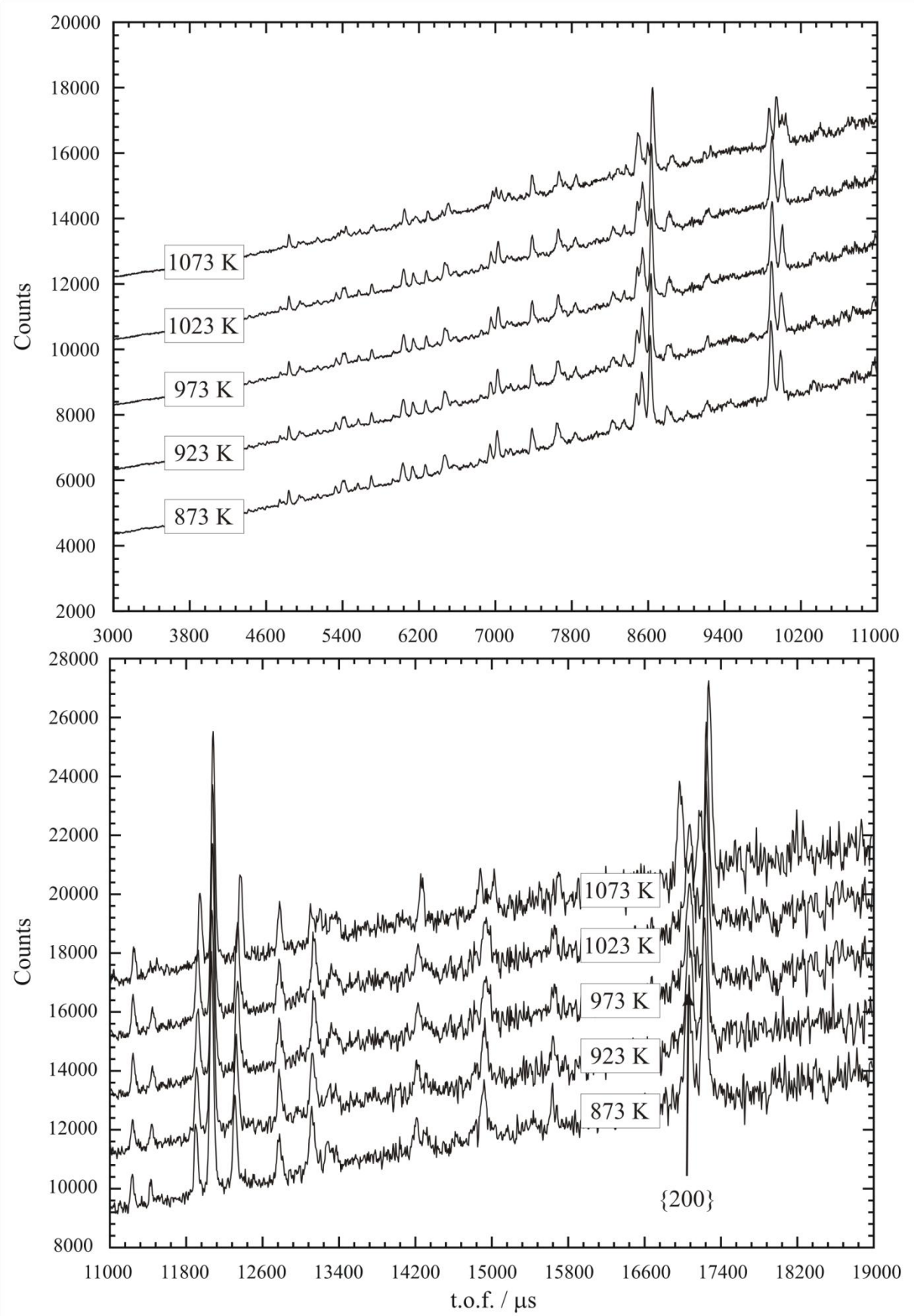

Figure 4.2 – Variable temperature powder neutron diffraction data collected on a sample of $^{160}Gd_2SrFe_2O_7$. The (200) parent peaks are emphasised to show the splitting of peaks.

Variable temperature powder neutron diffraction data on $Nd_2SrFe_2O_7$

Powder neutron diffraction data sets were collected on a sample of $Nd_2SrFe_2O_7$. The neutron absorption cross section of neodymium is small enough to allow neutron diffraction data to be collected on unenriched samples. The backscattered data collected on the POLARIS instrument at ISIS are shown in Figure 4.3. In the data set collected at 823 K, splitting is once again seen for various diffraction peaks, for example the (200) tetragonal phase peaks at ~ 17000 μs (labelled on figure).

Room temperature structure of $Nd_2SrFe_2O_7$

The room temperature diffraction data could not be modelled in *I*4/*mmm*. The model previously determined for $Gd_2SrCo_2O_7$ in *P*4$_2$/*mnm* gave a significant improvement in fitting, as shown in Figure 4.4.

Backscattered diffraction data were fitted in the range 2500 – 19000 μs in the space group *P*4$_2$/*mnm*. 35 parameters were refined: eight background parameters, one histogram scale factor, one histogram zero point error, three peak shape parameters, two lattice parameters, one fractional occupancy for the two Nd/Sr sites, eleven atomic coordinates and eight isotropic temperature factors. The profile fit is shown in Figure 4.5, and refined parameters are shown in Table 4.1. The fractional occupancy of the two *A* sites is not as well defined as for $Gd_2SrCo_2O_7$; the larger size of the Nd^{3+} ion reduces the preference of the lanthanide for the nine coordinate site.

Table 4.1 – Extracted structural parameters from refinement of room temperature structure of $Nd_2SrFe_2O_7$ in *P*4$_2$/*mnm* against powder neutron diffraction data. R_{wp} = 1.30 %, R_p = 2.93 %, χ^2 = 2.142.

Atom	*x/a*	*y/b*	*z/c*	U_{iso} / 10^{-2}Å^2	Site occupancy
Sr1	0.2604 (5)	0.2604 (5)	0	0.33 (5)	0.53(12)
Nd1	0.2604 (5)	0.2604 (5)	0	0.33 (5)	0.47(12)
Sr2	0.2642 (3)	0.2643 (3)	0.18156 (8)	0.16 (3)	0.23(6)
Nd2	0.2642 (3)	0.2643 (3)	0.18156 (8)	0.16 (3)	0.77(6)
Fe	0.2537 (3)	0.2537 (3)	0.40419 (7)	0.201 (15)	1
O1	0.7861 (5)	0.2139(5)	0	0.48 (6)	1
O2	0	0.5	0.10303 (14)	0.61 (4)	1
O3	0	0	0.1183 (2)	0.51 (6)	1
O4	0	0	0.41050 (20)	0.30 (5)	1
O5	0.2087 (4)	0.2087 (4)	0.29498 (19)	1.30 (6)	1

High temperature structure of $Nd_2SrFe_2O_7$

The 823 K neutron diffraction data set collected on $Nd_2SrFe_2O_7$ could not be adequately fitted in the tetragonal space group *P*4$_2$/*mnm*, see Figure 4.6.

The model previously developed for the high temperature orthorhombic phase in $Gd_2SrCo_2O_7$ was used to develop a model for the 823 K $Nd_2SrFe_2O_7$ phase in the space group *Bbmm*. The profile fit is shown in Figure 4.7, and the structural parameters shown in Table 4.2.

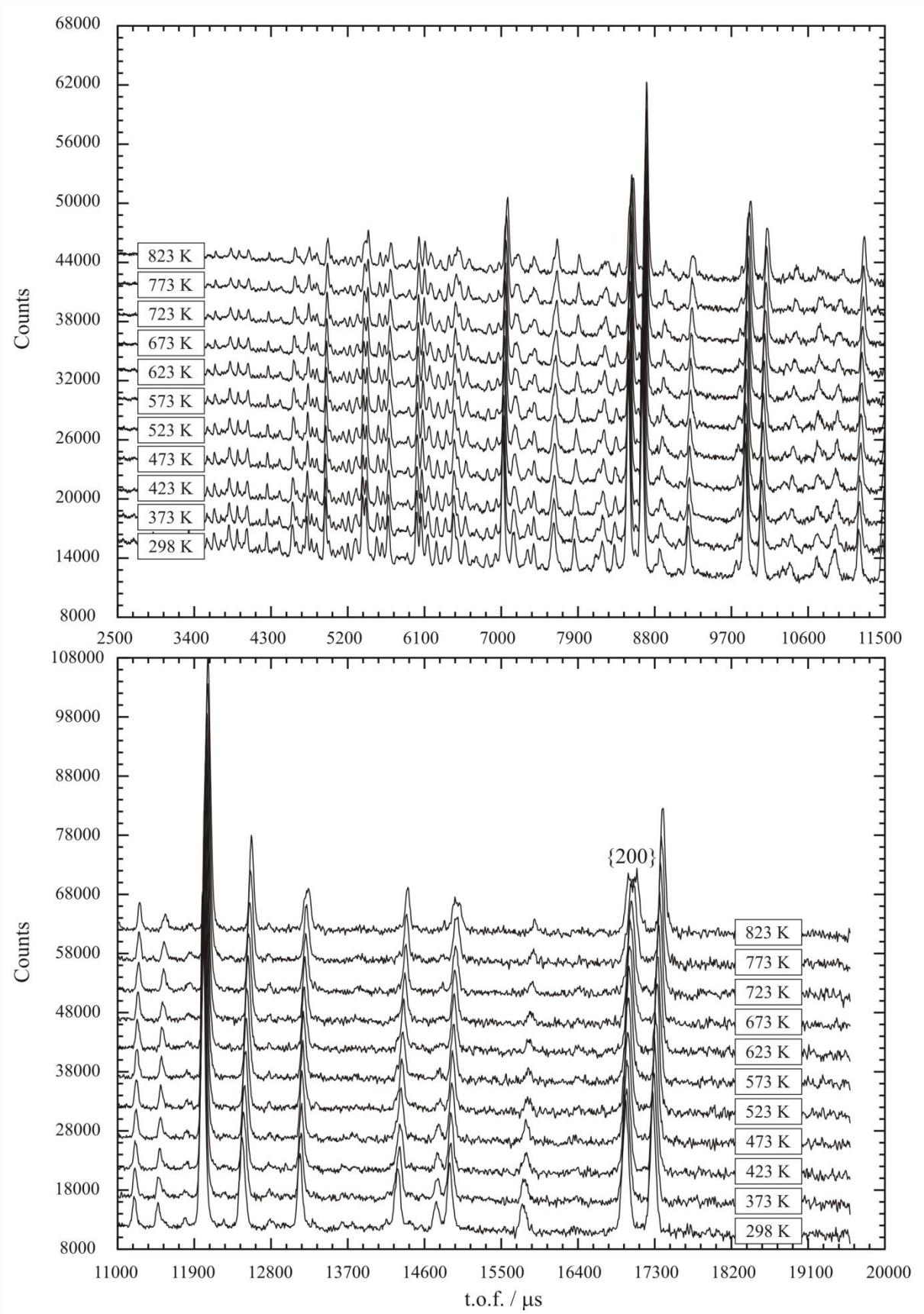

Figure 4.3 – Variable temperature neutron powder diffraction data collected on a sample of $Nd_2SrFe_2O_7$ with the backscattered detector bank at POLARIS.

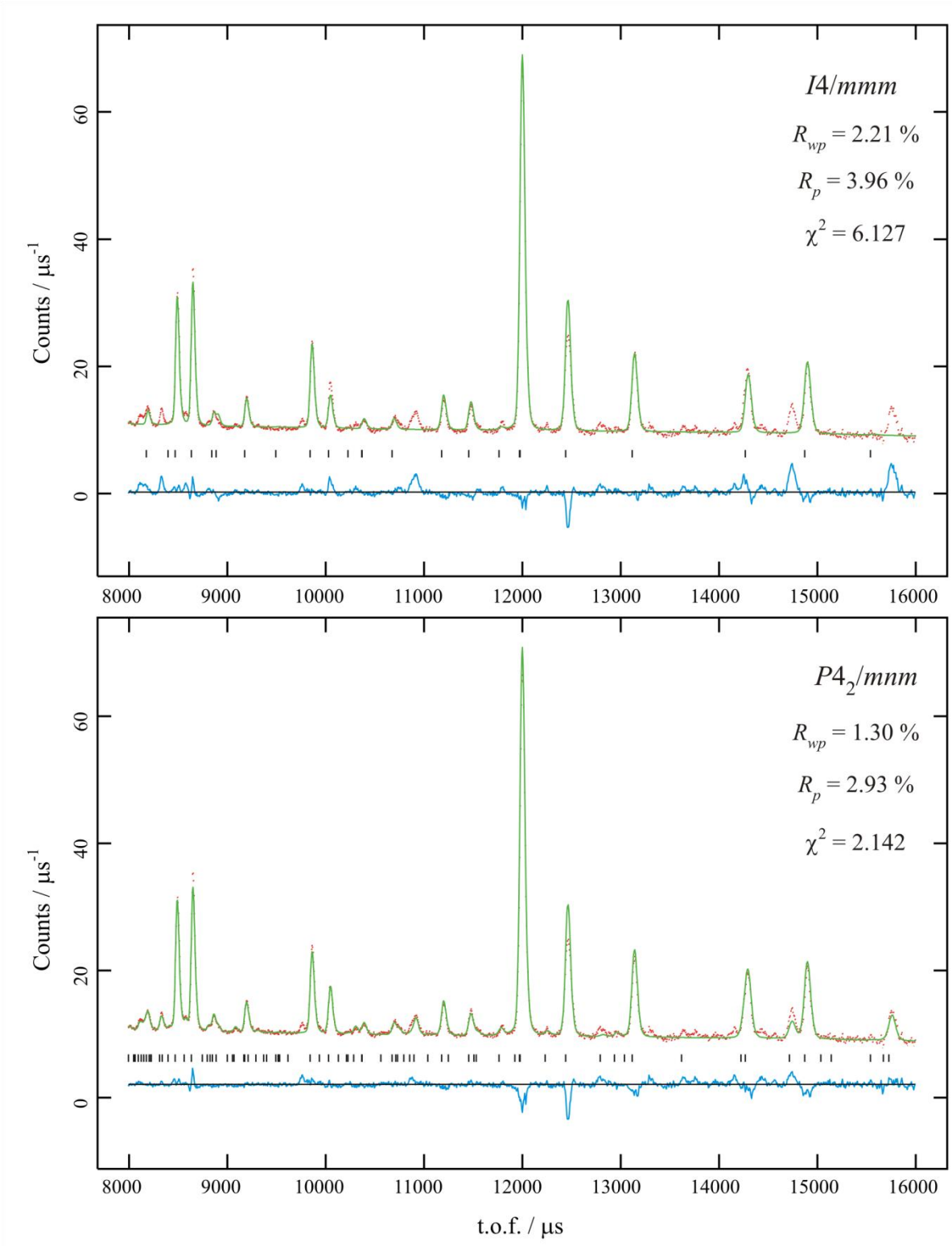

Figure 4.4 – Comparison between profile fits in *I*4/*mmm* and *P*4_2/*mnm* to room temperature neutron diffraction data collected on $Nd_2SrFe_2O_7$.

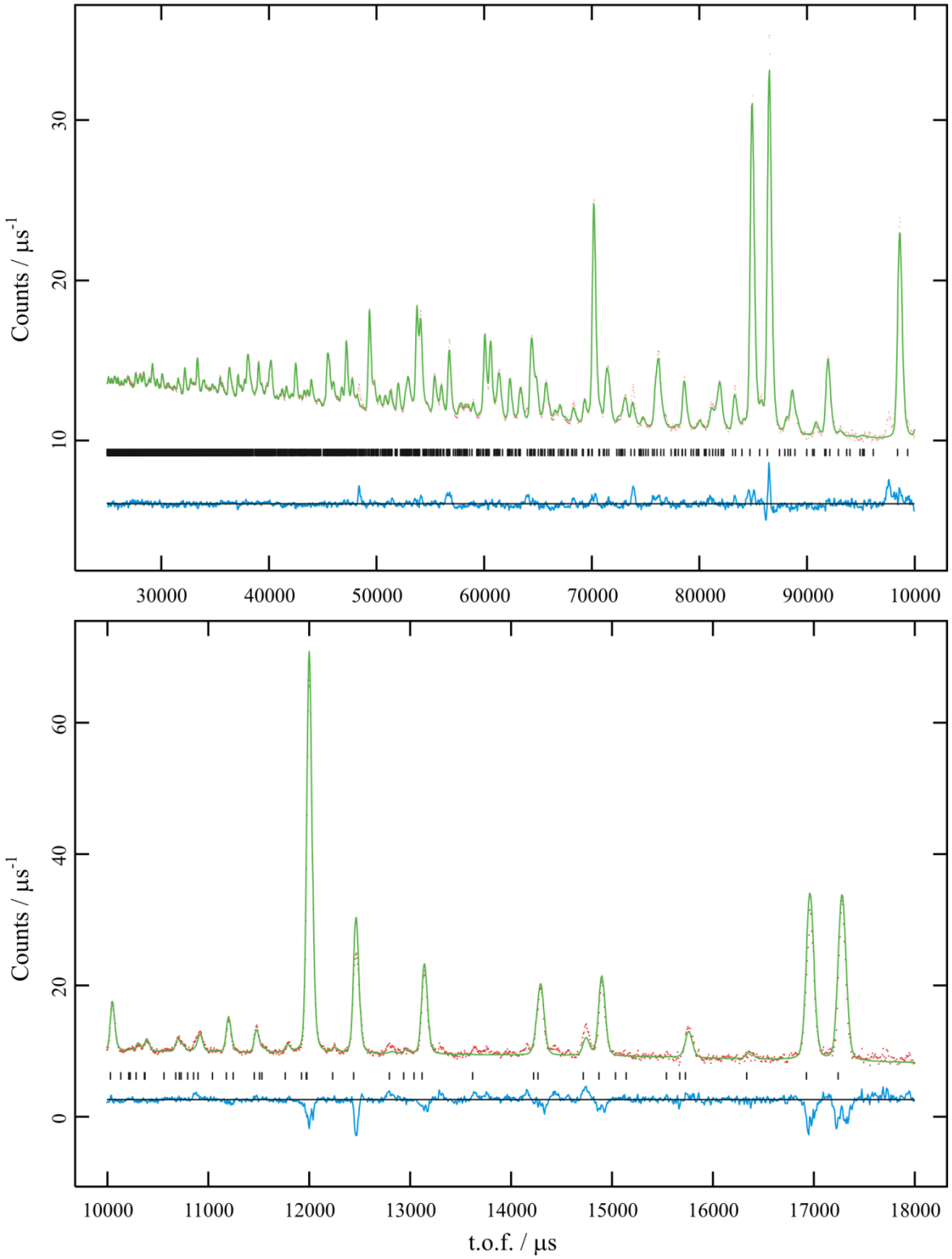

Figure 4.5 – Profile fit to the room temperature backscattered neutron diffraction data collected on $Nd_2SrFe_2O_7$ in $P4_2/mnm$. R_{wp} = 1.30 %, R_p = 2.93 %, χ^2 = 2.142.

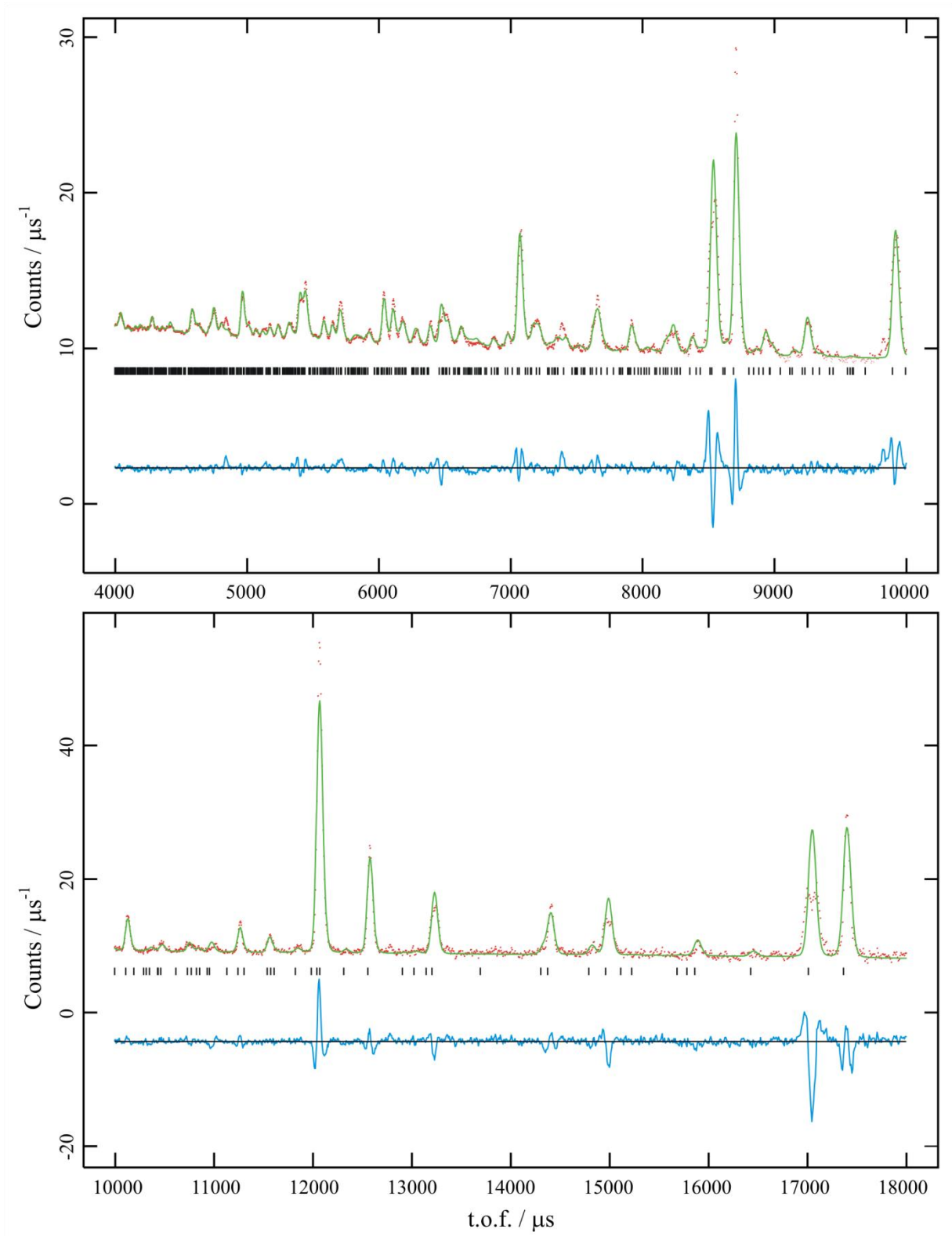

Figure 4.6 – Profile fit of 823 K neutron diffraction data collected on $Nd_2SrFe_2O_7$ in $P4_2/mnm$. (R_{wp} = 1.88 %, R_p = 3.78 %, χ^2 = 3.645)

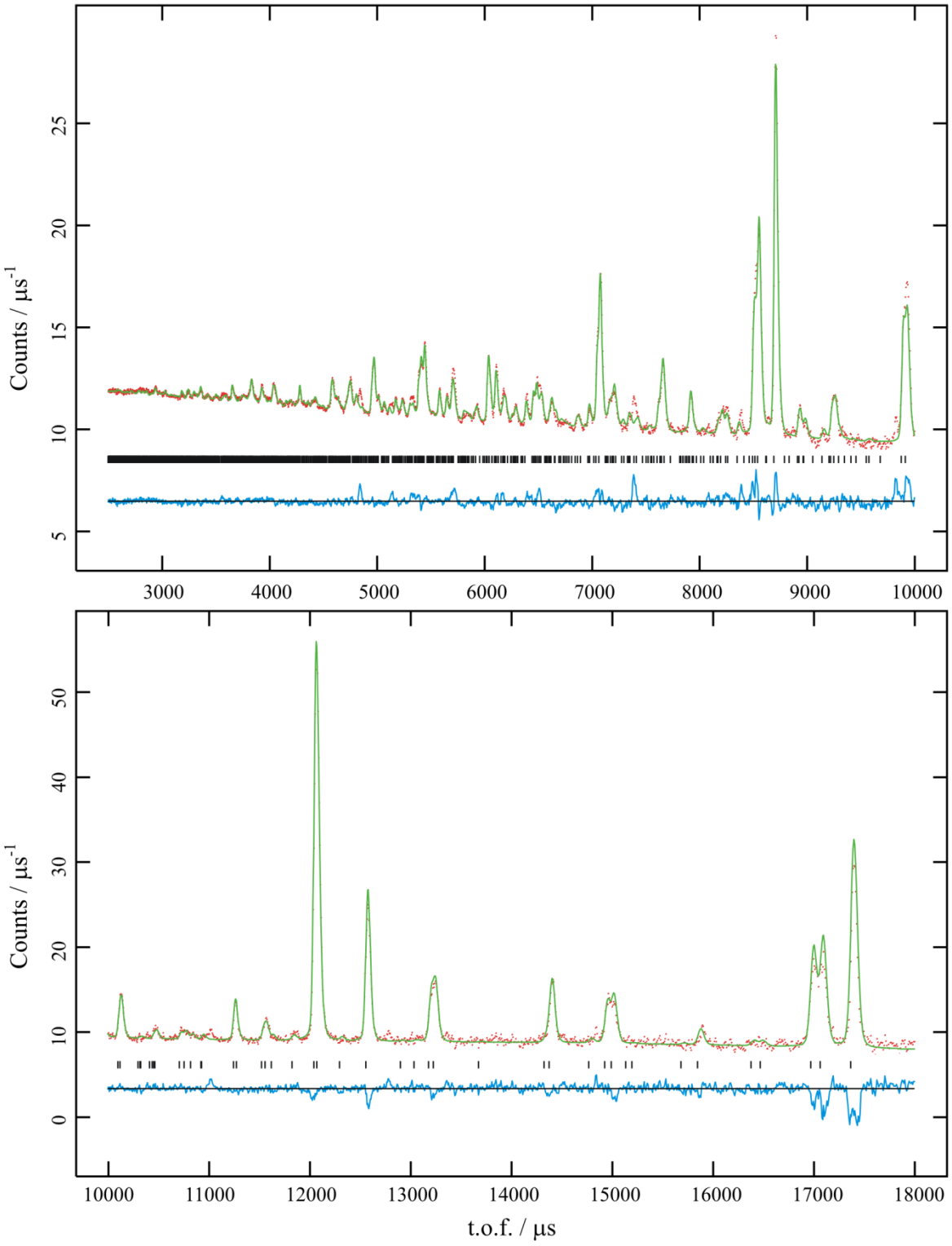

Figure 4.7 – Profile fit for the structure of $Nd_2SrFe_2O_7$ in *Bbmm*, to fit 823 K powder neutron diffraction data. R_{wp} = 1.33 %, R_p = 2.79 %, χ^2 = 1.839.

Table 4.2 – Structural parameters extracted from the refinement of 823 K diffraction data collected on $Nd_2SrFe_2O_7$ in *Bbmm*. R_{wp} = 1.33 %, R_p = 2.79 %, χ^2 = 1.839. Fractional occupancy of Nd/Sr sites fixed to those refined at room temperature.

Atom	*x/a*	*y/b*	*z/c*	U_{iso} / 10^{-2}Å^2
Sr1	0.2346(22)	0.25	0	1.47(10)
Nd1	0.2346(22)	0.25	0	1.47(10)
Sr2	0.2608(9)	0.75	0.31768(13)	0.99(5)
Nd2	0.2608(9)	0.75	0.31768(13)	0.99(5)
Fe	0.2515(9)	0.25	0.40273(12)	0.688(33)
O1	0.2836(39)	0.75	0	4.84(32)
O2	0	0	0.38743(24)	2.20(9)
O3	0.5	0	0.40494(26)	1.27(8)
O4	0.2727(22)	0.25	0.29522(35)	4.66(14)
O5	0.2346(22)	0.25	0	1.47(10)

Variable temperature refinement of $Nd_2SrFe_2O_7$

All diffraction sets were refined in the space group $P4_2/mnm$ in the range 298 – 773 K and *Bbmm* for the 823 K range. For all $P4_2/mnm$ data sets, 34 parameters were refined (the same parameters as for the room temperature refinement without refining fractional occupancy), 35 for *Bbmm* (one additional lattice parameter). The cell parameters and Fe-O bond lengths were extracted and are shown in Figure 4.8 and Figure 4.9 respectively. All extracted structural parameters are shown in Table 4.3.

Despite the large, abrupt splitting of peaks leading to a large divergence of *a* and *b* in the 823 K data set, there is no evidence for orthorhombic splitting below this temperature – refinement in *Bbmm* at 773 K gives equal *a* and *b* unit cell lengths within one standard error.

In-layer Fe-O bond lengths remain approximately constant throughout the temperature range, while bridging Fe-O bond lengths expand and apical contract. This can be interpreted as an increase in octahedral regularity as a function of temperature.

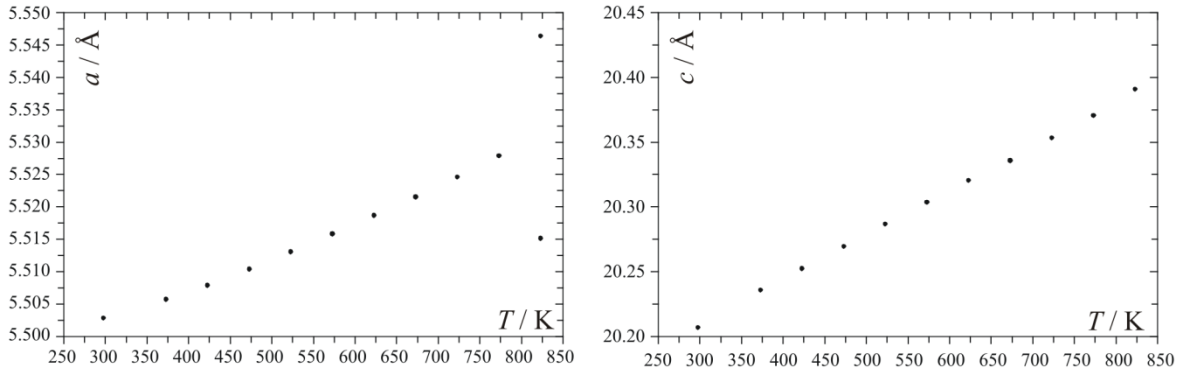

Figure 4.8 – Cell parameters extracted from the structural refinements of $Nd_2SrFe_2O_7$ based on powder neutron diffraction data sets. The *a* (lower) and *b* (upper) unit cell parameters are shown for the orthorhombic *Bbmm* phase at 823 K.

Table 4.3 – Structural parameters extracted from the refinements of powder neutron diffraction data collected on $Nd_2SrFe_2O_7$. * indicates that the parameter shown is (0.5-refined value) for comparison with $P4_2/mnm$ values.

T / K	Sr/Nd1 *x*/*a*	Sr/Nd1 U_{iso} / 10^{-2} Å^2	Sr/Nd2 *x*/*a*	Sr/Nd2 *z*/*c*	Sr/Nd2 U_{iso} / 10^{-2} Å^2	Fe *x*/*a*	Fe *z*/*c*	Fe U_{iso} / 10^{-2} Å^2
298	0.2604 (5)	0.34 (5)	0.2643 (3)	0.18156 (8)	0.16 (3)	0.2537 (3)	0.40419 (7)	0.20 (2)
373	0.2612 (5)	0.44 (5)	0.2636 (3)	0.18156 (8)	0.27 (3)	0.2532 (3)	0.40404 (7)	0.27 (2)
423	0.2605 (5)	0.56 (5)	0.2636 (3)	0.18161 (9)	0.34 (3)	0.2531 (3)	0.40392 (7)	0.31 (2)
473	0.2607 (5)	0.67 (5)	0.2631 (3)	0.18162 (9)	0.46 (3)	0.2527 (3)	0.40394 (8)	0.36 (2)
523	0.2605 (6)	0.77 (6)	0.2633 (4)	0.1818 (1)	0.51 (3)	0.2529 (3)	0.40385 (8)	0.38 (2)
573	0.2611 (6)	0.77 (6)	0.2628 (4)	0.1819 (1)	0.57 (3)	0.2528 (4)	0.40348 (9)	0.44 (2)
623	0.2610 (7)	1.00 (7)	0.2626 (4)	0.1818 (1)	0.60 (3)	0.2520 (4)	0.40360 (9)	0.50 (2)
673	0.2608 (7)	1.06 (7)	0.2632 (4)	0.1819 (1)	0.70 (4)	0.2521 (4)	0.40351 (9)	0.54 (2)
723	0.2623 (7)	1.16 (8)	0.2627 (5)	0.1818 (1)	0.71 (4)	0.2516 (4)	0.4035 (1)	0.58 (2)
773	0.2617 (9)	1.31 (9)	0.2634 (5)	0.1823 (1)	0.79 (4)	0.2515 (5)	0.4035 (1)	0.63 (3)
823	0.2654 (2)*	1.5 (1)	0.2608 (9)	0.1823 (1)*	0.99 (5)	0.2515 (9)	0.4027 (1)	0.69 (3)

T / K	O1 *x*/*a*	O1 U_{iso} / 10^{-2} Å^2	O2 *z*/*c*	O2 U_{iso} / 10^{-2} Å^2	O3 *z*/*c*	O3 U_{iso} / 10^{-2} Å^2	O4 *x*/*a*	O4 *z*/*c*	O4 U_{iso} / 10^{-2} Å^2
298	0.2139 (5)	0.48 (6)	0.1030 (1)	0.61 (4)	0.1183 (2)	0.51 (6)	0.2087 (4)	0.295 (2)	1.30 (6)
373	0.2150 (5)	0.53 (6)	0.1030 (2)	0.82 (5)	0.1179 (2)	0.52 (6)	0.2092 (4)	0.2949 (2)	1.47 (7)
423	0.2151 (5)	0.58 (6)	0.1030 (2)	0.97 (5)	0.1177 (2)	0.49 (7)	0.2097 (4)	0.2948 (2)	1.68 (7)
473	0.2154 (5)	0.68 (7)	0.1031 (2)	1.00 (6)	0.1177 (2)	0.62 (7)	0.2102 (4)	0.2949 (2)	1.75 (7)
523	0.2162 (6)	0.92 (8)	0.1033 (2)	1.17 (6)	0.1178 (3)	0.62 (8)	0.2115 (5)	0.2951 (2)	2.17 (9)
573	0.2150 (7)	1.07 (9)	0.1031 (2)	1.34 (7)	0.1177 (3)	0.68 (8)	0.2131 (6)	0.2953 (2)	2.31 (9)
623	0.2169 (7)	1.2 (1)	0.1034 (3)	1.52 (8)	0.1170 (3)	0.9 (1)	0.2126 (6)	0.2949 (2)	2.25 (9)
673	0.2159 (8)	1.5 (1)	0.1034 (3)	1.68 (9)	0.1168 (3)	0.8 (1)	0.2135 (7)	0.2954 (3)	2.6 (1)
723	0.2165 (8)	1.7 (1)	0.1036 (3)	1.8 (1)	0.1170 (4)	0.9 (1)	0.2139 (7)	0.2955 (3)	2.7 (1)
773	0.216 (1)	1.6 (1)	0.1039 (4)	1.9 (1)	0.1166 (4)	1.1 (1)	0.2144 (9)	0.2952 (3)	3.0 (1)
823	0.2164 (4)*	4.8 (3)	0.1126 (2)	2.20 (9)	0.0951 (3)*	1.3 (8)	0.273 (2)	0.2952 (4)	4.7 (1)

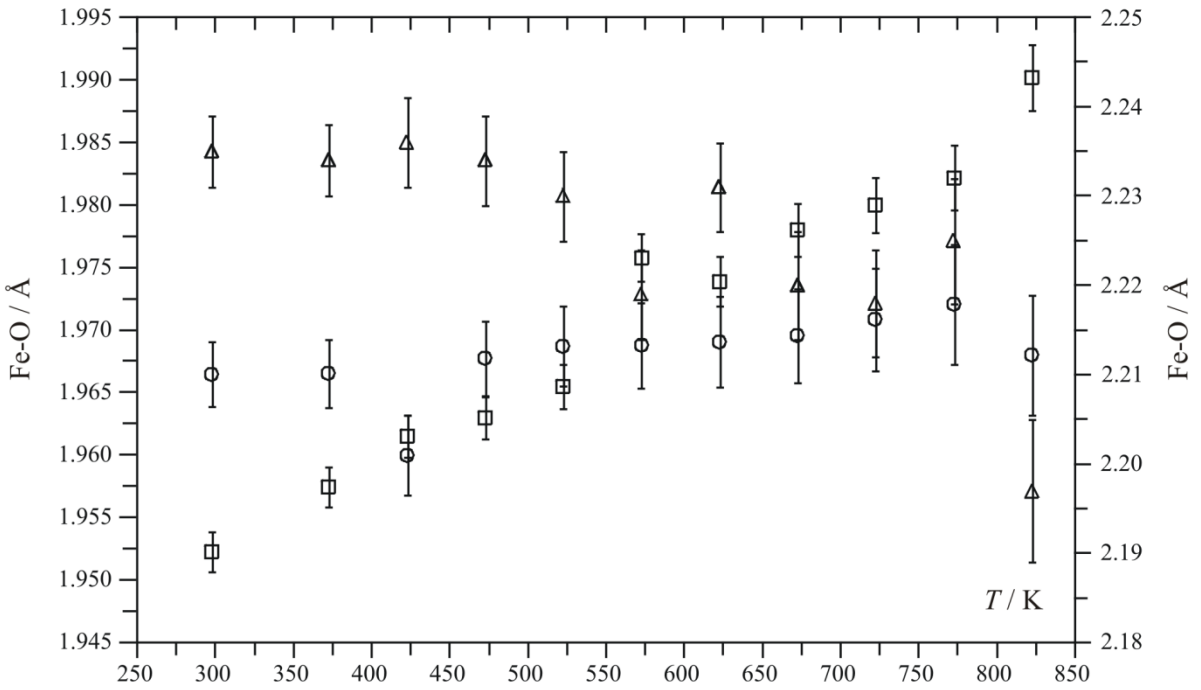

Figure 4.9 – Fe-O bond lengths extracted from the refinements of diffraction data collected on $Nd_2SrFe_2O_7$. ○ shows equatorial Fe-O (average of each in-layer Fe-O distance), □ shows bridging Fe-O, and Δ shows apical Fe-O (on right-hand axis). Error bars show one standard error.

Variable temperature refinement of $La_2SrFe_2O_7$

Variable temperature powder neutron diffraction data were collected on a sample of $La_2SrFe_2O_7$ in the temperature range 298 to 1073 K on the POLARIS instrument at ISIS. The backscattered diffraction data are shown in Figure 4.10.

Once again, the room temperature neutron diffraction data collected on a sample of $La_2SrFe_2O_7$ could not be fitted with an *I*4/*mmm* structural model. Additionally, when a $P4_2/mnm$ model based on the structure derived for $Nd_2SrFe_2O_7$ was used, several peaks were not fitted. By including additional impurity phases ($LaFeO_3$ and $LaSrFeO_4$) in the refinement, these peaks were adequately fitted – the relatively high levels of impurities suggest that the reaction did not go to completion, forming intermediates as discussed by Zvereva. [7] To fit room temperature data 60 parameters were refined: one histogram scale factor, twelve background parameters and zero point error; one scale factor, two atomic coordinates, four isotropic temperature factors, three peak shape parameters and two cell parameters for the $LaSrFeO_4$ phase; one scale factor, one peak parameter, three cell parameters and four isotropic temperature factors for $LaFeO_3$; eleven atomic coordinates, eight isotropic temperature factors, one fractional occupancy, three peak shape parameters and two cell parameters for the main phase. The profile fit to the room temperature diffraction data is shown in Figure 4.11, and the structural parameters extracted from the main phase shown in Table 4.4. Again, the increased size of the La^{3+} explains the more random *A*-site cation distribution (that is, closer to 2:1 La:Sr over each site).

Unlike the other $Ln_2SrFe_2O_7$ materials, no peak splitting is observed over the entire temperature range. All data sets could be fitted using a structural model in the tetragonal space group $P4_2/mnm$. 34 cell parameters were refined for all higher temperature data sets – the same parameters as for the refinement of $Nd_2SrFe_2O_7$. The impurity phases were refined independently of the final refinement at each temperature.

The extracted cell parameters and bond lengths are shown in Figure 4.12 and Figure 4.13, and the extracted structural parameters shown in Table 4.5. Again, in-layer and apical bond lengths remain approximately stable over the temperature range, while the bridging bond expands, producing a more regular FeO_6 octahedron.

Table 4.4 – Structural parameters extracted from the refinement of the room temperature structure of $La_2SrFe_2O_7$. $a = b = 5.52536$ (14) Å, $c = 20.4951$ (6) Å.

Name	x / a	y / b	z / c	U_{iso} / 10^{-2} Å^2	Fractional occupancy
Sr1	0.2577 (7)	0.2577 (7)	0	0.36 (7)	0.61 (9)
La1	0.2577 (7)	0.2577 (7)	0	0.36 (7)	0.39 (9)
Sr2	0.2591 (5)	0.2591 (5)	0.18182 (10)	0.38 (4)	0.19 (4)
La2	0.2591 (5)	0.2591 (5)	0.18182 (10)	0.38 (4)	0.81 (4)
Fe	0.2509 (5)	0.2509 (5)	0.40423 (10)	0.24 (2)	1
O6	0.7813 (9)	0.2187 (9)	0	1.07 (12)	1
O7	0	0.5	0.09936 (23)	0.63 (6)	1
O8	0	0	0.11009 (32)	0.55 (10)	1
O9	0	0	0.41470 (28)	0.23 (9)	1
O10	0.2210 (6)	0.2210 (6)	0.29805 (23)	1.21 (8)	1

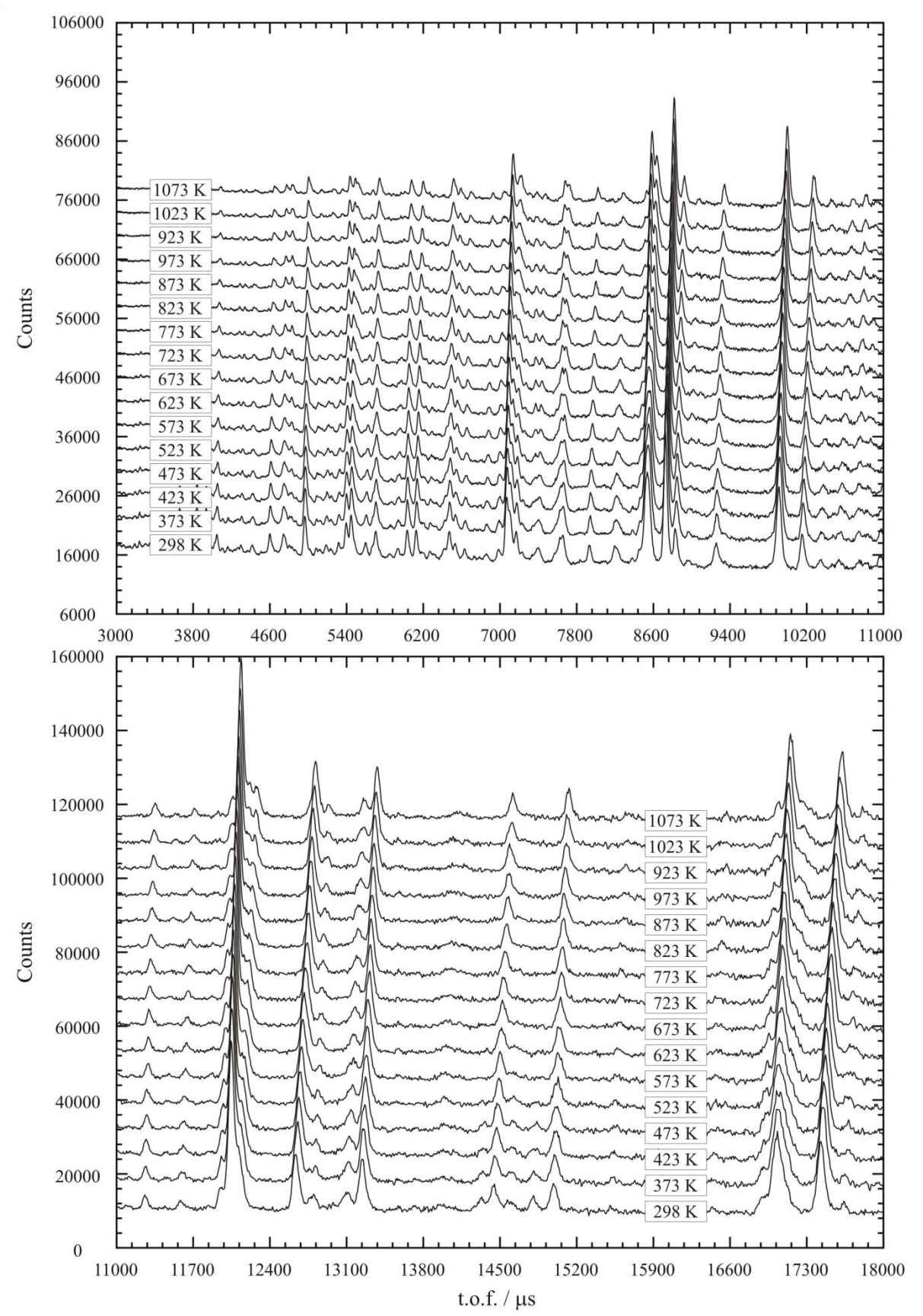

Figure 4.10 – Variable temperature powder neutron diffraction sets collected on a sample of $La_2SrFe_2O_7$.

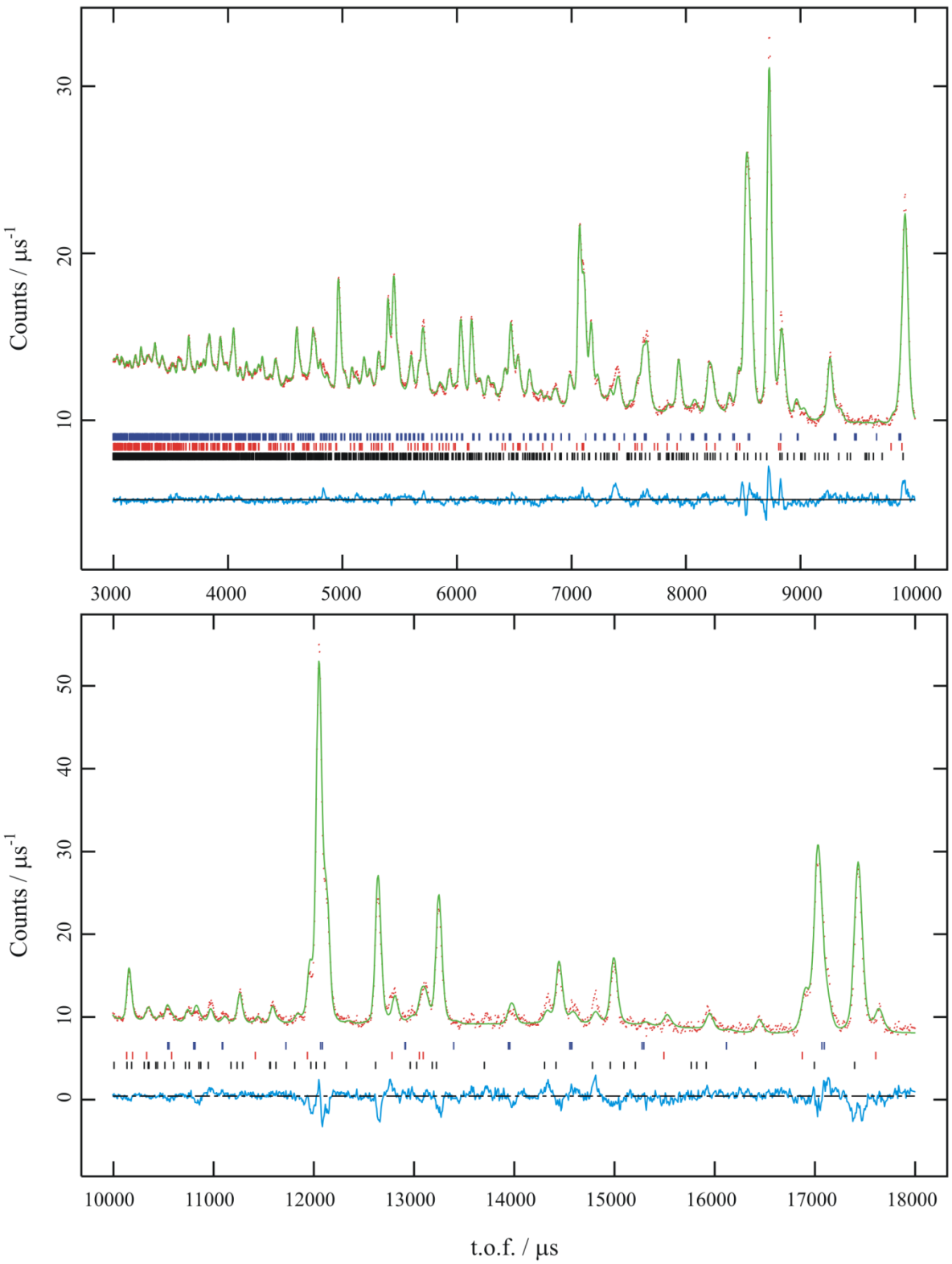

Figure 4.11 – Profile fit of room temperature structure of $La_2SrFe_2O_7$ against powder neutron diffraction data. Black tick marks show reflection positions for the main phase, red tick marks $LaSrFeO_4$ and blue tick marks $LaFeO_3$. R_{wp} = 1.32 %, R_p = 2.95 %, χ^2 = 1.847.

Table 4.5 – Structural parameters extracted from refinements based on powder neutron diffraction data collected on $La_2SrFe_2O_7$.

T / K	Sr/Nd1 *x*/*a*	Sr/Nd1 U_{iso} / 10^{-2} Å^2	Sr/Nd2 *x*/*a*	Sr/Nd2 *z*/*c*	Sr/Nd2 U_{iso} / 10^{-2} Å^2	Fe *x*/*a*	Fe *z*/*c*	Fe U_{iso} / 10^{-2} Å^2	O1 *x*/*a*	O1 U_{iso} / 10^{-2} Å^2
298	0.2618 (10)	0.42 (10)	0.2569 (8)	0.18176 (15)	1.16 (6)	0.2522 (7)	0.40315 (13)	0.64 (3)	0.2135 (12)	1.39 (16)
373	0.2624 (11)	0.53 (9)	0.2565 (9)	0.18194 (16)	1.32 (5)	0.2528 (7)	0.40297 (13)	0.74 (4)	0.2156 (15)	2.3 (2)
423	0.2630 (11)	0.55 (9)	0.2563 (9)	0.18185 (16)	1.38 (5)	0.2523 (8)	0.40285 (13)	0.82 (4)	0.2175 (18)	2.8 (3)
473	0.2625 (13)	0.74 (11)	0.2559 (10)	0.18213 (17)	1.48 (5)	0.2525 (9)	0.40286 (15)	0.88 (4)	0.219 (2)	3.1 (3)
523	0.2605 (15)	0.87 (11)	0.2538 (12)	0.18214 (17)	1.62 (5)	0.2515 (11)	0.40264 (14)	0.96 (4)	0.225 (3)	4.3 (4)
573	0.2553 (17)	1.12 (10)	0.2568 (13)	0.18209 (17)	1.69 (6)	0.2526 (8)	0.40235 (13)	1.05 (5)	0.220 (3)	4.7 (5)
623	0.2578 (17)	0.54 (11)	0.2542 (14)	0.18211 (17)	1.00 (5)	0.2505 (10)	0.40218 (13)	0.34 (4)	0.236 (4)	4.3 (4)
673	0.2572 (18)	1.27 (11)	0.2537 (15)	0.18185 (17)	1.93 (6)	0.2512 (10)	0.40228 (13)	1.14 (4)	0.222 (3)	4.8 (5)
723	0.2526 (19)	1.61 (13)	0.2553 (15)	0.18189 (17)	1.98 (6)	0.2500 (10)	0.40261 (14)	1.31 (5)	0.220 (3)	3.8 (4)
773	0.2505 (19)	2.10 (15)	0.2591 (13)	0.18208 (17)	1.89 (7)	0.2516 (9)	0.40260 (15)	1.41 (5)	0.211 (2)	4.1 (4)
823	0.2516 (20)	2.36 (17)	0.2588 (15)	0.18217 (18)	2.03 (7)	0.2516 (10)	0.40268 (16)	1.55 (5)	0.220 (3)	4.2 (4)
873	0.2517 (18)	2.88 (19)	0.2586 (15)	0.18189 (18)	2.11(7)	0.2519 (10)	0.40291 (16)	1.60 (5)	0.220 (2)	3.8 (4)
923	0.2522 (18)	3.11 (20)	0.2593 (15)	0.18186 (18)	2.17 (8)	0.2515 (10)	0.40291 (17)	1.73 (6)	0.220 (2)	4.1 (4)
973	0.2530 (20)	3.04 (21)	0.2592 (15)	0.18188 (19)	2.21 (9)	0.2522 (10)	0.40299 (18)	1.80 (6)	0.217 (2)	4.0 (4)
1023	0.2502 (18)	3.45 (22)	0.2562 (16)	0.18201 (19)	2.38 (8)	0.2506 (10)	0.40331 (18)	1.88 (6)	0.228 (2)	3.5 (4)
1073	0.2559 (18)	2.74 (20)	0.2517 (14)	0.18159 (19)	2.56 (8)	0.2513 (11)	0.40288 (17)	1.90 (6)	0.221 (3)	3.9 (4)

T / K	O2 *z*/*c*	O2 U_{iso} / 10^{-2} Å^2	O3 *z*/*c*	O3 U_{iso} / 10^{-2} Å^2	O4 / *z*/*c*	O4 U_{iso} / 10^{-2} Å^2	O5 / *x*/*a*	O5 *z*/*c*	O4 U_{iso} / 10^{-2} Å^2
298	0.0994 (3)	0.98 (8)	0.1151 (5)	1.49 (18)	0.4150 (3)	0.58 (12)	0.2214 (11)	0.2963 (3)	2.49 (14)
373	0.0993 (3)	1.04 (9)	0.1155 (5)	1.60 (19)	0.4142 (4)	0.88 (15)	0.2237 (13)	0.2961 (3)	2.95 (16)
423	0.0990 (3)	1.14 (10)	0.1154 (5)	1.65 (20)	0.4142 (4)	0.95 (16)	0.2248 (14)	0.2959 (4)	3.15 (17)
473	0.0990 (3)	1.08 (10)	0.1142 (6)	1.9 (2)	0.4146 (5)	1.38 (19)	0.2249 (15)	0.2957 (4)	3.34 (18)
523	0.0992 (3)	0.90 (9)	0.1141 (7)	2.7 (3)	0.4147 (5)	1.8 (2)	0.2251 (16)	0.2956 (4)	3.42 (19)
573	0.0988 (3)	0.87 (8)	0.1138 (6)	2.5 (2)	0.4155 (6)	2.3 (3)	0.2266 (17)	0.2955 (4)	3.74 (20)
623	0.0990 (4)	0.54 (10)	0.1119 (7)	1.6 (2)	0.4144 (5)	0.54 (18)	0.2231 (14)	0.2953 (4)	2.28 (18)
673	0.0979 (3)	1.23 (9)	0.1130 (6)	2.1 (2)	0.4152 (6)	2.7 (2)	0.2275 (19)	0.2956 (4)	4.05 (20)
723	0.0982 (3)	1.27 (9)	0.1134 (6)	2.6 (2)	0.4148 (7)	3.0 (2)	0.2276 (20)	0.2957 (4)	4.1 (2)
773	0.0980 (3)	1.21 (9)	0.1103 (7)	2.6 (3)	0.4175 (8)	4.1 (3)	0.233 (2)	0.2953 (4)	4.45 (20)
823	0.0982 (3)	1.14 (9)	0.1097 (7)	2.9 (3)	0.4172 (8)	4.8 (3)	0.230 (2)	0.2949 (4)	4.36 (2)
873	0.0976 (3)	1.37 (10)	0.1109 (7)	2.6 (3)	0.4163 (9)	4.8 (3)	0.228 (2)	0.2951 (4)	4.25 (2)
923	0.0972 (3)	1.40 (10)	0.1102 (8)	2.6 (3)	0.4169 (9)	5.7 (4)	0.228 (3)	0.2951 (5)	4.3 (2)
973	0.0968 (4)	1.53 (10)	0.1113 (8)	2.4 (3)	0.4157 (10)	5.8 (4)	0.228 (3)	0.2953 (5)	4.5 (2)
1023	0.0968 (4)	1.74 (11)	0.1138 (7)	2.3 (3)	0.4132 (10)	4.5 (3)	0.226 (3)	0.2955 (5)	4.6 (2)
1073	0.0971 (4)	2.16 (13)	0.1160 (6)	2.9 (4)	0.4105 (8)	3.1 (3)	0.222 (2)	0.2959 (5)	4.4 (2)

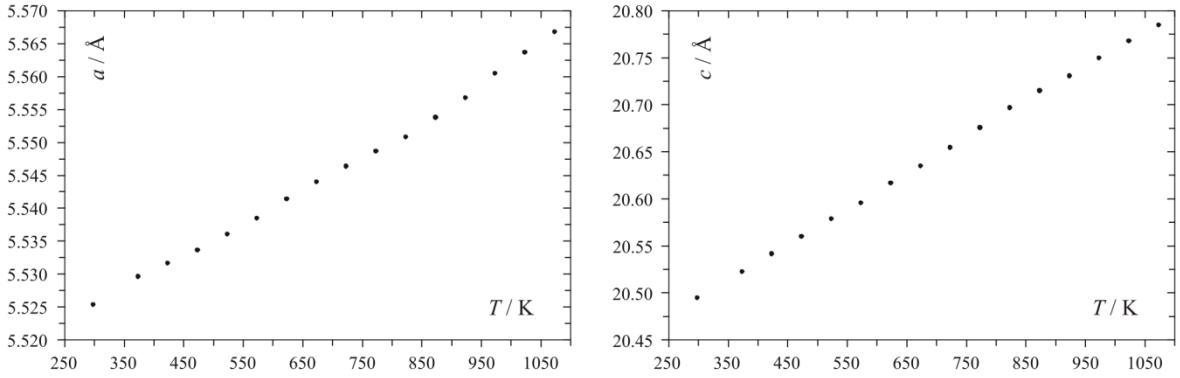

Figure 4.12 – Cell parameters extracted from structural refinements in $P4_2mnm$ based on neutron diffraction data collected on $La_2SrFe_2O_7$.

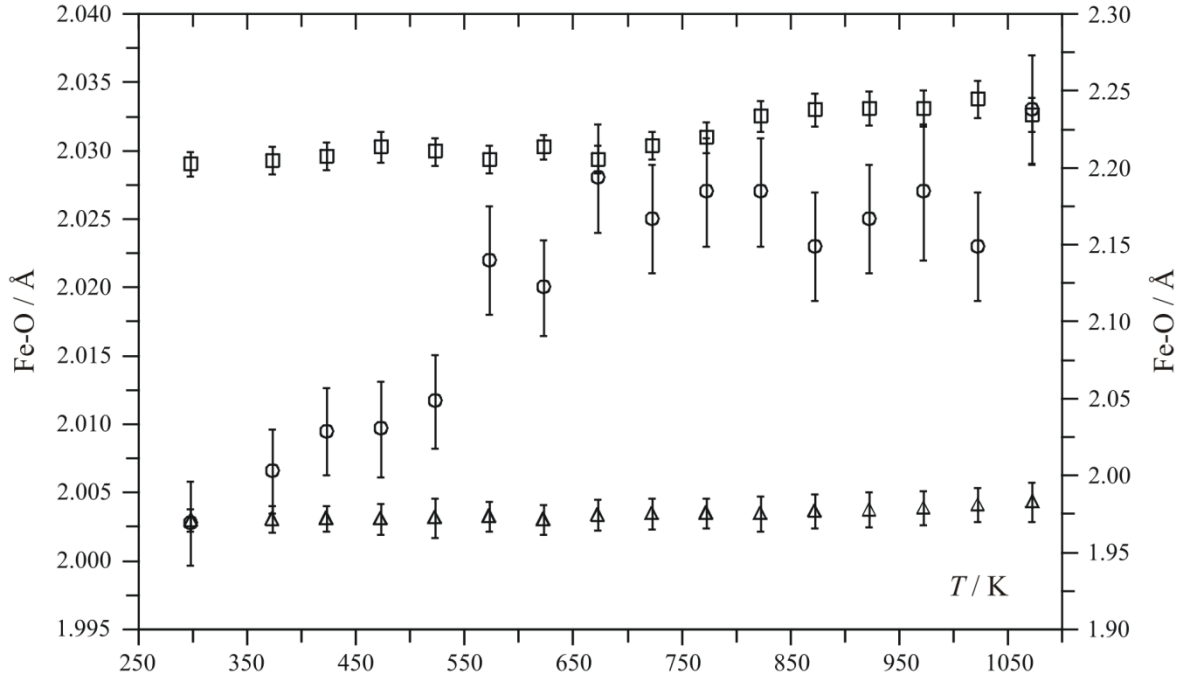

Figure 4.13 – Fe-O bond lengths extracted from structural refinement of $La_2SrFe_2O_7$ in $P4_2/mnm$ based on powder neutron diffraction data. Bridging Fe-O is shown as ○, in-layer as Δ and apical as □ (corresponding to the right-hand axis). Error bars show one standard error.

$Gd_2SrFe_2O_7$

With the structures of $Nd_2SrFe_2O_7$ and $La_2SrFe_2O_7$ successfully refined in $P4_2/mnm$ (*Bbmm* for orthorhombic high temperature phases), the starting model for the gadolinium phase was created based on these models.

All data sets in the range 298 – 1023 K were modelled with structures based on the $P4_2/mnm$ phases of $Nd_2SrFe_2O_7$ and $La_2SrFe_2O_7$. The 1073 K data set was fitted by structural refinement in *Bbmm*. In all $P4_2/mnm$ data sets, 34 parameters were refined as in the other ferrate refinements, with one additional lattice parameter for the *Bbmm* data set and one fractional occupancy at room temperature. At room temperature a linear absorption parameter was refined to compensate for the manual overcorrection of the data. This was refined independently of other parameters and fixed for all other data sets. The room temperature and 1073 K refinements are shown in Figure 4.14 and Figure 4.15.

Although impurity phases were present in the material ($GdFeO_3$ and $GdSrFeO_4$ identified by powder neutron diffraction, not detectable by X-ray diffraction), these were not included in the refinement as the refinement became very unstable on their inclusion. The low quality of the data may have been responsible for this.

The extracted structural parameters for all refinements are shown in Table 4.6. Cell parameters and Fe-O bond lengths are shown in Figure 4.16 and Figure 4.17.

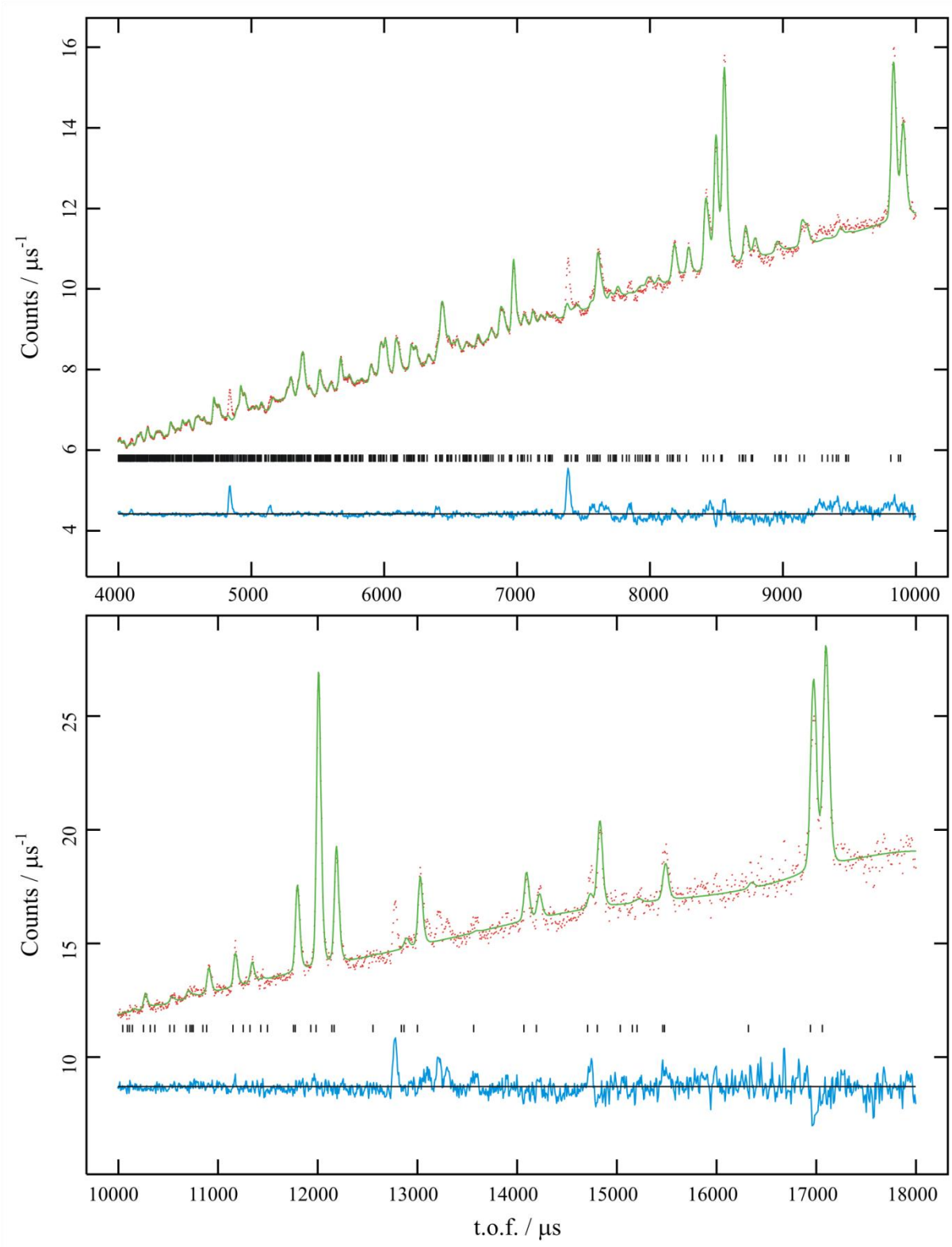

Figure 4.14 – Profile fit of room temperature data on $^{16O}Gd_2SrFe_2O_7$ in $P4_2/mnm$. R_{wp} = 0.94 %, R_p = 1.68 %, χ^2 = 2.653.

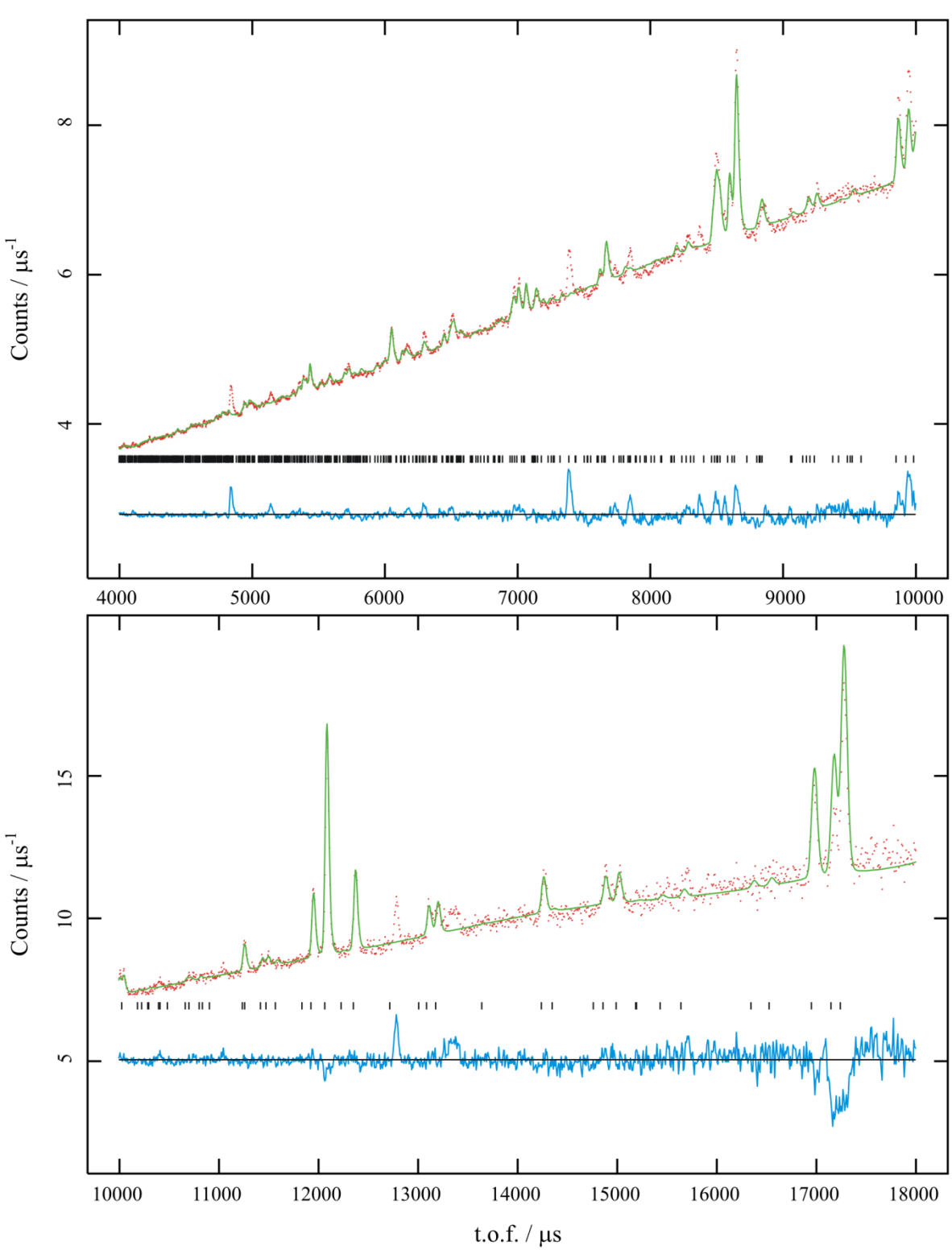

Figure 4.15 – Profile fit of the structure of $^{160}Gd_2SrFe_2O_7$ at 1073 K in *Bbmm* to powder neutron diffraction data. R_{wp} = 1.00 %, R_p = 2.07 %, χ^2 = 0.9402.

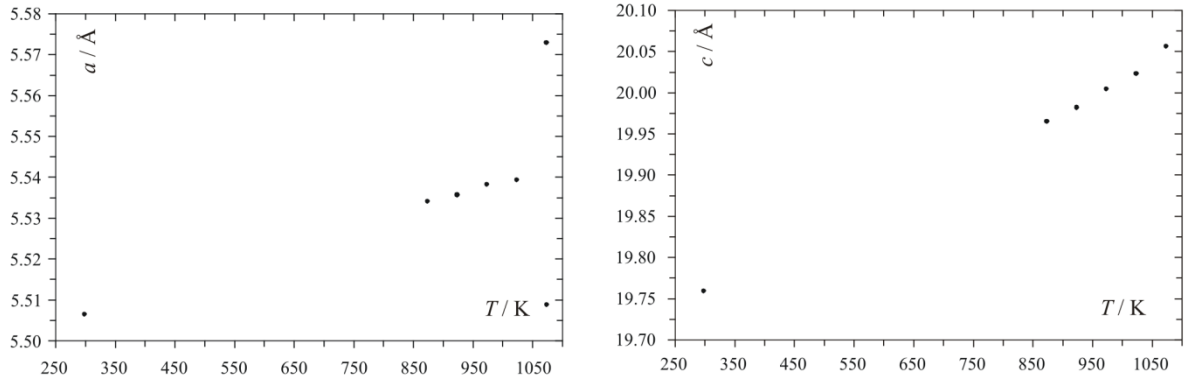

Figure 4.16 – Cell parameters extracted from the structural refinement of $^{160}Gd_2SrFe_2O_7$ based on powder neutron diffraction data. Refinements 298 – 1023 K in $P4_2/mnm$, at 1073 in *Bbmm*.

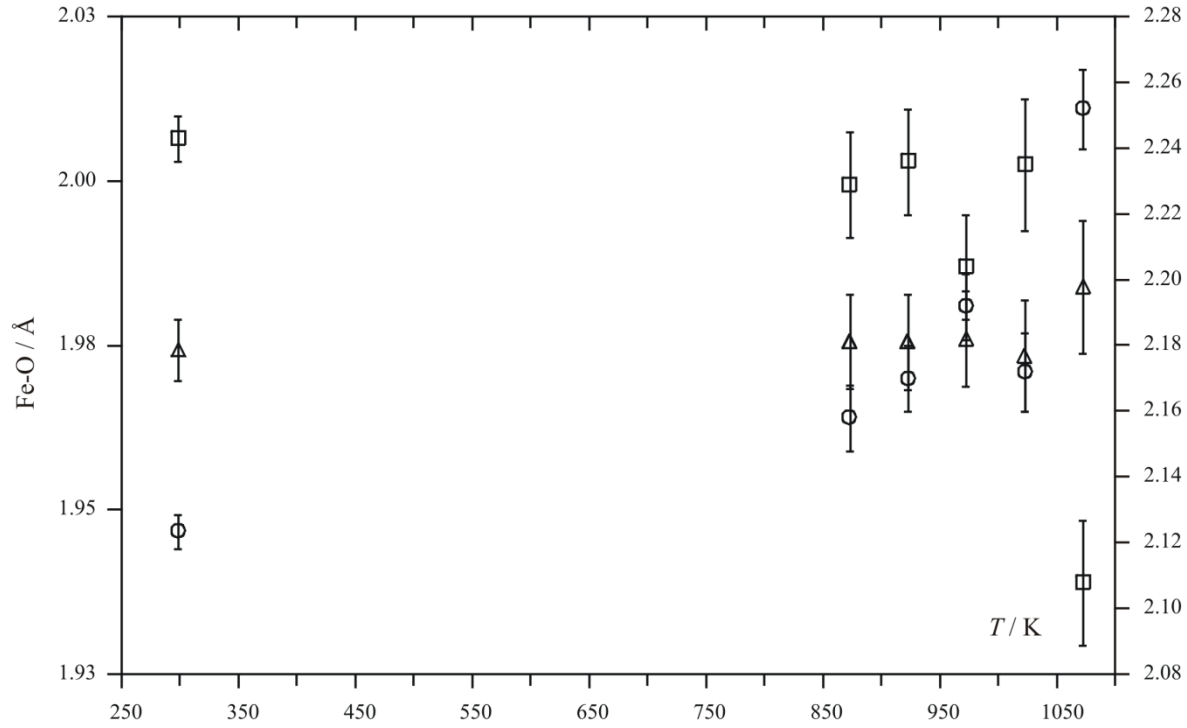

Figure 4.17 – Fe-O bond lengths extracted from structural refinement of $^{160}Gd_2SrFe_2O_7$ based on powder neutron diffraction data. Bridging Fe-O is represented by ○, apical by □ and in-layer by Δ (shown on secondary axis). Error bars show one standard error.

Table 4.6 – Structural parameters extracted from structural refinements of $^{160}Gd_2SrFe_2O_7$ based on powder neutron diffraction data.

T / K	Sr/Nd1 *x*/*a*	Sr/Nd1 U_{iso} / 10^{-2} Å^2	Sr/Nd2 *x*/*a*	Sr/Nd2 *z*/*c*	Sr/Nd2 U_{iso} / 10^{-2} Å^2	Fe *x*/*a*	Fe *z*/*c*	Fe U_{iso} / 10^{-2} Å^2	O1 *x*/*a*	O1 U_{iso} / 10^{-2} Å^2
298	0.2569 (9)	1.31 (13)	0.2736 (4)	0.18267 (14)	0.20 (6)	0.2562 (4)	0.40207 (12)	0.02 (3)	0.2164 (10)	0.96 (12)
873	0.2594 (20)	1.1 (2)	0.2732 (7)	0.1825 (2)	0.33 (8)	0.2516 (8)	0.4020 (2)	0.45 (6)	0.225 (2)	1.8 (3)
923	0.2592 (20)	1.3 (2)	0.2737 (7)	0.1825 (2)	0.40 (8)	0.2507 (9)	0.4017 (2)	0.54 (6)	0.230 (3)	2.5 (4)
973	0.2617 (20)	1.2 (2)	0.2744 (7)	0.1820 (2)	0.42 (8)	0.2508 (8)	0.4014 (2)	0.55 (6)	0.225 (3)	2.11 (3)
1023	0.256 (2)	1.5 (3)	0.2752 (9)	0.1822 (3)	0.55 (10)	0.2479 (11)	0.4016 (3)	0.60 (7)	0.241 (4)	2.5 (4)
1073	0.228 (3)	0.1 (2)	0.258 (4)	0.3186 (4)	1.98 (18)	0.254 (3)	0.3997 (3)	0.47 (11)	0.25 (2)	6 (1)

T / K	O2 *z*/*c*	O2 U_{iso} / 10^{-2} Å^2	O3 *z*/*c*	O3 U_{iso} / 10^{-2} Å^2	O4 / *z*/*c*	O4 U_{iso} / 10^{-2} Å^2	O5 / *x*/*a*	O5 *z*/*c*	O4 U_{iso} / 10^{-2} Å^2
298	0.1070 (3)	0.70 (7)	0.1239 (4)	0.08 (10)	0.4092 (5)	0.91 (13)	0.1974 (6)	0.2909 (3)	0.73 (8)
873	0.1064 (9)	2.1 (2)	0.1189 (8)	0.6 (2)	0.4088 (9)	0.7 (3)	0.1981 (14)	0.2924 (7)	1.9 (3)
923	0.1080 (8)	2.0 (2)	0.1176 (9)	0.8 (2)	0.4102 (8)	0.53 (2)	0.1976 (14)	0.2918 (7)	1.8 (2)
973	0.1070 (9)	2.3 (3)	0.1190 (8)	0.5 (2)	0.4085 (8)	0.4 (2)	0.1994 (16)	0.2930 (7)	2.2 (2)
1023	0.1096 (12)	3.1 (4)	0.1141 (12)	1.0 (3)	0.4103 (8)	0.10 (20)	0.1973 (19)	0.2918 (9)	2.5 (4)
1073	0.3825 (8)	1.9 (3)	0.4005 (11)	3.0 (4)			0.254 (12)	0.2947 (9)	4.3 (4)

Conclusions

Overview

New structures have been proposed for the room temperature tetragonal and elevated temperature orthorhombic phases of $Ln_2SrFe_2O_7$, *Ln* = La, Nd, Gd, based on refinements of powder neutron diffraction data. Important structural parameters, unit cell lengths and Fe-O bond lengths have been extracted and reported as a function of temperature.

Room temperature structures

The refined structure of $Nd_2SrFe_2O_7$ is shown in Figure 4.18. The ferrates are isostructural, with very similar octahedral tilts. All materials crystallise in $P4_2/mnm$, with a distorted Ruddlesden-Popper, $n = 2$ structure. Unit cell volumes reflect the size differences in lanthanide ions, with La > Nd > Gd (Figure 4.19).

Octahedra are distorted at room temperature, with one apical Fe-O bond lengths at ~ 2.2 Å and five Fe-O at ~ 2.0 Å.

High temperature structures for $Nd_2SrFe_2O_7$ and $Gd_2SrFe_2O_7$

The high temperature phases for $Nd_2SrFe_2O_7$ and $Gd_2SrFe_2O_7$ were refined in the space group *Bbmm*. They are isostructural, with similar octahedral tilts. The octahedra are less distorted than at room temperature, with all bond lengths at ~ 2.1 Å. A comparison of the room temperature and high temperature structures of $Nd_2SrFe_2O_7$ are shown in Figure 4.18. As all material low temperature phases are isostructural, and the high temperature structure of $Gd_2SrFe_2O_7$ is isostructural with the high temperature structure of $Nd_2SrFe_2O_7$, this figure shows all the structures determined in this chapter.

Variation of structures with temperature and comparison with $Gd_2SrCo_2O_7$

All three materials expand smoothly with temperature. Figure 4.19 shows the variation of unit cell volume with temperature. Despite the phase changes observed in $Nd_2SrFe_2O_7$ and $Gd_2SrFe_2O_7$, no discontinuities are seen over the temperature range for any of the materials. This supports the conclusion that the discontinuity in thermal expansion seen in $Gd_2SrCo_2O_7$ is caused by spin crossover. Spin crossover would not be expected in Fe (III), due to the stability of the high spin state over all temperatures.

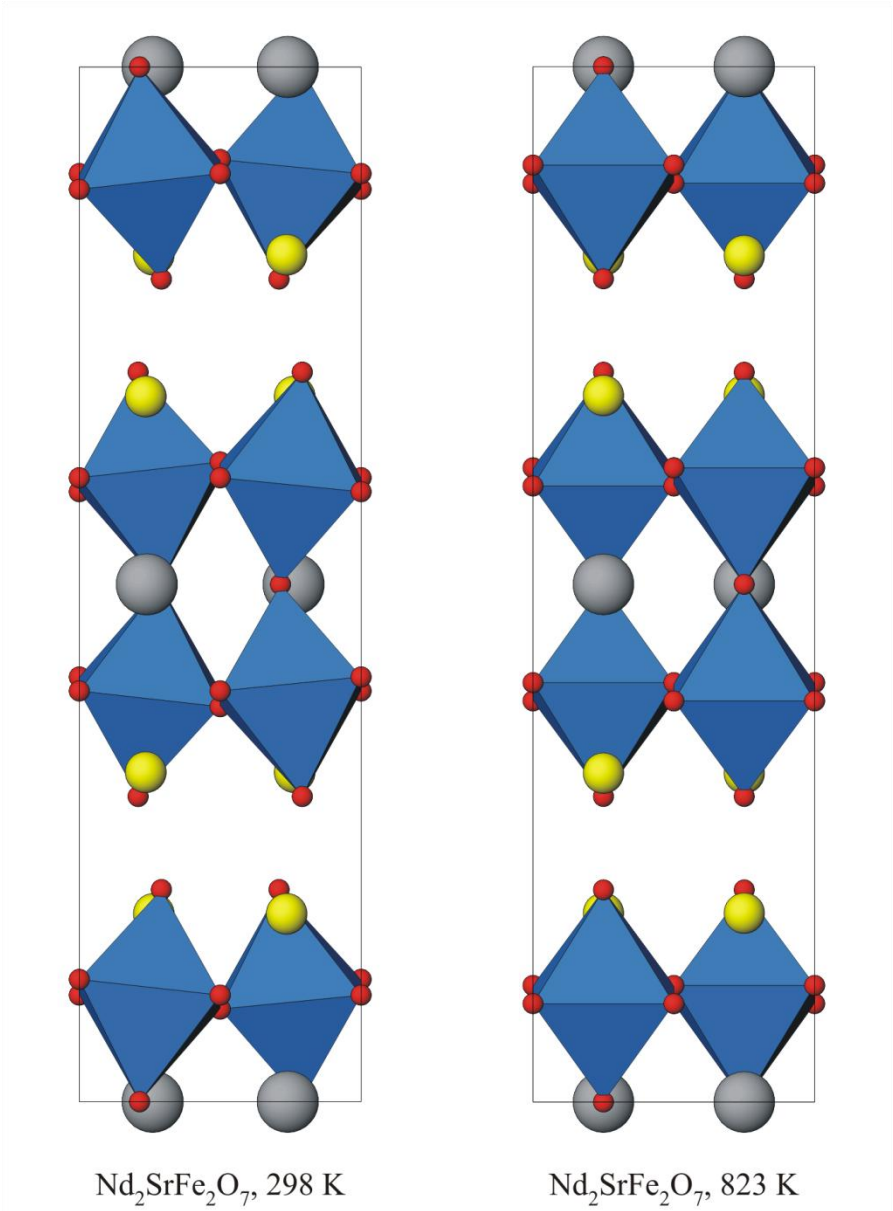

Figure 4.18 – Comparison between the room temperature and high temperature structures of $Nd_2SrFe_2O_7$. Yellow spheres show the rock salt Nd/Sr site, grey spheres the perovskite Nd/Sr site and blue octahedra the FeO_6.

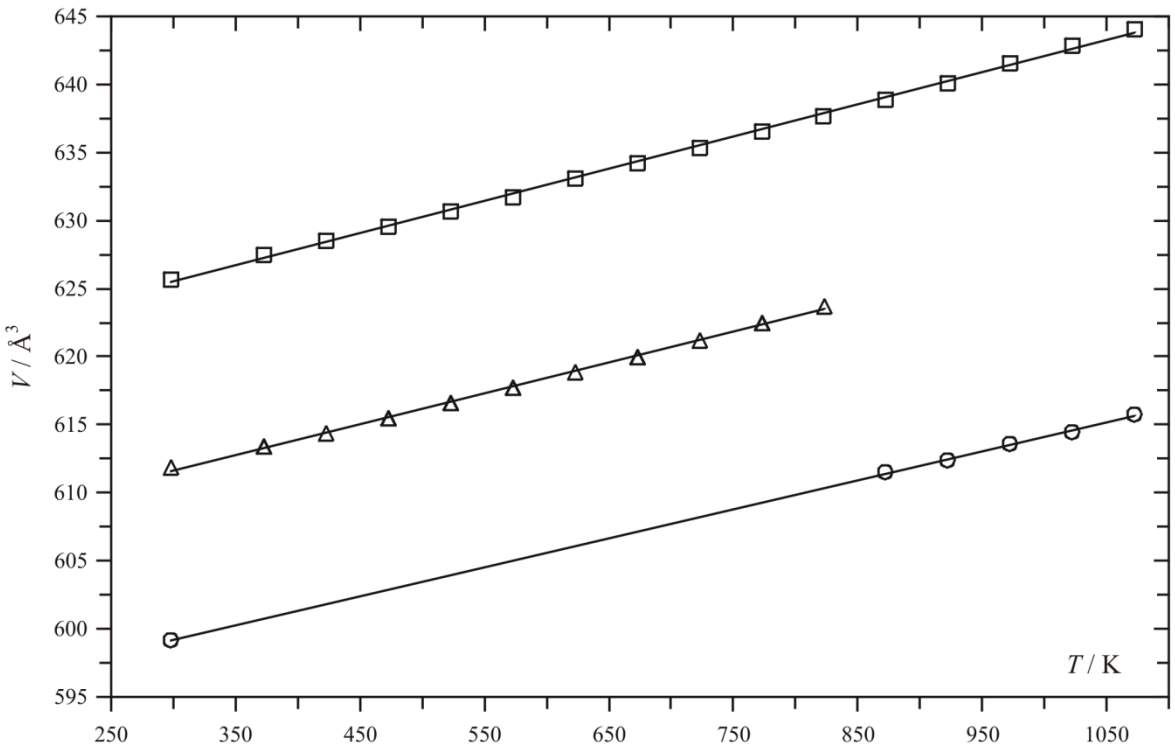

Figure 4.19 – Unit cell volumes as a function of temperature for $Ln_2SrFe_2O_7$ (*Ln* = La (□), Nd (Δ), Gd (○)) extracted from structural refinements based on variable temperature powder neutron diffraction data.

In Chapter 3 the nature of the structural transition was not fully addressed. The question of whether the spin crossover drove the structural transition or *vice versa* could not be answered definatively with structural evidence. A similar transition has now been observed in two materials where neither structural evidence nor chemical common sense allow spin crossover, demonstrating that the spin crossover does not cause the transition. However, comparison of the transition temperature in $Gd_2SrCo_2O_7$ (~ 623 K) and $Gd_2SrFe_2O_7$ (1073 K) suggests that the spin crossover may drive the transition to a lower temperature.

Origin of the phase transition in $Ln_2SrM_2O_7$

Comparing the room temperature and high temperature structures shown in Figure 4.18, the Fe-O-Fe angles appear more linear in the high temperature structure. Although the structure of $Sr_3Ti_2O_7$ is adopted by $A_3B_2O_7$ with uncompressed oxygen sublattices, [10] the 180 ° angles around the oxygen atoms are far from the ideal tetragonal angle. Distortion to the $P4_2/mnm$ structure in the materials $Ln_2SrFe_2O_7$ allows the bond angles around oxygen to tilt, reducing their strain. The transition can then be interpreted as an increase in temperature providing the thermal energy to compensate for the linear Fe-O-Fe. Although this results in the unusual observation of a transition to reduced symmetry with increasing temperature, the analogy with standard perovskite transitions can be drawn. In standard perovskite transitions, increasing temperature relaxes coordination requirements for *A* and *B* site cations. In each case, the constraint that most limits the structure that can be adopted in a material becomes less important to the structure as more thermal energy becomes available to the structure. The Fe-O-Fe angles in the room temperature and 1073 K structures of $^{160}Gd_2SrFe_2O_7$ and the

room temperature and 823 K structure of $Nd_2SrFe_2O_7$ are shown in Table 4.7 and Table 4.8. The increased linearity in the high temperature phases is clear.

Table 4.7 – Angles around oxygen atoms in $Gd_2SrFe_2O_7$ at 298 K and 1073 K.

298 K		1073 K	
Fe-O1-Fe / °	167.4 (5)	Fe-O1-Fe / °	177.0 (7)
Fe-O2-Fe / °	169.4 (4)	Fe-O2-Fe / °	160.1 (9)
Fe-O3-Fe / °	149.7 (4)	Fe-O3-Fe / °	179 (1)
Fe-O4-Fe / °	171.9 (4)		

Table 4.8 – Angles around oxygen atoms in $Nd_2SrFe_2O_7$ at 298 K and 823 K

298 K		1073 K	
Fe-O1-Fe / °	165.1 (2)	Fe-O1-Fe / °	172.7 (1)
Fe-O2-Fe / °	171.42 (18)	Fe-O2-Fe / °	161.9 (3)
Fe-O3-Fe / °	153.4 (3)	Fe-O3-Fe / °	177.1 (3)
Fe-O4-Fe / °	172.6 (3)		

References

1. C. Brisi and P. Rolando, *Atti della Accademia Nazionale dei Lincei*, 1971, **50**, 33-36
2. D. Samaras, A. Collomb and J. C. Joubert, *J. Solid State Chem*., 1973, **7**, 337-348
3. I. B. Sharma and D. Singh, *Proc. Indian Acad. Sci*., 1995, **107**, 189-196
4. I. B. Sharma, S. K. Magotra, D. Singh, S. Batra and K. D. S. Mudher, *J. Alloys Comp*., 1999, **291**, 16-20
5. T. Nishi, K. Toda, F. Kanamaru and T. Sakai, Key Engineering Materials, 1999, **169-170 (***Electroceramics in Japan II*), 235-238
6. L. Zhiyou, Z. Xiaoyong, H. Junfeng and Z. Kechao, *J. Cryst. Growth*, 2007, **305,** 265-270
7. E. A. Tugova, V. F. Popova, I. A. Zhvereva and V. V. Gusarov, *Russ. J. General Chem*., 2007, **77**, 979-981
8. I. A. Zhvereva, I. V. Otreping, V. G. Samenov, E. A. Tugova, V. F. Popova and V. V. Gusarov, *Russ. J. General Chem*, 2007, **77**, 973-978
9. M. I. Gomez, J. A. De Moran, R. E. Carbonio and P. J. Aymonino, *J. Solid State Chem*., 1999, **142**, 138-145
10. H. Shaked, J. Jorgensen, O. Chmaissem, S. Ikeda and Y. Maeno, *J. Solid State Chem*., 2000, **154**, 583-58

Chapter 5 – $Ln_2SrAl_2O_7$ aluminates

Introduction

The materials $La_2SrAl_2O_7$ and $Gd_2SrAl_2O_7$ were first reported in 1975 by Fava and le Flem. [1] The structure was reported in *I*4/*mmm*, with the $Sr_3Ti_2O_7$ structure and strontium and lanthanide ions distributed randomly over each crystallographic site ($La_{2/3}Sr_{1/3}$).

More recently, the structures of materials $Ln_2SrAl_2O_7$ (*Ln* = La, Nd, Sm, Gd) were reported by Zvereva *et al*. [3] The materials were formed by solid state reaction of Ln_2O_3, Al_2O_3 and $SrCO_3$ at 1723 K. All materials were again described as *I*4/*mmm*, $Sr_3Ti_2O_7$ isostructures. Much work has been carried out by the same group into the mechanism of formation, the phases, kinetics and thermodynamics of the reaction and the phase diagrams of the systems $LnAlO_3$-$LnSrAlO_4$-$Ln_2SrAl_2O_7$. [3-7, 9] As for other phases with the $Sr_3Ti_2O_7$ structure type, the reaction proceeds from starting materials through a mixture of $LnAlO_3$ and $LnSrAlO_4$ to the final products. [10-12]

Through Rietveld refinement of X-ray powder diffraction data the 2003 study demonstrated that as the Ln^{3+} ion became smaller, the *A*-site cations became increasingly ordered and the materials more stable. With increasing lanthanide ionic radius, the preference for the smaller, 9-coordinate site became less prevalent leading to more even distributions. Refinement of the structures of materials formed by substitution onto the *A* sites with calcium [2] and holmium [8] again illustrated this effect. With increasing *x* in the phases $La_2Sr_{1-x}Ca_xAl_2O_7$ the strontium ions in the 9-coordinate rock salt site are substituted for calcium; the approximately random La/Sr perovskite layer distribution remains unchanged. The stability of the material also decreases with *x* as the rock salt / perovskite layer mismatch increases. Increasing *x* in the phases $La_{2-x}Ho_xSrAl_2O_7$ leads to an ordered *A*-site distribution, with Ho preferentially occupying the 9-coordinate rock salt layer. The stability of the phases also increases with *x*.

In all previous studies, structures have been determined by X-ray diffraction. In this chapter, the structures of $Ln_2SrAl_2O_7$ (*Ln* = Nd, Sm, Gd, Dy) are re-examined, and powder neutron diffraction used as the preferred tool for investigation of the oxygen substructure.

Synthesis of $Ln_2SrAl_2O_7$

Ln_2O_3 (*Ln* = La, Nd, Sm, Gd, Dy, dried at 1073 K overnight), Al_2O_3 and $SrCO_3$ were mixed in a 1:1:1 ratio and ground under acetone. The mixture was heated to 1273 K overnight, then reground, pelletised and heated for two weeks at 1673 K with two regrinds. Initial samples for X-ray diffraction were made up to approximately 1 g sample size. Samples for neutron diffraction were prepared for *Ln* = Nd and Dy: these lanthanides offer low enough absorption cross-sections that unenriched oxides can be used. La would have been suitable for this study, however the material itself contained high levels of impurities, as previously discussed by Zvereva *et al*. Neutron samples were prepared by initially synthesising small 2 g samples of the required material, then selecting the best quality of these and combining to form one 10 g

sample. A large (30 mm diameter) pellet was prepared and annealed to ensure homogeneity of the final sample. All samples were thoroughly ground under acetone prior to diffraction.

Structural studies of $Ln_2SrAl_2O_7$

X-ray diffraction

For this work, isotopically enriched lanthanide oxides were not available. Structural information for the materials $Gd_2SrAl_2O_7$ and $Sm_2SrAl_2O_7$ were still of interest, so X-ray powder diffraction was used as a structural probe rather than simply overlooking these phases. While the oxygen substructure cannot be probed as accurately, the *A*-site distribution will also be of interest.

For the phases $Nd_2SrAl_2O_7$ and $Dy_2SrAl_2O_7$, X-ray diffraction was used to confirm the successful formation of the phases, but further analysis was deferred for neutron diffraction studies.

$Gd_2SrAl_2O_7$

X-ray powder diffraction data were collected on a sample of $Gd_2SrAl_2O_7$ using a Siemens D5000 diffractometer in the range 5 – 120 ° 2θ. A 0.02 ° step size was used, at a counting rate of four seconds per step (65 hours total scan time). Rietveld refinement was carried out to fit the data, based on a $Sr_3Ti_2O_7$ *I*4/*mmm* model.

In total, 36 parameters were refined: one histogram scale factor, one zero point error, sixteen shifted Chebyshev background parameters, five pseudo-Voight peak shape parameters, two lattice parameters, one fractional occupancy, four atomic coordinates and six isotropic temperature factors. The profile fit is shown in Figure 5.1, and the extracted atomic parameters shown in Table 5.1. A small, unidentified impurity phase was present in the sample: the unfitted peaks did not index to a supercell structure for $Gd_2SrAl_2O_7$. As expected from its larger ionic radius, the Sr^{2+} ion preferentially occupies the 12-coordinate perovskite *A*-site, with a 74.6 ± 0.7 % occupancy on site 1.

$Sm_2SrAl_2O_7$

X-ray powder diffraction data were collected on a sample of $Sm_2SrAl_2O_7$ using a Siemens D5000 diffractometer, in the range 20 – 70 ° 2θ with a 0.02 ° step size at a rate of two seconds per step. The structure was refined in the space group *I*4/*mmm* based on the $Sr_3Ti_2O_7$ model. 27 parameters were refined: one histogram scale factor, one zero point error, eight shifted Chebyshev background parameters, four pseudo-Voight peak shape parameters, two lattice parameters, one fractional occupancy, four atomic coordinates and six isotropic temperature factors. One oxygen temperature factor refined to a negative value; this is likely due to the small angular range of the data limiting the available data for refinement. The profile fit is shown in Figure 5.2, and the extracted parameters in Table 5.2.

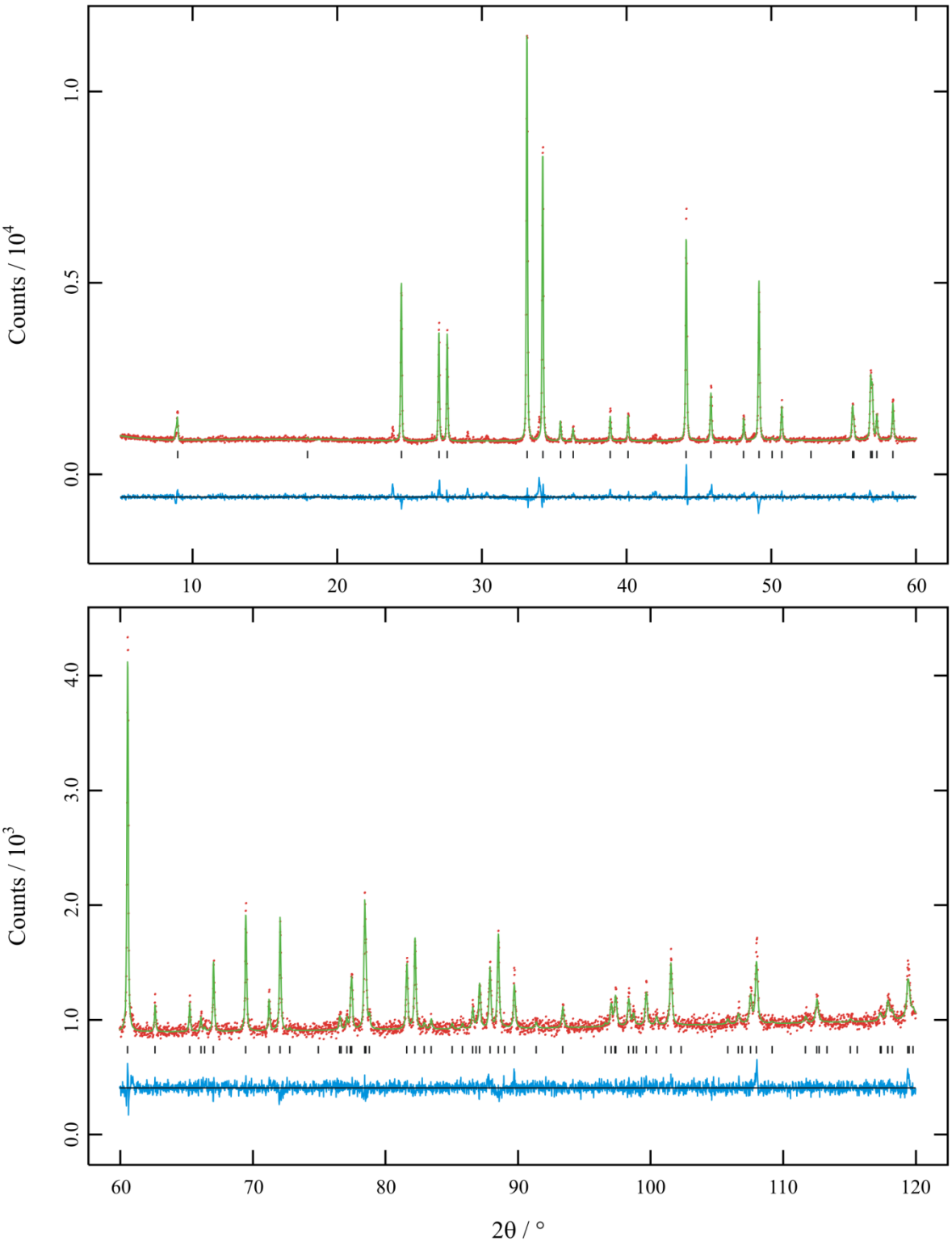

Figure 5.1 – Profile fit of the structure of $Gd_2SrAl_2O_7$ in the space group *I*4/*mmm* against powder X-ray diffraction data. R_{wp} = 4.11 %, R_p = 3.07 %, χ^2 = 1.702.

Table 5.1 – Structural parameters extracted from the refinement of the structure of $Gd_2SrAl_2O_7$ in *I*4/*mmm* to fit X-ray powder diffraction data. $a = b = 3.70511$ (4), $c = 19.7840$ (3).

Atom	*x*/*a*	*y*/*b*	*z*/*c*	U_{iso} / 10^{-2}Å	Site occupancy
Sr1	0.5	0.5	0	0.91 (9)	0.746 (7)
Gd1	0.5	0.5	0	0.91 (9)	0.254 (7)
Sr2	0.5	0.5	0.18113 (7)	0.84 (5)	0.127 (4)
Gd2	0.5	0.5	0.18113 (7)	0.84 (5)	0.873 (4)
Al	0	0	0.0956 (3)	1.28 (14)	1
O1	0	0	0	1.4 (6)	1
O2	0	0	0.1972 (5)	0.4 (3)	1
O3	0	0.5	0.1024 (4)	1.5 (2)	1

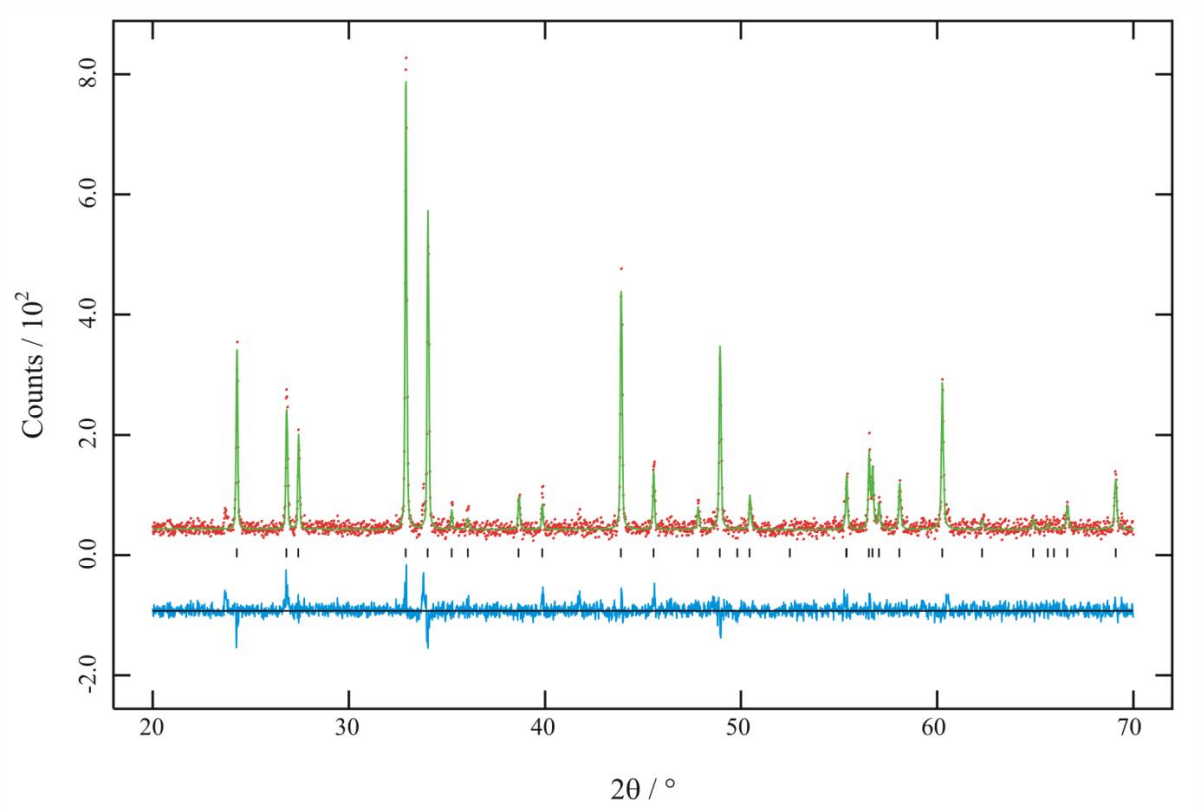

Figure 5.2 – Profile fit of $Sm_2SrAl_2O_7$ against X-ray powder diffraction. $R_{wp} = 15.22$ %, $R_p = 11.82$ %, $\chi^2 = 1.279$.

Table 5.2 – Structural parameters extracted from the refinement of the structure of $Sm_2SrAl_2O_7$ in *I*4/*mmm* to fit X-ray powder diffraction data. $a = b = 3.71489$ (16) Å, $c = 19.8730$ (10) Å.

Atom	*x*/*a*	*y*/*b*	*z*/*c*	U_{iso} / 10^{-2}Å	Site occupancy
Sr1	0.5	0.5	0	0.4 (5)	0.64 (4)
Sm1	0.5	0.5	0	0.4 (5)	0.37 (4)
Sr2	0.5	0.5	0.18160 (2)	0.6 (3)	0.182 (19)
Sm2	0.5	0.5	0.1816 (2)	0.6 (3)	0.818 (19)
Al	0	0	0.0982 (14)	1.9 (7)	1
O1	0	0	0	0.8 (2)	1
O2	0	0	0.1977 (19)	0.6 (13)	1
O3	0	0.5	0.1024 (14)	-0.8 (8)	1

Neutron diffraction

Room temperature neutron diffraction data were collected on 10 g samples of $Nd_2SrAl_2O_7$ and $Dy_2SrAl_2O_7$ on the D2B instrument at the Institut Laue-Langevin. Diffraction sets were collected using $\lambda = 1.59432$ Å neutrons, over a collection time of 12 hours per sample. Counting statistics were significantly poorer for $Dy_2SrAl_2O_7$, attributable to the high neutron absorption cross-section of Dy (994 barn compared to 50.5 barn for Nd).

$Nd_2SrAl_2O_7$

The room temperature structure of $Nd_2SrAl_2O_7$ was initially refined in the space group *I*4/*mmm*, as originally reported by Fava and le Flem. [1] Data were fitted in the range 10 – 140 ° 2θ, refining 32 parameters in total: one histogram scale factor, one zero point error, twelve Chebyshev background parameters, two lattice parameters, one fractional occupancy of the two *A* sites, six isotropic temperature factors and four atomic coordinates. The profile fit is shown in Figure 5.3, and extracted structural parameters and bond lengths and angles in Table 5.3 and Table 5.4.

Although the peaks corresponding to the main phase are well fitted by the structure, the negative isotropic temperature parameter obtained for the aluminium atom suggests that the model may not be correct. A further refinement was carried out based on the $P4_2/mnm$ structure of the cobaltates and ferrates as discussed in previous chapters.

41 parameters were refined: one histogram scale factor, one zero point error, twelve Chebyshev background fitting parameters, two lattice parameters, one fractional occupancy of the two *A* sites, eight isotropic temperature factors and eleven atomic coordinates. The profile fit is shown in Figure 5.4, and the structural parameters and bond lengths and angles shown in Table 5.5 and Table 5.6.

All temperature factors refine to positive values, and fit parameters are improved over those obtained for *I*4/*mmm*, for example $\chi^2 = 24.21$ for *I*4/*mmm* and 22.67 for $P4_2/mnm$. The material is isostructural with the cobaltates and ferrates previously discussed, however with a much smaller tilt.

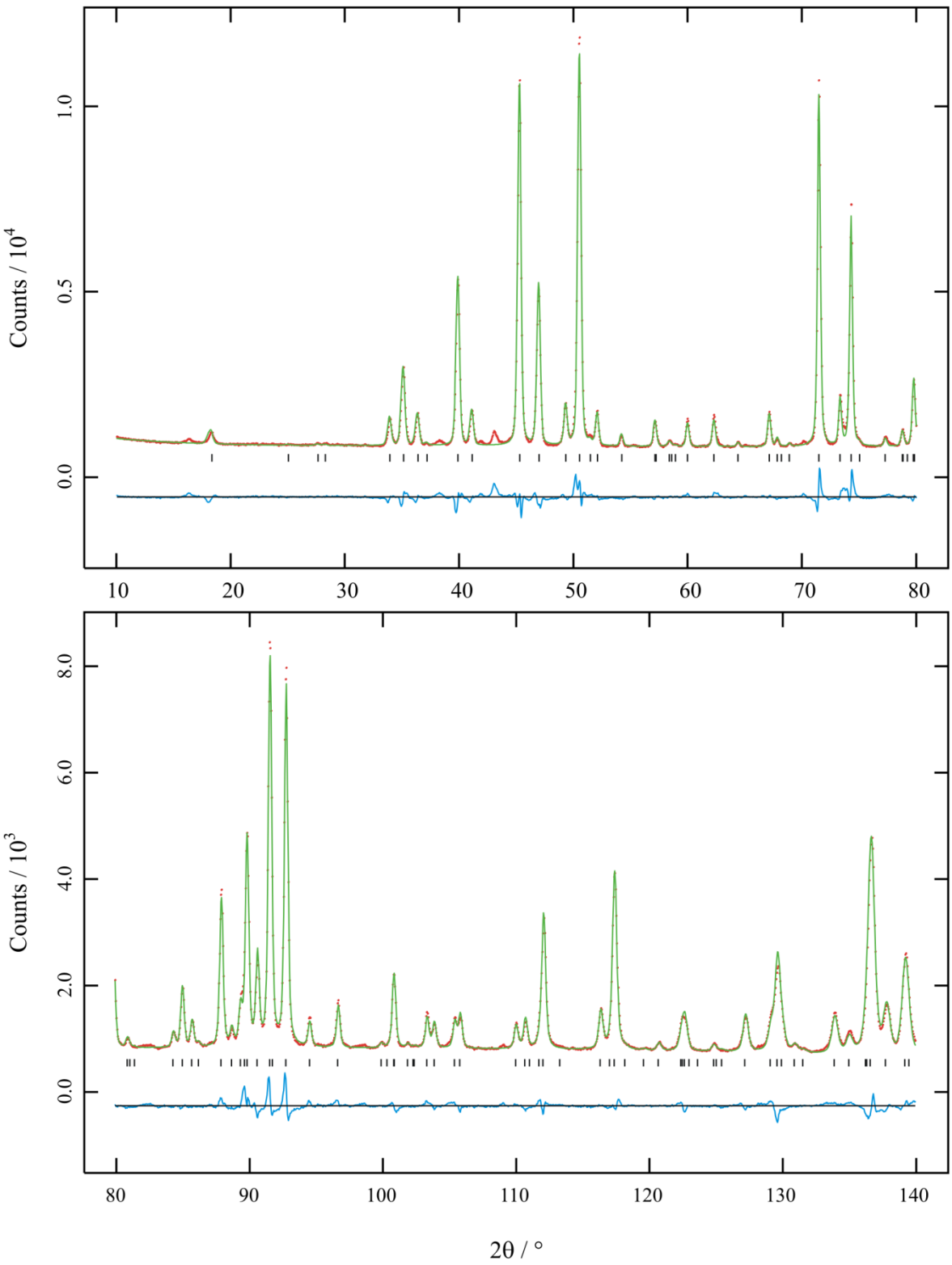

Figure 5.3 – Profile fit of the structure of $Nd_2SrAl_2O_7$ in *I*4/*mmm* to fit room temperature powder neutron diffraction data, λ = 1.59432 Å. R_{wp} = 4.73 %, R_p = 3.34 %, χ^2 = 24.21. Secondary phase omitted for comparative purposes.

Table 5.3 – Structural parameters extracted from the refinement of the structure of $Nd_2SrAl_2O_7$ in *I*4/*mmm*. $a = b = 3.73260\ (8)$ Å, $c = 19.9900\ (4)$ Å.

Atom	*x*/*a*	*y*/*b*	*z*/*c*	U_{iso} / 10^{-2}Å	Site occupancy
Sr1	0.5	0.5	0	0.48 (6)	0.22 (9)
Nd1	0.5	0.5	0	0.48 (6)	0.78 (9)
Sr2	0.5	0.5	0.18123 (8)	0.05 (4)	0.39 (5)
Nd2	0.5	0.5	0.18123 (8)	0.05 (4)	0.61 (5)
Al	0	0	0.09459 (17)	-0.04 (5)	1
O1	0	0	0	0.74 (6)	1
O2	0	0	0.19893 (10)	1.04 (5)	1
O3	0	0.5	0.09740 (8)	0.35 (3)	1

Table 5.4 – Bond lengths and angles extracted from the refinement of the structure of $Nd_2SrAl_2O_7$ in *I*4/*mmm*.

Al-O1 / Å	1.891 (3)
Al-O2 / Å	2.086 (4)
Al-O3 (× 4) / Å	1.86715 (11)
Al-O2-Al (× 3) / °	176.5 (2)

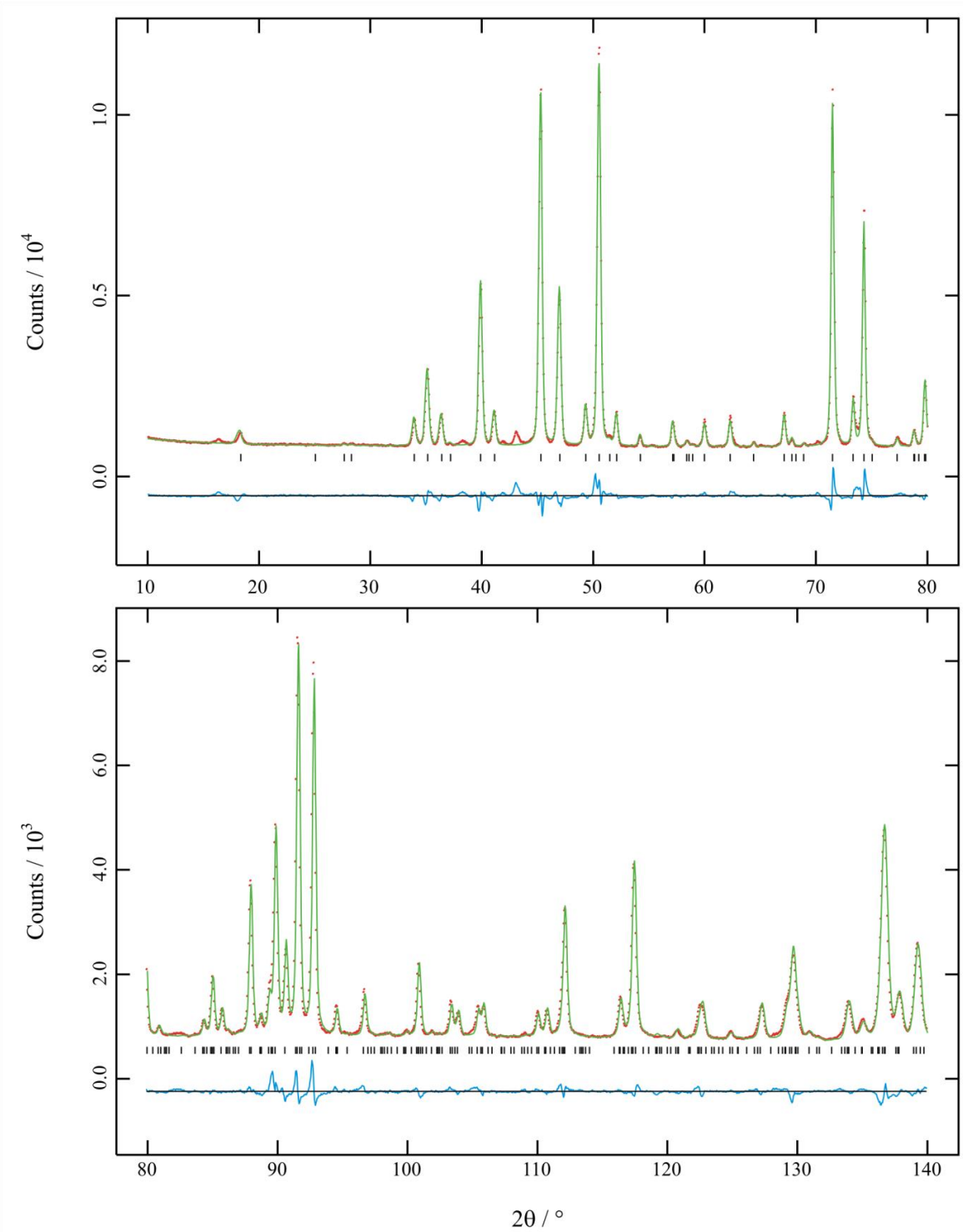

Figure 5.4 – Profile fit of the structure of $Nd_2SrAl_2O_7$ in $P4_2/mnm$ to fit room temperature powder neutron diffraction data, λ = 1.59432 Å. R_{wp} = 4.57 %, R_p = 3.19 %, χ^2 = 22.67. Secondary phase omitted for comparative purposes.

Table 5.5 – Structural parameters extracted from the refinement of the structure of $Nd_2SrAl_2O_7$ in $P4_2/mnm$. $a = b = 5.27852$ (11) Å, $c = 19.9891$ (4) Å.

Atom	*x*/*a*	*y*/*b*	*z*/*c*	U_{iso} / 10^{-2}Å	Site occupancy
Sr1	0.2535 (14)	0.2535 (14)	0	1.28 (7)	0.21 (9)
Nd1	0.2535 (14)	0.2535 (14)	0	1.22 (7)	0.79 (9)
Sr2	0.2502 (11)	0.2502 (11)	0.18133 (7)	0.86 (4)	0.39 (4)
Nd2	0.2502 (11)	0.2502 (11)	0.18133 (7)	0.86 (4)	0.61 (4)
Al	0.2558 (19)	0.2558 (19)	0.40541 (17)	0.65 (6)	1
O1	0.7578 (18)	0.2422 (18)	0	1.45 (8)	1
O2	0	0.5	0.0953 (2)	1.68 (18)	1
O3	0	0	0.1025 (4)	0.6 (3)	1
O4	0	0	0.4034 (3)	0.3 (2)	1
O5	0.2498 (14)	0.2498 (14)	0.30126 (9)	1.88 (5)	1

Table 5.6 – Bond lengths and angles extracted from the refinement of the structure of $Nd_2SrAl_2O_7$ in $P4_2/mnm$.

Al-O1 / Å	1.891 (3)
Al-O2 (× 2) / Å	1.8668 (3)
Al-O3 / Å	1.830 (14)
Al-O4 / Å	1.910 (14)
Al-O5 / Å	2.082 (4)
Al-O1-Al / °	179.1 (12)
Al-O2-Al / °	179.1 (3)
Al-O3-Al / °	170.0 (5)
Al-O4-Al / °	177.6 (5)

$Dy_2SrAl_2O_7$

Unlike $Nd_2SrAl_2O_7$, additional peaks corresponding to a superstructure were clearly visible in the powder neutron diffractogram obtained for $Dy_2SrAl_2O_7$. The data could be fitted by refinement of the structural model in $P4_2/mnm$.

41 parameters were refined: one histogram scale factor, one zero point error, twelve Chebyshev background parameters, two lattice parameters, one fractional occupancy of the two *A* sites, eight isotropic temperature factors and eleven atomic coordinates. The profile fit is shown in Figure 5.5, and the extracted atomic parameters and bond lengths and angles presented in Table 5.7 and Table 5.8. The *A*-site cation ordering and tilt angle in the Dy material are increased relative to $Nd_2SrAl_2O_7$.

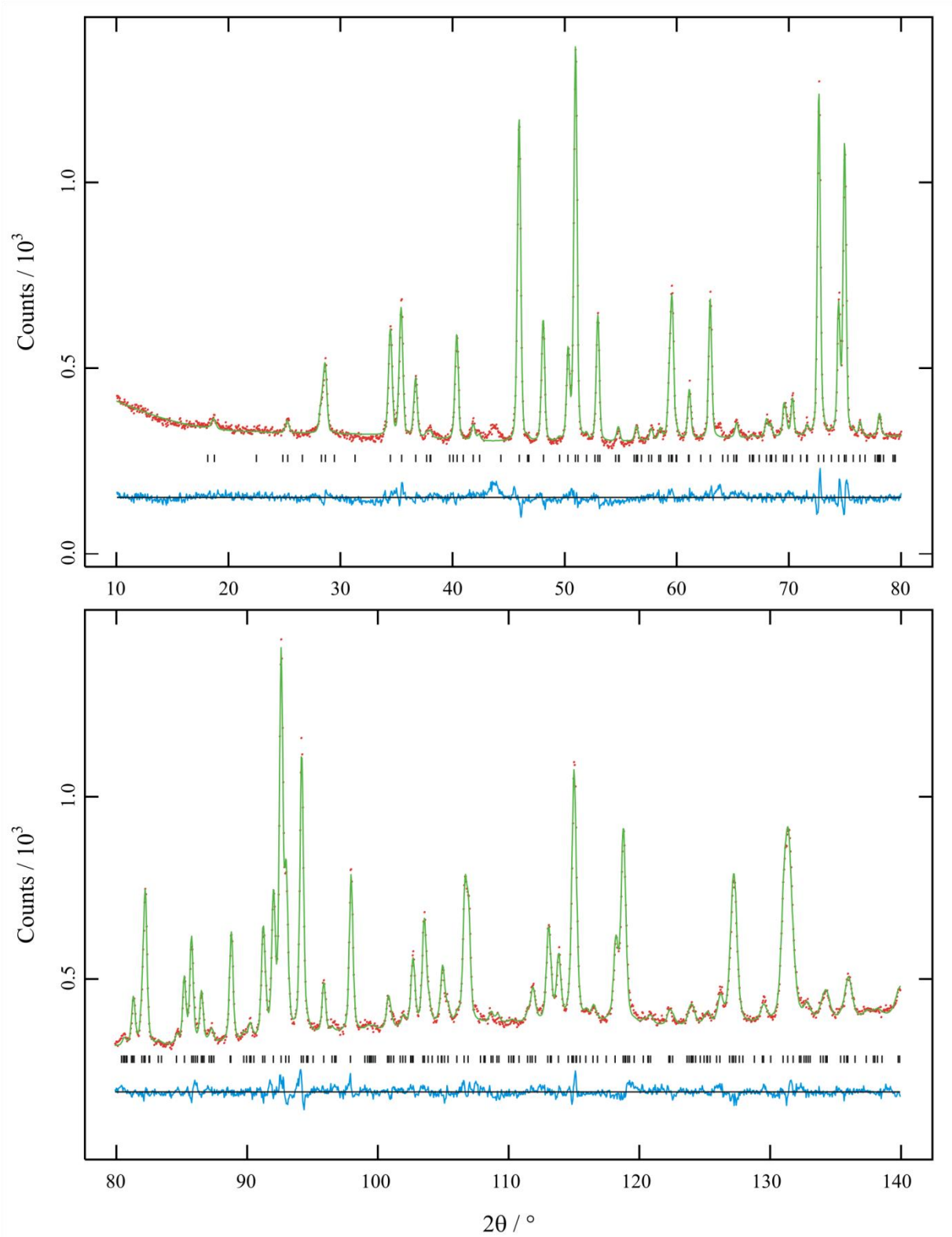

Figure 5.5 – Profile fit of the structure of $Dy_2SrAl_2O_7$ in $P4_2/mnm$ to fit room temperature powder neutron diffraction data, λ = 1.59432 Å. R_{wp} = 2.67 %, R_p = 2.07 %, χ^2 = 2.593. The $DyAlO_3$ impurity phase has been omitted for clarity.

Table 5.7 – Structural parameters extracted from the refinement of the structure of $Dy_2SrAl_2O_7$ in $P4_2/mnm$. $a = b = 5.24108$ (17) Å, $c = 19.5692$ (6) Å.

Atom	*x*/*a*	*y*/*b*	*z*/*c*	U_{iso} / 10^{-2}Å	Site occupancy
Sr1	0.2522 (8)	0.2522 (8)	0	0.94 (9)	0.873 (9)
Dy1	0.2522 (8)	0.2522 (8)	0	0.94 (9)	0.127 (9)
Sr2	0.2588 (3)	0.2588 (3)	0.18191 (5)	0.65 (2)	0.063 (4)
Dy2	0.2588 (3)	0.2588 (3)	0.18191 (5)	0.65 (2)	0.937 (4)
Al	0.2484 (14)	0.2484 (14)	0.40442 (24)	0.51 (6)	1
O1	0.7617 (14)	0.2383 (14)	0	1.58 (9)	1
O2	0	0.5	0.1052 (5)	0.20 (13)	1
O3	0	0	0.1099 (8)	1.9 (2)	1
O4	0	0	0.4050 (5)	1.2 (3)	1
O5	0.2256 (9)	0.2256 (9)	0.29596 (16)	1.65 (10)	1

Table 5.8 – Bond lengths and angles extracted from the refinement of the structure of $Dy_2SrAl_2O_7$ in $P4_2/mnm$

Al-O1 / Å	1.873 (5)
Al-O2 (× 2) / Å	1.8627 (11)
Al-O3 / Å	1.886 (10)
Al-O4 / Å	1.841 (11)
Al-O5 / Å	2.129 (6)
Al-O1-Al / °	174.0 (7)
Al-O2-Al / °	168.4 (6)
Al-O3-Al / °	162.9 (10)
Al-O4-Al / °	179.273 (7)

Conclusions

$Nd_2SrAl_2O_7$ and $Dy_2SrAl_2O_7$

New structures for $Nd_2SrAl_2O_7$ and $Dy_2SrAl_2O_7$ have been determined by Rietveld refinement to powder neutron diffraction data collected at room temperature. Both materials adopt the $P4_2/mnm$ structure already reported for other $Ln_2M_2O_7$ in this work.

In $Nd_2SrAl_2O_7$ the two *A* sites in the material are distributed close to the Nd_2Sr ratio implied by the structural formula. The tilts of octahedra are small, with the interlayer Al-O1-Al bond angle refined to 179.1 ± 1.2 °. The smaller Dy^{3+} ion preferentially occupies the smaller 9-coordinate rock salt *A*-site, its occupancy refined to 93.7 ± 0.4 % on this site. A significant increase in octahedral tilts (for example, a bond angle of 174.0 ± 0.7 ° for the interlayer Al-O1-Al) is also apparent compared to the neodymium material. The structures of the materials are shown in Figure 5.6

The structures reported here are derived from tilts of the octahedra from the $Sr_3Ti_2O_7$ structures reported previously for the materials. [3]

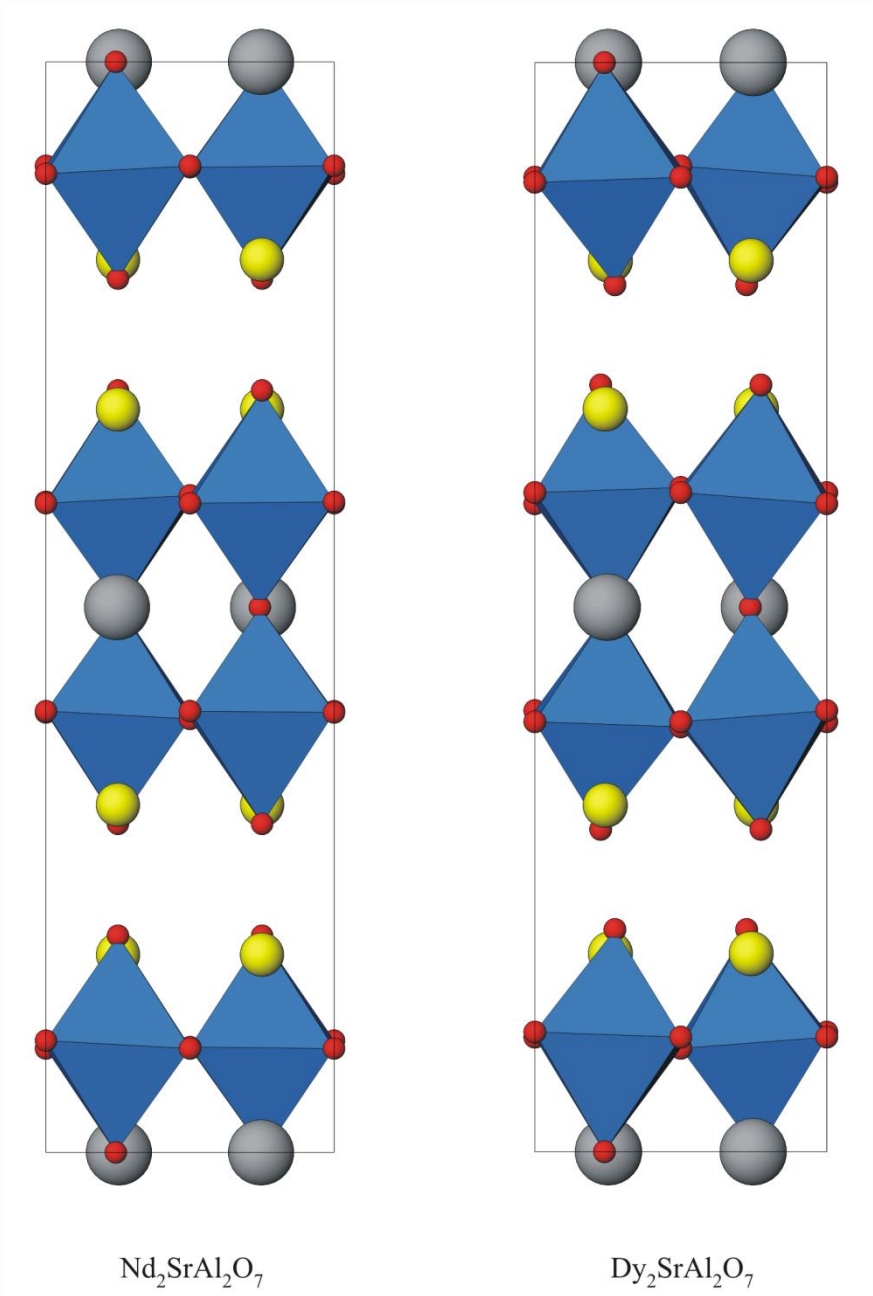

Figure 5.6 – Structures of $Nd_2SrAl_2O_7$ and $Dy_2SrAl_2O_7$ viewed along (100). AlO_6 octahedra are shown in blue, the perovskite *A* site (Sr/*Ln*1) in grey and the rock salt *A*-site (Sr/*Ln*2) in yellow.

$Sm_2SrAl_2O_7$ and $Gd_2SrAl_2O_7$

The high neutron absorption cross sections of natural Sm and Gd prevented collection of neutron diffraction data for these materials. Structural refinement of the materials to fit X-ray powder diffraction data allowed the extraction of lattice parameters and structural parameters in the space group *I*4/*mmm*. The supercell structures adopted by $Nd_2SrAl_2O_7$ and $Dy_2SrAl_2O_7$ imply that the two inner series members $Sm_2SrAl_2O_7$ and $Gd_2SrAl_2O_7$ may well also crystallise in the space group $P4_2/mnm$, however no reflections corresponding to a supercell were visible in the X-ray diffractograms for these materials, even after long collection times.

Refinement in the space group $P4_2/mnm$ could be carried out for the high quality diffraction data collected on $Dy_2SrAl_2O_7$, however fitting was not improved. Fitting parameters are shown in Table 5.9.

Table 5.9 – Fitting parameters for the refinement of the structure of $Gd_2SrAl_2O_7$ in $I4/mmm$ and $P4_2/mnm$ against powder X-ray diffraction data.

	$P4_2/mnm$	$I4/mmm$
R_{wp} / %	4.22	4.11
R_p / %	3.17	3.07
χ^2	1.797	1.702

Trends in the series $Ln_2SrAl_2O_7$

The extracted cell parameters from structural refinements of all $Ln_2SrAl_2O_7$ are shown in Figure 5.7. The $Sr_3Ti_2O_7$ lattice parameters are reported; for *Ln* = Nd and Dy $a_0 = a / \sqrt{2}$ and $c_0 = c$.

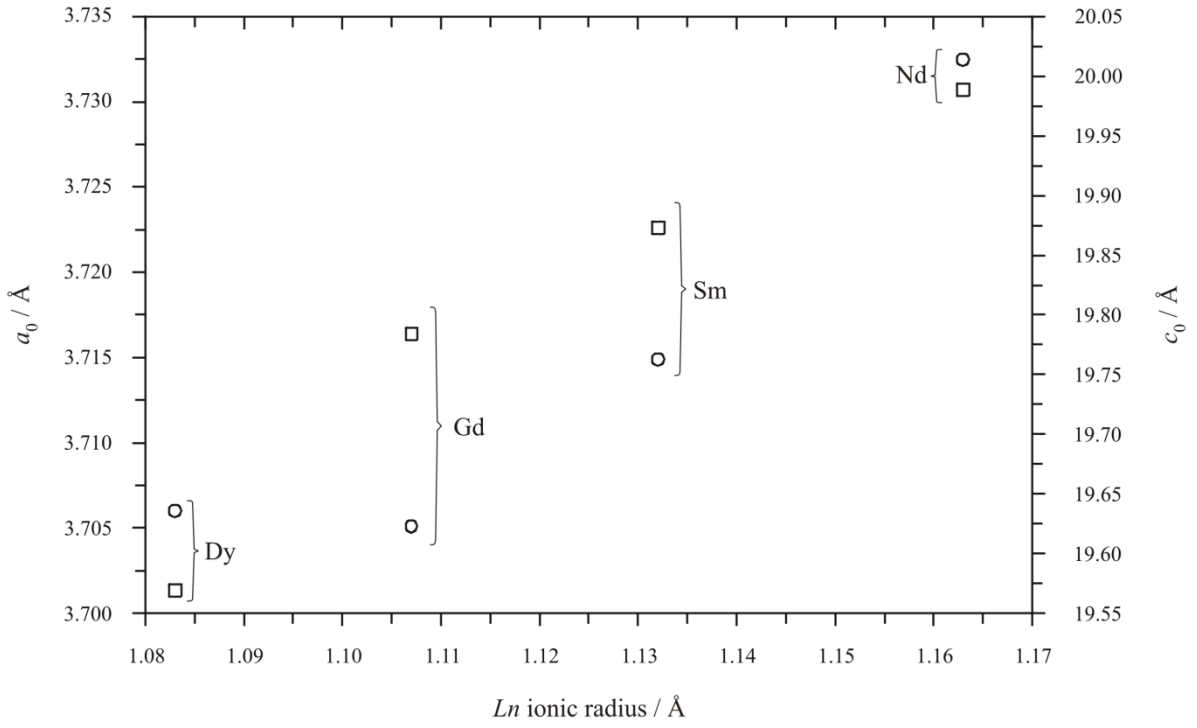

Figure 5.7 – Variation of *a* (○) and *c* (□) lattice parameters with ionic radius of *Ln* in the series $Ln_2SrAl_2O_7$ extracted from structural refinements based on powder X-ray and neutron diffraction. Errors in cell parameter lie within point size.

The lattice parameters expand with increasing *Ln* ionic radius. The *c* parameter increases constantly across the series, however the *a* parameter shows a discontinuity from Gd to Dy. A possible explanation for this observation is that for the series *Ln* = Nd > Sm > Gd, the decreasing size of lanthanide reduces the compression on the perovskite layers; but for Gd > Dy the decrease in ionic radius of *Ln* is overcompensated for by the increasing occupation of the significantly larger Sr^{2+} in the perovskite site. This is illustrated by the variation in occupancy of this site as in Figure 5.8.

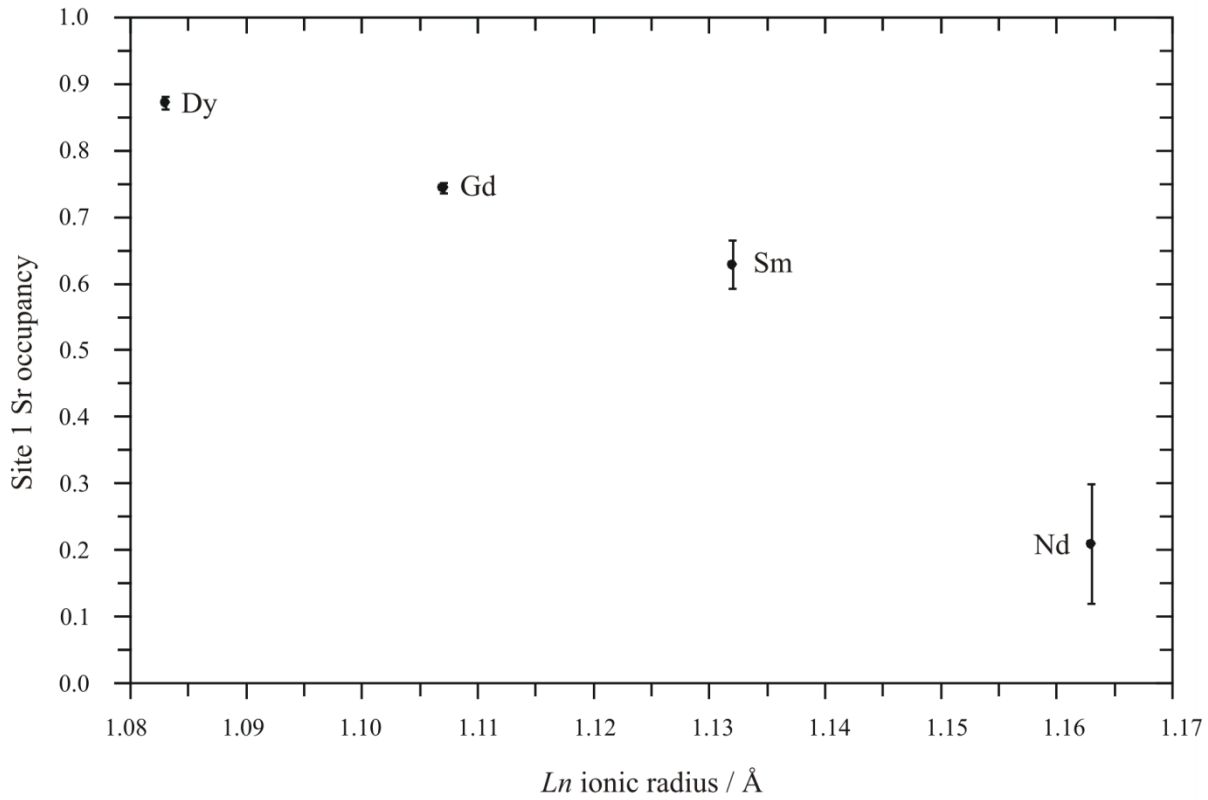

Figure 5.8 – Variation of the refined Sr occupancy on the perovskite block *A* site with increasing *Ln* ionic radius in the series $Ln_2SrAl_2O_7$ extracted from structural refinements based on powder X-ray and neutron diffraction. Error bars show one standard error.

References

1. J. Fava and G. le Flem, *Mat. Res. Bull*., 1975, 10, 75-80
2. I. A. Zvereva, V. F. Popova, D. A. Vagapov, A. M. Toikka and V. V. Gusarov, *Russ. J. General Chem*., 2001, **71**, 1181-1185
3. I. A. Zvereva, Y. Smirnov, V. Gusarov, V. Popova and J. Choisnet, *Solid State Sci*., 2003, **73**, 343-349
4. I. A. Zvereva, S. R. Seitabaeva and Y. Smirnov, *Russ. J. General Chem*., 2003, **73**, 31-36
5. V. F. Popova, E. A. Tugova, I. A. Zvereva and V. V. Gusarov, *Glass Phys. Chem*., 2004, **30**, 564-567
6. I. A. Zvereva, V. F. Popova, E. A. Tugova, N. S. Pylkina and V. V. Gusarov, *Glass Phys. Chem*., 2005, **31**, 808-811
7. V. F. Popova, E. A. Tugova, A. S. Isaeva, I. A. Zvereva and V. V. Gusarov, *Glass Phys. Chem*., 2007, **33**, 498-501
8. I. A. Zvereva, A. S. Isaeva and J. Choisnet, *Russ. J. General Chem*., 2009, **76**, 875-880
9. A. S. Isaeva, I. I. Kozhina, A. M. Toikka and I. A. Zvereva, *Glass Phys. Chem*., 2006, **32**, 106-112
10. L. Zhiyou, Z. Xiaoyong, H. Junfeng and Z. Kechao, *J. Cryst. Growth*, 2007, **305,** 265-270
11. E. A. Tugova, V. F. Popova, I. A. Zhvereva and V. V. Gusarov, *Russ. J. General Chem*., 2007, **77**, 979-981
12. I. A. Zhvereva, I. V. Otreping, V. G. Samenov, E. A. Tugova, V. F. Popova and V. V. Gusarov, *Russ. J. General Chem*, 2007, **77**, 973-978

Chapter 6 – Mixed *B*-site Ruddlesden-Popper phases

Introduction

In previous chapters, materials with the stochiometry $Ln_2AB_2O_7$ have been studied. In this chapter, the effect of substituting onto the *B* site for materials in the family $A_3B_2O_7$ is examined.

Double perovskite phases

The double perovskites are materials with the general formula $A_2BB'O_6$. As for standard perovskites, the *A* cations (typically large cations such as the alkali metals, alkali earths or rare earths) sit in the 12-coordinate sites while the *B* cations occupy the centre of a BO_6 octahedron. As with other perovskites, tilting of octahedra gives rise to a rich variety of structural chemistry for these phases, however ordering of the *B*-sites in these phases leads to additional structures and properties not possible for the unsubstituted parent materials. As well as the standard rock salt structures adopted by materials with randomly distributed *B* sites, cation ordering generates either a layered or rock salt arrangement of the metal ions, as shown in Figure 6.1. A full review of the possible structure types adopted by a wide range of double perovskites can be found in the work of Poeppelmeier *et al*. [1]

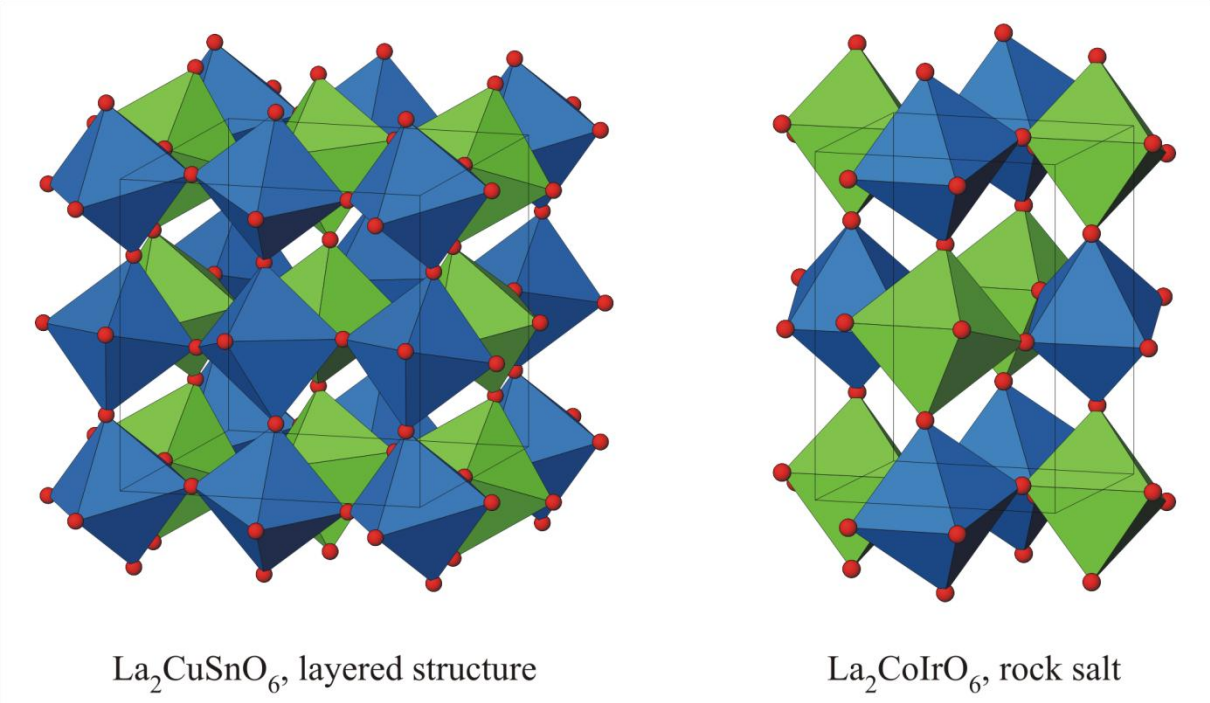

Figure 6.1 – Ordered double perovskite phases La_2CuSnO_6 and La_2CoIrO_6. *A* site cations have been omitted for clarity. Blue octahedra show CuO_6 and CoO_6, while green octahedra show SnO_6 and IrO_6.

As well as the interesting structural chemistry displayed by these phases, the properties of ordered double perovskites are of interest as the sublattice ordering leads to improved orbital overlap and the possibility of superexchange. This superexchange in turn leads to long range magnetic order in a host of double perovskite phases, and in many iron-based double perovskites to magnetoresistance with stability above room temperature. The structure-

property relationships demonstrated in many of these phases are discussed by Serrate *et al*., [2] and several notable double perovskite phases are discussed in chapter one of this work.

Mixed B-*site* $A_3B_2O_7$ *phases – "double Ruddlesden-Popper phases"*

The structures and properties of the double perovskites make them attractive targets for materials chemistry. By altering the stochiometry of starting materials, the layered Ruddlesen-Popper $A_3BB'O_7$ analogues can be formed. Recently published work on these phases has focussed on the cobaltates, [3-4] ferrates, [5-11] manganites [5, 12-14] and molybdates. [7, 15]

Boulahya *et al*. reported the synthesis of the materials Sr_2CoTaO_6 and Sr_3CoTaO_7 in the series $Sr_{n+1}(CoTa)_{n/2}O_{3n+1}$. [3] The $n = \infty$ end member shows short range ordering of the Co and Ta ions, and the structure is best described as an intergrowth of $SrCoO_3$, $SrTaO_3$ and the mixed phase, determined by synchrotron X-ray diffraction. The $n = 2$ phase crystallises in the space group *I*4/*mmm*, with completely random distribution of the *B*-site cations. Yoshii reported the phases $Sr_{n+1}(CoNb)_{n/2}O_{3n+1}$ ($n = \infty$, 1 and 2) in 2000, [4] with the $n = 1$ and 2 phases crystallising in the space group *I*4/*mmm* and exhibiting no long range magnetism.

The phases $Sr_3Mn_{2-x}Fe_xO_7$ in the range $0.15 \leq x \leq 1$ were synthesised by Min-Seok et al., [5, 10] with the intention of stabilising the manganites which cannot be formed stochiometrically. The stabilising effect was observed by the reduction in required reaction temperature with increasing *x*, from 1803 K for $Sr_3Mn_{1.85}Fe_{0.15}O_7$ to 1673 K for Sr_3MnFeO_7. For phases with $x < 0.5$ the materials display spin glass behaviour at low temperature. The structure of the material Sr_3FeTaO_7 was reported by Zhaofei *et al*., [6] and displays antiferromagnetic interactions at low temperature, but no long range magnetic ordering. The *B* site cations are randomly distributed over the one crystallographic site. The phase Sr_3FeMoO_7 has been reported by two groups. [7-8] Despite its analogous structure to the magnetoresistive double perovskite Sr_2FeMoO_6, [2] no magnetoresistance is observed in the material. Zhaofei *et al*. report an antiferromagnetic structure at low temperature, though Sher *et al*. do not observe long range magnetic ordering. The phases $Sr_3Fe_{2-x}Nb_xO_7$ ($x = 0.3$, 0.6, 1.0) were prepared by Sharma *et al*. [9] Once again, the B-site cations were randomly distributed in this group of antiferromagnetic phases. Battle *et al*. reported the structure of Sr_3FeRuO_7 in 1999. [11] The material is a spin glass at low temperature, demonstrating frustrated magnetism between the superexchanges of Fe^{3+} and Ru^{5+}. All the iron materials reported crystallise in *I*4/*mmm*, and in every case the *B*-site is disordered.

The phase Sr_3MnRuO_7 was originally reported by Sharma and Magotra, and its structure reported as determined by Rietveld refinement based on X-ray powder diffraction. [14] Galleon *et al*. later used powder neutron diffraction to determine the structure as a function of temperature. [13] At all the temperatures, the structure of the material refines in *I*4/*mmm*, based on $Sr_3Ti_2O_7$, with a disordered *B* site.

For all materials the $Sr_3BB'O_7$ materials previously discussed, the phases crystallise in the space group *I*4/*mmm*. The only previously studied mixed B-site material with a distorted oxygen sublattice was presented by Battle et al. [12] The crystal structure of La_3LiMnO_7 as refined to fit powder neutron diffraction data was reported as $P4_2/mnm$, with a random distribution of Li and Mn over the single *B* site.

In this chapter, the syntheses and structures of various $A_3B_2O_7$ materials with mixed *B* sites are examined. X-ray and neutron powder diffraction are used for structural analysis.

$Nd_{2-x}Sr_{1+x}Fe_{2-x}Ti_xO_7$ ($0 \leq x \leq 1$)

Our previous work on the structures of ferrates and aluminates suggested that the structure of Ruddlesden-Popper materials was heavily dependent on the *A*-site ions and distribution. By studying materials with mixed *A*-sites this effect could be investigated, however by selecting the series $Nd_{2-x}Sr_{1+x}Fe_{2-x}Ti_xO_7$ the distribution of the *A* site can be predicted based on previous studies in this work, and structural trends can be analysed by analogy with $Sr_3Ti_2O_7$ and $Nd_2SrFe_2O_7$ intergrowth.

Synthesis

The phases were all prepared by solid state reaction of TiO_2, Fe_2O_3, $SrCO_3$ and Nd_2O_3 (dried at 1273 K prior to use and used immediately on cooling). Materials were prepared with the stoichiometries x = 0, 0.2, 0.4, 0.6, 0.8 and 1. Starting reagents were ground together and heated to 1273 K overnight, before regrinding, pelletising and heating to 1573 K for one week, with one intermittent regrind. Materials were checked for purity with X-ray diffraction, then large (5 g) samples prepared for neutron powder diffraction.

Neutron diffraction

Room temperature powder neutron diffraction data sets were collected using neutrons monochromated to 1.59432 Å on the D2B diffractometer at the Institut Laue-Langevin. Three hour data sets were collected on the x = 0, 0.2, 0.4, 0.6 and 0.8 phases, and a twelve hour data set for x = 1.

The normalised diffraction data are shown in Figure 6.2. For the longer data set collected for $NdSr_2TiFeO_7$, 60 parameters were refined to fit the data: 24 background parameters, one histogram scale factor, one zero point error; two lattice parameters, five pseudo-Voight peak shape parameters, [16-17] eleven atomic coordinates, eight isotropic temperature factors and one fractional occupancy for the main phase; one scale factor, three peak shape parameters, one lattice parameter and three isotropic temperature factors for the double perovskite impurity phase.

For the phases x = 0.2, 0.4, 0.6 and 0.8, 50 parameters were refined per data set: 16 background parameters, one histogram scale factor, one zero point error; two lattice parameters, five pseudo-Voight peak shape parameters, eleven atomic coordinates and eight

isotropic temperature factors for the main phase; one scale factor, two peak shape parameters, one lattice parameter and three isotropic temperature factors for the double perovskite impurity phase.

For the $Nd_2SrFe_2O_7$ structure, 50 parameters were refined: 16 background parameters, one histogram scale factor, one zero point error; two lattice parameters, four pseudo-Voight peak shape parameters, eleven atomic coordinates, eight isotropic temperature factors and one fractional occupancy for the main phase; one scale factor, two peak shape parameters and three lattice parameter factors for the $NdFeO_3$ impurity phase.

The profile fits are shown in Figure 6.3, Figure 6.4, Figure 6.5, Figure 6.6, Figure 6.7 and Figure 6.8. Structural parameters extracted from the refinements are shown in Table 6.1, Table 6.2, Table 6.3, Table 6.4, Table 6.5 and Table 6.6. Bond lengths and angles extracted from the refinements are shown in Figure 6.9, Figure 6.10 and Table 6.7, and lattice parameters in Figure 6.11.

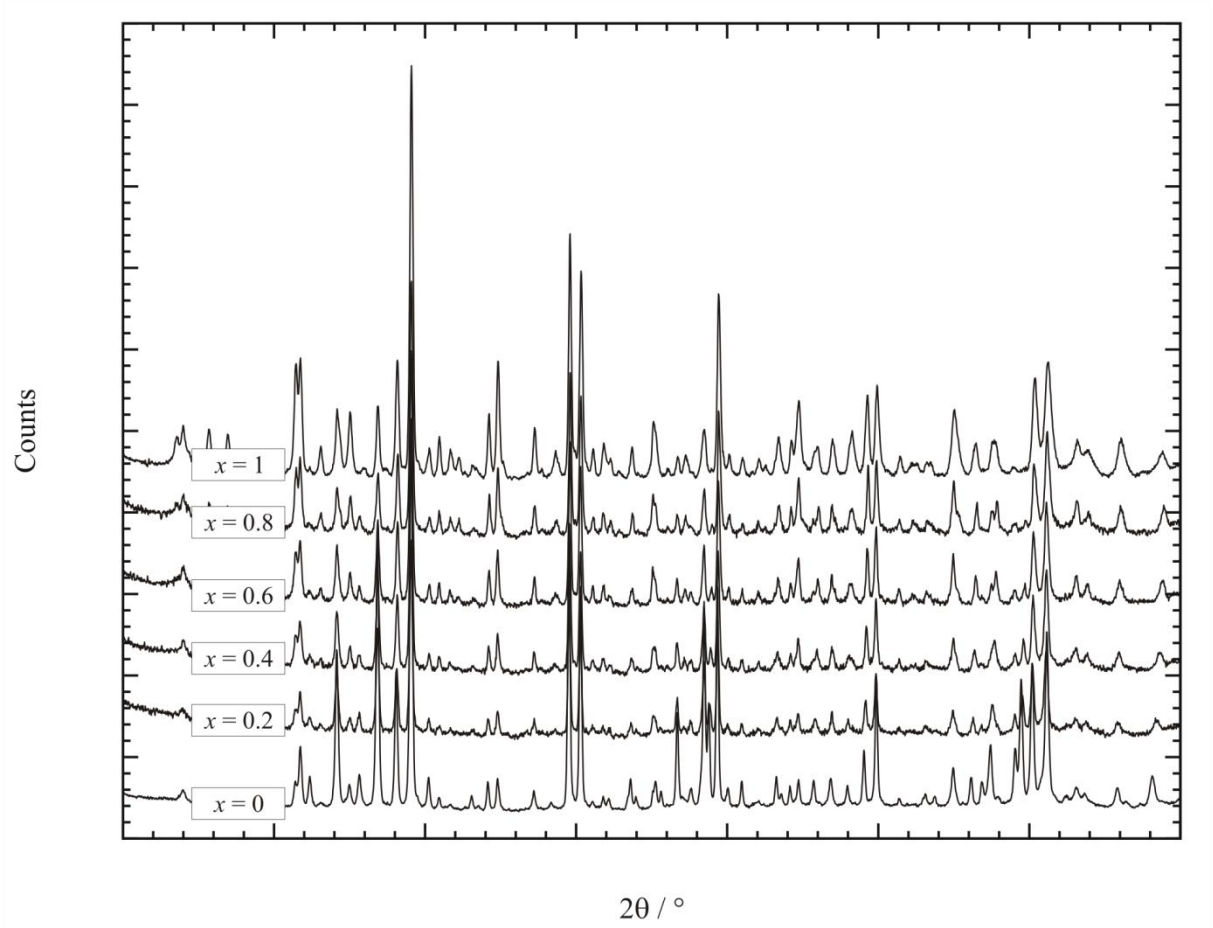

Figure 6.2 – Neutron powder diffraction patterns collected at room temperature on samples of $Nd_{2-x}Sr_{1+x}Fe_{2-x}Ti_xO_7$. λ = 1.59432 Å.

As the titanium content increases in the material series, the octahedral distortion and tilting decreases. The material $Sr_3Ti_2O_7$ contains relatively regular octahedra (this is discussed in the next chapter), with no tilting and all Ti-O bond lengths approximately equal. As x is increased, the structure tends to a more regular structure. For the x = 1 material, the octahedral tilts are small, at 174.4 ± 0.8 ° between perovskite sheets and 175.3 ± 0.5 ° within

each sheet. As previously observed by Sharma *et al.* for the phases $Sr_3Fe_{2-x}Nb_xO_7$, the a cell parameter is essentially invariant with changing composition, however the c cell parameter expands as the strontium content, *x*, increases. The $x = 0$ phase is the exception to the trend – the sample is somewhat older and the larger c could be due to water take-up by the material.

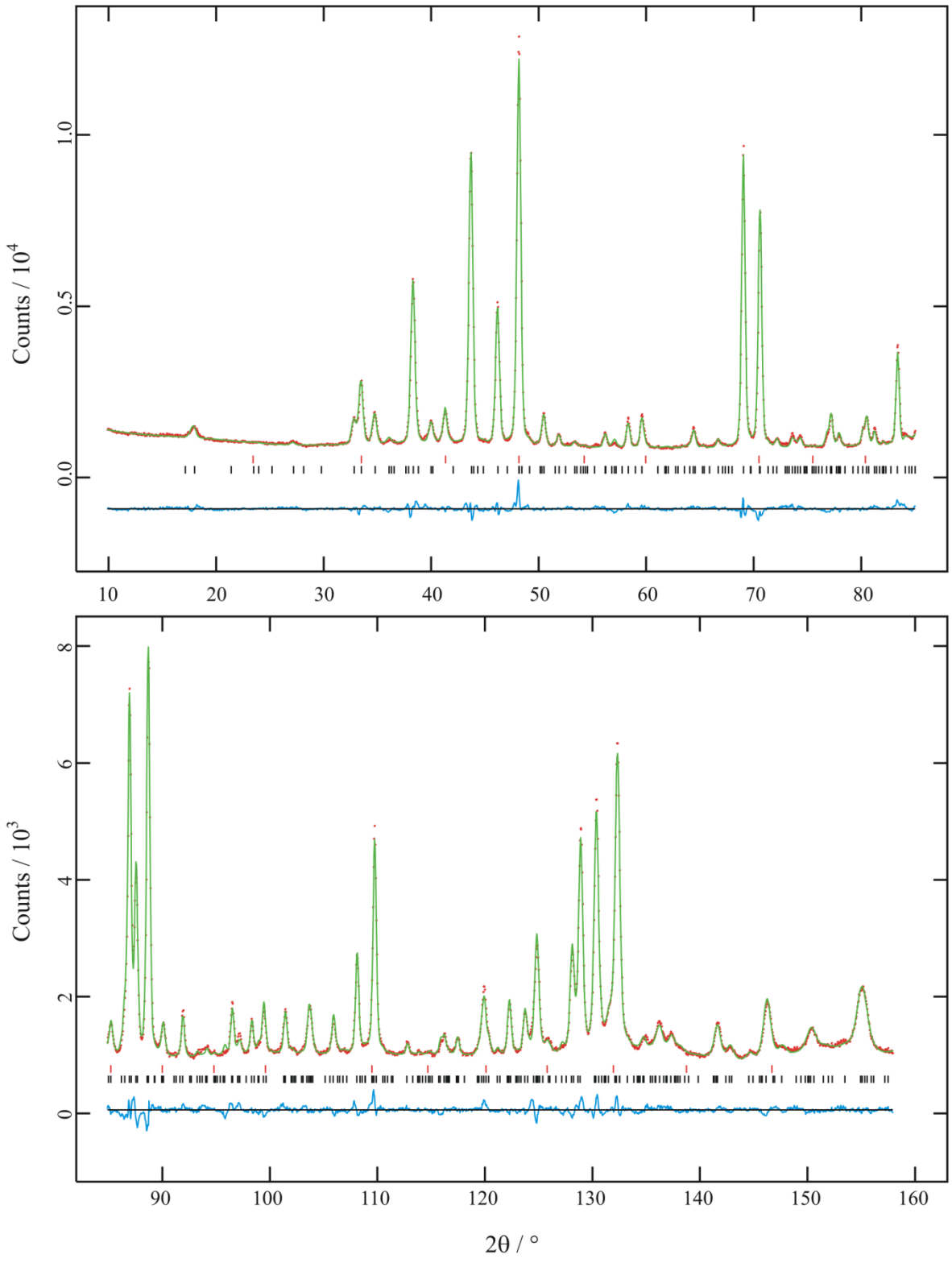

Figure 6.3 – Profile fit of $NdSr_2TiFeO_7$ to neutron diffraction data, $\lambda = 1.59432$ Å, in $P4_2/mnm$. $R_{wp} = 3.42$ %, $R_p = 2.68$ %, $\chi^2 = 1.697$. Red points show the data and the green and blue lines show the predicted diffraction pattern and difference plots.

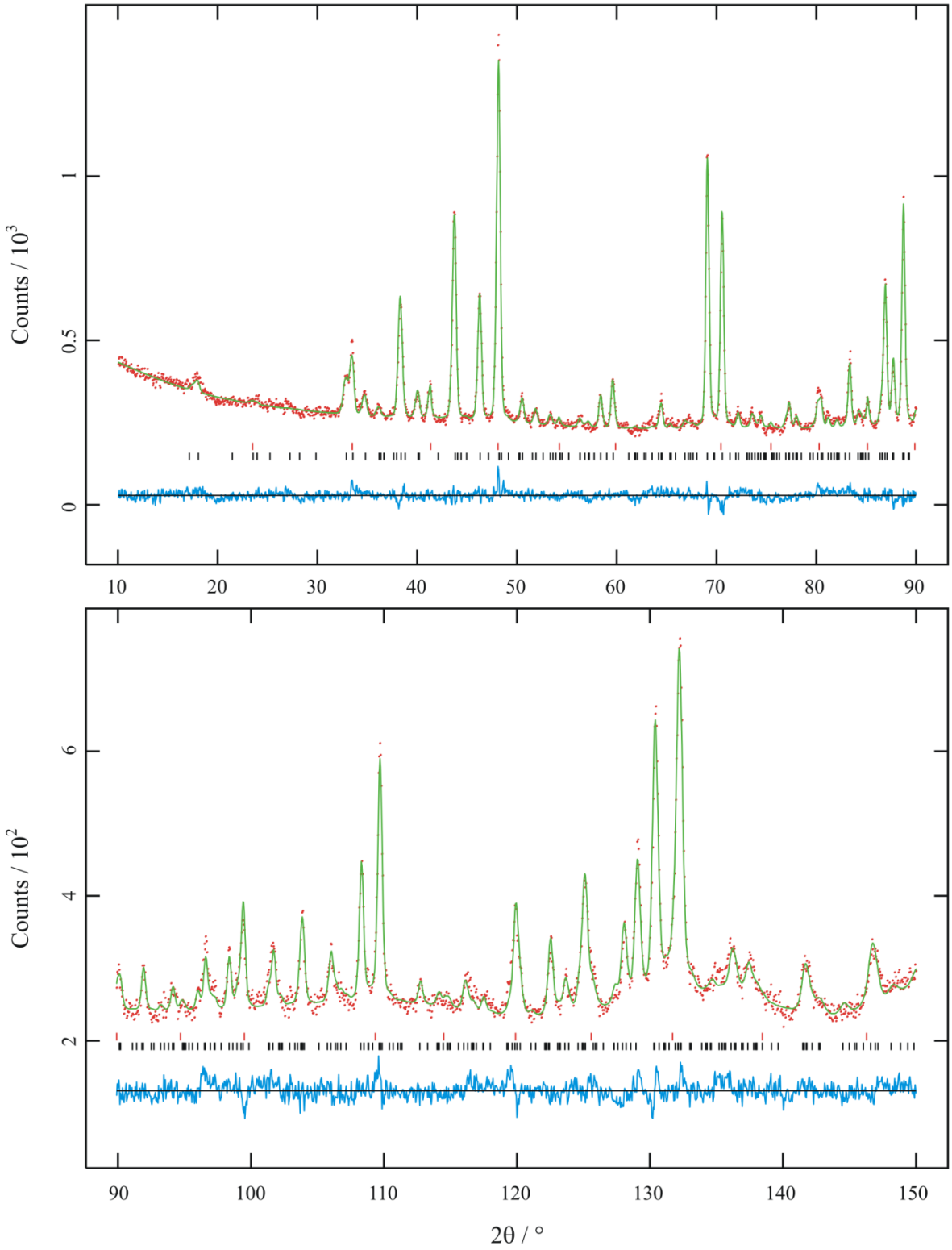

Figure 6.4 – Profile fit of $Nd_{1.2}Sr_{1.8}Ti_{0.8}Fe_{1.2}O_7$ to neutron diffraction data, λ = 1.59432 Å, in $P4_2/mnm$. R_{wp} = 3.74 %, R_p = 2.99 %, χ^2 = 0.4294.

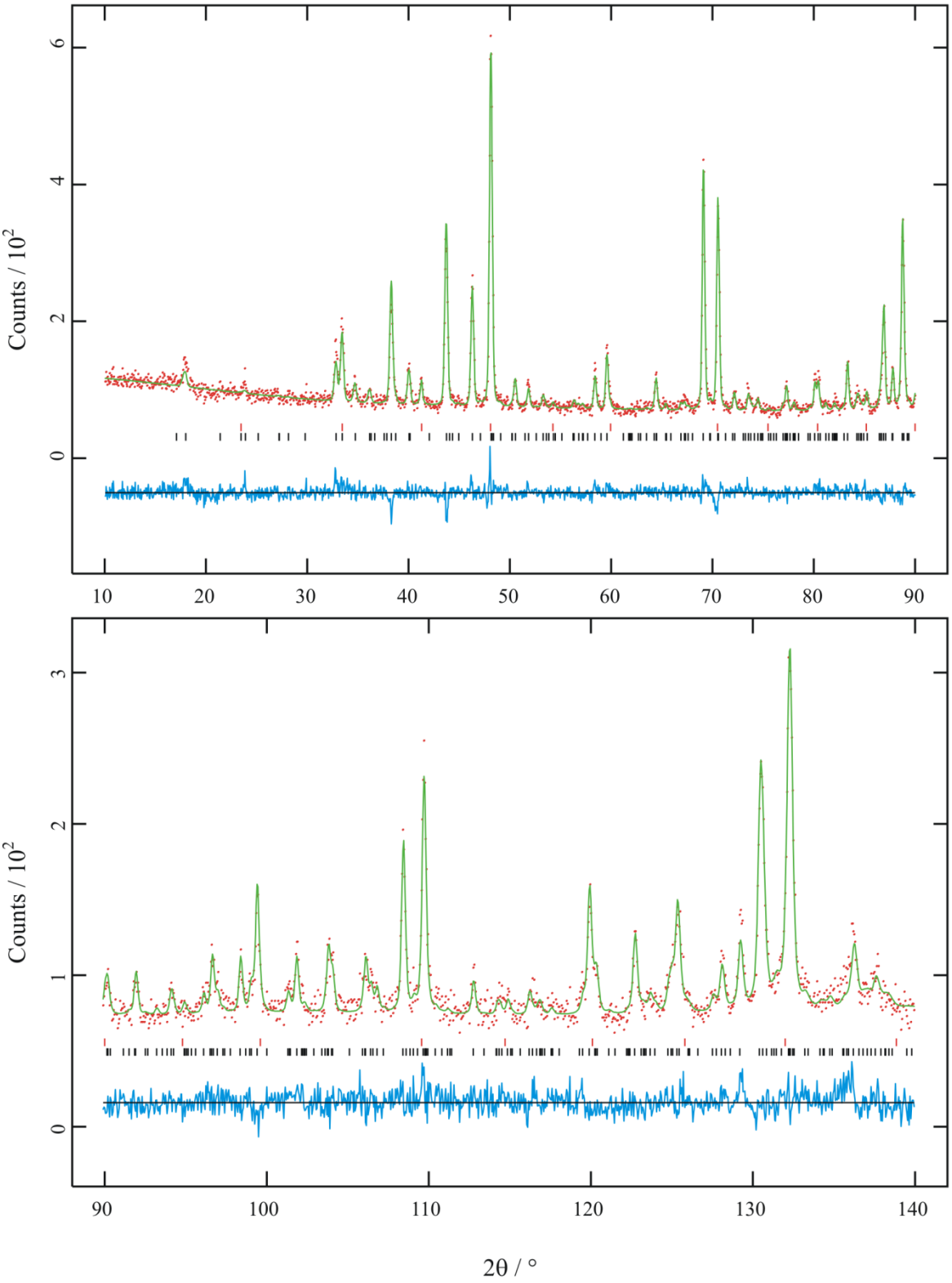

Figure 6.5 – Profile fit of $Nd_{1.4}Sr_{1.6}Ti_{0.6}Fe_{1.4}O_7$ to neutron diffraction data, λ = 1.59432 Å, in $P4_2/mnm$. R_{wp} = 6.73 %, R_p = 5.30 %, χ^2 = 0.4401.

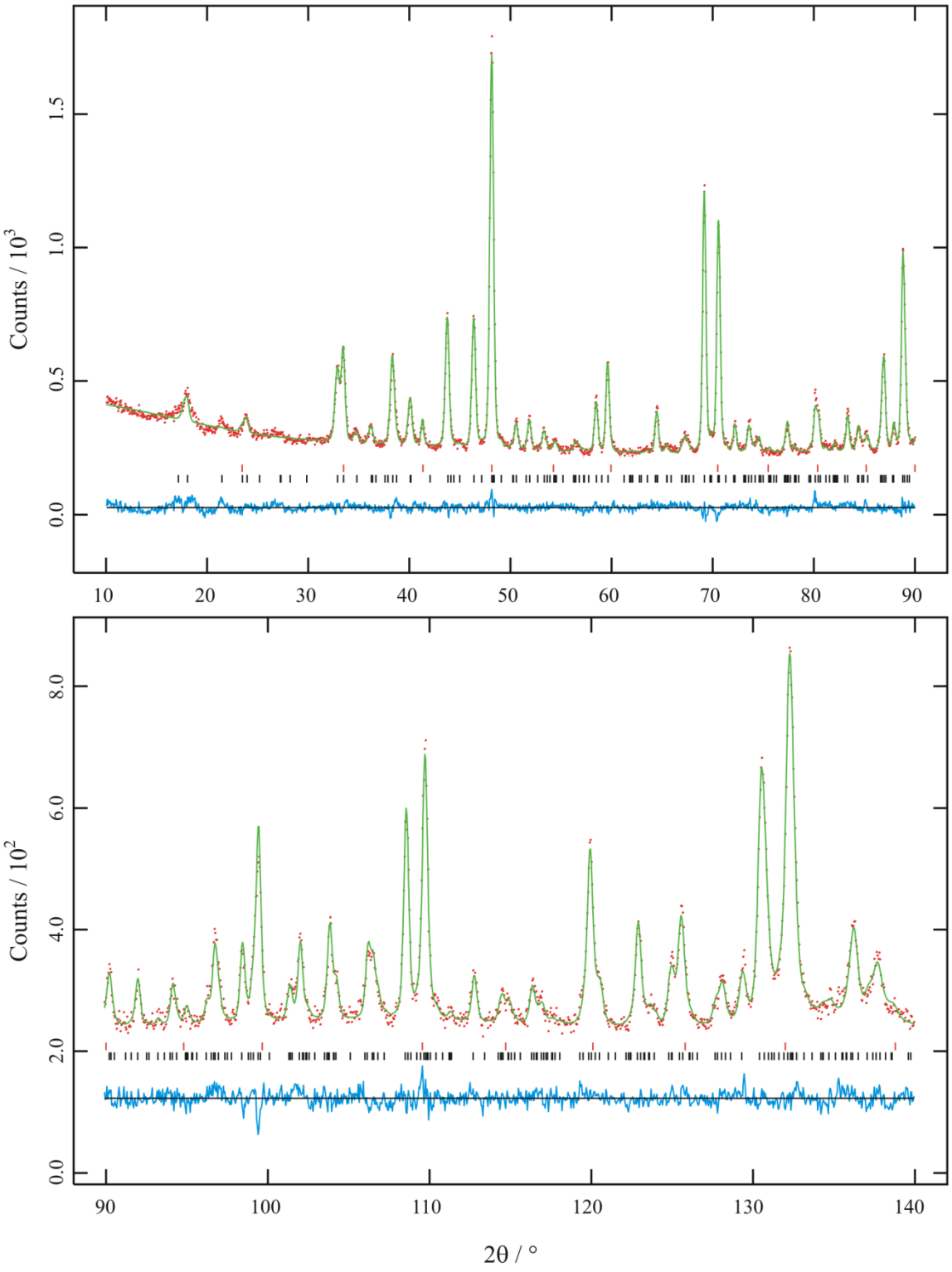

Figure 6.6 – Profile fit of $Nd_{1.6}Sr_{1.4}Ti_{0.4}Fe_{1.6}O_7$ to neutron diffraction data, λ = 1.59432 Å, in $P4_2/mnm$. R_{wp} = 3.80 %, R_p = 3.02 %, χ^2 = 0.4706.

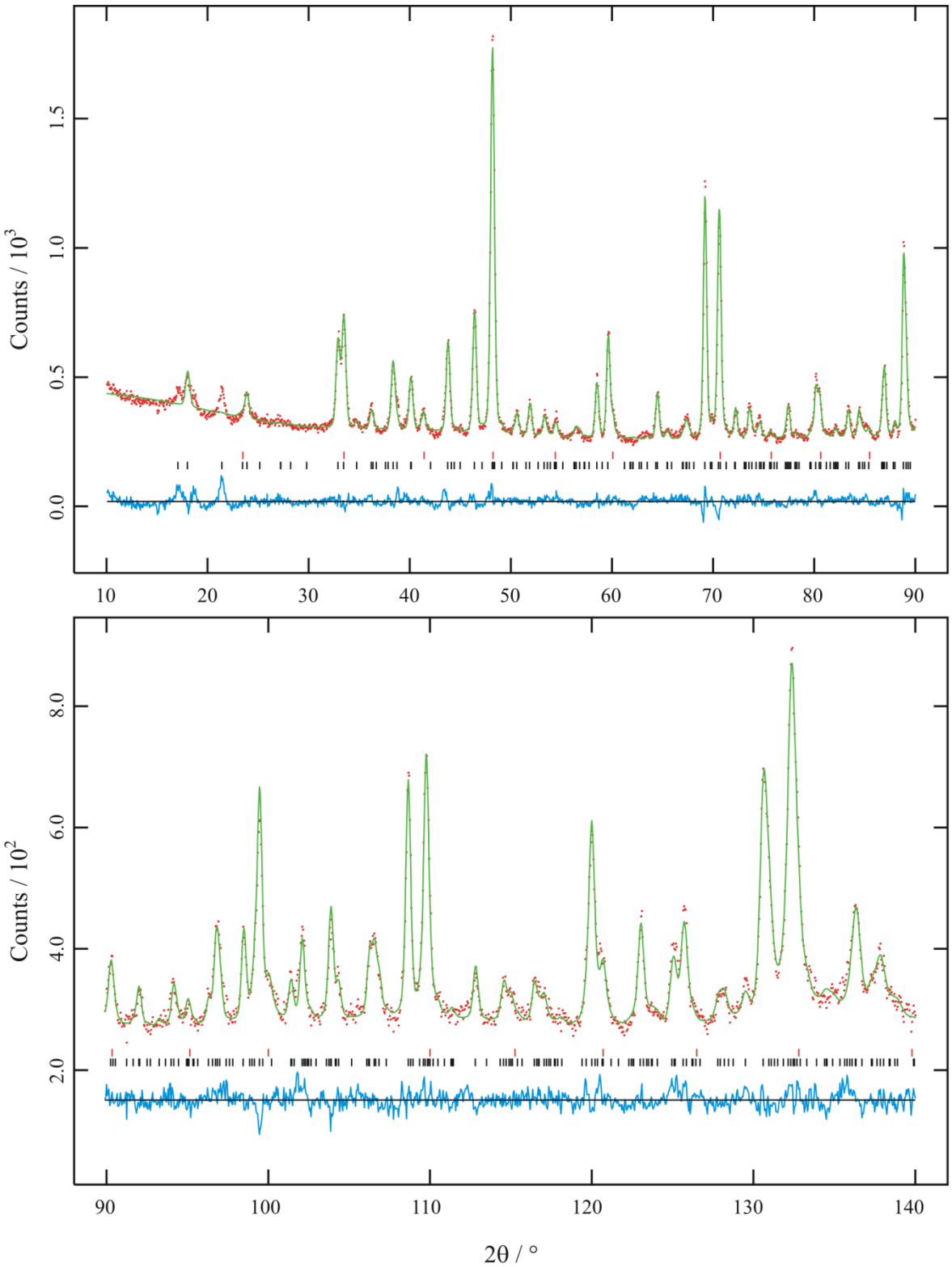

Figure 6.7 – Profile fit of $Nd_{1.8}Sr_{1.2}Ti_{0.2}Fe_{1.8}O_7$ to neutron diffraction data, λ = 1.59432 Å, in $P4_2/mnm$. R_{wp} = 4.19 %, R_p = 3.25 %, χ^2 = 0.6336.

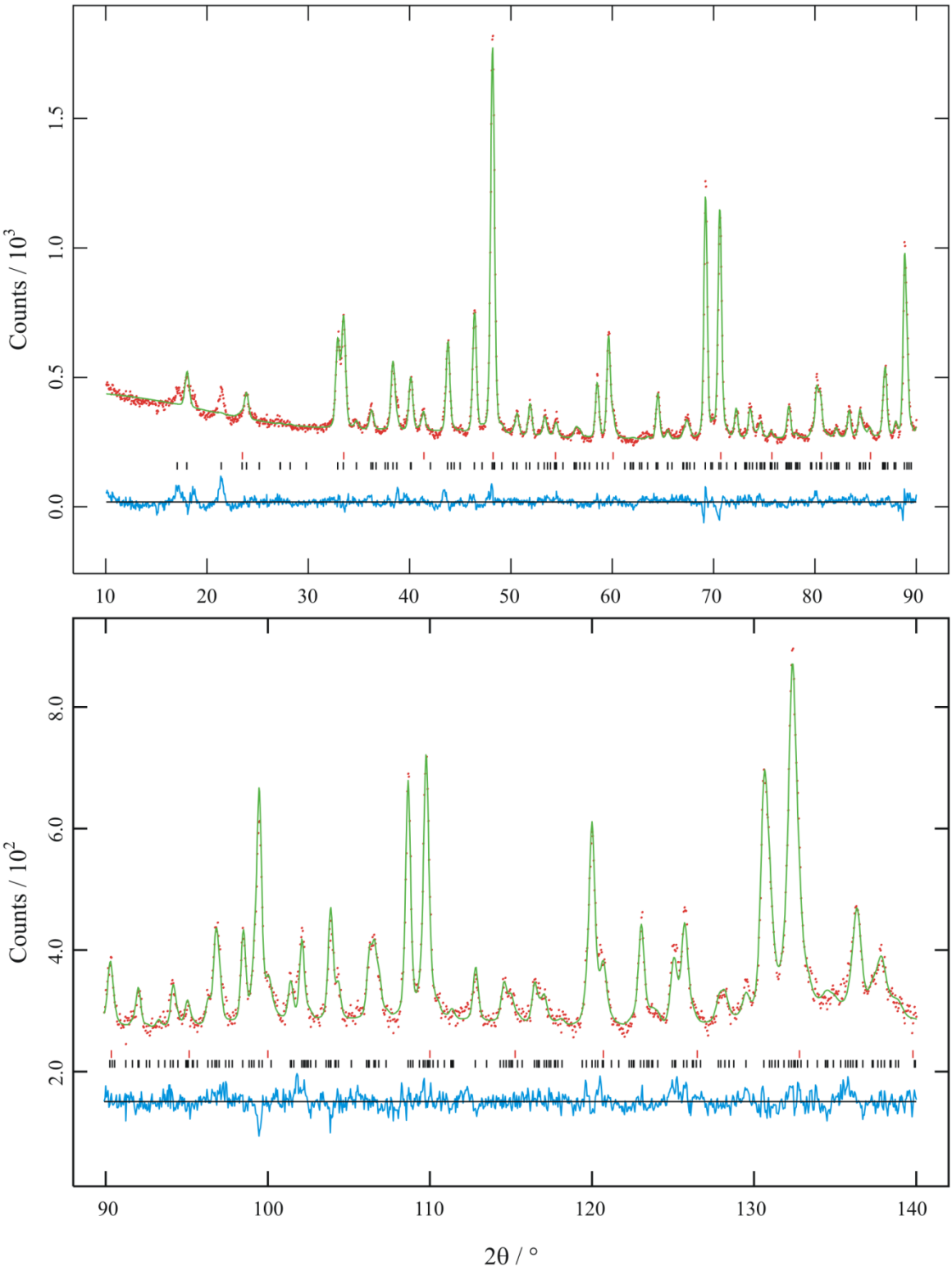

Figure 6.8 – Profile fit of $Nd_2SrFe_2O_7$ to neutron diffraction data, λ = 1.59432 Å, in $P4_2/mnm$. R_{wp} = 5.72 %, R_p = 4.03 %, χ^2 = 2.250.

Table 6.1 – Structural parameters extracted from the refinement of $NdSr_2TiFeO_7$. $a = b = 5.51063$ (9) Å, $c = 20.2719$ (4) Å.

Atom	*x/a*	*y/b*	*z/c*	U_{iso} / 10^{-2} Å	Site occupation
Sr1	0.2531 (8)	0.2531 (8)	0	1.40 (6)	0.59 (8)
Nd1	0.2531 (8)	0.2531 (8)	0	1.40 (6)	0.41(8)
Sr2	0.2521 (4)	0.2521 (4)	0.18344 (7)	1.32 (3)	0.71 (4)
Nd2	0.2521 (4)	0.2521 (4)	0.18344 (7)	1.32 (3)	0.29 (4)
Fe	0.2533 (15)	0.2533 (15)	0.40152 (14)	0.80 (5)	0.5
Ti	0.2533 (15)	0.2533 (15)	0.40152 (14)	0.80 (5)	0.5
O1	0.7658 (10)	0.2342 (10)	0	2.56 (9)	1
O2	0	0.5	0.09874 (20)	1.29 (6)	1
O3	0	0	0.1074 (2)	2.14 (12)	1
O4	0	0	0.4077 (3)	1.93 (11)	1
O5	0.2339 (8)	0.2339 (8)	0.30053 (10)	3.09 (6)	1

Table 6.2 – Structural parameters extracted from the refinement of $Nd_{1.2}Sr_{1.8}Ti_{0.8}Fe_{1.2}O_7$. $a = b = 5.51324$ (20) Å, $c = 20.2356$ (9) Å.

Atom	*x/a*	*y/b*	*z/c*	U_{iso} / 10^{-2} Å	Site occupation
Sr1	0.2533 (11)	0.2533 (11)	0	1.20 (10)	0.6
Nd1	0.2533 (11)	0.2533 (11)	0	1.20 (10)	0.4
Sr2	0.2580 (7)	0.2580 (7)	0.18375 (15)	1.30 (6)	0.6
Nd2	0.2580 (7)	0.2580 (7)	0.18375 (15)	1.30 (6)	0.4
Fe	0.2544 (15)	0.2544 (15)	0.4018 (2)	0.58 (7)	0.6
Ti	0.2544 (15)	0.2544 (15)	0.4018 (2)	0.58 (7)	0.4
O1	0.7786 (15)	0.2214 (15)	0	2.79 (20)	1
O2	0	0.5	0.0977 (4)	1.80 (13)	1
O3	0	0	0.1122 (4)	1.28 (20)	1
O4	0	0	0.4072 (5)	1.8 (2)	1
O5	0.2280 (12)	0.2280 (12)	0.2988 (2)	3.34 (13)	1

Table 6.3 – Structural parameters extracted from the refinement of $Nd_{1.4}Sr_{1.6}Ti_{0.6}Fe_{1.4}O_7$. $a = b = 5.5110$ (2) Å, $c = 20.2036$ (11) Å.

Atom	*x/a*	*y/b*	*z/c*	U_{iso} / 10^{-2} Å	Site occupation
Sr1	0.2559 (14)	0.2559 (14)	0	1.40 (16)	0.5333
Nd1	0.2559 (14)	0.2559 (14)	0	1.40 (16)	0.4667
Sr2	0.2607 (8)	0.2607 (8)	0.1826 (2)	1.37 (9)	0.5333
Nd2	0.2607 (8)	0.2607 (8)	0.1826 (2)	1.37 (9)	0.4667
Fe	0.2559 (14)	0.2559 (14)	0.4027 (3)	0.67 (9)	0.7
Ti	0.2559 (14)	0.2559 (14)	0.4027 (3)	0.67 (9)	0.3
O1	0.7818 (18)	0.2182 (18)	0	2.6 (3)	1
O2	0	0.5	0.0982 (5)	1.77 (17)	1
O3	0	0	0.1147 (6)	1.3 (3)	1
O4	0	0	0.4063 (7)	1.8 (3)	1
O5	0.2239 (14)	0.2239 (14)	0.2976 (4)	3.25 (18)	1

Table 6.4 – Structural parameters extracted from the refinement of $Nd_{1.6}Sr_{1.4}Ti_{0.4}Fe_{1.6}O_7$. $a = b = 5.51303$ (18) Å, $c = 20.1881$ (8) Å.

Atom	*x/a*	*y/b*	*z/c*	U_{iso} / 10^{-2} Å	Site occupation
Sr1	0.2526 (9)	0.2526 (9)	0	1.64 (10)	0.4667
Nd1	0.2526 (9)	0.2526 (9)	0	1.64 (10)	0.5333
Sr2	0.2618 (5)	0.2618 (5)	0.18248 (13)	1.19 (5)	0.4667
Nd2	0.2618 (5)	0.2618 (5)	0.18248 (13)	1.19 (5)	0.5333
Fe	0.2525 (7)	0.2525 (7)	0.40303 (16)	0.81 (5)	0.8
Ti	0.2525 (7)	0.2525 (7)	0.40303 (16)	0.81 (5)	0.2
O1	0.7857 (11)	0.2143 (11)	0	2.69 (20)	1
O2	0	0.5	0.1007 (3)	1.75 (10)	1
O3	0	0	0.1170 (4)	1.78 (18)	1
O4	0	0	0.4086 (4)	1.68 (18)	1
O5	0.2160 (8)	0.2160 (8)	0.2966 (2)	3.06 (12)	1

Table 6.5 – Structural parameters extracted from the refinement of $Nd_{1.8}Sr_{1.2}Ti_{0.2}Fe_{1.8}O_7$. $a = b = 5.50791$ (9) Å, $c = 20.1614$ (6) Å.

Atom	*x/a*	*y/b*	*z/c*	U_{iso} / 10^{-2} Å	Site occupation
Sr1	0.2547 (10)	0.2547 (10)	0	1.25 (13)	0.4
Nd1	0.2547 (10)	0.2547 (10)	0	1.25 (13)	0.6
Sr2	0.2644 (6)	0.2644 (6)	0.18243 (17)	1.18 (7)	0.4
Nd2	0.2644 (6)	0.2644 (6)	0.18243 (17)	1.18 (7)	0.6
Fe	0.2533 (7)	0.2533 (7)	0.40335 (18)	0.79 (6)	0.9
Ti	0.2533 (7)	0.2533 (7)	0.40335 (18)	0.79 (6)	0.1
O1	0.7899 (13)	0.2101 (13)	0	2.64 (26)	1
O2	0	0.5	0.1013 (4)	1.74 (11)	1
O3	0	0	0.1186 (4)	1.4 (2)	1
O4	0	0	0.4100 (4)	1.17 (20)	1
O5	0.2132 (9)	0.2132 (9)	0.2953 (3)	2.62 (14)	1

Table 6.6 – Structural parameters extracted from the refinement of $Nd_2SrFe_2O_7$. $a = b = 5.50923$ (16) Å, $c = 20.2084$ (8) Å.

Atom	*x/a*	*y/b*	*z/c*	U_{iso} / 10^{-2} Å	Site occupation
Sr1	0.2558 (9)	0.2558 (9)	0	0.39 (11)	0.53 (14)
Nd1	0.2558 (9)	0.2558 (9)	0	0.39 (11)	0.47 (17)
Sr2	0.2636 (5)	0.2636 (5)	0.18214 (14)	0.29 (6)	0.23 (7)
Nd2	0.2636 (5)	0.2636 (5)	0.18214 (14)	0.29 (6)	0.77 (7)
Fe	0.2538 (5)	0.2538 (5)	0.40422 (12)	0.30 (5)	1
O1	0.7902 (10)	0.2098 (10)	0	1.22 (17)	1
O2	0	0.5	0.1043 (3)	0.75 (10)	1
O3	0	0	0.1171 (4)	0.47 (17)	1
O4	0	0	0.4103 (4)	0.88 (20)	1
O5	0.2069 (6)	0.2069 (6)	0.2934 (3)	0.90 (10)	1

Table 6.7 – Bond lengths and angles extracted from the structural refinements of $Nd_{2-x}Sr_{1+x}Ti_xFe_{2-x}O_7$.

x	1	0.8	0.6	0.4	0.2	0
Fe-O1 / Å	1.999 (3)	1.996 (5)	1.976 (6)	1.975 (4)	1.969 (4)	1.956 (3)
Fe-O2 / Å (× 2)	1.94848 (16)	1.9496 (2)	1.9491 (3)	1.9507 (3)	1.9498 (4)	1.9556 (6)
Fe-O3 / Å	1.931 (12)	1.936 (11)	1.935 (11)	1.972 (6)	1.972 (5)	1.966 (4)
Fe-O4 / Å	1.978 (12)	1.986 (12)	1.996 (11)	1.972 (6)	1.977 (6)	1.981 (4)
Fe-O5 / Å	2.053 (3)	2.095 (6)	2.138 (9)	2.167 (6)	2.200 (7)	2.269 (6)
Fe-O1-Fe / °	174.4 (8)	169.1 (8)	168.3 (9)	164.9 (5)	163.3 (6)	163.3 (5)
Fe-O2-Fe / °	179.6 (2)	179.3 (6)	178.9 (7)	175.6 (4)	174.4 (5)	169.9 (4)
Fe-O3-Fe / °	169.2 (3)	163.1 (5)	159.0 (7)	156.4 (5)	154.1 (5)	154.7 (5)
Fe-O4-Fe / °	172.7 (3)	173.7 (7)	175.8 (9)	173.5 (5)	172.2 (5)	172.9 (5)

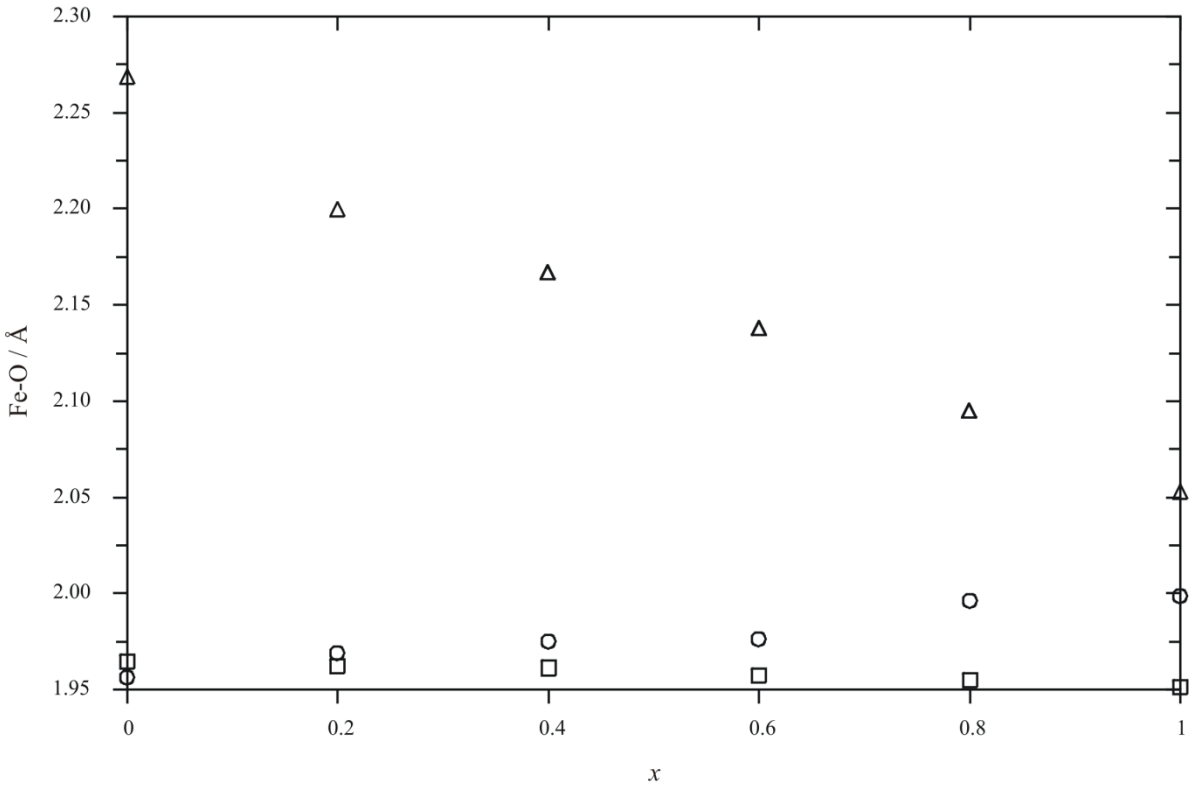

Figure 6.9 – Bridging (○), equatorial (□) and apical (Δ) Fe-O bonds in the materials $Nd_{2-x}Sr_{1+x}Ti_xFe_{2-x}O_7$. Errors lie within point size.

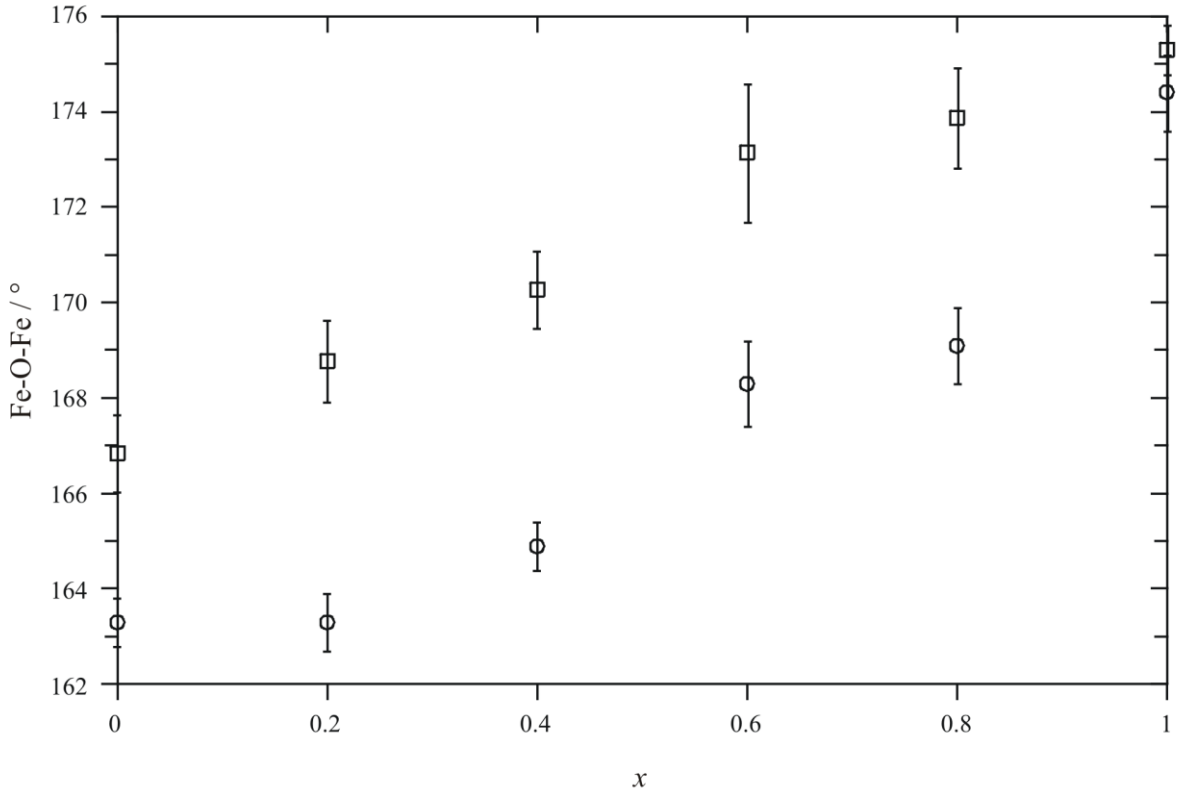

Figure 6.10 – In layer (○) and interlayer (□) Fe-O-Fe angles in the materials $Nd_{2-x}Sr_{1+x}Ti_xFe_{2-x}O_7$. In-layer angles are an average of the three refined angles. Error bars show one standard error.

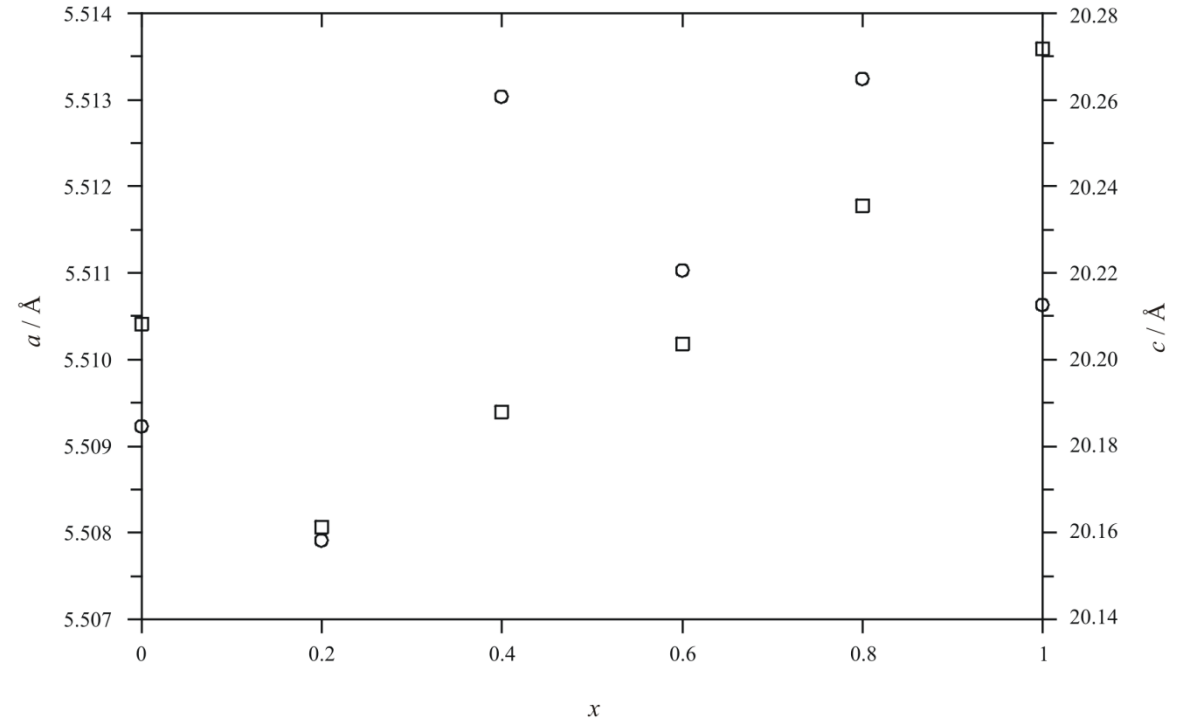

Figure 6.11 – *a* (○) and *c* (□) lattice parameters extracted from refinement of powder neutron diffraction data in the series $Nd_{2-x}Sr_{1+x}Ti_xFe_{2-x}O_7$. Errors lie within point size.

$Sr_3BB'O_7$

Synthesis

A range of syntheses for $Sr_3BB'O_7$ were attempted. The starting materials WO_3, CuO, NiO, ZnO, CoO, Fe_2O_3, Co_3O_4, Sc_2O_3, Ta_2O_5 and Nb_2O_5 were mixed stochiometrically with $SrCO_3$ to attempt the synthesis of the phases shown below. All mixtures were initially heated to 1273 K overnight, then pelletised and heated to 1473 K for one week. Products after this time were identified by powder X-ray diffraction, and if no reaction had taken place, then the mixture repelletised and heated to a higher temperature. The maximum temperature attempted was 1723 K. Several of the phases could be formed, however the only phase prepared in high enough purity for further study was the previously formed Sr_3CoNbO_7. [4] The results of the attempted syntheses are summarised in

Table 6.8.

Table 6.8 – Attempted syntheses of $Sr_3BB'O_7$.

	W
Cu	Sr_3WCuO_7 formed. Impurities: WO_3, CuO, Sr_2CuWO_6
Ni	No reaction
Zn	No reaction
Co	Possible perovskite Sr_2CoWO_6 phase; no target material

	Ta	Nb
Fe	Mixed perovskite phases, possible formation of target	Mixture of several perovskites
Sc	No reaction	No reaction
Co	Sr_3TaCoO_7 formed. Impurities: Ta_2O_5, Co_3O_4	Phase pure by X-ray diffraction
Al	No reaction	No reaction

A larger sample of Sr_3CoNbO_7 was prepared for structural study by neutron diffraction.

Sr_3CoNbO_7

A six hour powder diffraction set was collected at room temperature, λ = 1.59432 Å on the D2B instrument at the ILL. Low temperature diffraction data were collected at 3.4 K in the displex sample environment for twelve hours. The same wavelength was used.

Neither room temperature nor 3.4 K diffraction data displayed supercell peaks corresponding to either octahedral tilts, *B*-site or magnetic ordering. The main phase structure could be entirely fitted by the $Sr_3Ti_2O_7$ model, with random cation distribution.

40 parameters were refined for each data set: 12 background parameters, one histogram scale factor and one zero point error for the histogram; two lattice parameters, five pseudo-Voight peak shape parameters, four atomic coordinates and six isotropic temperature factors for the

main phase and one phase scale factor, one lattice parameter, five peak shapes and three isotropic temperature factors for the perovskite impurity phase. The fits to the diffraction data are shown in Figure 6.12 and Figure 6.13.

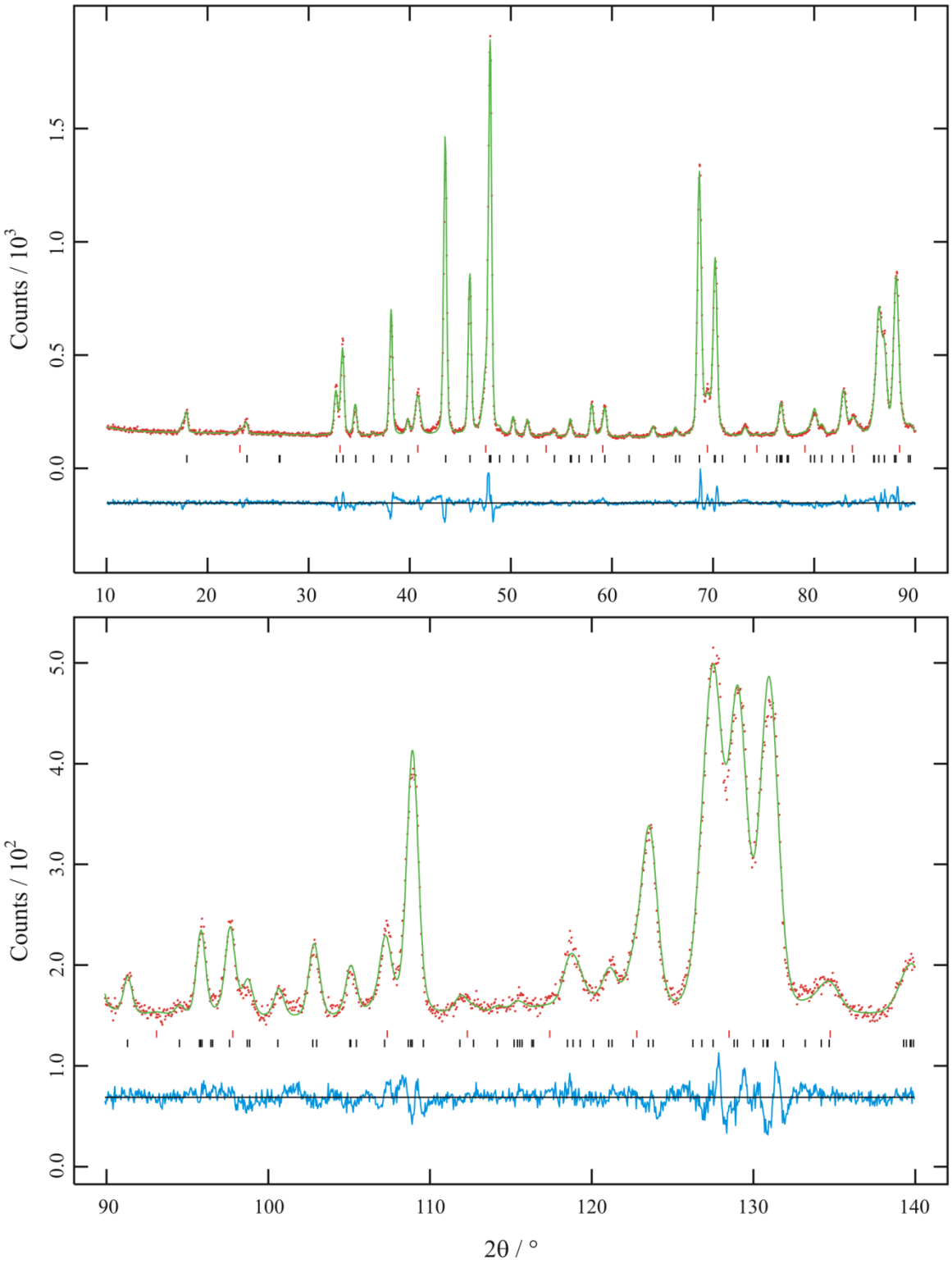

Figure 6.12 – Profile fit of Sr_3CoNbO_7 to the $Sr_3Ti_2O_7$ model to fit room temperature powder neutron diffraction data. R_{wp} = 4.68 %, R_p = 3.64 %, χ^2 = 4.400. $a = b$ = 3.91892 (12) Å, c = 20.4038 (8) Å. Lower tick marks show the positions of main phase reflections, upper tick marks the positions of Sr_2CoNbO_6 reflections.

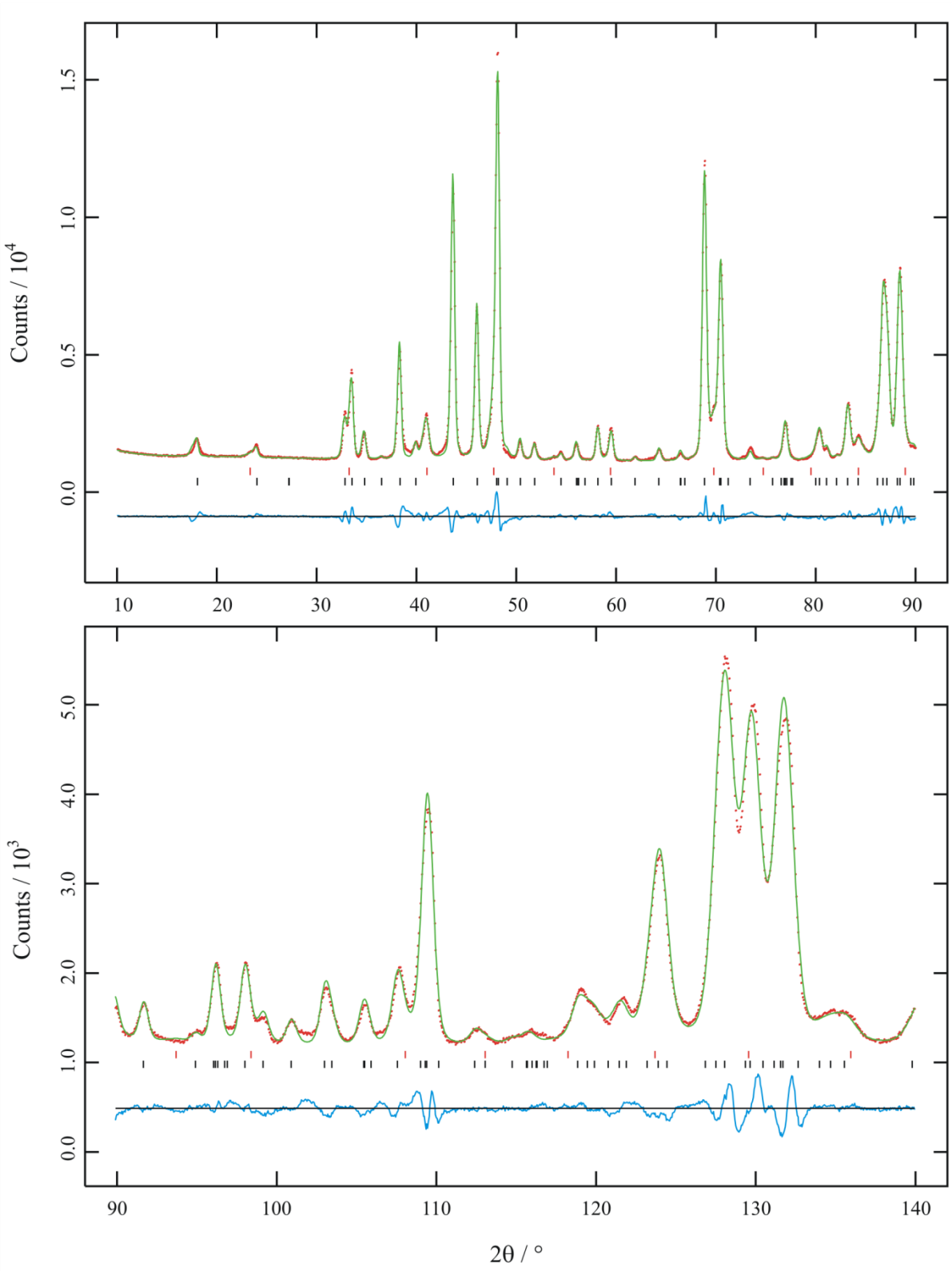

Figure 6.13 – Profile fit of Sr_3CoNbO_7 to the $Sr_3Ti_2O_7$ model to fit 3 K powder neutron diffraction data. R_{wp} = 4.10 %, R_p = 3.04 %, χ^2 = 28.90. $a = b$ = 3.90752 (11) Å, c = 20.3749 (7) Å. Lower tick marks show the positions of main phase reflections, upper tick marks the positions of Sr_2CoNbO_6 reflections.

The refinements to powder neutron diffraction data confirm that even at low temperature, the structure of Sr_3CoNbO_7 does not distort from the *I*4/*mmm* $Sr_3Ti_2O_7$ model.

Conclusions

The structures of the phases $Nd_{2-x}Sr_{1+x}Ti_xFe_{2-x}$ have been determined and structural trends examined as a function of *x*. As the Sr/Ti content increases, the octahedral tilting decreases and the Fe/Ti-O bond lengths all tend to the average value. The structures of the phases are shown in Figure 6.14. Note the reduction of the octahedral tilts as *x* increases. The end member of the series, $Sr_3Ti_2O_7$, has all bond lengths approximately equal, and is examined in the next chapter.

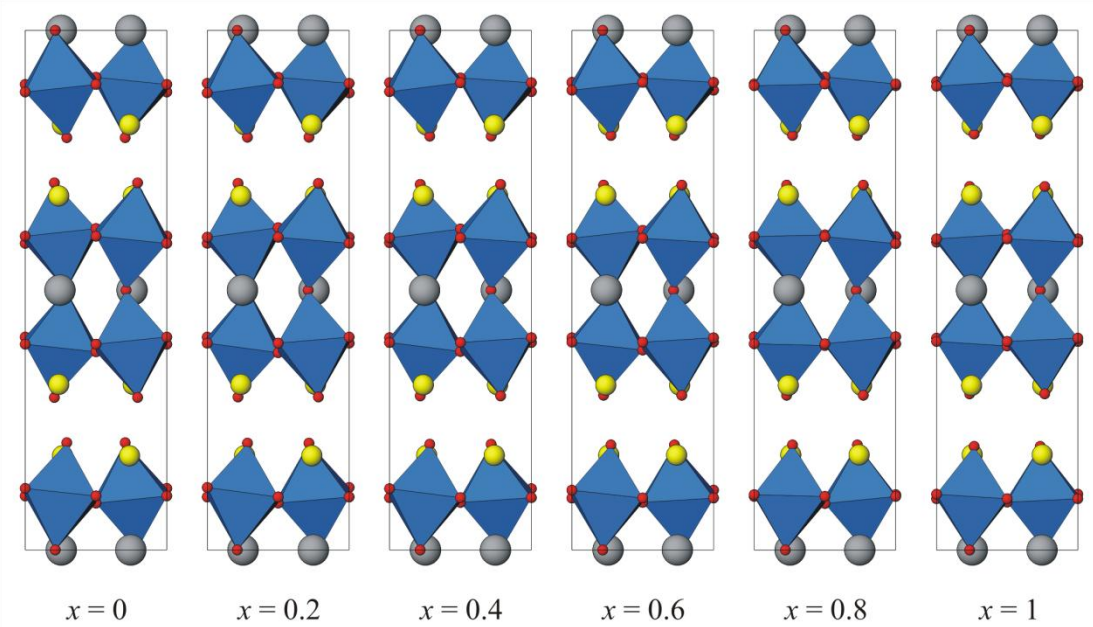

Figure 6.14 – The structures of the materials $Nd_{2-x}Sr_{1+x}Ti_xFe_{2-x}$. Yellow spheres show the rock salt, 9-coordinate site, grey spheres the 12 coordinate, perovskite *A* site, and blue octahedra the Fe/TiO_6.

The syntheses of a number of $Sr_3BB'O_7$ phases were attempted, with only Sr_3CoNbO_7 formed with suitable phase purity for further study. Its structure was determined with powder neutron diffraction at room temperature and 3.4 K, and was shown to be isostructural with $Sr_3Ti_2O_7$, with no oxygen lattice distortions, cation ordering or long-range magnetic ordering even at 3.4 K. From the undistorted structure, the spin state of the cobalt ions in the material can be deduced. Assuming a low spin Co (III) centre, the combined ionic radii of the two *B*-site ions is 0.5925 Å, which with an Sr^{2+} *A* site ion (ionic radius 1.44 Å) falls below the "zero strain" line, $\frac{R_A+R_O}{R_M+R_O} = \sqrt{2}$, [18] and would not be expected to distort. Assuming a high spin Co (III), the combined B-site ionic radius is 0.625 Å, above the zero strain line and equal to the value for the distorted material $Sr_3Ir_2O_7$. [19] The material is therefore assumed to be Co (III) low spin at the two temperatures studied.

References

1. M. T. Anderson, K. B. Greenwood, G. A. Taylor and K. R. Poeppelmeier, *Prog. Solid State Chem*., 1993, **22**, 197-233
2. D. Serrate, J. M. De Teresa and M. R. Ibarra, *J. Phys.: Condensed Matter*, 2007, **19**, 023201
3. K. Boulahya, M. Parras and J. M. Gonzalez-Calbert, *Chem. Europ. J*., 2007, **13**, 910-915
4. K. Yoshii, *J. Alloys Compd*., 2000, **307**, 119-123
5. S. Jinhyan, S. Minseok and L. Jaiyeoul, *J. Electroceramics*, 2006, **19**, 205-209,
6. L. Zhaofei, L. Guobao, S. Juhliang, W. Yinglia, Y. Liping and L. Jianhua, *Solid State Sci*., 2006, **8**, 1035-1040
7. L. Zhaofei, L. Guobao, S. Juhliang, W. Yinglia, Y. Liping and L. Jianhua, *J. Solid State Chem*., 2005, **178**, 3315-3322
8. F. Sher, A. J. Williams, A. Venimadhev, M. G. Blamire and J. P. Attfield, *Chem. Mater*., 2005, **17**, 1792-1796
9. I. B. Sharma, S. Jumari and S. Gupta, *J. Alloys Compd*., 2005, **402**, 12-16
10. S. Min-Seok, K. Suk-Young, L. Jai-Yeoul, *Ceramics*, 2004, **48**, 175-179
11. P. D. Battle, S. K. Bollen and A. V. Powell, *J. Solid State Chem*., 1992, **99**, 267-275
12. P. D. Battle, J. C. Burley, D. J. Galleon, C. P. Grey and J Sloan, *J. Solid State Chem*., 2004, **177**, 119-125
13. D. J. Galleon, P. D. Battle, S. J. Blundell, J. C. Burley, A. I. Coldea, E. J. Cussen, M. J. Rosseinsky and C. Steer, *Chem. Mater*., 2002, **14**, 3976-3983
14. I. B. Sharma and S. K. Magotra, *J. Alloys Compd*., 1999, **284**, 18-21
15. C. Bernuy, M. Allix, C. A. Bridges, J. B. Claridge and M. J. Rosseinsky, *Chem. Mater*., 2007, **19**, 1035-1043
16. C. J. Howard, *J. Appl. Cryst*., 1982, **15**, 615-620
17. P. Thomson, D. E. Cox and J. B. Hastings, *J. Appl. Cryst*., 1987, **20**, 79-83
18. H. Shaked, J. Jorgensen, O. Chmaissem, S. Ikeda and Y. Maeno, *J. Solid State Chem*., 2000, **154**, 583-586
19. M. A. Subramanian, M. K. Crawford and R. L. Harlow, Mat. Res. Bull., 29, 1994, 645-650

Chapter 7 – $Sr_3Ti_2O_7$

Introduction

In the previous chapters we have encountered Ruddlesden-Popper phases which crystallise in space groups characterised by their distorted oxygen sublattices. The crystal structures were all derived from tilts of oxygen octahedra in the published strontium titanate n = 2 Ruddlesden-Popper structure. For $Gd_2SrCo_2O_7$, the structure was also shown to change as a function of temperature, with a phase change at 673 K.

In this chapter the results of variable temperature diffraction experiments carried out on the archetypal Ruddlesden-Popper phase, $Sr_3Ti_2O_7$ are discussed. The unstrained oxygen sublattice in this material was not be expected to distort at room temperature, but by carrying out variable temperature diffraction on this material allowed previous results to be compared to the structure of a material with a d^0 metal ion that cannot undergo spin crossover.

Neutron diffraction was a valuable tool both to confirm that the room temperature structure of $Sr_3Ti_2O_7$ is undistorted by determining accurate oxygen positions, and to probe the change in structure as a function of temperature.

Previous $Sr_3Ti_2O_7$ studies

Structure determinations of $Sr_3Ti_2O_7$

Previous studies on $Sr_3Ti_2O_7$ have been limited considering the extensive chemistry of its derivatives. The structure was reported in 1958 by Ruddlesden and Popper, [1-2] along with the description of the full series of Ruddlesden-Popper phases, determined by X-ray diffraction. Later structural considerations of the family of materials based on substitution of cations in the $Sr_3Ti_2O_7$ structure were examined by Blasse. [3] This work showed that the distortions of Sr_2TiO_4 and $Sr_3Ti_2O_7$ structures (the n = 1 and n = 2 Ruddlesden-Popper phases) could be predicted by the Pauling electrostatic valence principle. Blasse also considered the extent to which spectroscopy could be used to measure these distortions.

Elcombe *et al*. used neutron diffraction to refine the room temperature structure of $Sr_3Ti_2O_7$ and determine the structure of three calcium substituted analogues ($Ca_3Sr_2O_7$, $Ca_{3.6}Sr_{0.4}Ti_3O_{10}$ and $Ca_4Ti_3O_{10}$). [4] While the room temperature structure of $Sr_3Ti_2O_7$ was confirmed to be an undistorted *I*4/*mmm* phase as reported by Ruddlesden and Popper, the calcium analogue crystallises in a phase with *Ccm*2_1 supercell symmetry, and the n = 3 materials both form *Pcab* supercells. The structures of all three distorted materials are derived from tilts of TiO_6 octahedra, similarly to the structure of the parent perovskite $CaTiO_3$. For the two three-layered materials, the partially substituted $Ca_{3.6}Sr_{0.4}Ti_3O_{10}$ is less distorted than the pure $Ca_4Ti_3O_{10}$, as would be expected from the undistorted structures of the strontium Ruddlesden-Popper phases.

Prior to this work, no variable temperature neutron diffraction studies had been reported for $Sr_3Ti_2O_7$.

Formation mechanism of $Sr_3Ti_2O_7$

Studies have been carried out by a number of groups into the changes in morphology of $Sr_3Ti_2O_7$ crystals encountered when the material is formed by molten salt synthesis. [5-7] By studying the phases present in the flux while the reaction proceeds, a growth mechanism has been proposed by Zhiyou *et al*. [7] A central core of $SrTiO_3$ forms, and two dimensional nucleation adds layers of $Sr_3Ti_2O_7$ to this core.

The effect of ball milling the starting materials on the synthetic conditions required to form $Sr_3Ti_2O_7$ has been examined by Hungria *et al*. [8] Ball milling (mixing products by mechanically shaking or rolling with steel balls prior to heating) reduces the final heating temperature required to produce perovskite phases by activating starting materials. The milling process aids reaction by mixing reactants more intimately than is possible by hand grinding, and reducing the crystallite size of starting materials to further improve crystallite mixing. Milling also damages the crystal structure of the starting materials, raising the internal energy and reducing the thermal activation and reaction time required for reaction. The effect of synthesis temperature, milling technique and time and choice of starting materials on crystallinity, morphology and purity of the final products was investigated by variable temperature powder X-ray diffraction. By optimising the reaction conditions, phase pure $Sr_3Ti_2O_7$ with good crystal homogeneity could be formed. The $SrTiO_3$ nucleation mechanism as suggested by the molten flux studies was confirmed by the formation of $SrTiO_3$ and $SrCO_3$ (from the reaction of $Sr(OH)_2$ and SrO with atmospheric CO_2) after the milling step of the synthesis.

Properties of $Sr_3Ti_2O_7$

Other studies of the material $Sr_3Ti_2O_7$ have not focussed primarily on the structure of the material. The stability of the $Sr_3Ti_2O_7$ lattice has been used to stabilise the uncommon Cr (IV) oxidation state by Zvereva *et al*. [9] This is reminiscent of the formation of $Gd_2SrCo_2O_7$ in which the lattice stabilises the uncommon Co (III), in particular the IS state as discussed previously in this work. The doping of the lattice by Cr (IV) is demonstrated by changes in the structure and magnetic and optical properties from the parent material.

By doping either the *A* or *B* site in $Sr_3Ti_2O_7$ with other metal ions, the conductivity of the material can be altered. By doping Al, Ga and Co onto the *B* site, Navas *et al*. formed the defect materials $Sr_3Ti_{2-x}M_xO_{7-\delta}$ (*M* = Al, Ga, Co) which exhibit either *p*- or *n*-type semiconductivity depending on the oxygen partial pressure and temperature. [10] High ionic conductivity ($>10^{-2}$ Scm^{-1}) with low activation energy (0.6 eV) is observed with intermediate oxygen partial pressures at 700 °C. The results are consistent with the proposed defect model. *n*-type semiconductivity has also been observed in materials based on $Sr_3Ti_2O_7$ doped with La/Nd and Nb. [11]

Two groups have examined the photocatalytic potential of doped $Sr_3Ti_2O_7$ for cracking water to produce hydrogen. Using a catalyst based on 1 % NiO supported on $Sr_3Ti_2O_7$, Jeong *et al*. increased the rate of water decomposition from 20 μmolhr^{-1} using solely ultraviolet irradiation to 80 μmolhr^{-1}. [12] Later work with a 1.5 % Cu/$Sr_3Ti_2O_7$ catalyst further increased this rate to 1140 μmolhr^{-1}. [13]

Synthesis

Six one gram batches of $Sr_3Ti_2O_7$ were prepared by a modification of the literature method. [1] $SrCO_3$ and TiO_2 were ground in a 3:2 ratio, then heated to 1273 K overnight. The reactants were reground, pelletised and heated to 1673 K for one week with two intermediate grinds. The purity of the products was checked by X-ray powder diffraction. Of the six samples, two appeared to be pure $Sr_3Ti_2O_7$, with no impurity peaks corresponding to either $SrTiO_3$ or Sr_2TiO_4 visible in the diffractograms. The materials were off-white, with a slight yellow colouration. The pure materials were combined, ground, pelletised and heated to 1673 K for two further days to homogenise the final product.

Structural study of $Sr_3Ti_2O_7$

X-ray diffraction

Powder X-ray powder diffraction was carried out on a Bruker D8 Advance diffractometer equipped with a PSD operating on monochromated Cu $K_{\alpha 1}$ incident X-rays. An Anton-Paar HTK 1200 furnace was fitted to the diffractometer to allow elevated temperature data sets to be collected. Diffraction sets were collected with 0.017 ° 2θ step size (one second per step) between 10 and 90 ° 2θ over the temperature range 323 to 1373 K. Figure 7.2 shows part of the thermodiffractogram. A refinement of the 323 K data is shown in Figure 7.1, confirming the purity of the target phase. 49 parameters were refined: 30 background parameters, four Pseudo-Voight peak shape parameters, one histogram scale factor, two lattice parameters, one zero point error, four atomic coordinates and five isotropic and two anisotropic temperature factors. Extracted structural parameters are shown in Table 7.1. The Ti temperature factor was refined anisotropically to $U_{11} = U_{22} = 0.0379\ (14)$ Å^2, $U_{33} = 0.0019\ (21)$ Å^2. The high background is caused by the furnace stage of the diffractometer as the Mylar windows of the furnace interpose the X-ray beams.

The refinement confirmed that the sample was single phase (as far as could be determined by X-ray diffraction), and could be used for variable temperature neutron diffraction experiments.

Table 7.1 – Extracted structural parameters from the refinement of 323 K diffraction data for $Sr_3Ti_2O_7$ in *I*4/*mmm*. $a = b = 3.89751$ (9) Å, c = 20.3344 (6). $R_{wp} = 7.72$ %, $R_p = 5.02$ %, $\chi^2 = 4.114$. * indicates the average of anisotropic temperature factors.

Atom	*x*/*a*	*y*/*b*	*z*/*c*	U_{iso} / 10^{-2}Å^2	Site Occupancy
Sr1	0.5	0.5	0	2.65 (11)	1
Sr2	0.5	0.5	0.18464 (8)	2.18 (7)	1
Ti	0	0	0.0976 (2)	2.59*	1
O1	0	0	0	1.7 (5)	1
O2	0	0	0.1939 (5)	2.2 (4)	1
O3	0	0.5	0.0979 (4)	2.6 (2)	1

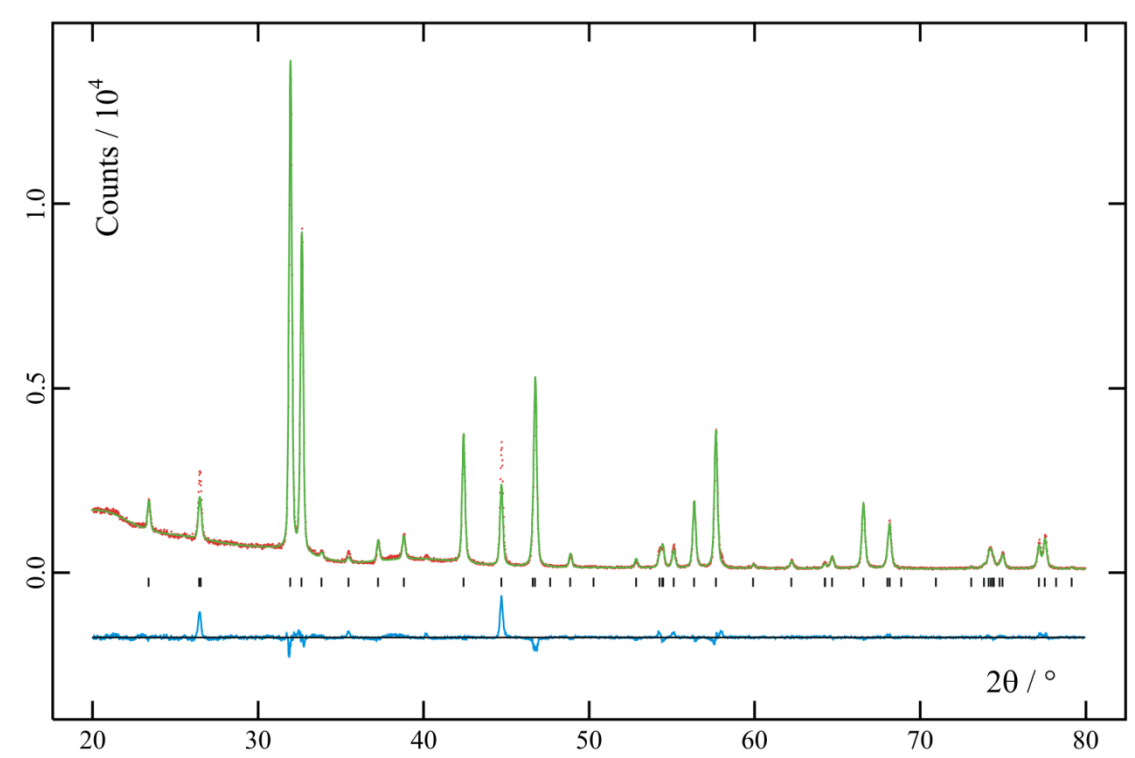

Figure 7.1 – Part of the profile fit of room temperature powder X-ray diffraction data collected on $Sr_3Ti_2O_7$.

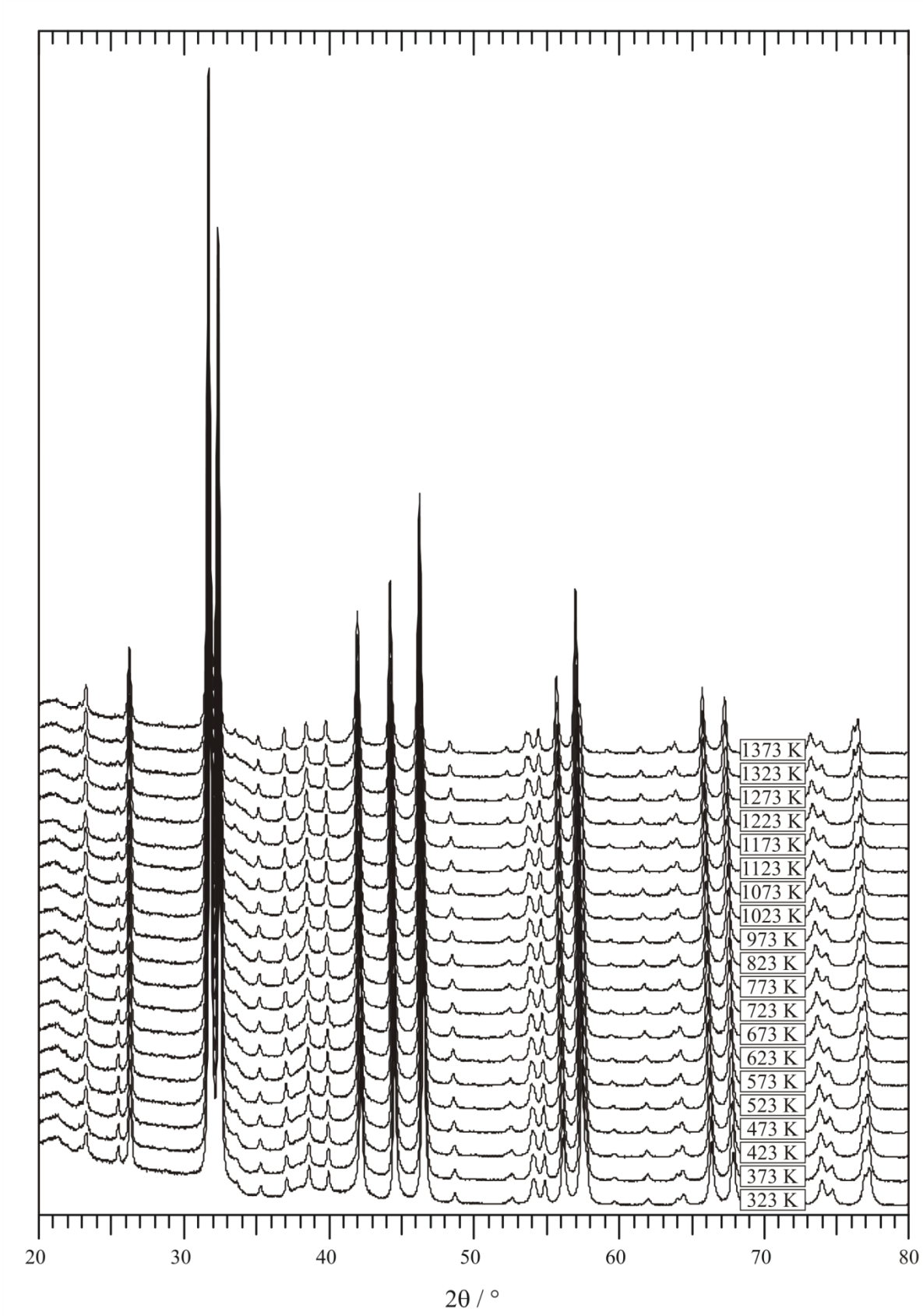

Figure 7.2 – Part of the X-ray thermodiffractogram collected on $Sr_3Ti_2O_7$ between 323 and 1373 K.

Powder neutron diffraction

Powder neutron diffraction was carried out on the HRPD instrument at the ISIS neutron source. The long flight path for this instrument gives the best possible resolution, which is

ideal for this study where it is possible that small distortions of the oxygen sublattice could cause very subtle splitting of peaks.

Diffraction data were collected at room temperature, then at 100 K intervals from 373 to 1073 K. The raw data from the backscattering (168 °) detector bank is shown in Figure 7.3.

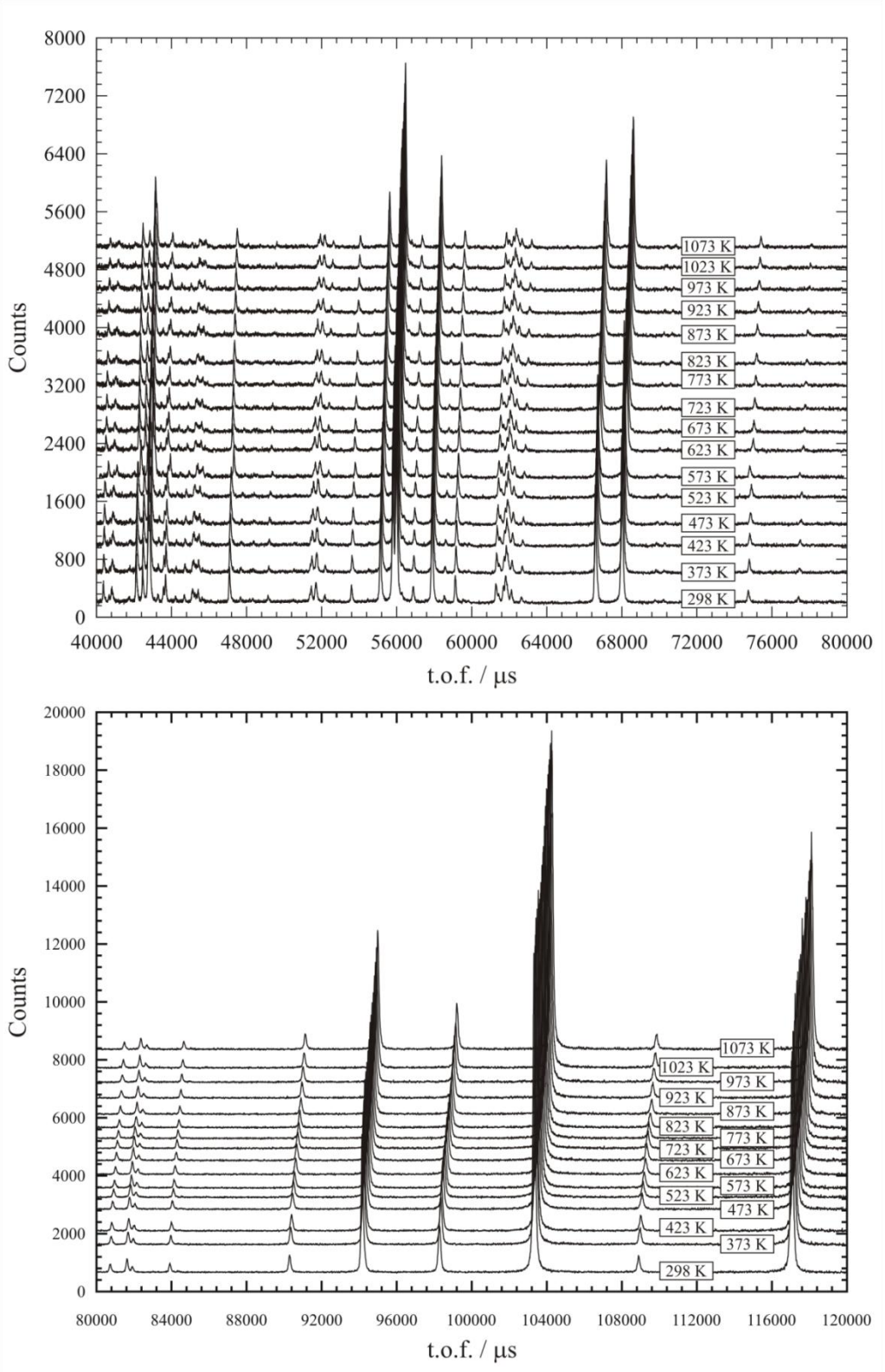

Figure 7.3 – Thermodiffractogram collected on $Sr_3Ti_2O_7$ on HRPD at ISIS. Backscattered (collection angle 168°) diffraction data are shown between 40000 and 80000 μs (top) and 80000 and 120000 μs (bottom).

The room temperature structure was confirmed by refinement of the 90 ° and backscattered detector banks. Overall, 48 parameters were refined: 12 parameters describing each histogram background; one atomic displacement for each of Ti, Sr and two O atoms; one isotropic temperature factor for each of six atoms; two pseudo-Voight peak parameters for each histogram for the $Sr_3Ti_2O_7$ phase; one phase scale factor for the small $SrTiO_3$ impurity phase; two zero point errors; two histogram scale factors and three lattice parameters, two for the $Sr_3Ti_2O_7$ phase and one for the $SrTiO_3$ phase. The atomic positions and peak shape parameters for the $SrTiO_3$ phase were refined independently of the final refinement of the main phase. The presence of a small impurity phase that was not observed in the XRD patterns explains the poor fitting to several peaks in Figure 7.1. The structural refinements to the backscattered and 90 ° detector bank data are shown in Figure 7.4 and Figure 7.5.

Extracted structural parameters are shown in Table 7.2. Despite the good fit to the data, the model produced by this refinement is not a good crystallographic model as several of the temperature factors are negative: this is not meaningful. None of the elements in the material have a significant neutron absorption cross-section, so this cannot explain the negative temperature factors. Refining only the backscattered diffraction data gives only positive temperature factors, indicating that this problem arises from poor fitting to the peak shape in the 90 ° bank. The refinement is shown in Figure 7.6. The parameters extracted from refining the structure based only on the backscattered bank are shown in Table 7.3. Only the backscattered bank data were used for all further refinements.

Table 7.2 – Extracted structural parameters from refinement of room temperature diffraction data (backscattered and 90 ° banks) for $Sr_3Ti_2O_7$ in *I*4/*mmm*. $a = b = 3.901589$ (19), $c = 20.36187$ (11), overall $\chi^2 = 9.477$.

Atom	*x*/*a*	*y*/*b*	*z*/*c*	U_{iso} / 10^{-2}Å^2	Site Occupancy
Sr1	0	0	0.09750 (6)	0.54 (3)	1
Sr2	0.5	0.5	0	0.13 (3)	1
Ti	0.5	0.5	0.184174 (3)	-0.22 (19)	1
O1	0	0	0	-0.13 (3)	1
O2	0	0.5	0.096222 (20)	-0.011 (15)	1
O3	0	0	0.19424 (4)	0.033 (3)	1

Table 7.3 – Extracted structural parameters from refinement of room temperature diffraction data (backscattered bank only) for $Sr_3Ti_2O_7$ in *I*4/*mmm*. $a = b = 3.900000$ (20), $c = 20.35426$ (12), $R_{wp} = 8.67$ %, $R_p = 7.48$ %, $\chi^2 = 1.309$.

Atom	*x*/*a*	*y*/*b*	*z*/*c*	U_{iso} / 10^{-2}Å^2	Site Occupancy
Sr1	0	0	0.09734 (12)	0.29 (4)	1
Sr2	0.5	0.5	0	0.57 (5)	1
Ti	0.5	0.5	0.18486 (6)	0.44 (3)	1
O1	0	0	0	0.36 (5)	1
O2	0	0.5	0.09604 (4)	0.54 (2)	1
O3	0	0	0.19377 (7)	0.56 (5)	1

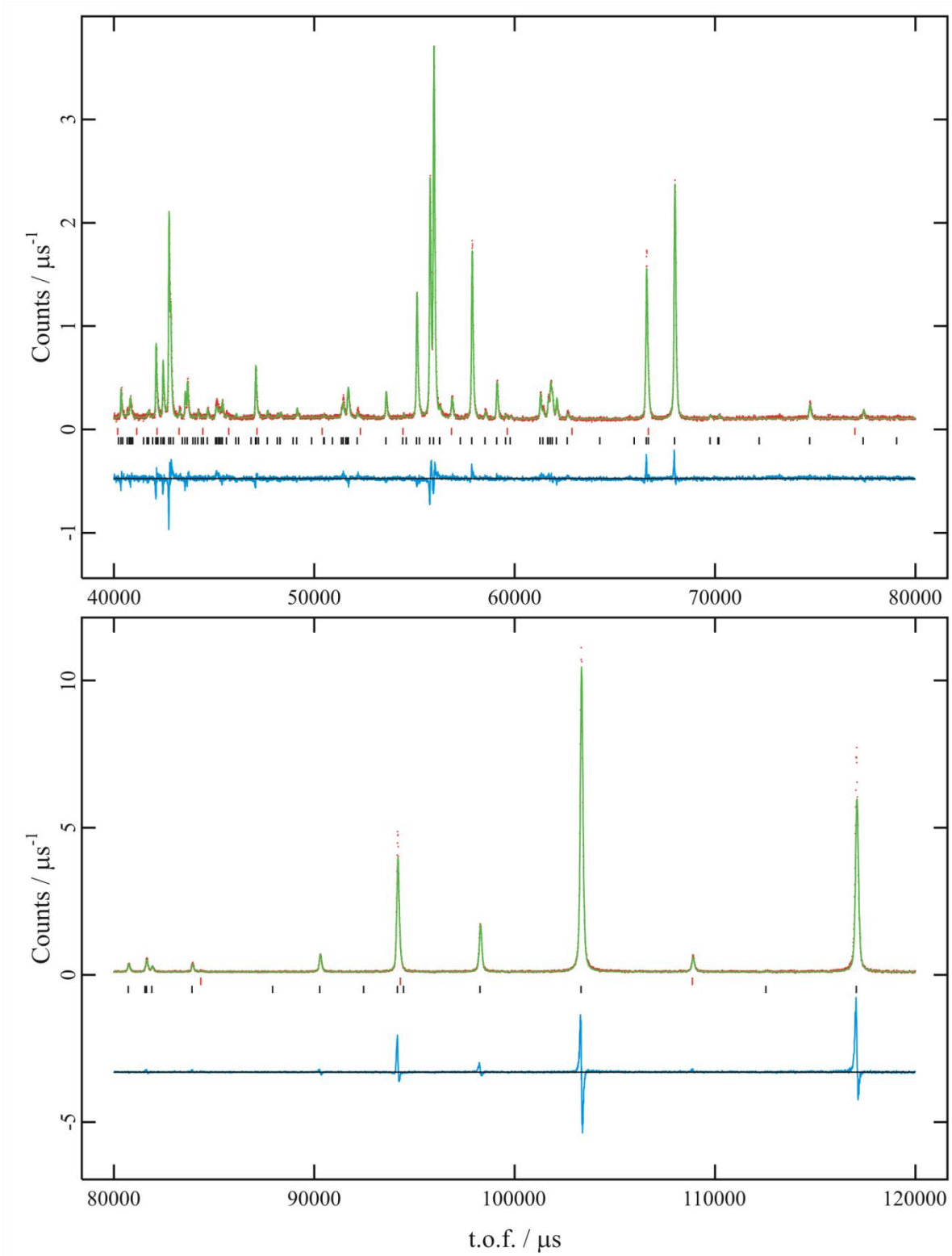

Figure 7.4 – Profile fit of room temperature backscattered PND data collected on $Sr_3Ti_2O_7$ in *I*4/*mmm*. Upper tick marks show $SrTiO_3$ impurity phase reflection positions. R_{wp} = 11.52 %, R_p = 11.39 %.

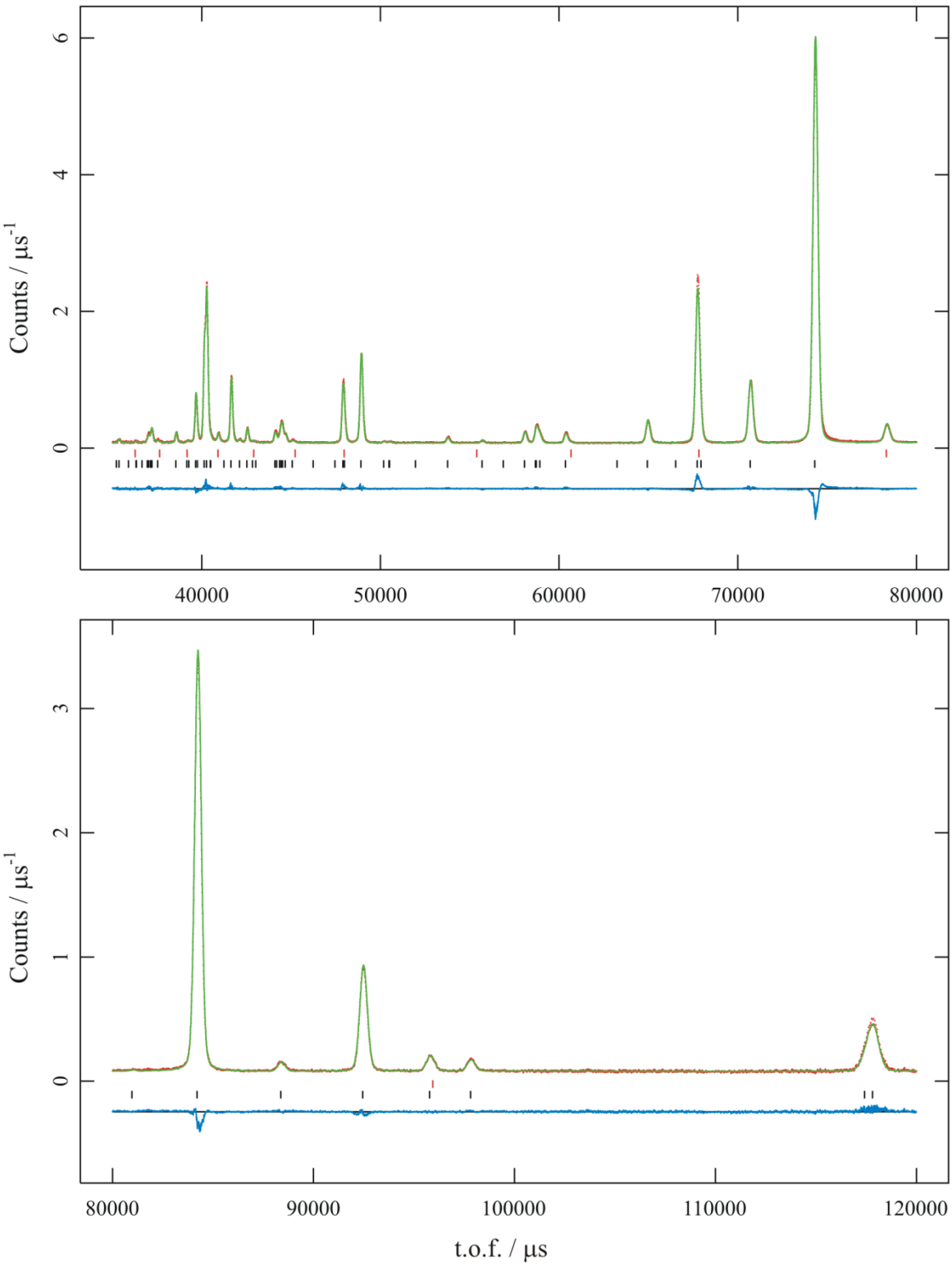

Figure 7.5 – Profile fit of room temperature 90° bank PND data collected on $Sr_3Ti_2O_7$ in *I*4/*mmm*. Upper tick marks show $SrTiO_3$ impurity phase reflection positions. R_{wp} = 5.53 %, R_p = 4.29 %.

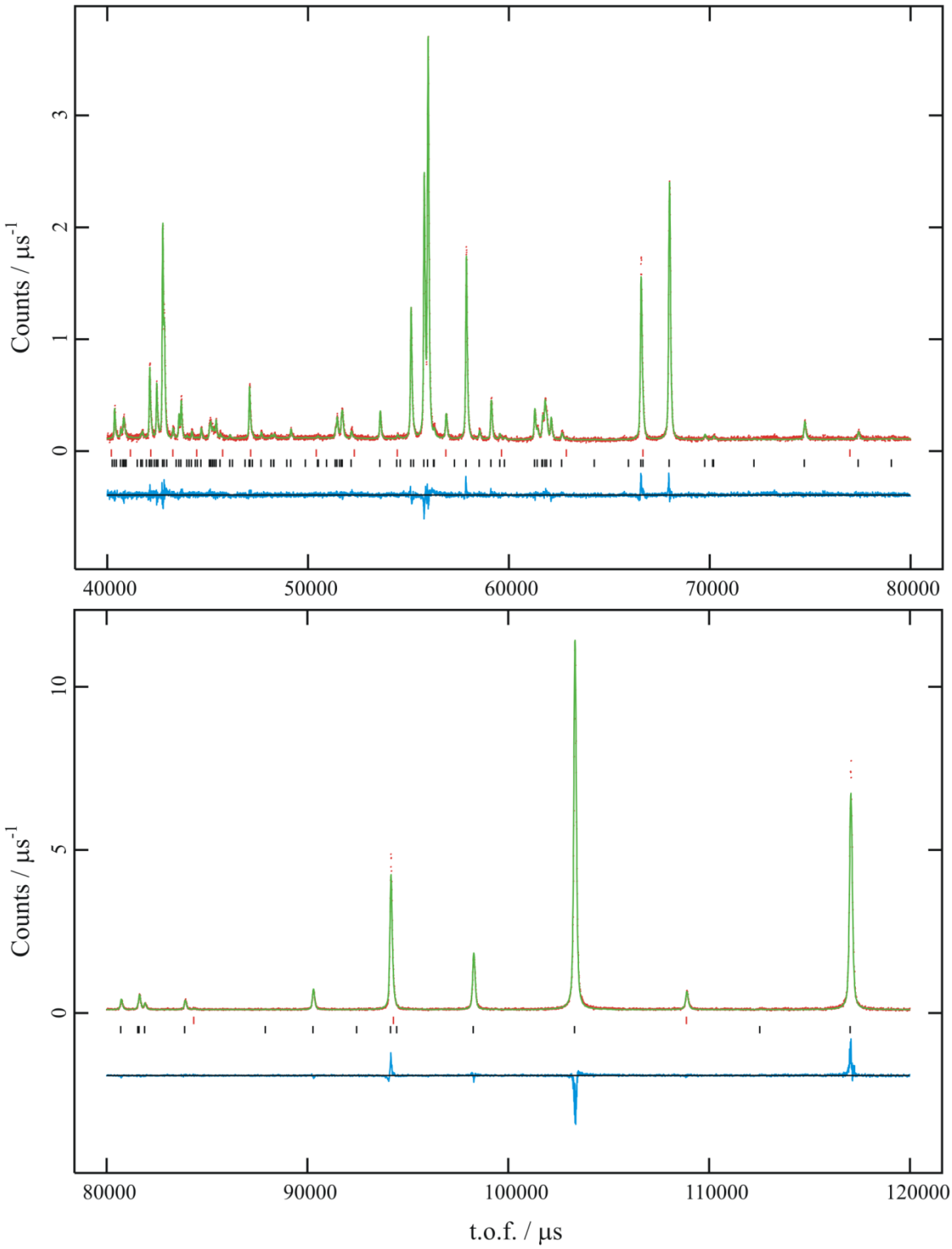

Figure 7.6 – Profile fit of room temperature backscattered diffraction data of $Sr_3Ti_2O_7$ in *I*4/*mmm*. Upper tick marks show $SrTiO_3$ reflection positions.

Variable temperature neutron diffraction

Structures were refined for $Sr_3Ti_2O_7$ at all temperatures based on the backscattered neutron diffraction data. For all data sets 27 parameters were refined: twelve background parameters, one histogram scale factor, two lattice parameters, one zero point error, four atomic coordinates and six isotropic temperature factors were varied. For the room temperature data set the phase fraction of $SrTiO_3$ was also included in the final refinement, however once again

the temperature factors and peak shape for this phase were refined independently to the final refinement.

The extracted structural parameters from these refinements are shown in Figure 7.8, Figure 7.9 and Figure 7.10. No discontinuities are observed in the thermal expansion as shown by the variation in lattice parameters with temperature, Figure 7.7. Before evaluating the structural changes in $Sr_3Ti_2O_7$ as a function of temperature, the bond lengths must be extracted. The structural parameters extracted are shown for illustrative purposes.

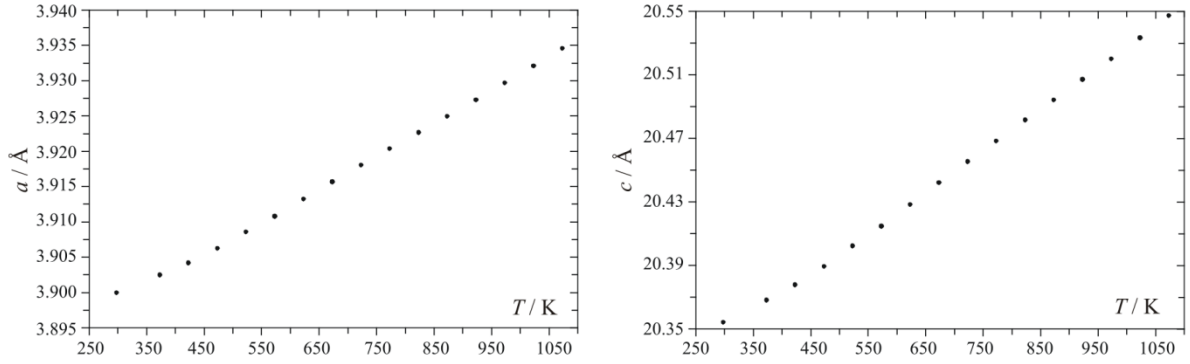

Figure 7.7 – *a* and *c* cell parameters extracted from refinements of backscattered diffraction data.

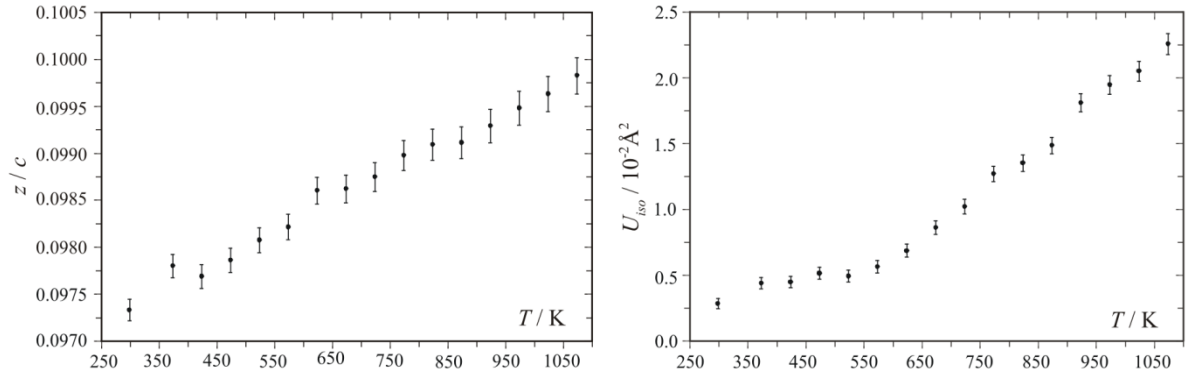

Figure 7.8 – Ti *z*/*c* (left) and isothermal temperature factor (right) extracted from refinements of backscattered diffraction data.

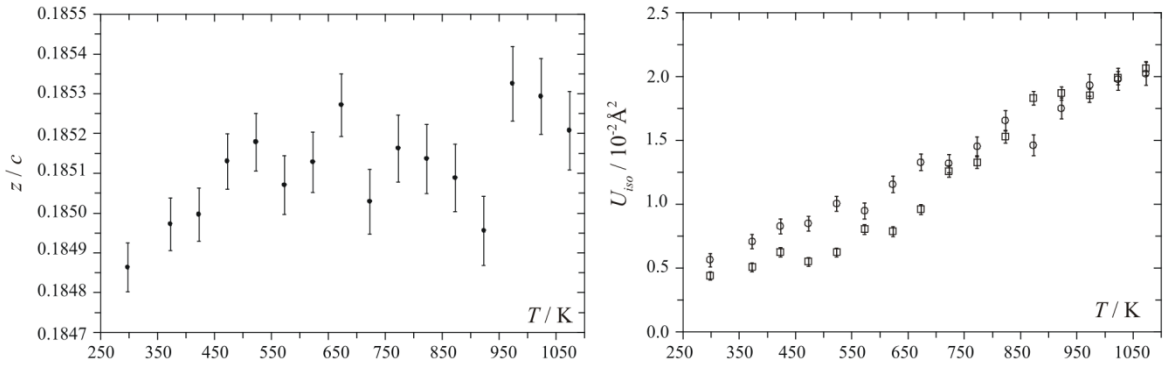

Figure 7.9 – Sr *z*/*c* (left) and isothermal temperature factors (Sr1 (○), Sr2 (□)) (right) extracted from refinements of backscattered diffraction data.

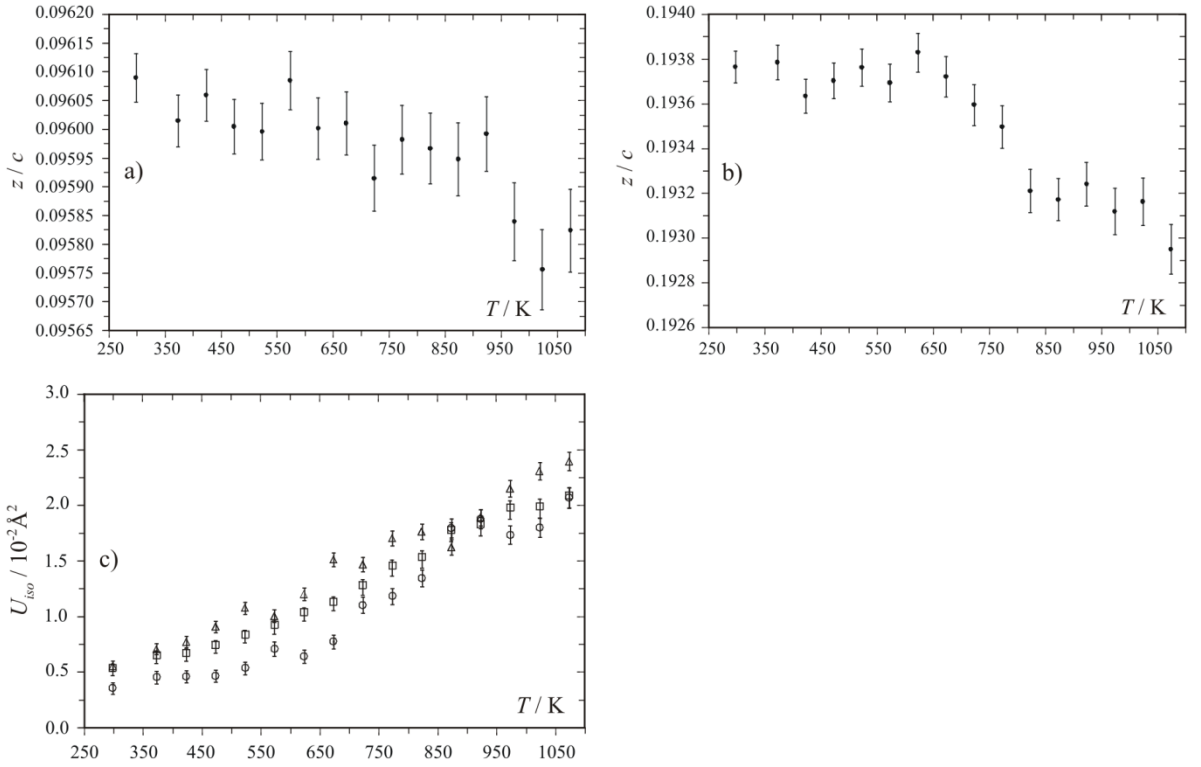

Figure 7.10 – O atomic positions and thermal expansion parameters extracted from refinements of backscattered diffraction data. a) O2 *z*/*c*; b) O3 *z*/*c*; c) O1 (○), O2 (□) and O3 (Δ) isothermal temperature factors.

Extracted bond lengths

Bond lengths extracted from structural refinements based on backscattered HRPD data are shown as a function of temperature in Figure 7.11. All Sr-O bond lengths and the average Ti-O bond lengths vary smoothly as a function of temperature. The bonds to bridging and apical oxygen atoms (Ti-O1 and Ti-O3) appear to expand and contract over the temperature range, however this appears to be an artefact of coupling between the two bond lengths. This can be compared to the behaviour of bond lengths previously observed for $Gd_2SrCo_2O_7$ in which the bridging Co-O bond undergoes an independent expansion at the transition temperature.

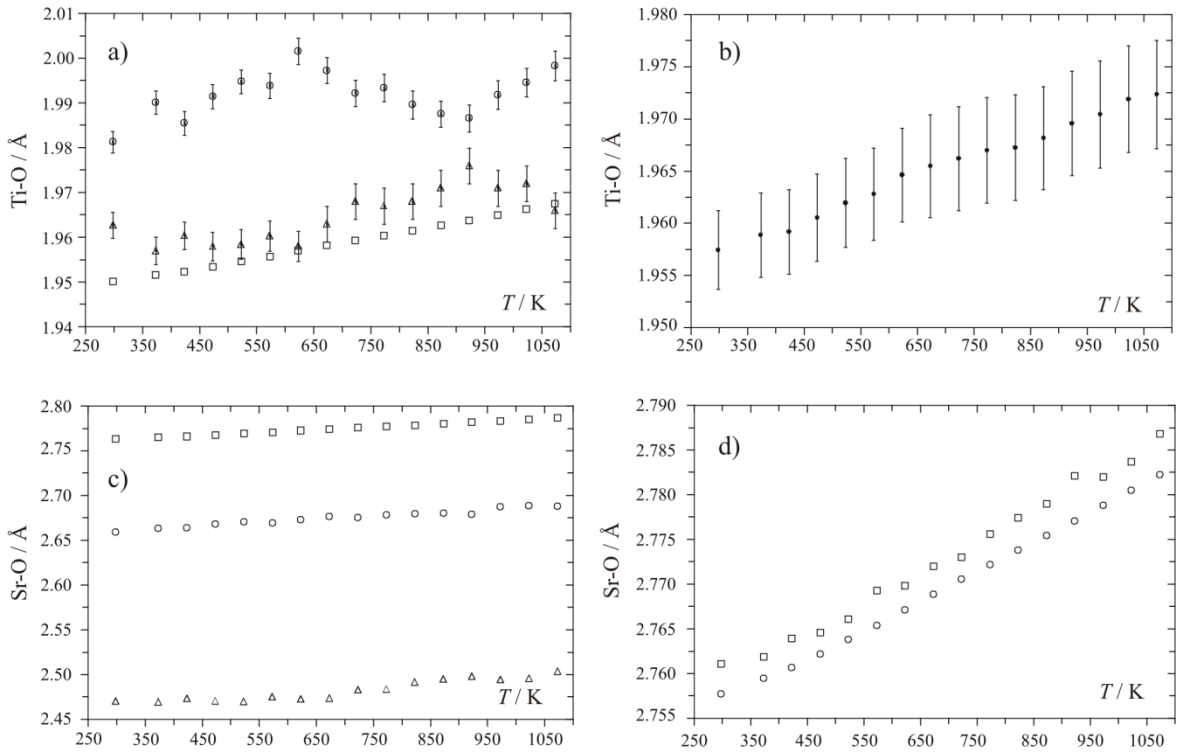

Figure 7.11 – Bond lengths extracted from refinements of PND data collected on HRPD at ISIS. a) Ti-O1 (○), Ti-O2 (□) and Ti-O3 (Δ); b) average Ti-O; c) Sr2-O2 (○), Sr2-O3 (□), Sr2-O3 (Δ); d) Sr1-O1 (○), Sr1-O2 (□). Error bars denote one standard error, no error bar displayed shows errors within point size.

Conclusions

The structure of $Sr_3Ti_2O_7$ has been determined as a function of temperature. Unlike other mixed-cation $A_3B_2O_7$ phases studied in this work, the room temperature structure is undistorted, crystallising in *I*4/*mmm*, a = 3.90000 Å, c = 20.3543 Å. This is consistent with its unstrained sublattice, [14] and with previous studies carried out on this material. It also supports the conclusion that a mixed *A*-site promotes distortion of the oxygen sublattice and a reduction of lattice symmetry.

On heating from 298 to 1073 K, the lattice parameters and bond lengths expand smoothly, again consistent with no structural changes on heating. The volume of the unit cell is shown in Figure 7.12.

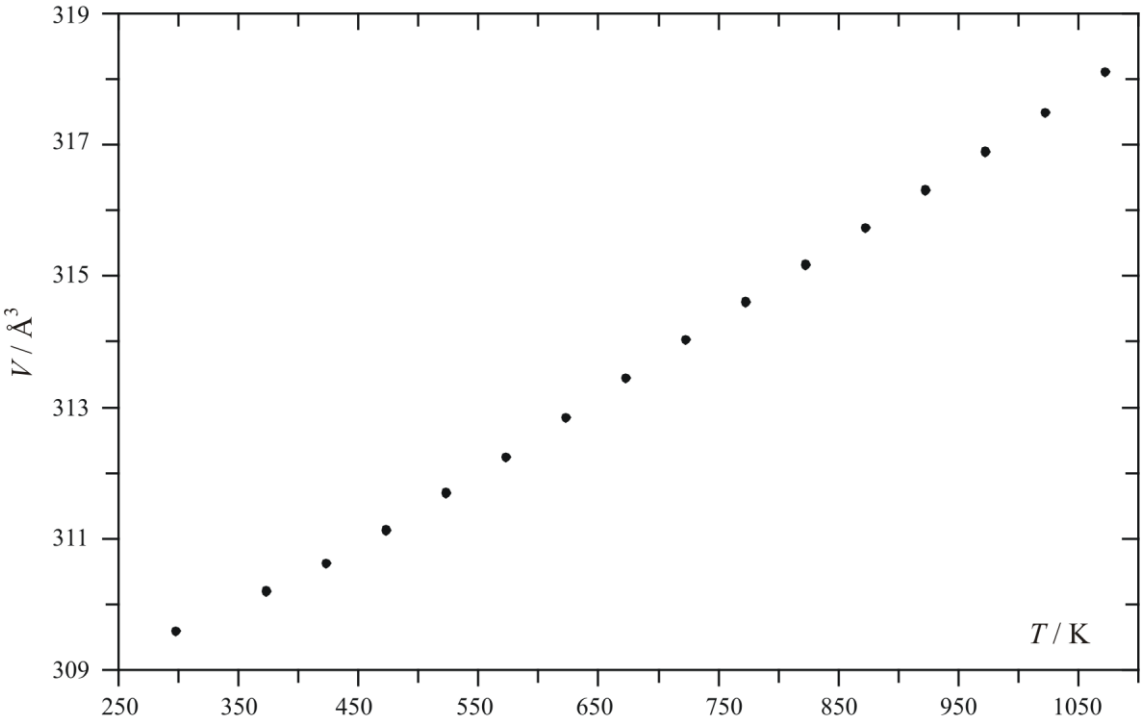

Figure 7.12 – Unit cell volume extracted from PND data collected on HRPD at ISIS. Errors lie within point size.

References

1. S. N. Ruddlesden and P. Popper, *Acta Cryst.*, 1957, **10**, 538
2. S. N. Ruddlesden and P. Popper, *Acta Cryst.*, 1958, **11**, 54-55
3. G. Blasse, *Chem. Phys. Lett.*, 1975, **33**, 616-618
4. M. M. Elcombe, E. H. Kisi, K. D. Hawkins, T. J. White, P. Goodman and S. Matheson, *Acta Cryst.*, 1991, **B47**, 305-314
5. E. K. Akdogan, R. E. Brennan, M. Allahverdi and A. Safari, *J. Electroceramics*, 2006, **16**, 159-165
6. Y. F. Liu, Y. N. Lu, M. Xu and L. F. Zhoun, *J. Am. Ceram. Soc.*, 2007, **90**, 1774-1779
7. L. Zhiyou, Z. Xiaoyong, H. Junfeng and Z. Kechao, *J. Cryst. Growth*, 2007, **305,** 265-270
8. T. Hungria, J. G. Lisoni and A. Castro, *Chem. Mater.*, 2002, **14**, 1747-1754
9. I. Zvereva, I. German, Y. Smirnov and J. Choisnet, *J. Mater. Sci. Lett.*, 2001, **20**, 127-130
10. C. Navas, H. L. Tuller, H. C. zur Loge, *J. Europ. Ceram. Soc.*, 1999, **19**, 737-740
11. K. H. Lee, Y. F. Wang, S. W. Kim, H. Ohta and K. Koumoto, *Int. J. Appl. Ceram. Tech.*, 2007, **4**, 326-331
12. H. Jeong, T. Kim, D. Kim and K. Kim, *Int. J. Hydrogen Energy*, 2006, **31**, 1142-1146
13. S. M. Fang, Y. Ou, J. D. Lin and D. W. Liao, *Acta Phisico-Chimica Sinica*, 2007, **24**, 601-604
14. H. Shaked, J. Jorgensen, O. Chmaissem, S. Ikeda and Y. Maeno, *J. Solid State Chem*., 2000, **154**, 361-367

Chapter 8 – Conclusions

Cobaltates

The material $Gd_2SrCo_2O_7$, known previously in the literature, [1-2] was prepared and its structure studied as a function of temperature using variable temperature powder diffraction. A phase transition was identified from the room temperature tetragonal to lower symmetry orthorhombic by the splitting of several peaks (particularly noted in the (110) group of peaks) at ~ 573 K. By carrying out powder neutron diffraction on a sample of $^{160}Gd_2SrCo_2O_7$ using the D20 instrument at the Institut Laue Langevin, it was determined that the room temperature structure of $Gd_2SrCo_2O_7$ is distorted from the reported *I*4/*mmm* through rotation of CoO_6 octahedra. The newly proposed structure is in $P4_2/mnm$, with $a = \sqrt{2}a_{I4/mmm}$ and is isostructural with several previously reported $n = 2$ Ruddlesden-Popper phases. [3-4] The *A* site is partially ordered, with the larger Sr^{2+} preferentially occupying the 12 coordinate perovskite block site, and the smaller Gd^{3+} preferentially occupying the smaller nine coordinate rock salt site. The structure of the high temperature phase has been determined by indexing powder neutron diffraction data collected at 673 K. The diffraction data are best refined in the space group *Bbmm*, a non-standard setting of the space group *Cmcm*, with $a \approx b \approx \sqrt{2}a_{I4/mmm}$. By refining all diffraction data collected while heating in the temperature range 298 – 973 K, cell parameters and Co-O bond lengths have been extracted for the entire temperature range. At the transition, the cell volume expansion shows a discontinuity, and Co-O bond lengths elongate parallel to the *c* axis. The results were consistent with a spin crossover in the Co (III) ions, which was supported by a deviation from linearity in the inverse susceptibility versus temperature plot at the transition temperature. The VSM data also suggest an intermediate spin state for room temperature $Gd_2SrCo_2O_7$ (supported by a recent study), [5] with the transition to high spin or mixed intermediate and high spin at the phase transition. Combined TGA/DSC measurements showed that the transition was endothermic, with an enthalpy of ~ 2.5 $kJmol^{-1}$, and showed that no mass was gained or lost at the transition.

The new material $Nd_2BaCo_2O_7$ has been prepared and its structure characterised by powder neutron and X-ray diffraction and Rietveld refinement. Room temperature powder diffraction data show that the material crystallises in a tetragonal space group, however as previously seen for $Gd_2SrCo_2O_7$, the powder neutron diffraction data cannot be well fitted using an *I*4/*mmm* $Sr_3Ti_2O_7$ model. The diffraction data are best fitted in the space group *Bbcb*, constrained to be metrically tetragonal. This phase is isostructural with the known material $Sr_3Ru_2O_7$. Variable temperature powder neutron diffraction data have been collected on the material $Nd_2BaCo_2O_7$ on the POLARIS instrument at ISIS. Over all temperatures 298 – 873 K, the material remains metrically tetragonal, and over the entire temperature range the diffraction data can be fitted with a *Bbcb* structural model. Unlike $Gd_2SrCo_2O_7$, no

significant structural changes are observed over the entire temperature range, with a smooth expansion of the cell volume and Co-O bond lengths.

Ferrates

The previously reported material $Gd_2SrFe_2O_7$ was prepared and its structure studied as a function of temperature with X-ray powder diffraction. The structural behaviour of the material was of interest due to its closeness in chemistry to the previously studied phase $Gd_2SrCo_2O_7$. At room temperature, the X-ray diffraction data could be indexed in the tetragonal space group *I*4/*mmm*. Above 873 K, peaks in the diffraction pattern split, indicating a reduction in unit cell symmetry from tetragonal to orthorhombic. Samples of $^{160}Gd_2SrFe_2O_7$, $La_2SrFe_2O_7$ and $Nd_2SrFe_2O_7$ were prepared for variable temperature powder neutron diffraction using the POLARIS instrument at ISIS. The Nd and La materials were prepared as the absorption cross sections of Nd and La are significantly lower than even the 98.2 % isotopically enriched ^{160}Gd used to prepare $^{160}Gd_2SrFe_2O_7$, allowing better counting statistics and more straightforward structural refinement. The variable temperature neutron diffraction data collected on $^{160}Gd_2SrFe_2O_7$ and $Nd_2SrFe_2O_7$ both showed peak splitting in the highest temperature ranges collected on each material: in the Gd material at 1073 K, and in the Nd material at 823 K. All three materials crystallise in the space group $P4_2/mnm$, isostructural with the material $Tb_2BaFe_2O_7$ reported by Samaras *et al*. [4] The diffraction patterns for the high temperature phases for $Nd_2SrFe_2O_7$ and $Gd_2SrFe_2O_7$ were indexed in the space group *Bbmm*, similarly to the high temperature structure of material $Gd_2SrCo_2O_7$. The observation of a phase transition in the iron materials shows that while spin crossover has a role in the transition in the cobalt analogue; it seems that the structural transition drives the spin crossover rather than the spin crossover driving the transition. The spin crossover in the cobaltate may be responsible for the significantly lower transition temperature in $Gd_2SrCo_2O_7$ when compared to $Gd_2SrFe_2O_7$ – 573 K compared to 873 K. Heating above the transition temperature appears to overcome an energy barrier for octahedral rotation caused by the increased stability of a structure with non-linear *M*-O-*M* bond angles.

Phase changes in cobaltates and ferrates: thermodynamic considerations

Both the cobaltate and ferrate materials studied in this work undergo phase transitions to reduced symmetry at elevated temperatures. This is counterintuitive, as discussed previously. Intuitively, it would be expected that on heating, increased thermal motion would cause averaging of non-equivalent sites to increase symmetry. This can be more rigorously explained by a thermodynamic argument.

When a material is heated, the material takes thermal energy from its surroundings. To compensate for this "ordering" of the energy entering the system, the internal entropy of the material must increase. When materials undergo a phase transition on heating, this increase in entropy is generally accommodated by increasing the symmetry of the material. Because a

previously defined crystallographic degree of freedom is lost by increasing the symmetry, the overall ordering in the system is reduced and entropy is increased.

In the systems described in this work, a reduction in symmetry is observed on heating through a phase transition. This corresponds to an increase in order, hence a decrease in entropy. For this type of transition to be possible, another source of entropy must exist to compensate for the apparently impossible reduction through symmetry reduction. Two possible explanations for the phase transitions have been previously discussed, which will now be revisited.

Spin crossover at the phase transition

One possible source of entropy for the phase transition could originate in a contribution from the electronic configuration. Figure 8.1 shows the possible electron configurations that are possible for low, intermediate and high spin cobalt (III). Magnetism data collected for $Gd_2SrCo_2O_7$ supports a change in spin state of cobalt (III) on heating through the transition, presumably from an intermediate spin ground state as calculated from magnetism data and discussed by Akiyama, [5] to either a high spin or a mixed intermediate and high spin state.

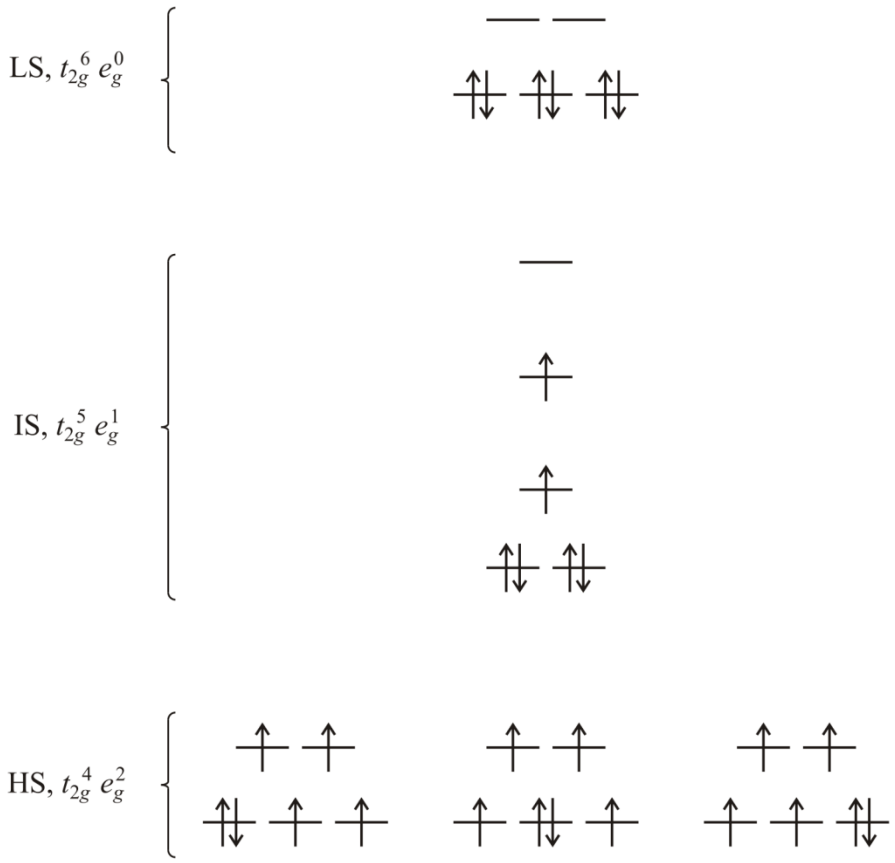

Figure 8.1 – Possible arrangements of electrons for low, intermediate and high spin d^6 configurations.

In the case of a transition to a pure high spin state, a possible source of entropy is an increase in available configurations for the electrons within the orbitals (a choice of whether to pair the d_{xy}, d_{xz} or d_{yz} electron). A transition to a mixed state would allow a choice or intermediate or high spin on each cobalt centre, and a choice of electron configuration on each high spin

centre. Assuming that these configurations are randomly occupied, this provides a possible source of "electronic entropy".

While this could explain the origin of the phase transition for the cobalt materials, this type of phase transition is not possible for the ferrates investigated in this work.

Point symmetry at the phase transition

Although the crystal symmetry of the materials decreases on heating through the phase transition, the point symmetry of several of the crystallographic sites in the structure above the transition is increased. The effect is to increase the multiplicity of many of the bond lengths and angles in the resultant structure. This effectively provides a decrease in ordering of these parameters, and an increase in entropy.

The change in point group symmetry is observed for all the phase transitions discussed in this work, and could explain the transition for both ferrate and cobaltate materials. With the observation of similar phase transitions in both of these material groups, it is tempting to attribute the transition for all materials to this change in point group. Without further evidence, however, this is impossible to confirm.

Nature of the phase transition: thermodynamic considerations

In order to compensate for the reduction in entropy caused by a reduction in crystal symmetry on heating through the phase transition in the materials studied in this work, an alternative source of entropy must be present. Two possible sources are "electronic entropy" or entropy owing to an increase in point symmetry on heating through the phase transition. Without further study, the exact nature of the transition cannot be confirmed.

Aluminates

The materials $Ln_2SrAl_2O_7$ (*Ln* = Nd, Sm, Gd, Dy) were prepared and their room temperature structures examined by powder X-ray diffraction. The room temperature diffraction data can be indexed to a tetragonal space group, consistent with the previous work on the material. [6] Because the materials were similar to the previously studied cobaltates and ferrates, the structures of these materials were of interest as comparisons could be made with the structure of a d^0 material. Powder neutron diffraction data were collected on the materials $Nd_2SrAl_2O_7$ and $Dy_2SrAl_2O_7$ on the D2B instrument at the Institut Laue-Langevin: their neutron absorption cross sections were small enough that expensive isotopically enriched lanthanides were not required for good counting statistics. The materials $Sm_2SrAl_2O_7$ and $Gd_2SrAl_2O_7$ were not used for this experiment due to their high natural absorption cross sections, however assumptions about their structures can be made based on the structural trends seen between the Nd and Dy materials (the outer members of the series). $Nd_2SrAl_2O_7$ and $Dy_2SrAl_2O_7$ both crystallise in the space group $P4_2/mnm$, with much larger octahedral tilts (identified by the magnitude of Al-O-Al angles) observed in the Dy material. The small Dy ions preferentially

occupy the nine coordinate rock salt site, which may be responsible for the large tilting of the octahedra.

Mixed *B* site Ruddlesden-Popper phases

The materials $Nd_{2-x}Sr_{1+x}Ti_xFe_{2-x}O_7$ (x = 0, 0.2, 0.4, 0.6, 0.8 and 1) were prepared, and their structures determined with powder neutron diffraction on the instrument D2B at the Institute Laue-Langevin. All materials crystallise in the space group $P4_2/mnm$, with octahedral tilts decreasing as x increases. The change in c unit cell parameter reflects the increasing proportion of the larger strontium ions on the *A* sites; however the variation of a across the series is less pronounced. This reflects the behaviour that would be expected with the strontium substituting onto the rock salt-like *A* site, with the perovskite block composition largely unchanged. The structural changes over the series are easily understood when the materials are considered as an intergrowth of $Sr_3Ti_2O_7$ and $Nd_2SrFe_2O_7$, with the degree of octahedral tilting and octahedral distortion decreasing as x increases in the series.

The syntheses of a number of $Sr_3MM'O_7$ phases were attempted by standard solid state synthetic methods, and the outcomes of the reactions analysed by powder diffraction data. Despite the wide range of *M* and *M*' used for the attempted syntheses, only the known phase Sr_3CoNbO_7 [7] was prepared in suitable purity for further structural study. Powder neutron diffraction data were collected on a sample of the material at room temperature and 3.4 K on the D2B instrument at the Institute Laue-Langevin to confirm its structure. At both room temperature and 3.4 K the material can be indexed in the tetragonal space group $I4/mmm$, with no superstructure corresponding to long range B-site cation order or octahedral tilting. No peaks were identified that could be attributed to Co (III) magnetic ordering, even at 3.4 K. From the undistorted structure, the spin state of the cobalt ions can be assumed to be low spin, as high spin would move the ratio $\frac{R_A+R_O}{R_M+R_O}$ above the critical value of $\sqrt{2}$, leading to distortion.

The structure of $Sr_3Ti_2O_7$ had not been studied by variable temperature powder diffraction prior to this work. As three materials with structures based on its lattice type studied for this work showed structural phase transitions at elevated temperature, the structural trends with varying temperature would be useful for comparison to these materials. Powder neutron diffraction data were collected between room temperature and 1073 K. Over the entire temperature range the diffraction patterns could be fitted with the standard $I4/mmm$ $Sr_3Ti_2O_7$ model. Lattice parameters and Sr-O and Ti-O bond lengths expanded smoothly with temperature. No unexpected distortion from the room temperature model was observed over the heating range.

References

1. L. Siwen and R. Yufang, *Mat. Res. Bull*., 1994, **29**, 993-1000
2. L. Siwen and R. Yufang, *J. Solid State Chem*., 1995, **114**, 286-288
3. P. D. Battle, J. E. Millburn, M. J. Rosseinsky, L. E. Spring and V. F. Vente, *Chem. Mater*., 1997, **9**, 3136-3143
4. D. Samaras, A. Collomb and J. C. Joubert, *J. Solid State Chem*., 1973, **7**, 337-348
5. K. Akiyama, H. Aoyama, N. Abe, T. Tojo, H. Kawaji and T. Atake, *J. Therm. Anal. Calorimetry*, 2005, **81**, 583-586
6. I. A. Zvereva, Y. Smirnov, V. Gusarov, V. Popova and J. Choisnet, *Solid State Sci*., 2003, **73**, 343-349
7. K. Yoshii, *J. Alloys Compd*., 2000, **307**, 119-123